Microhydrodynamics of active colloids

By

Rajesh Singh

PHYS10201204001

The Institute of Mathematical Sciences, Chennai

A thesis submitted to the

Board of Studies in Physical Sciences

In partial fulfillment of requirements

For the Degree of

DOCTOR OF PHILOSOPHY

of

HOMI BHABHA NATIONAL INSTITUTE

September, 2017

Homi Bhabha National Institute

Recommendations of the Viva Voce Board

As members of the Viva Voce Committee, we certify that we have read the dissertation prepared by Rajesh Singh entitled "Microhydrodynamics of active colloids" and recommend that it maybe accepted as fulfilling the dissertation requirement for the Degree of Doctor of Philosophy.

_____ **Date:**
Chair - Balachandran Sathipalan

_____ **Date:**
Guide/Convener - Ronojoy Adhikari

_____ **Date:**
Examiner -

_____ **Date:**
Member 1 - S. R. Hassan

_____ **Date:**
Member 2 - Purusattam Ray

_____ **Date:**
Member 3 - Sibasish Ghosh

Final approval and acceptance of this dissertation is contingent upon the candidate's submission of the final copies of the dissertation to HBNI.

I hereby certify that I have read this dissertation prepared under my direction and recommend that it may be accepted as fulfilling the dissertation requirement.

Date:

Place: **Guide**

STATEMENT BY AUTHOR

This dissertation has been submitted in partial fulfillment of requirements for an advanced degree at Homi Bhabha National Institute (HBNI) and is deposited in the Library to be made available to borrowers under rules of the HBNI.

Brief quotations from this dissertation are allowable without special permission, provided that accurate acknowledgement of source is made. Requests for permission for extended quotation from or reproduction of this manuscript in whole or in part may be granted by the Competent Authority of HBNI when in his or her judgement the proposed use of the material is in the interests of scholarship. In all other instances, however, permission must be obtained from the author.

_____

Rajesh Singh

DECLARATION

I, hereby declare that the investigation presented in the thesis has been carried out by me. The work is original and has not been submitted earlier as a whole or in part for a degree / diploma at this or any other Institution / University.

_____

Rajesh Singh

List of Publications arising from the thesis

a. Published

1. **Many-body microhydrodynamics of colloidal particles with active boundary layers**

   R. Singh, S. Ghose, and R. Adhikari, J. Stat. Mech. P06017 (2015), [arXiv:1411.0278]

2. **Universal hydrodynamic mechanisms for crystallization in active colloidal suspensions**

   R. Singh, and R. Adhikari, Phys. Rev. Lett. 117, 228002 (2016), [arXiv:1610.06528]

3. **Fluctuating hydrodynamics and the Brownian motion of an active colloid near a wall**

   R. Singh, and R. Adhikari, Eur. J. Comp. Mech. (2017), [arXiv:1702.01403]

b. Submitted

1. **Generalized Stokes laws for active colloids and their applications**

   R. Singh, and R. Adhikari, [arXiv:1603.05735]

2. **Boundaries determine the collective dynamics of self-propelled particles**

   S. Thutupalli, D. Geyer, R. Singh, R. Adhikari, and H. A. Stone, [arXiv:1710.10300]

3. **Electrohydrodynamic assembly of ambient ion-derived nanoparticles**

   D. Sarkar, R. Singh, A. Som, Manju C. K., R. Adhikari, and T. Pradeep

c. Under preparation

1. **Smoluchowski description of active colloids with hydrodynamic interactions**

   R. Singh, and R. Adhikari

2. **The rheology of active colloidal suspensions**

   R. Singh, and R. Adhikari

d. Other publications (not included in the thesis)

1. **Fast Bayesian inference of optical trap stiffness and particle diffusion**

   S. Bera, S. Paul, R. Singh, D. Ghosh, A Kundu, A Banerjee, and R. Adhikari, Sci. Rep. 7, 41648, 2017, [arXiv:1610.00315]

2. **Fast Bayesian inference of the multivariate Ornstein-Uhlenbeck process**

   R. Singh, D. Ghosh, and R. Adhikari, [arXiv:1706.04961]

3. **Direct verification of the fluctuation-dissipation relation in viscously coupled oscillators**

   S. Paul, A. Laskar, R. Singh, B. Roy, and R. Adhikari, and A Banerjee, Phys. Rev. E 96, 050102 (2017), [arXiv:1707.00660]

_____

Rajesh Singh

List of presentation and participation in conferences

- **Bayes by the Bay**

  Pondicherry, January 2013

- **RRI school on Statistical Physics**

  Bangalore, April 2013

- **SERC school and symposium on Rheology of Complex Fluids**

  Delhi, December 2013

- **Soft Matter Young Investigators Meetings - I**

  Pondicherry, January, 2014

- **Soft Matter Young Investigators Meetings - II**

  Pondicherry, December 2014 | Poster: Many-body microhydrodynamics of colloidal particles with active boundary layers

- **Eighth Symposium on Complex Fluids (CompFlu 2014)**

  Bangalore, December 2014 | Poster: Many-body microhydrodynamics of colloidal particles with active boundary layers

- **Chennai Python Users Group (Chennaipy)**

  Chennai, January 2015 | Invited talk: PyStokes - A case study of accelerating Python using Cython

- **International Conference on Discrete Simulation of Fluid Dynamics**

  DSFD-2015, Edinburgh, July 2015 | Contributed talk: Many-body microhydrodynamics of colloidal particles with active boundary layers

- **Soft Matter Young Investigators Meetings - III**

  Pondicherry, December 2015

- **International Complex Fluids Conference (CompFlu 2016)**

  Pune, January 2016 | Poster: Hydrodynamically mediated forces and torques between active colloids

- **Indian Statistical Physics Community Meeting 2016**

  Bangalore, February 2016 | Poster: Universal Hydrodynamic Mechanisms for Crystallization in Active Colloidal Suspensions

- **IASBS-ICTP School on Active Matter and Chemotaxis**

  Zanjan, May 2016 | Poster and contributed talk: Universal Hydrodynamic Mechanisms for Crystallization in Active Colloidal Suspensions

- **International Conference on Soft Materials (ICSM 2016)**

  Jaipur, December 2016 | Poster: Generalized Stokes laws for active colloids and their applications

List of corrections and changes as suggested by the examiners

Synopsis

- Fixed typographical errors.

Chapter 1

- Section 1.1: Defined the active slip velocity $\boldsymbol{v}^{\mathcal{A}}$.

Chapter 2

- Section 2.3.1: Added cross-referencing to explain the tensorial spherical harmonic coefficients of force per unit area and boundary velocity.
- Section 2.6: Added more details of the assumptions made.

Chapter3

- Section 3.1: Updated the description for configuration dependent friction tensors.
- Section 3.2: Fixed a factor of $1/2$ in the definition of power dissipation.
- Section 3.5: Explained the reduction in computation time due to exact evaluation of the matrix elements, which obviates the need of numerical quadrature, and thus, the number of unknowns is considerably reduced.

Chapter 4

- Section 4.4: Rephrased wordings to indicate that the pressure is measured at the confining surface.
- Section 3.4: Added a comparison of Brown number and Péclet number.

Chapter 5

- Section 5.2: Added more description to the numerical observation that the uniform state is unstable at any volume fraction.
- Figure 5.1: Updated the panel (g) by adding a fit of $1/N$ to it.
- Section 5.5: Added a description on the initial orientations and positions of the particles. Defined all the symbols.
- Section 5.6: Clarified that the rotation/non-rotation of an active crystal depends on the symmetry of the positions and orientations of the colloids about the center of the crystal.

Chapter 6

- Section 6.2: Fixed typos before Eq. (6.1).
- Section 6.3: Updated the description of model for better clarity.

Chapter 7

- Section 7.2: Updated the description of the model.
- Section 7.2: Added cross references to the appendix where the Green's function used to satisfy the boundary conditions in each geometry is given.
- Section 7.4: Added a detailed description of the terms - stable and unstable lines of swimmers.

Chapter 8

- Section 8.3: Added details about the limitation of a Hamilton-Jacobi approach to the solution of Smoluchowski equation.

Chapter 9

- Section 9.3: Updated the description of surface charge density and permittivity.
- Section 9.3: Added description of Figure (9.2) in the main text of the chapter.

Chapter 10

- Section 10.2: Updated the opening paragraph.
- Figure 10.2: Updated the benchmark of PyStokes by using a 16-core machine. The plot is now drawn on a log scale.
- Section 10.5: Added a more inclusive description to obtain faster numerical scalings.

Appendix

- Section A.1: Updated notation for the fundamental solution of Stokes equation.
- Section A.2: Clarified notation in the definition of planar Fourier transforms.
- Section A.3: Added description on the derivation of matrix elements.

The corrections and changes suggested by the Thesis and Viva Voce Examiners have been incorporated in the thesis.

Guide

DEDICATIONS

My Parents

ACKNOWLEDGEMENTS

Firstly, I would like to express my deepest gratitude to my advisor, Ronojoy Adhikari, for being an active force in the completion of this thesis. His depth and breadth of understanding, coupled with the clarity of thoughts, enthusiasm, and tenacity, have been a perennial source of inspiration. My understanding of various topics, which are not limited to the present work, have improved significantly due to numerous discussions with him. I also thank him for his words of wisdom at critical instants.

I thank my doctoral committee members - S. Ghosh, S. R. Hassan, P. Ray, and B. Sathipalan - for support and encouragements. Collaborative works with A. Banerjee, T. Pradeep, D. Sarkar, H. A. Stone, and S. Thutupalli have been very productive and is gratefully acknowledged. I also express my gratitude to M. E. Cates for several suggestions and discussions on the manuscripts of the publications arising out of this thesis. I am also thankful to Abhrajit Laskar, Rajeev Singh, Reshma Maiya, Somdeb Ghose, Raj Kumar Manna, Rishu Kumar Singh, Pratik Tale, and Sudhir Narayan Pathak for various discussions and help at important stages of the work.

Discussions on many aspects of the work presented in this thesis with S. Ansumali, B. Chakrabarti, P. Chaudhuri, G. Date, A. Dua, S. M. Fielding, R. Golestanian, S. Granick, D. Frenkel, H. Kusumaatmaja, J. Prost, T. V. Ramakrishnan, S. Ramaswamy, A. Saha, M. Sano, H. Stark, P. B. Sunil Kumar, G. Subramanian, J. Tailleur, S. Thampi, R. G. Winkler, and J. Yeomans is thankfully acknowledged. I would also like to extend my gratefulness for several exciting courses I have attended, over the years. In this regard, I thank R. Anishetty, P. Ashdhir, V. Deoarshi, P. Jain, M. C. Jain, K. Khare, S. N. Mazumdar, G. I. Menon, M. V. N. Murthy, V. S. Nemani, S. Puri, R. Rajesh, S. A. Ramakrishna, D. Sahdev, R. Shankar, N. Sharma, V. Subrahmanyam, M. K. Verma, and R. Vijaya.

Finally, I would like to thank my family members for their everlasting love and patience.

Contents

Abstract

Colloidal suspensions have been studied extensively in the past several decades. In the recent years a new class of colloids, called active colloids, have been synthesized. These active colloids are capable of producing flow, and possibly motion, in absence of external forces or torques. Thus microorganisms naturally belong to this category. In this thesis, we study the interplay of activity, fluid-mediated interactions, and external potentials in active colloidal suspensions and derive several testable predictions. We use the boundary-domain integral representation of the Stokes flow to obtain the full expression of the force per unit area on the surface of active colloids. The result is expressed as an infinite set of linear relations - generalized Stokes laws - between the tensorial spherical harmonic coefficients of the force per unit area and the boundary velocity. The generalized friction tensors give the linear relations between these coefficients. These are many-body functions of the colloidal configuration and can be obtained to any desired accuracy by solving a system of linear equations. The expression of the force per unit is then used to derive forces, torques, and thus, to obtain the Langevin description of active colloids in terms of the familiar mobility matrices and, the newly introduced, propulsion tensors. These Langevin equations have been implemented in a homegrown library to perform the numerical simulations reported in the thesis. The formalism is then applied to study various experimentally realizable settings. Our applications include the identification of the universal mechanisms of crystallization of active colloids at a plane wall. We also elucidate the role of boundaries in determining the collective behavior of active colloids. We show that the collective steady-states are characterized using the flow-induced phase separation mechanisms, which are of dynamical origin, and obtained from the balance of forces and torques. Our predictions are in excellent agreements with recent experiments on microorganisms, self-propelling droplets, and synthetic microswimmers.

Synopsis

Introduction

This thesis explores the role of hydrodynamic interaction in determining the collective behavior of active colloids. Active colloids are common in many physical, chemical, and biological contexts, where the nonequilibrium processes on their surfaces drive exterior flow and allow them to self-propel without external potential gradient. Their examples include auto-phoretic synthetic colloids [1–5], and microorganisms [6–8].

The force per unit area on the colloidal surface is a fundamental dynamical quantity in the mechanics and statistical mechanics of colloidal suspensions. We derive the force per unit area on the surface of the active colloids using the boundary-domain integral formulation of the Stokes equation. The expression of the force per unit area gives forces and torques on these colloids. Langevin equations for active colloids are then derived from the explicit forms of the forces and the torques.

The Langevin equations are implemented in a homegrown library, PyStokes, to perform the numerical simulations reported in this thesis. Using the analytical and numerical methods of this thesis, we derive several testable predictions by studying the interplay of active propulsion, hydrodynamic interaction, and external potential. We find excellent agreements of our theory with experiments on synthetic active colloids and microorganisms [9]. A detailed summary of the main results follows.

Generalized Stokes laws and boundary integrals

The non-equilibrium processes occurring in a thin layer around the colloidal surface manifest themselves as the active slip. We model active colloids by a slip velocity on the surface of a sphere. The active slip drives the exterior fluid flow and, possibly, leads to the motion of the colloid. Given the active slip, we seek a solution for the force per unit area on the surface of the colloid. The most direct way of obtaining the force per unit area is through the boundary integral representation of the Stokes equation. Expanding the force per unit and the slip in the basis of tensorial spherical harmonics, we obtain a solution of the boundary integral equation [10]. The solution leads to a system of linear equations for the unknown force per unit area in terms of the boundary velocity. We call the infinite set, the *generalized Stokes laws* [11]. The tensorial harmonic coefficients of the boundary velocity and the force per unit area, in the generalized Stokes laws, are related by the generalized friction tensors. We derive explicit forms of the generalized friction tensors in terms of the Green's function of Stokes flow. The solution is then valid for any geometry of Stokes flow. These laws have been applied to obtain exact expressions for forces, torques and stresslets on the colloids; and flow, pressure and entropy production in the fluid [11].

Langevin equations and boundary-domain integral equation

The Brownian contribution to the force per unit area is derived using the boundary-domain formulation of the fluctuating Stokesian fluid [12]. From the passive, active and Brownian contributions to forces and torques, we derive the Langevin description of active colloids. The solution linearly relates the unknown rigid body motion to the known values of the expansion coefficients, motivating the introduction of propulsion tensors. These tensors completely characterize hydrodynamic interactions in active suspensions just as mobility matrices completely characterize hydrodynamic interactions in passive suspensions. The hydrodynamic interactions of active colloids are then computed exactly without the need to explicitly resolve the fluid degrees of freedom. Dynamic simulation of hundreds of

thousand of hydrodynamically interacting colloids on a multi-core computational architecture is thus possible.

Unbounded flows: Active colloids in external potentials

Using the Langevin description, we study the dynamics of polar active colloids in a harmonic trap. We demonstrate the formation of orbits in a system of two active colloids by the interplay of leading one-body force and two-body torque [10]. These individual orbits coalesce to produce sustained convection-rolls, the so-called 'self-assembled pump' [13]. We then study synchronization of active colloids in a 2D lattice of harmonic traps and show that the entropy production in the lattice is related to the synchronization [11]. We have also studied dynamics of apolar and chiral active colloids and the distribution of the fluid pressure on a spherical surface confining them. We find that the dynamics and the distribution of fluid pressure are different for suspensions of extensile and contractile colloids. The difference is understood qualitatively from the fluid flow created by the active colloids.

Wall-bounded flows: Crystallization of active colloids at a plane wall

We then consider Stokes flows bounded by a plane wall. From the expressions for active forces and torques, we identify the universal mechanisms for the crystallization of active colloids near a plane wall [9]. We show that fluid flow produced by polar or apolar active colloids near plane walls mediates attractive hydrodynamic forces that drive crystallization of active colloids observed in experiments [5, 8]. Hydrodynamically mediated torques tend to destabilize the crystal but stability can be regained through critical amounts of bottom-heaviness or chiral activity. Normal modes of these active crystals relax diffusively, vanishing quadratically with wavenumber.

Stokes flows in periodic geometry

Calculations of transport properties in an infinite suspension leads to divergent quantities while there are no such divergences in experiments. We explicitly remove the divergent

contributions to the flow and then use the Ewald summation procedure to sum the absolutely convergent expression. The resulting convergent answer is then used to estimate the renormalized self-propulsion speed of active colloids as a function of volume fraction. We also study a lattice of polar active colloids in periodic geometry. The vectorial nature of the flow produced by polar colloids leads to a Crowley-like instability in this system.

Boundaries determine the collective dynamics of active colloids

We theoretically study the collective dynamics of active colloids at the air-water interface, fluid-solid wall and in a Hele-Shaw cell. We find, both in experiments and theory, that the collective behavior of active colloids crucially depends on the boundaries of the flow. The fluid flow is distorted by the presence of nearby boundaries and thus qualitatively new features appear. The results of the numerical simulations are in excellent agreements with the experiments for respective geometries of the flow.

Smoluchowski description of active colloids

We then present a study of the Smoluchowski equation for active colloidal suspensions. We derive a solution of the Smoluchowski equation by considering the Hamilton-Jacobi method [14, 15]. This is achieved by using a large deviation form of the distribution function, which reduces the Smoluchowski equation to a Hamilton-Jacobi equation. The Hamilton-Jacobi equation is then solved using well-established methods to obtain the distribution function.

Electrohydrodynamic flows: Formation of nanosheets

In collaboration, with the experimental group of Prof. T. Pradeep, we provide mechanism for the formation of nanosheets at the air-water interface by studying the electrohydrodynamic flow in a rectangular geometry. In the experiment, free charged ions are sprayed using electrospray on the air-water interface of the container with an electrode on its surface. The motion of the charged ions, due to the electrode, on the air-water interface drives the electrohydrodynamic flows at the surface [16]. The surface flow drives bulk

flow which recirculates the nanoparticles at the interface. The combined surface and bulk flow produce growing nanosheet at the interface, on opposite wall to the electrode.

PyStokes: Cython library for simulating active colloidal suspensions

PyStokes is a Cython library for computing rigid body motion of active colloidal spheres and fluid flows produced by them [17]. The library currently supports unbounded, wall-bounded, and periodic geometries of Stokes flow. Fluid flows near a fluid-fluid boundary is also supported. All the simulations reported in the thesis are performed using PyStokes.

Summary

To summarize, we have developed a formalism for studying the hydrodynamic interaction between active colloids that does not need to resolve the explicit fluid degrees of freedom. Using the boundary-domain integral representation of the Stokes flow, we derive new force laws for active colloids by expanding the boundary fields - force per unit area and the slip - in the tensorial spherical harmonics. The force laws are expressed as a set of linear relations, *generalized Stokes laws*, between the coefficients of the force per unit and the slip. The generalized Stokes laws have been used to directly obtain the forces, torques, fluid flow, fluid pressure, power dissipation and suspension stress. Since forces and torques are fundamental dynamical quantities in Newtonian or Langevin descriptions of particle dynamics, our contribution forms the basis for a microscopic theory of active suspension mechanics and statistical mechanics that conserves momentum in both the bulk fluid and at fluid-solid boundaries. The formalism is, then, applied to experimentally realizable situation. We find excellent agreements of our theory with experimental observations.

List of Figures

List of Tables

List of Symbols

The Einstein summation convention is used in this thesis. We use $i, j, \ldots$ for particle indices and Greek letters $\alpha, \beta, \ldots$ for Cartesian indices. In this list, we have used the abbreviate rigid body motion as RBM and boundary integral equation as BIE.

Symbol	*Meaning*
$\boldsymbol{R}_i$	coordinate of the centre of the i-th colloid
$\boldsymbol{p}_i$	orientation of the i-th colloid
$\boldsymbol{\rho}_i$	radius vector of the i-th colloid
$\boldsymbol{r}_i$	a point on the surface of the i-th colloid
S_i	surface of the i-th colloid
$\mathbf{F}_i^H$	hydrodynamic force on the i-th colloid
$\mathbf{F}_i^P$	body force on the i-th colloid
$\hat{\mathbf{F}}_i$	Brownian force on the i-th colloid
$\mathbf{T}_i^H$	hydrodynamic torque on the i-th colloid
$\mathbf{T}_i^P$	body torque on the i-th colloid
$\hat{\mathbf{T}}_i$	Brownian torque on the i-th colloid
$\mathbf{V}_i$	translational velocity of the i-th colloid
$\boldsymbol{\Omega}_i$	angular velocity of the i-th colloid

Symbol	*Meaning*
$\boldsymbol{v}_i$	boundary velocity of the i-th colloid
$\boldsymbol{v}_i^{\mathcal{D}}$	boundary velocity due to RBM
$\boldsymbol{v}_i^{\mathcal{A}}$	active slip at the surface of the i-th colloid
$\boldsymbol{f}$	force per unit area (traction) on the i-th colloid
$\boldsymbol{f}^{\mathcal{D}}$	force per unit area due to RBM
$\boldsymbol{f}^{\mathcal{A}}$	force per unit area due to active slip
$\hat{\boldsymbol{f}}$	force per unit area due to Brownian motion
$\mathbf{V}_i^{\mathcal{A}}$	active velocity of the i-th colloid
$\boldsymbol{\Omega}_i^{\mathcal{A}}$	active angular velocity of the i-th colloid
$\mathbf{Y}^{(l)}$	l-th tensorial spherical harmonics
$\mathbf{F}_i^{(l)}$	l-th coefficient of traction expansion
$\mathbf{V}_i^{(l)}$	l-th coefficient of slip expansion
$\mathbf{P}^{(l\sigma)}$	Projection operator: $\mathbf{V}_i^{(l\sigma)} = \mathbf{P}^{(l\sigma)} \cdot \mathbf{V}_i^{(l)}$
$\mathbf{V}_i^{(ls)}$	symmetric irreducible part of $\mathbf{V}_i^{(l)}$
$\mathbf{V}_i^{(la)}$	antisymmetric part of $\mathbf{V}_i^{(l)}$
$\mathbf{V}_i^{(lt)}$	trace of $\mathbf{V}_i^{(l)}$
$\boldsymbol{G}_i^{(l)}$	single-layer integral for fluid flow
$\boldsymbol{K}_i^{(l)}$	double-layer integral for fluid flow
$\boldsymbol{P}_i^{(l)}$	single-layer integral for fluid pressure
$\boldsymbol{Q}_i^{(l)}$	double-layer integral for fluid pressure
$\boldsymbol{S}_i^{(l)}$	single-layer integral for fluid stress
$\boldsymbol{M}_i^{(l)}$	double-layer integral for fluid stress
$\boldsymbol{G}_{ij}^{(l,l')}$	single-layer matrix elements
$\boldsymbol{K}_{ij}^{(l,l')}$	double-layer matrix elements

Symbol	*Meaning*
$\boldsymbol{\gamma}_{ij}^{(l'\sigma',l\sigma)}$	generalized friction tensors
$\boldsymbol{\mu}_{ij}^{\alpha\beta}$	mobility matrix for $\alpha,\beta = T,R$
$\boldsymbol{\pi}_{ij}^{(\alpha,l\sigma)}$	propulsion tensors
$\mathbf{\Pi}_i^{(l\sigma)}$	contribution to flow from slip mode $(l\sigma)$
$\mathbf{\Lambda}_i^{(l\sigma)}$	contribution to pressure from slip mode $(l\sigma)$
$\mathbf{\Gamma}_i^{(l\sigma)}$	contribution to stress from slip mode $(l\sigma)$
$\mathcal{F}_i^l$	operator encoding finite size of colloids
$\mathbf{G}$	Green's function of Stokes equation
$\mathbf{K}$	stress tensor associated with $\mathbf{G}$
$\mathbf{P}$	pressure tensor associated with $\mathbf{G}$
$\mathbf{G}^{\mathrm{w}}$	Lorentz-Blake tensor
$\mathbf{G}^{\mathrm{o}}$	Oseen tensor
$\boldsymbol{G}$	single-layer operator of the BIE
$\boldsymbol{K}$	double-layer operator of the BIE
$\mathbf{\Psi}$	distribution function for active colloids
$c^{(n)}$	n-body density
k_B	Boltzmann constant
T	temperature
$\boldsymbol{w}$	Brownian velocity field
$\boldsymbol{u}$	Harmonic excitation of a lattice
$\mathbf{\Delta}^{(l)}$	symmetrization operator: $\mathbf{F}_i^{(ls)} = \mathbf{\Delta}^{(l)} \cdot \mathbf{F}_i^{(l)}$
$\boldsymbol{\varepsilon}$	Levi-Civita tensor
$\boldsymbol{\delta}$	Kronecker delta
$\boldsymbol{I}$	identity tensor

Symbol	*Meaning*
b	radius of a colloid
v_s	self-propulsion speed of an active colloid
ω_s	self-rotation speed of an active colloid
V	volume of the fluid
N	number of colloids
ϕ	volume fraction
η	dynamic viscosity of the fluid
$\boldsymbol{\sigma}$	stress tensor
$\boldsymbol{\sigma}^H$	hydrodynamic stress tensor
$\boldsymbol{\sigma}^E$	electrostatic stress tensor
$\boldsymbol{v}$	fluid velocity
p	fluid pressure
$\boldsymbol{v}^\infty$	externally imposed flow
U	external potential
$\boldsymbol{\xi}$	thermal force acting on the fluid
$\dot{\mathcal{E}}$	power dissipation in the fluid
$\dot{\mathcal{S}}$	entropy production in the fluid
$\boldsymbol{\Sigma}^H$	hydrodynamic suspension stress
$\boldsymbol{\Sigma}^P$	particle contribution to the stress
$\mathcal{A}_T$	translational Activity number
$\mathcal{A}_R$	rotational Activity number
$\mathcal{B}_T$	translational Brown number
$\mathcal{B}_R$	rotational Brown number

Chapter 1

Introduction

The study of colloids - particles of size between few nanometers to several microns - suspended in a fluid medium is of importance for fundamental research as well as for practical applications [18–21]. Colloids are small enough to exhibit Brownian motion, and yet, large enough for them to be studied by methods like optical microscopy [22] and confocal microscopy [23]. Colloidal size allows tuning of interaction between them to desired strengths [24], and thus colloids form the backbone of the ubiquitous soft matter systems. Examples of colloidal systems include day-to-day things like, toothpaste, shaving cream, paint, liquid crystal displays, etc. Representative biological examples are bacterial suspensions, blood and cell cytoskeleton. The study of colloids can also be used for technological applications in guided self-assembly of functional materials and to design novel catalytic nanomotors for targeted drug delivery.

The study of colloidal suspensions has a long and distinguished history. The molecular nature of the matter was confirmed by Einstein [25] and Perrin [26] using the balance of the Brownian fluctuation and the dissipation in an equilibrium colloidal suspension. They showed that the Brownian motion of colloidal particles is a striking proof of the 'graininess' (molecular nature) of the ambient fluid. The investigation on colloids has since developed in many directions and continues to hold current research [20, 27–32].

More recently, a new class of colloids has been synthesized which are capable of producing flow in the absence of external forces or torques [1–5]. The resulting fluid stress can act back on the colloids and may cause them to translate or rotate. Microorganisms [6–8], then naturally belong to the same category of *active colloids*, which are capable of producing flow, and possibly motion, in absence of external forces or torques.

A system of many active colloids is an example of active matter [33–37]. Active matter describes systems driven out-of-equilibrium by input of energy at the level of each "active agent", where it is continuously dissipated into mechanical work. These systems spans over a wide range of length scales. Examples of active matter include bird flocks, fish schools, synthetic colloids, microorganisms etc [33, 36]. In this thesis, we only consider systems of active matter where each active agent is of colloidal dimensions. These active colloids interact hydrodynamically through the ambient fluid.

We now provide a brief introduction to the field of active colloids. An outline of the material covered in the thesis is also provided.

1.1 Active colloids

The classical phoretic motion of passive colloids is observed in systems with gradients of external imposed fields. These external fields interacts with the interfacial boundary layer of each colloid, resulting in colloidal transport [38]. Examples of phoretic phenomena include thermophoresis, where a colloid moves due to interfacial forces caused by externally imposed temperature gradient. In case of synthetic active colloids, on the other hand, the gradient of the field is created by the colloid itself [4]. These autophoretic colloids can be experimental realized in various settings by inducing surface forces from locally generated fields. This is achieved by designing asymmetric (Janus) colloids, such that a gradient of local field is established at the colloidal level, leading to interfacial forces driving the self-phoretic motion [4, 39].

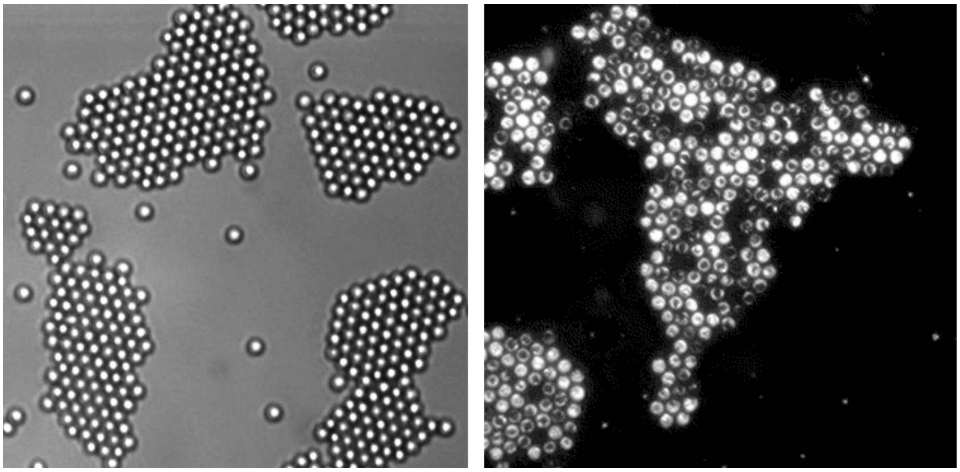

Figure 1.1: Examples of collective behaviour of active colloids observed in experiments. *Left:* Synthetic active colloids, which catalyze hydrogen peroxide when optically illuminated, crystallize into two-dimensional hexagonal crystals, when confined by a plane wall [5]. *Right:* Crystallization of chiral fast-swimming bacteria of the species *Thiovulum Majus* at a plane wall [8].

The principal feature common to both synthetic active colloids and classical phoretic motion is the appearance of interfacial forces on the colloid-fluid boundary. The typical width of this boundary layer is approximately a thousand times smaller than the size of the colloidal particle. This wide separation of scales makes it possible to partition the problem of determining the global fluid flow into an interior problem inside the boundary layer, where the flow is driven by the surface forces, and an exterior problem outside the boundary layer, where the exterior fluid is presented with a boundary condition determined by the flow in the boundary layer. The non-universal aspects of the problem are contained, therefore, entirely within the boundary layer leaving the exterior fluid flow to assume universal forms determined by the boundary conditions. We owe this method of analysis to Smoluchowski who applied it first to his study of electrophoresis [40]. With Derjaguin's analysis of diffusiophoresis [41] and its subsequent application to other kinds of phoretic motion [42], the generality and the power of this approach is now well-established [38].

The swimming of ciliated microorganisms presents another instance of the separation of scales, as the length of the cilium on the surface of such organisms is typically a hundred times smaller than the dimensions of their body [43, 44]. The flow in the ciliary layer can

be obtained from the prescribed kinematics of each cilium and the exterior fluid fluid then obtained by matching boundary conditions at the interface. This analysis has been developed extensively by Blake [44], following Lighthill's abstract analysis of the squirming motion of a sphere [43]. These authors only considered axisymmetric squirming motion and it is only recently that the most general non-axisymmetric motion has been studied systematically [45–48].

Though the microscopic mechanisms that generate motility in the various autophoretic systems and in microorganisms are vastly different, a remarkable similarity emerges at the length scale of the colloid and beyond. This is substantiated by the fact that two disparate experiments on synthetic active colloids [5] and microorganisms [8] have observed crystallization when these colloids are confined by a plane wall (see Fig. 1.1). The rationale behind these observations is the fact that the surface forces, be they of synthetic or biological origin, act on a thin interfacial region whose thickness is between a hundred to a thousand times smaller than the colloidal radius. The flow in this thin boundary layer appears at the macroscopic scale as an apparent violation of the no-slip boundary condition. Thus, microscopic details determine the form of the "slip", but to the exterior fluid, these appear only as a boundary condition. To these, we add the recent observation that the slip velocity ($\boldsymbol{v}^{\mathcal{A}}$) need not be identified with the material surface of the colloid but can, instead, be thought of as the velocity at the surface of an effective sphere enclosing a non-spherical active body such as the biflagellate green algae *C. Reinhardti* [45].

Thus, a sphere with slip provides a good representation for a surprisingly large variety of active flows and should be preferred as the simplest dynamical model of a finite-sized active body. It has also been realized that the phoretic phenomena in gradients of externally applied fields [38], the swimming of micro-organisms [49], and the self-propulsion of droplets [50, 51], though distinct in the microscopic mechanisms that produce fluid flow, share many points of similarity with synthetic active colloids when viewed at the suspension scale, and are subsumed in the field of active colloids.

1.2 Outline of the thesis

The thesis is organized as follows. In Chapter 2 we use the boundary integral representation of the Stokes flow to obtain the force per unit on the surface of active colloids. To determine the solution, we expand the force per unit area and the slip in the basis of tensorial spherical harmonics [10]. The solution of the boundary integral equation leads to a linear system of equations between the coefficients of the slip and the force per unit area. These relations are called the *generalized Stokes laws* [11]. These laws have been applied to obtain exact expressions for active suspension stress, fluid pressure and entropy production in the fluid [11].

In Chapter 3, we derive the Brownian contribution to the force per unit area using the boundary-domain formulation of the fluctuating Stokesian fluid [12]. From the passive, active and Brownian contributions to forces and torques, we derive the Langevin description of active colloids [10, 11]. These Langevin equations have been used to do numerical simulations of active colloids in distinct natural and engineered settings.

In Chapter 4, we study the dynamics of active colloids in an unbounded geometry of Stokes flow. In particular, we study the effects of confinements on active colloids by studying: (a) polar active colloids in a harmonic potential, (b) polar active colloids in two-dimensional lattice of harmonics traps, and (c) apolar active colloids in a spherical confinement.

In Chapter 5, we investigate Stokes flows bounded by a plane no-slip walls. From the expressions for active forces and torques, derived in the preceding chapter, we identify the universal mechanisms for the crystallization of active colloids near a plane wall [9]. We show that fluid flow produced by polar or apolar active colloids near plane walls mediates attractive hydrodynamic forces that drive crystallization of active colloids observed in experiments [5, 8]. Hydrodynamically mediated torques tend to destabilize the crystal but stability can be regained through critical amounts of bottom-heaviness or chiral activity.

In Chapter 6, we study active colloidal suspensions in the periodic geometry of Stokes flow. We, first, explicitly remove the divergent contributions to the flow using O'Brien's method [52]. The resulting expression has been summed using the Ewald procedure for accelerated convergence in numerical simulations. The formalism is then used to study suspensions of polar active colloids in periodic Stokes flow.

In Chapter 7, we explore the role of boundaries in determining the collective behaviour of active colloids. We find that for a given system of active colloids, strikingly new phenomena emerges by changing the geometry of the flow. We rationalize these behaviors from the qualitative and quantitative changes of the active forces and torques due to the boundaries of the flow.

In Chapter 8, we study the Smoluchowski contraction of hydrodynamic interactions in active colloidal suspensions. Explicit activity-induced breakdown of the fluctuation-dissipation relation is shown from the Smoluchowski equations. Using the Smoluchowski description, we derive one-body and two-body density for active colloidal suspension. We then use a suitable closure to determine the dynamics.

Study of electrohydrodynamic flows is presented in Chapter 9. In particular, we demonstrate the necessary and sufficient conditions for sustained electrohydrodynamic flows are (a) free charges at the surface and (b) tangential electric field at the surface. By studying the flow, we explain the formation of nanoparticle-nanosheet at the air-water interface.

Chapter 10 provides an introduction and examples of usage of PyStokes. PyStokes is a Cython library to compute rigid body motion and fluid flow produced by active colloidal spheres. A brief description of a solver which explicitly resolves the fluid degrees of freedom is also presented.

Finally, we conclude the thesis in Chapter 11 by summarizing the main analytical and numerical results of the thesis. We also provide future directions in which the results of this thesis can be used to explore new avenues of research in statistical physics.

Chapter 2

Generalized Stokes laws and boundary integrals

2.1 Introduction

G. G. Stokes, in 1851, derived the force per unit area acting on the surface of a sphere moving slowly in an incompressible viscous fluid and thus obtained the celebrated eponymous law for the drag force on a moving sphere. The solution for a rotating sphere would provide the drag torque. Einstein used these laws in his phenomenological theory of Brownian motion and obtained a relation between the diffusion coefficient of a spherical colloid and the friction constant in Stokes law, the so-called Stokes-Einstein relation, the first example of a fluctuation-dissipation theorem [25, 53, 54]. Smoluchowski, in 1911, presented an iterative method to calculate the force per unit area on a moving sphere in the presence of another and thereby initiated the study of hydrodynamic interactions between colloidal particles [55]. The method was refined by many authors culminating in the "induced force" method of Mazur and coworkers [56, 57]. The theory of Brownian motion with hydrodynamic interactions developed in parallel with major contributions from Kirkwood [58, 59], Zwanzig [60, 61], and Batchelor [62, 63], amongst others [64, 65].

Through these studies it became apparent that the force per unit area on the surface of the colloid is the key dynamical quantity necessary for developing both the mechanics and the statistical mechanics of suspensions. Despite this long and distinguished history the study of colloidal suspensions remains a research area of sustained fecundity [19].

In Chapter 1 we presented a brief introduction to active colloids which includes synthetic active colloids and microorganisms. In these examples, the matching condition at the edge of the boundary layer is the continuity of the fluid velocity, which now contains, in addition to the rigid body motion of the colloid, the contribution from the active flow $\boldsymbol{v}^{\mathcal{A}}$. This "slip" velocity is a general, possibly time-dependent, vector field on the colloid surface, subject only to the constraint of mass conservation $\int \boldsymbol{v}^{\mathcal{A}} \cdot \mathbf{n} dS = 0$. The fluid mechanical problem is solved when the exterior flow is obtained in terms of the slip. The force per unit area on the colloidal surface follows directly from the Cauchy stress in the fluid and the motion of the colloid is obtained, when colloidal inertia is negligible, by setting the net force and net torque to zero.

The correct expression for the force per unit area was first obtained by Blake [44] for the special case of axisymmetric slip on an isolated sphere distant from all boundaries. This expression was used to compute the work done on the fluid by the slip. However, extensions of this analysis to (i) the most general form of slip in (ii) a suspension of many spheres and (iii) including the effect of proximate boundaries remain to be completed. The availability of such an expression would immediately allow the mechanics and statistical mechanics of active colloidal suspensions to reach the level of development of their passive counterparts. We address ourselves to this task here.

In this chapter, we obtain the force per unit area in a suspension of N spherical active colloids with the most general form of slip and including the effect of proximate boundaries such as plane walls. Our results are best expressed as an infinite set of linear relations between the irreducible coefficients of a tensorial harmonic expansion of the force per unit area and the slip. As these contain the Stokes laws for the force and torque as special

cases, we refer to them as "generalized Stokes laws".

The generalization has several aspects. First, expressions are obtained for every irreducible mode of the force per unit area, and not just the first two modes representing the force and the torque. Second, we consider the many-body nature of the force per unit area in a suspension of N colloids, while Stokes laws in their original form apply only to a single particle. Third, we consider the effect of proximate boundaries, such as plane walls, obtaining corrections of the kind first derived by Faxén [66] to the original form of Stokes laws. The generalized Stokes laws contain new coefficients, similar to the translational and rotational friction tensors, that are many-body functions of the colloidal configuration. We show how these generalized friction tensors can be calculated, to any desired degree of accuracy, from the solution of a linear system. This material is covered in sections 2.2 and 2.3.

The generalized Stokes laws immediately provide the quantities of interest to suspension mechanics: the force, the torque, and the stresslet on the colloids. Through their use, succinct expressions are obtained for the fluid flow, the fluid pressure, and the entropy production. We apply these results in the following chapters of this thesis to demonstrate their utility. In particular, the formalism presented here has been applied to identify the dissipative active forces and torques that drive crystallization of active colloids at plane walls in Chapter 5.

In section 2.6 of this chapter, we use the result for the stresslet to obtain an exact expression for the Landau-Lifshitz-Batchelor suspension stress as a function of colloidal configuration. We confirm that the active contribution to the suspension stress vanishes to linear order in volume fraction in an isotropic suspension. In contrast, the active contributions for a non-isotropic suspension of contractile (or extensile) active colloids leads to an increase (or decrease) of the suspension stress. We conclude in section 2.7 by discussing other theoretical and numerical methods for studying active suspensions and by suggesting further applications of the generalized Stokes laws.

2.2 Generalized Stokes laws

In this section, we present our result for the hydrodynamics contributions to the force per unit area (or the traction) $\boldsymbol{f}^H$ on the surface of active colloidal spheres of radius b suspended in an incompressible viscous fluid of viscosity η. The i-th sphere centered at $\boldsymbol{R}_i$ has radius vector $\boldsymbol{\rho}_i$ and orientation vector $\boldsymbol{p}_i$ as shown in Fig. (2.1). The velocity and angular velocity of the sphere is $\mathbf{V}_i$ and $\boldsymbol{\Omega}_i$ respectively. In the microhydrodynamic regime, Newton's equations reduce to instantaneous balance condition on forces and torques

$$\mathbf{F}_i^H + \mathbf{F}_i^P + \hat{\mathbf{F}}_i = 0, \quad \mathbf{T}_i^H + \mathbf{T}_i^P + \hat{\mathbf{T}}_i = 0. \tag{2.1}$$

Here $\mathbf{F}_i^H = \int \boldsymbol{f}^H \, d\mathrm{S}_i$ are hydrodynamic forces, $\mathbf{F}_i^P$ are body forces and $\hat{\mathbf{F}}_i$ are Brownian forces, while $\mathbf{T}_i^H = \int \boldsymbol{\rho}_i \times \boldsymbol{f}^H \, d\mathrm{S}_i$, $\mathbf{T}_i^P$ and $\hat{\mathbf{T}}_i$ are corresponding torques. The velocity $\boldsymbol{v}(\boldsymbol{r}_i)$ of the fluid at a point $\boldsymbol{r}_i = \boldsymbol{R}_i + \boldsymbol{\rho}_i$ on the boundary of i-th colloid is a sum of its rigid body motion and the active slip $\boldsymbol{v}_i^{\mathcal{A}}$

$$\boldsymbol{v}(\boldsymbol{R}_i + \boldsymbol{\rho}_i) \equiv \boldsymbol{v}_i(\boldsymbol{R}_i + \boldsymbol{\rho}_i) = \mathbf{V}_i + \boldsymbol{\Omega}_i \times \boldsymbol{\rho}_i + \boldsymbol{v}_i^{\mathcal{A}}(\boldsymbol{\rho}_i). \tag{2.2}$$

Both the slip and the force per unit area are vector fields on the sphere and which invites harmonic expansions. We choose the tensorial spherical harmonics

$$\mathbf{Y}^{(l)}(\hat{\boldsymbol{\rho}}) = (-1)^l \rho^{l+1} \boldsymbol{\nabla}^{(l)} \rho^{-1},$$

where $\boldsymbol{\nabla}^{(l)} = \boldsymbol{\nabla}_{\alpha_1} \ldots \boldsymbol{\nabla}_{\alpha_l}$, as the expansion basis for reasons discussed below. The expansion of the slip and the force per unit area on the surface of i-th colloid is

$$\boldsymbol{v}_i^{\mathcal{A}}(\boldsymbol{R}_i + \boldsymbol{\rho}_i) = \sum_{l=1}^{\infty} \frac{1}{(l-1)!(2l-3)!!} \mathbf{V}_i^{(l)} \cdot \mathbf{Y}^{(l-1)}(\hat{\boldsymbol{\rho}}_i), \tag{2.3a}$$

$$\boldsymbol{f}^H(\boldsymbol{R}_i + \boldsymbol{\rho}_i) = \sum_{l=1}^{\infty} \frac{2l-1}{4\pi b^2} \mathbf{F}_i^{(l)} \cdot \mathbf{Y}^{(l-1)}(\hat{\boldsymbol{\rho}}_i). \tag{2.3b}$$

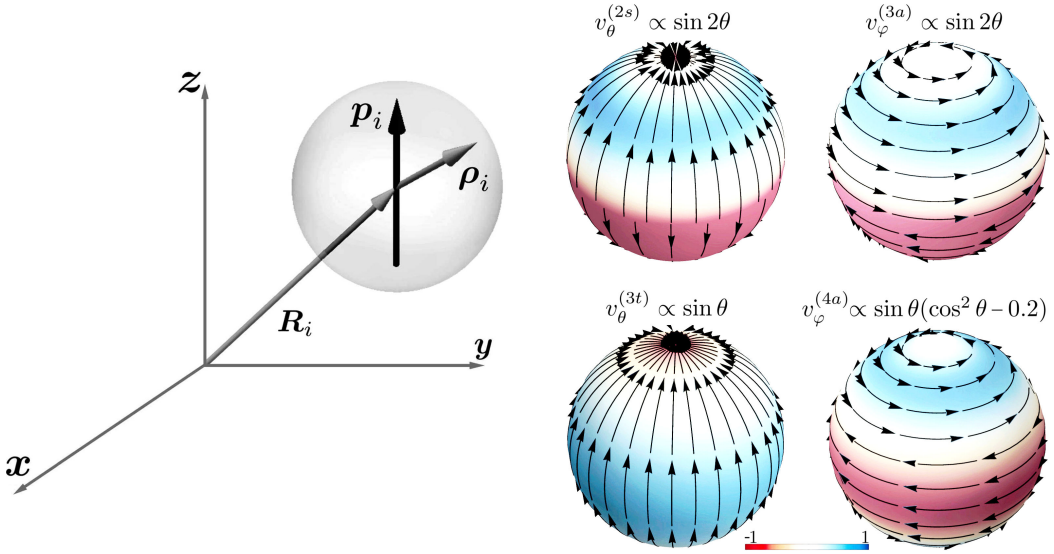

Figure 2.1: Coordinate system to describe spherical active colloids (left panel). The center of mass of ith colloid is at $\boldsymbol{R}_i$ and a unit vector $\mathbf{p}_i$ describes its orientation while $\boldsymbol{\rho}_i$ is the radius vector. The plots on the right are the streamlines of the surface velocity, overlaid on the pseudo-color plot of the logarithm of the normalized flow speed, due to four leading slip modes as described in the in Table 2.1. The modes are parameterized uniaxially in terms of $\boldsymbol{p}$, which is chosen to be along $\hat{\boldsymbol{z}}$ direction, without losing generality, such that $\boldsymbol{p} = \cos\theta\hat{\boldsymbol{\rho}} - \sin\theta\hat{\boldsymbol{\theta}}$, where $(\hat{\boldsymbol{\rho}}, \hat{\boldsymbol{\theta}}, \hat{\boldsymbol{\varphi}})$ are the spherical polar unit vectors.

The expansion coefficients $\mathbf{V}_i^{(l)}$ and $\mathbf{F}_i^{(l)}$, of dimensions of force and velocity respectively, are tensors of rank l, symmetric and irreducible in their last $l-1$ indices [10]. Elementary group theory assures [67] that they can be expressed as the sum of three irreducible tensors of rank l, $l-1$ and $l-2$. The three irreducible parts are

$$\mathbf{V}_i^{(l\sigma)} = \mathbf{P}^{(l\sigma)} \cdot \mathbf{V}_i^{(l)}, \qquad \mathbf{F}_i^{(l\sigma)} = \mathbf{P}^{(l\sigma)} \cdot \mathbf{F}_i^{(l)}, \tag{2.4}$$

where the index $\sigma = s$, a and t, labels the symmetric irreducible, antisymmetric and trace parts of the reducible tensors. The operator $\mathbf{P}^{(ls)} = \boldsymbol{\Delta}^{(l)}$ extracts the symmetric irreducible part, $\mathbf{P}^{(la)} = \boldsymbol{\Delta}^{(l-1)}\boldsymbol{\varepsilon}$ the antisymmetric part and $\mathbf{P}^{(lt)} = \boldsymbol{\delta}$ the trace of the operand. Here $\boldsymbol{\Delta}^{(l)}$ is tensor of rank $2l$, projecting any lth order tensor to its symmetric irreducible form [68], $\boldsymbol{\varepsilon}$ is the Levi-Civita tensor and $\boldsymbol{\delta}$ is the Kronecker delta. As the $\mathbf{V}_i^{(l\sigma)}$ are irreducible tensors, it is natural to parametrize them in terms of the tensorial spherical harmonics.

Their *uniaxial* parametrizations are

$$\mathbf{V}_i^{(ls)} = V_0^{(ls)}\mathbf{Y}^{(l)}(\boldsymbol{p}_i), \qquad \mathbf{V}_i^{(la)} = V_0^{(la)}\mathbf{Y}^{(l-1)}(\boldsymbol{p}_i), \qquad \mathbf{V}_i^{(lt)} = V_0^{(lt)}\mathbf{Y}^{(l-2)}(\boldsymbol{p}_i). \tag{2.5}$$

It follows that the coefficients are either even (apolar) or odd (polar) under inversion symmetry $\boldsymbol{p}_i \to -\boldsymbol{p}_i$. The leading terms of the expansion, categorized according to their symmetry under inversion and mirror reflection, are

$$\begin{aligned}\boldsymbol{v}_i^{\mathcal{A}}(\boldsymbol{\rho}_i) = &-\underbrace{\mathbf{V}_i^{\mathcal{A}} + \tfrac{1}{15}\mathbf{V}_i^{(3t)}\cdot\mathbf{Y}^{(2)}(\hat{\boldsymbol{\rho}}_i)}_{\text{achiral, polar}} + \underbrace{\mathbf{V}_i^{(2s)}\cdot\mathbf{Y}^{(1)}(\hat{\boldsymbol{\rho}}_i)}_{\text{achiral, apolar}} \\ &\underbrace{-\boldsymbol{\Omega}_i^{\mathcal{A}}\times\boldsymbol{\rho}_i - \tfrac{1}{60}\boldsymbol{\varepsilon}\cdot\mathbf{V}_i^{(4a)}\cdot\mathbf{Y}^{(3)}(\hat{\boldsymbol{\rho}}_i)}_{\text{chiral, polar}} \underbrace{-\tfrac{1}{9}\boldsymbol{\varepsilon}\cdot\mathbf{V}_i^{(3a)}\cdot\mathbf{Y}^{(2)}(\hat{\boldsymbol{\rho}}_i)}_{\text{chiral, apolar}},\end{aligned} \tag{2.6}$$

$$\mathbf{V}_i^{\mathcal{A}} = -\frac{1}{4\pi b^2}\int \boldsymbol{v}_i^{\mathcal{A}}(\boldsymbol{\rho})\,d\mathrm{S}_i, \qquad \boldsymbol{\Omega}_i^{\mathcal{A}} = -\frac{3}{8\pi b^4}\int \boldsymbol{\rho}_i\times\boldsymbol{v}_i^{\mathcal{A}}(\boldsymbol{\rho})\,d\mathrm{S}_i, \tag{2.7}$$

where the first two modes of the slip, $\mathbf{V}_i^{(1s)} \equiv -\mathbf{V}_i^{\mathcal{A}}$ and $\mathbf{V}_i^{(2a)} \equiv -b\boldsymbol{\Omega}_i^{\mathcal{A}}$, are respectively, the active translational velocity and the active angular velocity for a sphere in unbounded medium [45, 69, 70]. The tangential flows generated by these leading terms are shown in Fig. (2.1). Their complete form, including radial terms, is provided in Table 2.1 of the Appendix.

The tensorial spherical harmonics are dimensionless, symmetric, irreducible Cartesian tensors of rank l that form a complete, orthogonal basis on the sphere [68, 71, 72]. The tensorial harmonics have several advantages over the more common vector spherical harmonics or surface polynomials [73, 74]. First, both basis functions and expansion coefficients transform as Cartesian tensors which allows physical quantities like the force, the torque and the stresslet to be represented covariantly. Second, the linear independence of the basis functions ensures that linear systems for the coefficients are always of full rank. Third, the basis functions are well-suited for Taylor expansions [10] and their addition

theorems are considerably simpler than the usual vector spherical harmonics. This property allows for fast methods of summing long-ranged harmonics [75] that are less complex than the classical methods [76]. Previous studies of spherical passive suspensions have amply demonstrated some of these advantages [10, 45, 56, 57, 77]. The problem, now, is to relate the unknown values of the force coefficients $\mathbf{F}_i^{(l\sigma)}$ to the known values of the slip coefficients $\mathbf{V}_i^{(l\sigma)}$.

In the regime of slow viscous flow, the fluid velocity $\boldsymbol{v}$ in Eq. (2.2) obeys the Stokes equation. The linearity of the governing equation and of the boundary condition implies, then, a linear relation between the velocity and force coefficients

$$\mathbf{F}_i^{(l\sigma)} = \underbrace{-\boldsymbol{\gamma}_{ij}^{(l\sigma,1s)} \cdot \mathbf{V}_j - \boldsymbol{\gamma}_{ij}^{(l\sigma,2a)} \cdot \boldsymbol{\Omega}_j}_{\text{rigid body motion}} - \sum_{l'\sigma'=1s}^{\infty} \underbrace{\boldsymbol{\gamma}_{ij}^{(l\sigma,l'\sigma')} \cdot \mathbf{V}_j^{(l'\sigma')}}_{\text{activity}}. \tag{2.8}$$

Here repeated particle indices are summed over. We call the above infinite set the *generalized Stokes laws.* Their best-known special cases are Stokes laws for translation $\mathbf{F}_i = -6\pi\eta b\mathbf{V}_i$ and rotation $\mathbf{T}_i = -8\pi\eta b^3\boldsymbol{\Omega}_i$. The first two terms are passive frictional contributions due to rigid body motion while the remaining terms are active contributions due to slip. The $\boldsymbol{\gamma}_{ij}^{(l\sigma,l'\sigma')}$ are generalized friction tensors and their symmetry properties, to which we shall return below, allow them to be interpreted as generalized Onsager coefficients. Their rank varies from $l+l'$ to $l+l'-4$ depending on the values of σ and σ'. The friction tensors depend on the positions of *all* spheres, reflecting the many-body character of the hydrodynamic interaction but, due to isotropy, are independent of the sphere orientations. The force coefficients, however, depend on the orientations of the spheres carried in the coefficients of the slip. Given the velocity at the boundary of each sphere, the friction tensors completely determine the force per unit area on every sphere. In the next section, we derive exact expressions for the generalized friction tensors in terms of Green's functions of Stokes flow.

2.3 Boundary integral solution

The most direct way of computing the generalized friction tensors is through the boundary integral representation of Stokes flow [10, 73, 78–84]

$$v_\alpha(\boldsymbol{r}) = -\int G_{\alpha\beta}(\boldsymbol{r}, \boldsymbol{r}_j) f^H_\beta(\boldsymbol{r}_j)\, d\mathrm{S}_j + \int K_{\beta\alpha\gamma}(\boldsymbol{r}, \boldsymbol{r}_j)\hat{\rho}_\gamma v_\beta(\boldsymbol{r}_j)\, d\mathrm{S}_j, \tag{2.9a}$$

$$p(\boldsymbol{r}) = -\int P_\beta(\boldsymbol{r}, \boldsymbol{r}_j) f^H_\beta(\boldsymbol{r}_j)\, d\mathrm{S}_j + \int Q_{\alpha\beta}(\boldsymbol{r}, \boldsymbol{r}_j)\hat{\rho}_\alpha v_\beta(\boldsymbol{r}_j)\, d\mathrm{S}_j. \tag{2.9b}$$

In the above, repeated Cartesian and particle indices are summed over and points on the boundary of the sphere are given by $\boldsymbol{r}_i = \boldsymbol{R}_i + \boldsymbol{\rho}_i$. The kernels in the boundary integral representations are the Green's function $\mathbf{G}$, the pressure vector $\mathbf{P}$, its gradient $\mathbf{Q} = 2\eta\boldsymbol{\nabla}\mathbf{P}$, and the stress tensor $\mathbf{K}$. They satisfy

$$\nabla_\alpha G_{\alpha\beta}(\boldsymbol{r}, \boldsymbol{r}') = 0, \qquad -\nabla_\alpha P_\beta(\boldsymbol{r}, \boldsymbol{r}') + \eta\nabla^2 G_{\alpha\beta}(\boldsymbol{r}, \boldsymbol{r}') = -\delta(\boldsymbol{r} - \boldsymbol{r}')\,\delta_{\alpha\beta}, \tag{2.10a}$$

$$K_{\alpha\beta\gamma}(\boldsymbol{r}, \boldsymbol{r}') = -\delta_{\alpha\gamma} P_\beta(\boldsymbol{r}, \boldsymbol{r}') + \eta\left(\nabla_\gamma G_{\alpha\beta}(\boldsymbol{r}, \boldsymbol{r}') + \nabla_\alpha G_{\beta\gamma}(\boldsymbol{r}, \boldsymbol{r}')\right). \tag{2.10b}$$

The flow $\boldsymbol{v}$ and pressure p satisfying the Stokes equation, $\nabla \cdot \boldsymbol{v} = 0$ and $\nabla \cdot \boldsymbol{\sigma}^H = 0$, with $\boldsymbol{\sigma}^H = -p\boldsymbol{I} + \eta(\boldsymbol{\nabla v} + (\boldsymbol{\nabla v})^T)$ the Cauchy stress in a fluid of viscosity η, is the sum of the "single-layer" integral of the local per unit area and the "double-layer" integral of the boundary velocity.

Enforcing the boundary conditions in the integral representation of Eq. (2.9a) produces a Fredholm integral equation of the first kind for the unknown force per unit area. The problem is thereby reduced from the solution of a partial differential equation in a three-dimensional volume to the solution of an integral equation over two-dimensional surfaces. This reduction of dimensionality is the main advantage of the integral equation approach. Several methods of solution have been developed for Fredholm integral equations for Stokes flows [10, 57, 73, 80–83, 85]. These differ in their choice of formulation, discretization, and strategy of minimizing the residual. Here, we use a direct formulation,

in which the single-layer density is the physical force per unit area, in contrast to other formulations where such an interpretation is unavailable [57, 73]. The choice of discretization in terms of the tensorial spherical harmonics is natural for spheres and such global basis functions yield the greatest accuracy for the least number of unknowns [82]. Finally, Galerkin's method of minimizing the residual is chosen as it yields a self-adjoint linear system for the coefficients, an advantageous property for numerical solutions.

The boundary velocity of Eq. (2.2), $\boldsymbol{v}(\boldsymbol{R}_i + \boldsymbol{\rho}_i) \equiv \boldsymbol{v}_i = \boldsymbol{v}_i^{\mathcal{D}} + \boldsymbol{v}_i^{\mathcal{A}}$, is a sum of rigid body motion $\boldsymbol{v}_i^{\mathcal{D}} = \mathbf{V}_i + \boldsymbol{\Omega}_i \times \boldsymbol{\rho}_i$ and the active slip velocity $\boldsymbol{v}_i^{\mathcal{A}}$. It is also convenient to express the hydrodynamic force per unit area (or traction) $\boldsymbol{f}^H$ as a sum of rigid body $\boldsymbol{f}^{\mathcal{D}}$ and active contributions $\boldsymbol{f}^{\mathcal{A}}$, with corresponding expansion coefficients $\mathbf{F}_i^{\mathcal{D}(l)}$ and $\mathbf{F}_i^{\mathcal{A}(l)}$. By linearity of the Stokes equations, the two parts of the traction satisfy *independent* boundary integral equations obtained by evaluating Eq. (2.9a) on the surface of the colloids. Recalling that rigid body motion is an eigenvector of the double-layer integral operator [10, 85], these boundary integral equations are

$$V_\alpha + \epsilon_{\alpha\beta\gamma}\Omega_\beta \rho_\gamma = -\int G_{\alpha\beta}(\boldsymbol{r}_i, \boldsymbol{r}_j) f_\beta^{\mathcal{D}}(\boldsymbol{r}_j)\, d\mathrm{S}_j, \qquad \text{(rigid body)} \quad (2.11)$$

$$\frac{1}{2} v_\alpha^{\mathcal{A}}(\boldsymbol{r}_i) = -\int G_{\alpha\beta}(\boldsymbol{r}_i, \boldsymbol{r}_j) f_\beta^{\mathcal{A}}(\boldsymbol{r}_j)\, d\mathrm{S}_j + \int K_{\beta\alpha\gamma}(\boldsymbol{r}_i, \boldsymbol{r}_j) \hat{\rho}_\gamma v_\beta^{\mathcal{A}}(\boldsymbol{r}_j)\, d\mathrm{S}_j. \qquad \text{(active)} \quad (2.12)$$

Defining the single-layer and double-layer integral operators $\boldsymbol{G}$ and $\boldsymbol{K}$ as

$$\boldsymbol{G} \cdot \boldsymbol{f} = \int \mathbf{G}(\boldsymbol{r}_i, \boldsymbol{r}_j) \cdot \boldsymbol{f}(\boldsymbol{r}_j)\, d\mathrm{S}_j, \qquad \boldsymbol{K} \cdot \boldsymbol{v} = \int \hat{\boldsymbol{\rho}}_j \cdot \boldsymbol{K}(\boldsymbol{r}_i, \boldsymbol{r}_j) \cdot \boldsymbol{v}(\boldsymbol{r}_j)\, d\mathrm{S}_j, \quad (2.13)$$

the hydrodynamic traction is the sum of contribution from rigid body motion and activity

$$\boldsymbol{f}^H = \boldsymbol{f}^{\mathcal{D}} + \boldsymbol{f}^{\mathcal{A}} = -\boldsymbol{G}^{-1} \cdot \boldsymbol{v}_i^D - \boldsymbol{G}^{-1} \cdot \left(\tfrac{1}{2}\boldsymbol{I} - \boldsymbol{K}\right) \cdot \boldsymbol{v}_i^{\mathcal{A}}. \quad (2.14)$$

We now derive explicit expression for this formal solution.

2.3.1 Rigid body traction

The linear algebraic system for the rigid body contribution to the traction, with the summation convention for repeated indices, is

$$-\boldsymbol{G}_{ij}^{(l,l')}(\boldsymbol{R}_i, \boldsymbol{R}_j)\cdot\mathbf{F}_j^{\mathcal{D}(l')} = \mathbf{V}_i^{\mathcal{D}(l)}, \tag{2.15}$$

where $\boldsymbol{G}_{ij}^{(l,l')}$ are the matrix elements of the single-layer operator $\boldsymbol{G}$. In the tensorial harmonic basis, they are given as

$$\boldsymbol{G}_{ij}^{(l,l')}(\boldsymbol{R}_i, \boldsymbol{R}_j) = \frac{2l-1}{4\pi b^2}\frac{2l'-1}{4\pi b^2}\int \mathbf{Y}^{(l-1)}(\hat{\boldsymbol{\rho}}_i)\mathbf{G}(\boldsymbol{R}_i+\boldsymbol{\rho}_i, \boldsymbol{R}_j+\boldsymbol{\rho}_j)\mathbf{Y}^{(l'-1)}(\hat{\boldsymbol{\rho}}_j)\,d\mathrm{S}_i\,d\mathrm{S}_j. \tag{2.16}$$

We have also used Eq. (2.3) to define the l-th tensorial harmonic coefficients of the rigid body motion $\boldsymbol{v}^{\mathcal{D}}$ and the traction $\boldsymbol{f}^{\mathcal{D}}$ as $\mathbf{V}^{\mathcal{D}(l)}$ and $\mathbf{F}^{\mathcal{D}(l)}$ respectively. Clearly, the only non-zero coefficients of $\mathbf{V}^{\mathcal{D}(l)}$ are $\mathbf{V}$ and $\boldsymbol{\Omega}$, corresponding to $l\sigma = 1s$ and $l\sigma = 2a$ respectively. The solution of the linear system for rigid body traction is

$$\mathbf{F}_i^{\mathcal{D}(l\sigma)} = -\boldsymbol{\gamma}_{ij}^{(l\sigma,1s)}\cdot\mathbf{V}_j - \boldsymbol{\gamma}_{ij}^{(l\sigma,2a)}\cdot\boldsymbol{\Omega}_j. \tag{2.17}$$

Here $\boldsymbol{\gamma}_{ij}^{(l\sigma,1s)}$ and $\boldsymbol{\gamma}_{ij}^{(l\sigma,2a)}$ are friction tensors

$$\boldsymbol{\gamma}_{ij}^{(l\sigma,1s)} = \mathbf{P}^{(l\sigma)}\cdot\left[\boldsymbol{G}^{-1}\right]_{ij}^{(l,1)}\cdot\mathbf{P}^{(1s)}, \quad \boldsymbol{\gamma}_{ij}^{(l\sigma,2a)} = \mathbf{P}^{(l\sigma)}\cdot\left[\boldsymbol{G}^{-1}\right]_{ij}^{(l,2)}\cdot\mathbf{P}^{(2a)}. \tag{2.18}$$

Here $\boldsymbol{G}$ is single-layer operator whose (l, l') element in the ij block is $\boldsymbol{G}_{ij}^{(l,l')}(\boldsymbol{R}_i, \boldsymbol{R}_j)$. The friction tensors above give the contribution to the traction from rigid body motion [56, 57, 86–89]. Explicit expression for the matrix elements and the friction tensors have been provided in Appendix A. These expressions have been obtained in terms of the Green's functions of the Stokes flow by expanding the kernels of the boundary integrals in tensorial spherical harmonics. The integration is then performed using the orthogonality of the tensorial spherical harmonics.

2.3.2 Active traction

The linear algebraic system for the active contribution to the traction follows from Eq. (2.12) using the tensorial spherical harmonic expansions of Eq. (2.3) as

$$-\boldsymbol{G}_{ij}^{(l,l')}(\boldsymbol{R}_i,\boldsymbol{R}_j)\cdot\mathbf{F}_j^{\mathcal{A}(l')}+\boldsymbol{K}_{ij}^{(l,l')}(\boldsymbol{R}_i,\boldsymbol{R}_j)\cdot\mathbf{V}_j^{(l')}=\tfrac{1}{2}\mathbf{V}_i^{(l)}, \tag{2.19}$$

where $\boldsymbol{K}_{ij}^{(l,l')}$ are the matrix elements of the double-layer operator $\boldsymbol{K}$. In the tensorial harmonic basis, they are given as

$$\boldsymbol{K}_{ij}^{(l,l')}(\boldsymbol{R}_i,\boldsymbol{R}_j)=\tfrac{2l-1}{4\pi b^2(l'-1)!(2l'-1)!!}\int\mathbf{Y}^{(l-1)}(\hat{\boldsymbol{\rho}}_i)\mathbf{K}(\boldsymbol{R}_i+\boldsymbol{\rho}_i,\boldsymbol{R}_j+\boldsymbol{\rho}_j)\cdot\hat{\boldsymbol{\rho}}_j\mathbf{Y}^{(l'-1)}(\hat{\boldsymbol{\rho}}_j)\,d\mathrm{S}_i\,d\mathrm{S}_j. \tag{2.20}$$

We now use the irreducible parts of the traction and slip coefficients as defined in Eq. (2.4). The solution of the linear system is

$$\mathbf{F}_i^{\mathcal{A}(l\sigma)}=-\sum_{l'\sigma'=1s}^{\infty}\boldsymbol{\gamma}_{ij}^{(l\sigma,l'\sigma')}\cdot\mathbf{V}_j^{(l'\sigma')}. \tag{2.21}$$

The generalized friction tensors $\boldsymbol{\gamma}_{ij}^{(l\sigma,l'\sigma')}$ give the active contribution to the traction. These tensors were first introduced in [11] and are given by

$$\boldsymbol{\gamma}_{ij}^{(l\sigma,l'\sigma')}=\mathbf{P}^{(l\sigma)}\cdot\left[\boldsymbol{G}^{-1}\cdot\left(\tfrac{1}{2}\boldsymbol{I}-\boldsymbol{K}\right)\right]_{ij}^{(l,l')}\cdot\mathbf{P}^{(l'\sigma')}. \tag{2.22}$$

In the above, we have used the definition of single and double-layer operator $\boldsymbol{G}$ and $\boldsymbol{K}$, whose (l,l') element in the ij are $\boldsymbol{G}_{ij}^{(l,l')}(\boldsymbol{R}_i,\boldsymbol{R}_j)$ and $\boldsymbol{K}_{ij}^{(l,l')}(\boldsymbol{R}_i,\boldsymbol{R}_j)$, respectively. The many-body character of the friction tensors is apparent from this expressions, as the inverse of $\boldsymbol{G}$ cannot be expressed in terms of sums of the pairwise interactions encoded in its matrix elements. Since the matrix elements only involve particle positions and not orientations, the friction tensors are, likewise, independent of particle orientation. They can be interpreted as Onsager coefficients of the linear response of the traction to the surface slip.

The above expression is identical to Eq. (2.18) for $l'\sigma' = 1s, 2a$ since rigid body motion is an eigenvector of the double layer operator. Therefore, both active *and* passive friction tensors can be recovered from the general expression above.

The method of solution for the linear system, or equivalently, of inverting $\boldsymbol{G}$ must be chosen according to need. For analytical solutions, Jacobi's iterative method is straightforward and its widespread use in Stokes flows can be traced back to Smoluchowski's method of reflections [90]. Other tractable analytical methods rely on series expansion of $\boldsymbol{G}^{-1}$ in powers of $\mathbf{G}$ [91]. We give explicit analytical expressions for the friction tensors obtained from the Jacobi method in Appendix A.4. For numerical solutions, iterative solvers with faster rates of convergence must be used. Typically, these search for the inverse in the Krylov subspace of $\boldsymbol{G}$ and have the advantage of requiring, instead of $\boldsymbol{G}$, only its action on a vector of the appropriate size. The need to store a large dense matrix is thereby avoided. For the self-adjoint linear system above, the stable, efficient and accurate conjugate gradient method [92] may be used. This requires $\mathcal{O}(M^2)$ computational effort for M unknowns when matrix-vector products are computed directly. The use of fast summation methods can reduce the cost to $\mathcal{O}(M \log M)$ [93, 94] or even $\mathcal{O}(M)$ [76, 95, 96].

Adding the contributions from the above Eq. (2.21) and Eq. (2.17) gives the expression for the generalized Stokes equations of Eq. (2.8) such that

$$\mathbf{F}_i^{(l\sigma)} = \mathbf{F}_i^{\mathcal{D}(l\sigma)} + \mathbf{F}_i^{\mathcal{A}(l\sigma)}. \tag{2.23}$$

Thus the generalized Stokes laws give the contribution to the traction from body rigid motion and the activity of the colloids. To summarize, the main result of this section is Eq. (2.22), which gives exact expressions for the generalized friction tensors in terms of the matrix elements of the discretized boundary integral equation. An approximate solution to this, in leading powers of distance between the colloids, is detailed in Appendix A.4. It should be noted that we use the terms traction and force per unit area interchangeably.

2.4 Flow, pressure, and stress in the fluid

The boundary integral representation of stress [97] can be obtained from Eq. (2.9), using the definition $\sigma^H_{\alpha\beta} = -p\delta_{\alpha\beta} + \eta(\nabla_\alpha v_\beta + \nabla_\beta v_\alpha)$ as

$$\sigma^H_{\alpha\beta}(\boldsymbol{r}) = -\int S_{\alpha\gamma\beta}(\boldsymbol{r}, \boldsymbol{r}_j)\, f^H_\gamma(\boldsymbol{r}_j)\, d\mathrm{S}_j + \int M_{\alpha\gamma\delta\beta}(\boldsymbol{r}, \boldsymbol{r}_j)\hat{\rho}_\gamma\, v_\delta(\boldsymbol{r}_j)\, d\mathrm{S}_j, \tag{2.24}$$

$$\begin{aligned} S_{\alpha\beta\gamma}(\boldsymbol{r}, \boldsymbol{r}') &= -\delta_{\alpha\gamma} P_\beta(\boldsymbol{r}, \boldsymbol{r}') + \eta\Big(\nabla_\gamma G_{\alpha\beta}(\boldsymbol{r}, \boldsymbol{r}') + \nabla_\alpha G_{\beta\gamma}(\boldsymbol{r}, \boldsymbol{r}')\Big) = K_{\alpha\beta\gamma}(\boldsymbol{r}, \boldsymbol{r}'), \\ M_{\alpha\beta\gamma\delta}(\boldsymbol{r}, \boldsymbol{r}') &= -\delta_{\alpha\delta} Q_{\beta\gamma}(\boldsymbol{r}, \boldsymbol{r}') + \eta\Big(\nabla_\delta K_{\beta\gamma\alpha}(\boldsymbol{r}, \boldsymbol{r}') + \nabla_\alpha K_{\beta\gamma\delta}(\boldsymbol{r}, \boldsymbol{r}')\Big). \end{aligned} \tag{2.25}$$

By expanding the traction and velocity in the respective boundary integrals, we obtain expression for fluid flow, pressure, and stress in terms of the tensorial coefficients

$$\boldsymbol{v}(\boldsymbol{r}) = \sum_{l=1}^{\infty}\Big(-\boldsymbol{G}^{(l)}_j(\boldsymbol{r}, \boldsymbol{R}_j)\cdot\mathbf{F}^{(l)}_j + \boldsymbol{K}^{(l)}_j(\boldsymbol{r}, \boldsymbol{R}_j)\cdot\mathbf{V}^{(l)}_j\Big), \tag{2.26a}$$

$$p(\boldsymbol{r}) = \sum_{l=1}^{\infty}\Big(-\boldsymbol{P}^{(l)}_j(\boldsymbol{r}, \boldsymbol{R}_j)\cdot\mathbf{F}^{(l)}_j + \boldsymbol{Q}^{(l)}_j(\boldsymbol{r}, \boldsymbol{R}_j)\cdot\mathbf{V}^{(l)}_j\Big), \tag{2.26b}$$

$$\boldsymbol{\sigma}^H(\boldsymbol{r}) = \sum_{l=1}^{\infty}\Big(-\boldsymbol{S}^{(l)}_j(\boldsymbol{r}, \boldsymbol{R}_j)\cdot\mathbf{F}^{(l)}_j + \boldsymbol{M}^{(l)}_j(\boldsymbol{r}, \boldsymbol{R}_j)\cdot\mathbf{V}^{(l)}_j\Big), \tag{2.26c}$$

where the boundary integrals are

$$\boldsymbol{G}^{(l)}_j(\boldsymbol{r}, \boldsymbol{R}_j) = \frac{2l-1}{4\pi b^2}\int \mathbf{G}(\boldsymbol{r}, \boldsymbol{R}_j + \boldsymbol{\rho}_j)\mathbf{Y}^{(l-1)}(\hat{\boldsymbol{\rho}}_j)\, d\mathrm{S}_j, \tag{2.27a}$$

$$\boldsymbol{K}^{(l)}_j(\boldsymbol{r}, \boldsymbol{R}_j) = \frac{1}{(l-1)!(2l-3)!!}\int \mathbf{K}(\boldsymbol{r}, \boldsymbol{R}_j + \boldsymbol{\rho}_j)\cdot\hat{\boldsymbol{\rho}}_j\mathbf{Y}^{(l-1)}(\hat{\boldsymbol{\rho}}_j)\, d\mathrm{S}_j, \tag{2.27b}$$

$$\boldsymbol{P}^{(l)}_j(\boldsymbol{r}, \boldsymbol{R}_j) = \frac{2l-1}{4\pi b^2}\int \mathbf{P}(\boldsymbol{r}, \boldsymbol{R}_j + \boldsymbol{\rho}_j)\mathbf{Y}^{(l-1)}(\hat{\boldsymbol{\rho}}_j)\, d\mathrm{S}_j, \tag{2.27c}$$

$$\boldsymbol{Q}^{(l)}_j(\boldsymbol{r}, \boldsymbol{R}_j) = \frac{1}{(l-1)!(2l-3)!!}\int \mathbf{Q}(\boldsymbol{r}, \boldsymbol{R}_j + \boldsymbol{\rho}_j)\cdot\hat{\boldsymbol{\rho}}_j\mathbf{Y}^{(l-1)}(\hat{\boldsymbol{\rho}}_j)\, d\mathrm{S}_j, \tag{2.27d}$$

$$\boldsymbol{S}^{(l)}_j(\boldsymbol{r}, \boldsymbol{R}_j) = \frac{2l-1}{4\pi b^2}\int \mathbf{S}(\boldsymbol{r}, \boldsymbol{R}_j + \boldsymbol{\rho}_j)\mathbf{Y}^{(l-1)}(\hat{\boldsymbol{\rho}}_j)\, d\mathrm{S}_j, \tag{2.27e}$$

$$\boldsymbol{M}^{(l)}_j(\boldsymbol{r}, \boldsymbol{R}_j) = \frac{1}{(l-1)!(2l-3)!!}\int \mathbf{M}(\boldsymbol{r}, \boldsymbol{R}_j + \boldsymbol{\rho}_j)\cdot\hat{\boldsymbol{\rho}}_j\mathbf{Y}^{(l-1)}(\hat{\boldsymbol{\rho}}_j)\, d\mathrm{S}_j. \tag{2.27f}$$

These boundary integrals are analytically obtained in terms of the respective Green's functions and their derivatives, as shown in Appendix A.3. Thus we have arrived at exact expression for the fluid flow, pressure and stress produced by active colloids in a Stokes flow. The computations of these quantities provides specific insights about active suspensions. In particular, it can be seen that quantities like stress and pressure in an active suspension depends on presence of boundary and specific form of activity of colloids.

Using the generalized Stokes laws of Eq. (2.8) and balance conditions of Eq. (2.1), the unknown force coefficients can be written in terms of the known slip coefficients, body forces and body torques, giving

$$\boldsymbol{v}(\boldsymbol{r}) = \boldsymbol{G}_j^{(1s)}(\boldsymbol{r}, \boldsymbol{R}_j)\cdot\mathbf{F}_j^P + \boldsymbol{G}_j^{(2a)}(\boldsymbol{r}, \boldsymbol{R}_j)\cdot\mathbf{T}_j^P + \sum_{l\sigma=2s}^{\infty} \boldsymbol{\Pi}_j^{(l\sigma)}\cdot\mathbf{V}_j^{(l\sigma)}, \tag{2.28a}$$

$$p(\boldsymbol{r}) = \boldsymbol{P}_j^{(1)}(\boldsymbol{r}, \boldsymbol{R}_j)\cdot\mathbf{F}_j^P + \sum_{l=2}^{\infty} \boldsymbol{\Lambda}_j^{(ls)}\cdot\mathbf{V}_j^{(ls)}, \tag{2.28b}$$

$$\boldsymbol{\sigma}^H(\boldsymbol{r}) = \boldsymbol{S}_j^{(1s)}(\boldsymbol{r}, \boldsymbol{R}_j)\cdot\mathbf{F}_j^P + \boldsymbol{S}_j^{(2a)}(\boldsymbol{r}, \boldsymbol{R}_j)\cdot\mathbf{T}_j^P + \sum_{l\sigma=2s}^{\infty} \boldsymbol{\Gamma}_j^{(l\sigma)}\cdot\mathbf{V}_j^{(l\sigma)}. \tag{2.28c}$$

Here $\boldsymbol{G}_i^{(1s)}$ and $\boldsymbol{G}_i^{(2a)}$ are matrices which, respectively, relate the fluid velocity with body forces and torques, while the tensors $\boldsymbol{\Pi}_i^{(l\sigma)}$ give the contributions of active slip to the fluid velocity. Similarly, $\boldsymbol{P}_i^{(1s)}$ and relate body forces to pressure, while $\boldsymbol{\Lambda}_i^{(ls)}$ give contributions the active slip. The tensors $\boldsymbol{S}_i^{(1s)}$ and $\boldsymbol{S}_i^{(2a)}$ gives contributions to the fluid stress from the body forces and torques on the colloids respectively, while the contributions from the slip is given by the tensors $\boldsymbol{\Gamma}_i^{(l\sigma)}$.

It is instructive to note that only symmetric traceless parts $\mathbf{V}^{(ls)}$, of the slip modes contribute to the fluid pressure, as pressure is harmonic, unlike the fluid velocity which is biharmonic. $\boldsymbol{\Pi}_i^{(l\sigma)}$,$\boldsymbol{\Lambda}_i^{(l\sigma)}$, and $\boldsymbol{\Gamma}_i^{(l\sigma)}$ are tensors of rank l, $l+1$, and $l+2$, respectively. The contributions from the slip makes active suspensions intrinsically more rich and leads to novel phenomena with no analogues in passive suspensions.

2.5 Entropy production in the fluid

The rate of dissipation of the fluid kinetic energy, or the power dissipation $\dot{\mathcal{E}}$, due to the viscosity of the fluid is related to the entropy production $\dot{\mathcal{S}}$ in the fluid as [98]

$$\dot{\mathcal{S}} = \frac{1}{T}\,\dot{\mathcal{E}}. \tag{2.29}$$

For a Newtonian fluid, the rate of dissipation of kinetic energy in the volume V of the fluid is written as [98]

$$\dot{\mathcal{E}} \;= \int \boldsymbol{\sigma}^H : (\nabla \boldsymbol{v})\, dV. \tag{2.30}$$

The power dissipation in the volume of the fluid can be reduced to integrals on the colloidal boundaries using the divergence theorem

$$\dot{\mathcal{E}} \;= \int \boldsymbol{\sigma}^H : (\nabla \boldsymbol{v})\, dV = \;-\sum_i^N \int \boldsymbol{f}^H(\boldsymbol{R}_i + \boldsymbol{\rho}_i) \cdot \boldsymbol{v}(\boldsymbol{R}_i + \boldsymbol{\rho}_i)\, d\mathrm{S}_i. \tag{2.31}$$

The above equation can be simplified further by using Eq. (2.3b) along with the orthogonality of the basis functions, to obtain

$$\dot{\mathcal{E}} = -\sum_i^N \left(\mathbf{F}_i^H \cdot \mathbf{V}_i + \mathbf{T}_i^H \cdot \boldsymbol{\Omega}_i + \sum_{l\sigma=1s}^{\infty} \mathbf{F}_i^{(l\sigma)} \cdot \mathbf{V}_i^{(l\sigma)} \right). \tag{2.32}$$

The generalized Stokes laws can now be used to eliminate the unknown force coefficients for the known velocity coefficients to obtain

$$\begin{aligned} \dot{\mathcal{E}} \;&=\; -\mathbf{F}_i^H \cdot \mathbf{V}_i - \mathbf{T}_i^H \cdot \boldsymbol{\Omega}_i + \mathbf{V}_i^{(l\sigma)} \cdot \boldsymbol{\gamma}_{ij}^{(l\sigma,1s)} \cdot \mathbf{V}_j \\ &+\; \mathbf{V}_i^{(l\sigma)} \cdot \boldsymbol{\gamma}_{ij}^{(l\sigma,2a)} \cdot \boldsymbol{\Omega}_j + \mathbf{V}_i^{(l\sigma)} \cdot \boldsymbol{\gamma}_{ij}^{(l\sigma,l'\sigma')} \cdot \mathbf{V}_j^{(l'\sigma')}. \end{aligned} \tag{2.33}$$

The positivity of power dissipation ensures that the friction tensors are positive-definite.

2.6 Active suspension stress

Landau and Lifshitz showed that the stress $\boldsymbol{\Sigma}^H$ in a suspension of force-free particles, averaged over scales large compared to the particle size, is given by $\boldsymbol{\Sigma}^H = 2\eta\mathbf{E} + \boldsymbol{\Sigma}^P$, where $\mathbf{E}$ is the macroscopic strain rate in a suspension of volume V and

$$\boldsymbol{\Sigma}^P = \frac{1}{V}\sum_i \int \left[\boldsymbol{f}^H(\boldsymbol{R}_i+\boldsymbol{\rho}_i)\,\boldsymbol{\rho}_i - \eta\left\{\boldsymbol{v}(\boldsymbol{R}_i+\boldsymbol{\rho}_i)\,\hat{\boldsymbol{\rho}}_i + \hat{\boldsymbol{\rho}}_i\,\boldsymbol{v}(\boldsymbol{R}_i+\boldsymbol{\rho}_i)\right\}\right] d\mathrm{S}_i,$$

is the contribution to the stress from the particles [98]. The symmetric part of the particle contribution to the bulk stress was denoted by Batchelor as the stresslet [99]. From the tensorial harmonic expansion of Eq. (2.3), it follow that

$$\boldsymbol{\Sigma}^P = \frac{1}{V}\sum_i \left[b\mathbf{F}_i^{(2)} - \frac{8\pi\eta b^2}{3}\mathbf{V}_i^{(2s)}\right].$$

To obtain the rheological response of the suspension, the above quantity has to be calculated in the presence of an externally imposed flow $\boldsymbol{v}^\infty$. The irreducible coefficients of external flow

$$\mathbf{V}_i^{\infty(l)} = \frac{2l-1}{4\pi b^2}\int \boldsymbol{v}^\infty(\boldsymbol{R}_i+\boldsymbol{\rho}_i)\,\mathbf{Y}^{(l-1)}(\hat{\boldsymbol{\rho}}_i)\,d\mathrm{S}_i, \tag{2.34}$$

gives coefficients of the traction $\mathbf{F}_i^{\infty(l\sigma)}$ from the solution of corresponding linear system

$$\mathbf{V}_i^{\infty(l)} = \boldsymbol{G}_{ij}^{(l,l')}\cdot\mathbf{F}_j^{\infty(l')},$$
$$\mathbf{F}_i^{\infty(l\sigma)} = \hat{\boldsymbol{\gamma}}_{ij}^{(l\sigma,T)}\cdot\mathbf{V}_j^{\infty} + \hat{\boldsymbol{\gamma}}_{ij}^{(l\sigma,R)}\cdot\boldsymbol{\Omega}_j^{\infty} + \hat{\boldsymbol{\gamma}}_{ij}^{(l\sigma,l'\sigma')}\cdot\mathbf{V}_j^{\infty(l'\sigma')}.$$

Here $\hat{\boldsymbol{\gamma}}^{(l\sigma,l'\sigma')} = \mathbf{P}^{(l\sigma)}\cdot\left[\boldsymbol{G}^{-1}\right]^{(l,l')}\cdot\mathbf{P}^{(l'\sigma')}$ are generalized friction tensors encoding the response to external flow and its explicit expression is obtained by repeating the steps in Section 2.2. The particle contribution to the suspension stress is then,

$$V\boldsymbol{\Sigma}^P = \underbrace{\left[\hat{\boldsymbol{\gamma}}_{ij}^{(2s,l\sigma)} + \tfrac{1}{2}\boldsymbol{\varepsilon}\cdot\hat{\boldsymbol{\gamma}}_{ij}^{(2a,l\sigma)} + \tfrac{\boldsymbol{I}}{3}\hat{\boldsymbol{\gamma}}_{ij}^{(2t,l\sigma)}\right]\cdot\mathbf{V}_j^{\infty(l\sigma)}}_{\text{External flow}} - \underbrace{\left[\boldsymbol{\gamma}_{ij}^{(2s,l\sigma)} + \tfrac{1}{2}\boldsymbol{\varepsilon}\cdot\boldsymbol{\gamma}_{ij}^{(2a,l\sigma)} + \tfrac{\boldsymbol{I}}{3}\boldsymbol{\gamma}_{ij}^{(2t,l\sigma)}\right]\cdot\mathbf{V}_j^{(l\sigma)}}_{\text{Active slip}}.$$

All particle and coefficient indices are summed over in the above. The explicit expression for generalized friction tensors, obtained in Appendix A.4, can be used to estimate the active contribution to the suspension stress. The above expression must be statistically averaged over the position and orientation of the colloids to obtain the average stress in the suspension using distribution function $\Psi(\boldsymbol{R}^N, \boldsymbol{p}^N)$ defined in Eq. (8.1).

We now consider a force-free, torque-free suspension and assume that the leading contributions from the external flow produces a pure strain on the surface of the colloids. Thus, the first symmetric traceless moment of the external flow $\boldsymbol{v}^\infty$ is most-dominant and is parametrize as $\mathbf{V}_i^{\infty(2s)} = b\mathbf{E}$. Expression for $\boldsymbol{\Sigma}^P$ then reduces to

$$\boldsymbol{\Sigma}^P = \sum_i \frac{20\pi\eta b^3}{3}\mathbf{E} - \sum_i \frac{28\pi\eta b^2}{3}\mathbf{V}_i^{(2s)} + O(\phi^2),$$

where the first two terms are the leading order one-body contribution due to external flow and activity respectively. They are the $O(\phi)$ contribution to the deviatoric suspension stress, where ϕ is the suspension volume fraction. At $O(\phi)$, the average stress depends on the average of the irreducible dipole $\langle \mathbf{V}_i^{(2s)} \rangle_{\{\boldsymbol{p}_i\}}$ over the orientational distribution function. The orientational distribution function of spheres remains unchanged in a shear flow. In an isotropic suspension, therefore, the average $\langle \mathbf{V}_i^{(2s)} \rangle_{\{\boldsymbol{p}_i\}}$ vanishes and there is no contribution to the deviatoric part of the suspension stress at $O(\phi)$ due to activity, as was first pointed out by Pedley and Ishikawa [100]. However, if the distribution is not isotropic, then the average of $\langle \mathbf{V}_i^{(2s)} \rangle_{\{\boldsymbol{p}_i\}}$ is proportional to $V_0^{(2s)}$ and non-zero. In particular, if the first symmetric moment of the orientational distribution function is non-zero, then, the stress may increase or decrease depending on $V_0^{(2s)}$ being negative (for contractile colloids) or positive (for extensile colloids). The exact relation between the suspension stress and the generalized friction tensor obtained above can be used to derive the $O(\phi^2)$ and higher corrections to the suspension stress, and will be presented in a future work.

$l\sigma$	v_ρ	v_θ	v_φ
$2s$	$V_0^{(2s)}(\frac{2}{3}-\sin^2\theta)$	$-\frac{1}{2}V_0^{(2s)}\sin 2\theta$	0
$3s$	$V_0^{(3s)}\cos\theta\left(\cos^2\theta-\frac{1}{15}\right)$	$-V_0^{(3s)}\sin\theta\left(\cos^2\theta-\frac{1}{5}\right)$	0
$3a$	0	0	$\frac{1}{18}V_0^{(3a)}\sin 2\theta$
$3t$	$\frac{1}{45}V_0^{(3t)}\cos\theta$	$\frac{1}{45}V_0^{(3t)}\sin\theta$	0
$4a$	0	0	$\frac{1}{60}V_0^{(4a)}\sin\theta\left(\cos^2\theta-\frac{1}{5}\right)$

Table 2.1: Active slip velocity $\mathbf{v}^{\mathcal{A}}$ on the colloidal surface in terms of spherical polar coordinates $(\hat{\boldsymbol{\rho}}, \hat{\boldsymbol{\theta}}, \hat{\boldsymbol{\varphi}})$, for leading coefficients of polar, apolar and chiral symmetry. Without any loss of generality, we choose $\boldsymbol{p}$ to be along $\hat{\boldsymbol{z}}$-axis, such that $\boldsymbol{p} = \cos\theta\hat{\boldsymbol{\rho}} - \sin\theta\hat{\boldsymbol{\theta}}$.

2.7 Conclusion

By exploiting the linearity of slow viscous flow, as clearly manifested in the boundary-domain integral representation, we have derived linear relations between the coefficients of the traction and the active slip in a suspension of active colloidal spheres. These linear relations are the "generalizes Stokes laws" and the tensors which determine the coefficients of traction in terms of the coefficients of the velocity are called the generalized friction tensors. The generalized friction tensors are obtained from the boundary integral representation in terms of the Green's function of the Stokes flow.

In this chapter, we assume a spherical particle with active slip on its surface, which is then expanded in a Galerkin basis to obtain the force per unit area. Thus, any generic mechanism generating the active velocity can be modeled in our approach. Typically, the slip mechanism for synthetic active colloids is phoretic and then, we do need to solve separately for a concentration field [101]. Here, we have assumed that the non-hydrodynamic parts of the problem have been solved separately. This assumption requires the decoupling of advection and diffusion and, therefore, is restricted to low Péclet numbers.

Chapter 3

Langevin equations and boundary-domain integral equation

3.1 Introduction

A detailed derivation of the dissipative part of the traction was presented in the previous chapter. In this chapter, we consider the effects of thermal fluctuations in the fluid and obtain an explicit expression for the Brownian traction. At low Reynolds number and at finite temperature the Cauchy stress in the fluid obeys the fluctuating Stokes equation, a linear stochastic partial differential equation containing zero-mean Gaussian random fluxes with variances determined by the fluctuation-dissipation relation. The solenoidal fluid velocity obeys the slip boundary condition at the colloid-fluid boundary. For a given rigid body motion and slip, the solution of the fluctuating Stokes equation provides the Cauchy stress in the fluid and, hence, the traction on the boundary. This solution for the traction only contains the boundary condition and the random fluxes; the fluid is, therefore, "projected out". The Brownian forces and torques on the colloid are the zeroth and the first antisymmetric moments of the stochastic part of the traction. Their variance, by linearity of the governing equations, is proportional to the variance of the random fluxes.

The Langevin equations for the position and orientation of the colloid follow straightforwardly by inserting the expressions for the net force and torque in the corresponding Newton's equation.

Fox and Uhlenbeck were the first to derive the Langevin equation for the position of a *passive* spherical colloid from the fluctuating hydrodynamic equations for the fluid [102]. The fluid was taken to satisfy the no-slip boundary condition on the surface of the colloid and to be quiescent at the remote boundaries. The Lorentz reciprocal identity was used to relate the deterministic (Stokes) and stochastic (Einstein) parts of the force and to derive, thereby, the fluctuation-dissipation relation for the Brownian force from that of the random fluxes in the fluid. This approach was extended by several authors to include fluid inertia, particle inertia, Brownian fluxes at the colloid-fluid boundary and to many colloidal particles [103–107]. Zwanzig, in an earlier contribution, derived the variance of the Brownian force on a spherical colloid in an unbounded fluid using the Faxén relation. The use of this variance in the Green-Kubo relation for the transport coefficient recovered the correct value of the Stokes friction [60].

In the previous chapter, we have derived the deterministic part of the traction on the surface of the colloids by projecting out the fluid degrees of freedom. In this chapter, we extend our derivation to obtain the Brownian traction on surface of the colloids. Our derivation provides the complete distribution of the Brownian traction, and not just its first two moments as has been customary. This provides, in addition to the Brownian force and torque, the Brownian stresslet, a quantity important in suspension rheology. The traction is obtained in terms of the friction tensors tensors which, for example near a wall, are configuration dependent. The configuration-dependent friction requires, by the fluctuation-dissipation relation, configuration-dependent Brownian forces and torques and necessitates a "prescription" to render the Langevin equations mathematically meaningful [108–116]. The procedure is to adiabatically eliminate the momentum, considered as a fast variable, from underdamped Langevin equations [109, 117]. Due to the linearity

of the governing equations, this method of imputing meaning to configuration-dependent Brownian forces and torques remains valid in the presence of activity, as we show below. To the best of our knowledge, ours is the first systematic derivation of the Langevin equations for an active (and, as a special case, of a passive) colloid when the Stokes friction is configuration-dependent.

The remainder of the chapter is organized as follows. In section 3.2, we transform the fluctuating Stokes equation to its boundary-domain integral representation. From the integral representation we obtain a linear integral equation for the force per unit area (or the traction) on the colloid-fluid boundary. A formal solution, expressed in terms of the inverse of the single-layer operator of the integral equation (see below), clearly identifies the passive, active and Brownian parts of the traction. In section 3.3, we consider a spherical colloid and provide an explicit solution of the Brownian traction from the boundary-domain integral equation. We derive, through a Galerkin discretization, an equivalent linear *algebraic* system for the coefficients of the expansion of the Brownian traction in a complete orthogonal basis of tensorial spherical harmonics. The solution of the linear system shows that the each tensorial coefficient of the Brownian traction is a zero-mean Gaussian random variable and provides their variances in terms of the variance of the stochastic term in the fluctuating Stokes equation. Variances of the Brownian force, torque and stresslet follow immediately. In section 3.4, we use the previous results to construct the overdamped Langevin equations for the position and orientation of the colloid. Finally, we conclude with a discussion of our results and comparison with existing descriptions of active matter at different scales. We also compare our results with existing theories of colloidal suspension and indicate their limiting relationships.

3.2 Boundary-domain integral solution

We consider, in this section, the motion of active colloidal spheres in an incompressible fluid of viscosity η at a temperature k_BT. The boundary condition induces a local force per unit area $\boldsymbol{f} = \hat{\boldsymbol{\rho}} \cdot \boldsymbol{\sigma}$ on the colloid boundary which now also has Brownian contribution [98]. To obtain the Brownian contribution to the traction $\boldsymbol{f}$, it is necessary to consider fluctuating Stokes equation

$$\boldsymbol{\nabla} \cdot \boldsymbol{v} = 0, \quad \boldsymbol{\nabla} \cdot \boldsymbol{\sigma} + \boldsymbol{\xi} = 0, \tag{3.1}$$

where $\boldsymbol{\sigma} = -p\boldsymbol{I} + \eta(\boldsymbol{\nabla}\boldsymbol{v} + (\boldsymbol{\nabla}\boldsymbol{v})^T)$ is the Cauchy stress, p is the fluid pressure, $\boldsymbol{\xi}$ is the thermal force acting on the fluid of volume V. The thermal force is a zero-mean Gaussian random field whose variance is given by the fluctuation-dissipation relation

$$\left\langle \int \boldsymbol{v}^{\mathcal{D}}(\boldsymbol{r}) \cdot \boldsymbol{\xi}(\boldsymbol{r}, t)\, dV \int \boldsymbol{v}^{\mathcal{D}}(\boldsymbol{r}') \cdot \boldsymbol{\xi}(\boldsymbol{r}', t')\, dV' \right\rangle = 2k_BT\, \dot{\mathcal{E}}(\boldsymbol{v}^{\mathcal{D}})\delta(t - t'). \tag{3.2}$$

Here $\langle \cdot \rangle$ denotes the expectation with respect the random variable in the bracket, $\boldsymbol{v}^{\mathcal{D}}$ is any flow field that satisfies the rigid body boundary condition on S and $\dot{\mathcal{E}}$, the rate of dissipation of the fluid kinetic energy due to rigid body motion is given by [98]

$$\dot{\mathcal{E}}(\boldsymbol{v}^{\mathcal{D}}) = \frac{1}{2}\eta \int \left[\boldsymbol{\nabla}\boldsymbol{v}^{\mathcal{D}} + \left(\boldsymbol{\nabla}\boldsymbol{v}^{\mathcal{D}}\right)^T\right]^2 dV. \tag{3.3}$$

This manner of describing the thermally fluctuating fluid, due to Hauge and Martin-Löf [103], is specially suited for flows with boundaries. The addition of a random flux, the more conventional manner of description first introduced by Landau and Lifshitz [98], contains ambiguities in the presence of boundaries and is best used, therefore, when the fluid is unbounded in all directions [103].

The key property of the above problem, which makes it possible to eliminate the fluid degrees of freedom *exactly*, is linearity. It is most clearly expressed in terms of the

boundary-domain integral representation of slow viscous flow which provides the fluid flow in the bulk in terms of the boundary condition and the thermal force. The traction $\boldsymbol{f}(\boldsymbol{r}_i)$ on i-th colloids is obtained as a solution of the boundary-domain integral equation

$$\begin{aligned}\tfrac{1}{2}v_\alpha(\boldsymbol{r}_i) = &\int G_{\alpha\beta}(\boldsymbol{r}_i,\boldsymbol{r}')\xi_\beta(\boldsymbol{r}')\,dV' - \int G_{\alpha\beta}(\boldsymbol{r}_i,\boldsymbol{r}_j)f_\beta(\boldsymbol{r}_j)\,d\mathrm{S}_j \\ &+ \int K_{\beta\alpha\gamma}(\boldsymbol{r}_i,\boldsymbol{r}_j)\hat{\rho}_\gamma v_\beta(\boldsymbol{r}_j)\,d\mathrm{S}_j,\end{aligned} \tag{3.4}$$

where $G_{\alpha\beta}(\boldsymbol{r},\boldsymbol{r}')$ is a Green's function of the Stokes equation and $K_{\alpha\beta\gamma}(\boldsymbol{r},\boldsymbol{r}')$ is the associated stress tensor as described in the last chapter. Implicit in the above is a choice of Green's function that satisfies no-slip boundary conditions at any boundary of the fluid that is not part of S.

Using the definition of the single-layer and double-layer integral operators $\boldsymbol{G}$ and $\boldsymbol{K}$ from Eq. (2.13), and a Brownian velocity field $\boldsymbol{w}$ as

$$\boldsymbol{w} = \int \mathbf{G}(\boldsymbol{r}_i,\boldsymbol{r}')\cdot\boldsymbol{\xi}(\boldsymbol{r}')\,dV', \tag{3.5}$$

the solution of the boundary-domain integral equation can be expressed formally in terms of the inverse of the single-layer integral operator as

$$\boldsymbol{f} = \boldsymbol{G}^{-1}\cdot\boldsymbol{w} - \boldsymbol{G}^{-1}\cdot\boldsymbol{v}_i^{D} - \boldsymbol{G}^{-1}\cdot\left(\tfrac{1}{2}\boldsymbol{I}-\boldsymbol{K}\right)\cdot\boldsymbol{v}_i^{\mathcal{A}}. \tag{3.6}$$

This formal solution shows that: (i) the traction is a sum of a Brownian contribution $\hat{\boldsymbol{f}} = \boldsymbol{G}^{-1}\cdot\boldsymbol{w}$ from the fluctuations in the fluid and a deterministic contribution from the boundary condition, containing both the rigid body motion $\boldsymbol{f}^{\mathcal{D}} = -\boldsymbol{G}^{-1}\cdot\boldsymbol{v}^{\mathcal{D}}$ and the active slip $\boldsymbol{f}^{\mathcal{A}} = -\boldsymbol{G}^{-1}\cdot\left(\frac{1}{2}\boldsymbol{I}-\boldsymbol{K}\right)\cdot\boldsymbol{v}^{\mathcal{A}}$ (ii) the Brownian traction is a zero-mean Gaussian random variable whose variance is linearly related to the variance of the thermal force $\boldsymbol{\xi}$ and (iii) the variance of the Brownian traction can be determined from the inverse of the single-layer operator and the fluctuation-dissipation relation for the thermal force. In the

next section, we provide a solution for the boundary-domain integral equation in a basis adapted for a spherical active colloid and, thereby, derive the explicit form of the traction in terms of generalized friction tensors.

3.3 Brownian traction

As show in previous section, the expression of traction has contribution from rigid body motion, activity and Brownian motion. Accordingly, we write the traction $\boldsymbol{f}$ as the sum

$$\boldsymbol{f} = \boldsymbol{f}^{H} + \hat{\boldsymbol{f}} = \boldsymbol{f}^{\mathcal{D}} + \boldsymbol{f}^{\mathcal{A}} + \hat{\boldsymbol{f}}, \tag{3.7}$$

with corresponding expansion coefficients $\mathbf{F}_i^{\mathcal{D}(l)}$, $\mathbf{F}_i^{\mathcal{A}(l)}$ and $\hat{\mathbf{F}}_i^{(l)}$ in terms of tensorial spherical harmonics, following Eq. (2.3b). By linearity, the three parts of the traction satisfy *independent* boundary integral equations.

$$V_\alpha + \epsilon_{\alpha\beta\gamma}\Omega_\beta\rho_\gamma = -\int G_{\alpha\beta}(\boldsymbol{r}_i, \boldsymbol{r}_j) f_\beta^{\mathcal{D}}(\boldsymbol{r}_j)\, d\mathrm{S}_j, \qquad \text{(rigid body)} \tag{3.8a}$$

$$\frac{1}{2} v_\alpha^{\mathcal{A}}(\boldsymbol{r}_i) = -\int G_{\alpha\beta}(\boldsymbol{r}_i, \boldsymbol{r}_j) f_\beta^{\mathcal{A}}(\boldsymbol{r}_j)\, d\mathrm{S}_j + \int K_{\beta\alpha\gamma}(\boldsymbol{r}_i, \boldsymbol{r}_j)\hat{\rho}_\gamma v_\beta^{\mathcal{A}}(\boldsymbol{r}_j)\, d\mathrm{S}_j, \qquad \text{(active)} \tag{3.8b}$$

$$0 = \int G_{\alpha\beta}(\boldsymbol{r}_i, \boldsymbol{r}')\xi_\beta(\boldsymbol{r}')\, dV' - \int G_{\alpha\beta}(\boldsymbol{r}_i, \boldsymbol{r}_j)\, \hat{f}_\beta(\boldsymbol{r}_j)\, d\mathrm{S}_j. \qquad \text{(Brownian)} \tag{3.8c}$$

The solution of the first two parts have already been obtained in Chapter 2 (see 2.3.1 and 2.3.2). The third integral equation for the Brownian traction is pursued here. Physically, the Brownian traction corresponds to the distribution of surface forces necessary to keep the sphere stationary in the incident Brownian velocity field $\boldsymbol{w}(\mathbf{r})$. From this, it is particularly clear that the Brownian traction is a zero-mean Gaussian random variable whose variance is related to that of $\boldsymbol{\xi}$. We now present explicit solutions for each of the integral equations using Galerkin's method of discretization. Linear algebraic systems are derived by inserting the basis expansions on each side of the integral equations, weighting the result by another basis function and integrating over the boundary.

The linear algebraic system for the Brownian contribution to the traction is

$$\boldsymbol{G}_{ij}{}^{(l,l')}(\boldsymbol{R}_i, \boldsymbol{R}_i) \cdot \hat{\mathbf{F}}_j^{(l')}(t) = \boldsymbol{W}_i^{(l)}(\boldsymbol{R}_i, t), \tag{3.9}$$

where $\boldsymbol{W}_i^{(l)}$ are coefficients of the irreducible tensor expansion

$$\boldsymbol{w}(\boldsymbol{R}_i + \boldsymbol{\rho}_i) = \sum_{l=1}^{\infty} \frac{1}{(l-1)!(2l-3)!!} \boldsymbol{W}_i^{(l)}(\boldsymbol{R}_i) \cdot \mathbf{Y}^{(l-1)}(\hat{\boldsymbol{\rho}}), \qquad \text{on } S, \tag{3.10}$$

of the Brownian velocity field incident on the surface of the colloid. From the definition of the Brownian velocity field, Eq. (3.5), these coefficients are given by

$$\boldsymbol{W}^{(l)}(\boldsymbol{R}_i) = \int \boldsymbol{G}^{(l)}(\boldsymbol{R}_i, \boldsymbol{r}') \cdot \boldsymbol{\xi}(\boldsymbol{r}')\, dV'. \tag{3.11}$$

The solution of the linear system for the Brownian traction is

$$\hat{\mathbf{F}}_i^{(l)}(t) = \left[\boldsymbol{G}^{-1}\right]_{ij}^{(l,l')} \cdot \boldsymbol{W}^{(l')}(\boldsymbol{R}_j, t). \tag{3.12}$$

The coefficients of the Brownian traction are proportional to the coefficients of the Brownian velocity field incident on the surface of the colloid and, by Eq. (3.5), to the thermal force in the fluctuating Stokes equation. It is clear, then, that the traction coefficients are zero-mean Gaussian random variables and to fully specify their distribution it is necessary, then, to only determine their variance. By the previous equation, their variance is related to that of the Brownian velocity coefficients as

$$\langle \hat{\mathbf{F}}_i^{(l)}(t) \hat{\mathbf{F}}_j^{(l')}(t') \rangle = \left[\boldsymbol{G}^{-1}(\boldsymbol{R})\right]_{ip}^{(l,k)} \langle \boldsymbol{W}^{(k)}(\boldsymbol{R}_p, t') \boldsymbol{W}^{(k')}(\boldsymbol{R}_m, t') \rangle \left[\boldsymbol{G}^{-1}(\boldsymbol{R})\right]_{jm}^{(l',k')}. \tag{3.13}$$

To determine the variance of Brownian velocity coefficients we use the boundary integral representation of $\boldsymbol{v}^{\mathcal{D}}$ given above (see also previous chapter). Inserting this on the left of

the fluctuation-dissipation relation for the thermal force, Eq. (3.2), gives

$$\left\langle \int \boldsymbol{v}^{\mathcal{D}}(\mathbf{r})\cdot\boldsymbol{\xi}(\boldsymbol{r},t)\,dV \int \boldsymbol{v}^{\mathcal{D}}(\boldsymbol{r}')\cdot\boldsymbol{\xi}(\boldsymbol{r}',t')\,dV' \right\rangle = \mathbf{F}_i^{\mathcal{D}(l)}\cdot\left\langle \boldsymbol{W}^{(l)}(\boldsymbol{R}_i,t')\boldsymbol{W}^{(l')}(\boldsymbol{R}_j,t')\right\rangle\cdot\mathbf{F}_j^{\mathcal{D}(l')}. \tag{3.14}$$

On the other hand, the power dissipated by the rigid body motion, Eq. (3.3), on the right of the fluctuation-dissipation relation can be expressed as

$$\dot{\mathcal{E}}(\boldsymbol{v}^{\mathcal{D}}) = -\int \boldsymbol{f}^{\mathcal{D}}(\boldsymbol{R}_i+\boldsymbol{\rho}_i)\cdot\boldsymbol{v}^{\mathcal{D}}(\boldsymbol{R}_i+\boldsymbol{\rho}_i)\,d\mathrm{S}_i = -\mathbf{F}_i^{\mathcal{D}(l)}\cdot\mathbf{V}_i^{\mathcal{D}(l)} = \mathbf{F}_i^{\mathcal{D}(l)}\cdot\boldsymbol{G}_{ij}{}^{(l,l')}(\boldsymbol{R})\cdot\mathbf{F}_j^{\mathcal{D}(l')}. \tag{3.15}$$

The above expression has been derived from Eq. (3.3) following steps of section 2.5. Comparing the above two equations, we obtain the key identity for the variance of the Brownian velocity coefficients,

$$\langle \boldsymbol{W}^{(l)}(\boldsymbol{R}_i,t')\boldsymbol{W}^{(l')}(\boldsymbol{R}_j,t')\rangle = 2k_BT\,\boldsymbol{G}^{(l,l')}(\boldsymbol{R}_i,\boldsymbol{R}_j)\,\delta(t-t'). \tag{3.16}$$

Using this expression in Eq. (3.13) yields the variance of Brownian traction coefficients

$$\langle \hat{\mathbf{F}}_i^{(l)}(t)\hat{\mathbf{F}}_j^{(l')}(t')\rangle = 2k_BT\,[\boldsymbol{G}^{-1}]_{ij}^{(l,l')}\delta(t-t'). \tag{3.17}$$

These are an infinite number of fluctuation-dissipation relations between the variance of the tensorial harmonic modes of the Brownian traction and the matrix elements, in the irreducible tensorial harmonic basis, of the *inverse* of the single-layer operator. To the best of our knowledge, the complete statistics of the Brownian traction is derived for the first time in [12] and is an important result of this chapter.

The variance of the irreducible parts of the Brownian traction follow straightforwardly

$$\langle \hat{\mathbf{F}}_i^{(l\sigma)}(t)\hat{\mathbf{F}}_j^{(l'\sigma')}(t')\rangle = 2k_BT\,\mathbf{P}^{(l\sigma)}\cdot[\boldsymbol{G}^{-1}]_{ij}^{(l,l')}\cdot\mathbf{P}^{(l'\sigma')}\delta(t-t'). \tag{3.18}$$

The first two coefficients of the Brownian traction are the force and torque, and choosing $l\sigma = 1s, 2a$ we obtain

$$\langle \hat{\mathbf{F}}_i \rangle = 0, \quad \langle \hat{\mathbf{F}}_i(t)\hat{\mathbf{F}}_j(t')\rangle = 2k_BT\,\boldsymbol{\gamma}_{ij}^{TT}\delta(t-t'), \quad \langle \hat{\mathbf{F}}_i(t)\hat{\mathbf{T}}_j(t')\rangle = 2k_BT\,\boldsymbol{\gamma}_{ij}^{TR}\delta(t-t'), \tag{3.19}$$

$$\langle \hat{\mathbf{T}}_i \rangle = 0, \quad \langle \hat{\mathbf{T}}_i(t)\hat{\mathbf{F}}_j(t')\rangle = 2k_BT\,\boldsymbol{\gamma}_{ij}^{RT}\delta(t-t'), \quad \langle \hat{\mathbf{T}}_i(t)\hat{\mathbf{T}}_j(t')\rangle = 2k_BT\,\boldsymbol{\gamma}_{ij}^{RR}\delta(t-t'). \tag{3.20}$$

where $\boldsymbol{\gamma}^{\alpha\beta}$, with $\alpha,\beta = T,R$, are the one-particle friction tensor and are ($l\sigma = 1s, 2a$) elements of $\mathbf{P}^{(l\sigma)} \cdot [\boldsymbol{G}^{-1}]^{(l,l')} \cdot \mathbf{P}^{(l'\sigma')}$. The fluctuation-dissipation relation for the Brownian force and torque are, thus, derived from the fluctuation-dissipation relation for the thermal force on the fluid.

We make the following remarks about the above derivation. First, the explicit form of the inverse of the single-layer operator is not necessary to obtain Eq. (3.17); it is sufficient to know that the inverse exists. Therefore, the fluctuation-dissipation relation for the irreducible coefficients, Eq. (3.18), is valid for any geometry bounding the fluid, provided the flow vanishes there. In particular, it holds for colloids near a plane wall. Second, our derivation provides the fluctuation-dissipation relation for *all* modes of the Brownian traction. Earlier derivations have focused on only the force and torque. Therefore, our derivation provides the fluctuating stresslet ($l\sigma = 2s$) which is needed to compute the Brownian contribution to the suspension stress. Third, the configuration-dependence of both the fluctuation, Eq. (3.9), and the dissipation, Eq. (3.18), is made explicit in our derivation. The configuration-dependent "noise" variance follows from this automatically. The interpretation of the resulting multiplicative noise in the Langevin equation that we derive below is obtained by recalling that the momentum and angular momentum of the colloid are fast variables that have, implicitly, been adiabatically eliminated [117]. The form of the Smoluchowski equation for this problem is well-known and is used below to consistently interpret the multiplicative noise in the Langevin equation [118–122].

3.4 Langevin description of active colloids

The net hydrodynamic force $\mathbf{F}_i^H$ and torque $\mathbf{T}_i^H$ acting on the i-th colloid are related to its first two irreducible coefficients of the traction $\boldsymbol{f}$ and from the generalized Stokes laws these are

$$\mathbf{F}_i^H = -\boldsymbol{\gamma}_{ij}^{TT}\cdot\mathbf{V}_j - \boldsymbol{\gamma}_{ij}^{TR}\cdot\boldsymbol{\Omega}_j - \sum_{l\sigma=1s}^{\infty} \boldsymbol{\gamma}_{ij}^{(T,l\sigma)}\cdot\mathbf{V}_j^{(l\sigma)}, \tag{3.21a}$$

$$\mathbf{T}_i^H = -\boldsymbol{\gamma}_{ij}^{RT}\cdot\mathbf{V}_j - \boldsymbol{\gamma}_{ij}^{RR}\cdot\boldsymbol{\Omega}_j - \sum_{l\sigma=1s}^{\infty} \boldsymbol{\gamma}_{ij}^{(R,l\sigma)}\cdot\mathbf{V}_j^{(l\sigma)}. \tag{3.21b}$$

Here, the $\boldsymbol{\gamma}_{ij}^{\alpha\beta}$ with $\alpha,\beta = T,R$ are relabellings of the four friction tensors $\boldsymbol{\gamma}_{ij}^{(l\sigma,l'\sigma')}$ with $l\sigma,l'\sigma' = 1s,2a$, where the correspondences are $T \leftrightarrow 1s$ and $R \leftrightarrow 2a$. The $\boldsymbol{\gamma}_{ij}^{(T,l\sigma)}$ and $\boldsymbol{\gamma}_{ij}^{(R,l\sigma)}$ are relabellings of the friction tensors $\boldsymbol{\gamma}_{ij}^{(1s,l\sigma)}$ and $\boldsymbol{\gamma}_{ij}^{(2a,l\sigma)}$ respectively. The first two terms in the force and torque expressions above are the usual rigid body drag [56, 57] while the remaining terms are the contributions from the slip. The effect of activity is then clear: it adds long-ranged, many-body correlated, orientation-dependent dissipative forces and torques to the familiar Stokes drags.

Expressions for the generalized friction tensors, in terms of Green's functions of the Stokes equation, have been derived in Appendix A.4. Their leading order form is

$$\boldsymbol{\gamma}_{ij}^{(l\sigma,l'\sigma')} \sim \nabla_i^{l-1}\nabla_j^{l'-1}\mathbf{G}(\boldsymbol{R}_i,\boldsymbol{R}_j). \tag{3.22}$$

In an unbounded fluid, this decays as $|\boldsymbol{R}_i - \boldsymbol{R}_j|^{-(l+l'-1)}$ and is thus long-ranged for $l+l' \leq 4$. Thus, all slip modes up to $l = 3$ produce long-ranged forces and up to $l = 2$ produce long-ranged torques. Notably, the active forces and torques have contributions even without self-propulsion, $\mathbf{V}_i^{\mathcal{A}} = 0$, or self-rotation, $\boldsymbol{\Omega}_j^{\mathcal{A}} = 0$, indicating that colloids can be "active" without necessarily being self-propelling or self-rotating. The friction tensors depend on the positions of all the particles and are thus many-body functions of the instantaneous colloidal configurations.

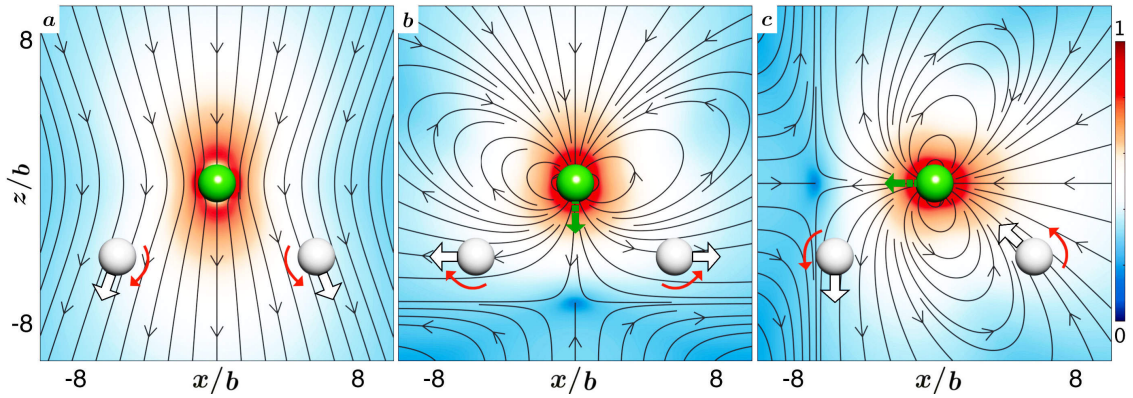

Figure 3.1: Forces and torques depend on orientation of colloids as friction is both non-local and orientation-dependent. Streamlines of the flow are plotted over the pseudo color plot of normalized logarithm of the flow speed, along with two tracer colloids (white) to show the direction of force (white arrows) and torque (curved red arrows) acting on them. Panel (a) has the flow due to an external force on the colloid in negative $\hat{\mathbf{z}}$ direction, while panel (b) and (c) contain the flow due to active slip modes $l\sigma = 2s$ and $l\sigma = 3t$.

A remarkable feature of active forces and torques is that they depend not only on the relative position of the particles, as in a passive suspension of spheres, but also through the slip moments, on their orientations. Thus active colloids, even if they are geometrically isotropic, are hydrodynamically anisotropic. An intuitive understanding of the same can be gained from Fig. (3.1). The first panel plots the flow around a passive particle where the direction of the velocity is determined solely by the sum of the body forces. Changing the particle orientation does not change the flow and, therefore, produces no change in the force, shown by the white arrows, on the two test particles. The second panel shows the flow around an active particle where the slip contains the modes $l\sigma = 2s$ and $3t$. In the third panel, the active particle is rotated clockwise by $\pi/2$, without any change in position. The forces are now different, even though there has been no changes in relative positions. Similar considerations apply for the torque as the reader can easily verify. It is precisely these orientation-dependent forces and torques that lead to the rich and intriguing dynamics in active suspensions and distinguishes them from passive suspensions. Finally, though these forces and torques appear in Newton's equations, they are, emphatically, not body forces and torques: they are the sum of the dissipative surface forces that act at the fluid-solid boundary.

The hydrodynamic forces and torques obtained above can be used to construct the Langevin equations describing the motion of active colloids in a thermally fluctuating fluid. This is obtained from the balance of hydrodynamic, body and Brownian forces and torques as provided in Eq. (2.1). The Brownian forces and torques, $\hat{\mathbf{F}}_i$ and $\hat{\mathbf{T}}_i$, are zero-mean, Gaussian white noises and the fluctuation-dissipation relation fixes their variances (see section 3.3). We do not consider any fluctuations corresponding to activity, since its inherently non-equilibrium nature precludes any possible balance between fluctuation and dissipation. Using explicit forms, the Langevin equations for active colloids with hydrodynamic interactions are

$$-\boldsymbol{\gamma}_{ij}^{TT}\cdot\mathbf{V}_j-\boldsymbol{\gamma}_{ij}^{TR}\cdot\boldsymbol{\Omega}_j+\mathbf{F}_i^P+\hat{\mathbf{F}}_i-\sum_{l\sigma=1s}^{\infty}\boldsymbol{\gamma}_{ij}^{(T,l\sigma)}\cdot\mathbf{V}_j^{(l\sigma)}=0, \tag{3.23a}$$

$$-\boldsymbol{\gamma}_{ij}^{RT}\cdot\mathbf{V}_j-\boldsymbol{\gamma}_{ij}^{RR}\cdot\boldsymbol{\Omega}_j+\mathbf{T}_i^P+\hat{\mathbf{T}}_i-\sum_{l\sigma=1s}^{\infty}\boldsymbol{\gamma}_{ij}^{(R,l\sigma)}\cdot\mathbf{V}_j^{(l\sigma)}=0. \tag{3.23b}$$

Explicit Langevin equations for the velocity and angular velocity are obtained by inverting above equation. Since the $\boldsymbol{\gamma}_{ij}^{\alpha\beta}$ and the $\boldsymbol{\gamma}_{ij}^{(\alpha,l\sigma)}$are identical for $l\sigma=1s,2a$, it is convenient to group the velocity with the self-propulsion and the angular velocity with the self-rotation so that the summation is from $l\sigma=2s$ onward. With this regrouping, the result is [11, 12]

$$\begin{aligned}
\mathbf{V}_i &= \boldsymbol{\mu}_{ij}^{TT}\cdot\mathbf{F}_j^P+\boldsymbol{\mu}_{ij}^{TR}\cdot\mathbf{T}_j^P+\sqrt{2k_BT\boldsymbol{\mu}_{ij}^{TT}}\cdot\boldsymbol{\eta}_j^T+\sqrt{2k_BT\boldsymbol{\mu}_{ij}^{TR}}\cdot\boldsymbol{\zeta}_j^R+\sum_{l\sigma=2s}^{\infty}\boldsymbol{\pi}_{ij}^{(T,l\sigma)}\cdot\mathbf{V}_j^{(l\sigma)}+\mathbf{V}_i^{\mathcal{A}},\\
\boldsymbol{\Omega}_i &= \underbrace{\boldsymbol{\mu}_{ij}^{RT}\cdot\mathbf{F}_j^P+\boldsymbol{\mu}_{ij}^{RR}\cdot\mathbf{T}_j^P}_{\text{Passive}}+\underbrace{\sqrt{2k_BT\boldsymbol{\mu}_{ij}^{RT}}\cdot\boldsymbol{\zeta}_j^T+\sqrt{2k_BT\boldsymbol{\mu}_{ij}^{RR}}\cdot\boldsymbol{\eta}_j^R}_{\text{Brownian}}+\underbrace{\sum_{l\sigma=2s}^{\infty}\boldsymbol{\pi}_{ij}^{(R,l\sigma)}\cdot\mathbf{V}_j^{(l\sigma)}+\boldsymbol{\Omega}_i^{\mathcal{A}}}_{\text{Active}}.
\end{aligned} \tag{3.24}$$

Here $\boldsymbol{\eta}^\alpha$, $\boldsymbol{\zeta}^\alpha$are Gaussian white noises with zero-mean and variances 1, $1/b$ respectively. The matrix square roots are to be interpreted as Cholesky factors. The mobility matrices $\boldsymbol{\mu}_{ij}^{\alpha\beta}$ are inverses of the friction matrices $\boldsymbol{\gamma}_{ij}^{\alpha\beta}$ [56, 57, 85, 123–129]. The propulsion tensors $\boldsymbol{\pi}_{ij}^{(\alpha,l\sigma)}$, first introduced in [10], relate the rigid body motion to modes of the active slip

velocity. They are related to the slip friction tensors as [11]

$$-\boldsymbol{\pi}_{ij}^{(T,l\sigma)} = \boldsymbol{\mu}_{ik}^{TT} \cdot \boldsymbol{\gamma}_{kj}^{(T,l\sigma)} + \boldsymbol{\mu}_{ik}^{TR} \cdot \boldsymbol{\gamma}_{kj}^{(R,l\sigma)}, \tag{3.25a}$$

$$-\boldsymbol{\pi}_{ij}^{(R,l\sigma)} = \boldsymbol{\mu}_{ik}^{RT} \cdot \boldsymbol{\gamma}_{kj}^{(T,l\sigma)} + \boldsymbol{\mu}_{ik}^{RR} \cdot \boldsymbol{\gamma}_{kj}^{(R,l\sigma)}. \tag{3.25b}$$

The translational propulsion tensors $\boldsymbol{\pi}_{ij}^{(T,l\sigma)}$ are dimensionless while the rotational propulsion tensors $\boldsymbol{\pi}_{ij}^{(R,l\sigma)}$ have dimensions of inverse length. The above form of the propulsion tensors is particularly useful when mobilities are evaluated by combining the far-field and near-field lubrication contributions. Through this approximation, the need to resolve the rapidly varying flow at particle contact can be avoided, and accurate results can be obtained by keeping only the long-ranged contributions when solving the linear system. This Langevin equations was first obtained in [130] using heuristic arguments.

Stochastic trajectories can be obtained by integrating the kinematic equations

$$\dot{\boldsymbol{R}}_i = \mathbf{V}_i, \quad \dot{\boldsymbol{p}}_i = \boldsymbol{\Omega}_i \times \boldsymbol{p}_i. \tag{3.26}$$

using the standards Brownian dynamics integrators, for example that due Ermak and McCammon [131]. In this integrator, the noise variances are computed using mobilities in the configuration at time t but a "spurious" drift, proportional to the configurational divergence of the mobilities, is added to to arrive at the configuration at time $t + \Delta t$. There is nothing particularly spurious about this drift; it is simply the residual effect of the adiabatically eliminated degrees of freedom [109].

Eq. (3.23) contain forces due to Stokes drags, body forces, Brownian fluctuations, and activity. Their relative importance can be captured by two ratios. We choose the first of these to be the ratio of active and body forces and the second to be the ratio of thermal and active forces. Similar considerations apply for the torque balance. These motivate the

introduction of the following dimensionless numbers

$$\mathcal{A}_T = \frac{\left|\boldsymbol{\gamma}_{ij}^{(T,l\sigma)} \cdot \mathbf{V}_j^{(l\sigma)}\right|}{\left|\mathbf{F}_i^P\right|}, \quad \mathcal{A}_R = \frac{\left|\boldsymbol{\gamma}_{ij}^{(R,l\sigma)} \cdot \mathbf{V}_j^{(l\sigma)}\right|}{\left|\mathbf{T}_i^P\right|}, \tag{3.27a}$$

$$\mathcal{B}_T = \frac{\left|\hat{\mathbf{F}}_i\right|}{\left|\boldsymbol{\gamma}_{ij}^{(T,l\sigma)} \cdot \mathbf{V}_j^{(l\sigma)}\right|}, \quad \mathcal{B}_R = \frac{\left|\hat{\mathbf{T}}_i\right|}{\left|\boldsymbol{\gamma}_{ij}^{(R,l\sigma)} \cdot \mathbf{V}_j^{(l\sigma)}\right|}. \tag{3.27b}$$

Here $\mathcal{A}_T$ and $\mathcal{A}_R$ are "activity" numbers quantifying the relative importance of active and body terms [130, 132, 133] while $\mathcal{B}_T$ and $\mathcal{B}_R$ are "Brown" numbers quantifying the relative importance of thermal and active terms. It is useful to compare the Brown numbers with the usually studied Péclet number, which is a ratio of the rate of advection by the flow to the rate of diffusion [98]. In contrast, the Brown numbers are the ratios of Brownian forces/torques to active forces/torques.

We now estimate Brownian numbers for typical experiments. An active particle moving at a speed v_s has a typical active force $F \sim 6\pi\eta b v_s$ acting on it. Similarly the torque acting on a colloid due to active spin on its axis at an angular speed ω_s is $T \sim 8\pi\eta b^3\omega_s$. We estimate the typical active force and torque for the experiment in [8], where the radius of the colloid is $b = 4\,\mu$m, $v_s = 500\,\mu$m/s and fluid viscosity $\eta = 10^{-3}\,$kg/ms. The active force is then $F \sim 40 \times 10^{-12}\,$N, while the typical Brownian forces are of order $O(k_B\mathrm{T/b}) \sim 10^{-15}\,$N. This implies that the dimensionless Brown number $\mathcal{B}_T \sim 10^{-4}$ is very small. For the same experiment, the angular speed of the colloids is $\omega_s \sim 50\,s^{-1}$, which implies typical active torque is of order $T \sim 10^{-16}$Nm. The Brownian torques are of order $O(k_B\mathrm{T}) \sim 10^{-21}\,$N, which implies that the rotational Brown number $\mathcal{B}_R$ is of the order of 10^{-5}. The radius of the green algae in [134] is $\sim 3\mu m$ and it swimming speed is $134\mu/s$. The Brown number for this experiment is then $\mathcal{B}^T \sim 10^{-3}$. In another set of experiment on bacteria [135, 136] and Janus colloids [3, 5], the size $b \sim 1\,\mu$m, and the speed $v_s \sim 10\,\mu$m/s. This leads to active force $F \sim 10^{-13}\,$N, which implies that the Brown number is $\mathcal{B}_T \sim 10^{-2}$. Thus Brown numbers $\mathcal{B}_T, \mathcal{B}_R \to 0$ for commonly studied active colloids.

3.5 Conclusion

The force per unit area (or traction) on the surface of active colloids in a fluctuating Stokesian fluid has three parts, due to rigid body motion, activity and Brownian fluctuations. The contributions from the deterministic part of traction was obtained in the previous chapter, while the Brownian traction was derived in this chapter. Here, we also obtained a prescription for computing the configuration-dependent variances of the Brownian force and torque. The complete expression for the traction gives expressions for forces and torques. Since forces and torques are fundamental dynamical quantities in Newtonian or Langevin descriptions of particle dynamics, our contribution forms the basis for a microscopic theory of active suspension mechanics and statistical mechanics that conserves momentum in both the bulk fluid and at fluid-solid boundaries. The Langevin description of active colloids is obtained in terms of mobility matrices and the propulsion tensors. The far-field limit of the mobility matrices are obtained in terms of the Green's function of the Stokes flow while a lubrication approximation is used when the colloids are close to each other [89, 128]. The propulsion tensors are obtained in terms of the lubrication-corrected mobilities and the friction tensors. Thus we account for both the far-field hydrodynamic interactions, to any order of desired accuracy, and the near-field lubrication interactions.

It is instructive to compare our approach with existing descriptions of active matter. These can be broadly classified into kinematic theories [137–145] that prescribe active motion, without considering the balance of mass, momentum, angular momentum and energy, and dynamic theories which derive the active motion from the balance of these conserved quantities [33, 34, 36, 146–148]. The models, both kinematic and dynamic, can be also be classified by the length and time scales at which they resolve matter. Hydrodynamic theories operate at the coarsest length and time scales, and retain only variables that relax slowly. Kinetic theories operate at smaller length and time scales and contain in them the hydrodynamic description. Finally, particulate models offer a scale of resolution higher than both of hydrodynamic and kinetic theories.

In the context of the above classification, our approach is a momentum-conserving particulate model for active matter. Active motion in our approach appears as a consequence of the dynamical balance of forces and torques on the colloids. In contrast to models that retain explicit fluid degrees of freedom to enforce momentum conservation [13, 132, 149–152], our approach eliminates explicit fluid degrees of freedom and yet retains momentum conservation. This is possible at low Reynolds numbers, as the momentum balance equation for the fluid reduces to an elliptic partial differential equation whose solution can be represented as integrals over the domain boundaries. Momentum conservation is enforced at the boundaries and is automatically ensured in the bulk through the integral representation of Stokes equation. The integral equations for the motion of spherical active colloids in Stokes flow are discretized using a Galerkin method by expanding the boundary fields in tensorial spherical harmonics to obtain a infinite-dimensional system of linear equations. The Galerkin discretization of the boundary integral equation provides most accurate results for smooth boundaries, like spheres, for least number of unknowns and preserves the self-adjointness of the problem [80, 82]. Remarkably, the matrix elements of the linear system can be evaluated analytically [10] for spheres and the numerical quadrature can be avoided entirely. The linear system involves matrices of size $O(N \times N)$, in contrast to a direct simulation, resolving the three-dimensional fluid degrees of freedom, which requires an $O(N^3)$ box. Thus massive computational gains are achieved and dynamic simulations of hundreds of thousands of active colloids on current multi-core computational architectures are possible.

It is also useful to compare the results presented here with the existing work in the literature for the hydrodynamic interactions of many colloidal spheres, where a truncation of the modes along with the lubrication approximation is used. Excluding the contribution from active slip and truncating the Galerkin expansion at $l = 2$, results in the method of computing far-field hydrodynamic interactions in the so-called 'FTS' Stokesian dynamics method of Brady and coworkers [127, 128]. Thus, this method ignores the entire $l = 3$ contribution which decay as r^{-3} for unbounded flow and are long-ranged. This low-order

truncation has been subsequently extended up to to 7th order in polynomials by Ichiki [74]. Ichiki's method extension requires six separate steps to relate the 21 velocity coefficients to the traction coefficients, while the method here, using identical basis functions for both velocity and traction, directly provides expressions for the coefficients and the problem is reduced, directly, to solving the linear system. The basis used here ensured that all the modes at l decay as r^{-l}, this is in contrast to the complicated accounting necessary for the basis sets used in the works of Cichocki [129] and Ichiki [74]. Earlier work closest in spirit to ours is that of Ishikawa *et al* [153–155] where axisymmetric slip velocities, truncated to the first two non-trivial modes, are considered. In contrast, we include the most general form of the slip and use an irreducible basis function for Galerkin discretization which gives a systematic way of evaluating hydrodynamic interaction up to any order of desired accuracy.

Chapter 4

Unbounded flows: Active colloids in external potentials

4.1 Introduction

In this chapter, we study the dynamics of active colloids in an unbounded Stokes flow by confining them in external potentials. The simplest system in which an interplay of non-uniform external fields, activity, and Brownian motion can be studied is an active colloid confined in a three-dimensional harmonic potential. As this system is both experimentally realizable in optical trapping experiments [3, 156] and analytically tractable [10, 13, 140] it serves as the "Ising model" of active colloidal physics. We study polar active colloids in a single trap and in a square lattice of traps. We also consider the motion of apolar active colloids in a spherical confinement.

The chapter is organized as follows. In section 4.2, we use the Langevin equations derived in Chapter 3 to study the collective motion of active colloids in a harmonic trap. Through detailed numerical simulations, we find that steady-state convective currents are established and, the so-called self-assembled pump is formed in the trap. We explain

this phenomenon by the interplay of hydrodynamic torques due to confinement and active forces due to self-propulsion of the colloids. We, then, study the dynamics of active colloids in lattices of harmonics traps in section 4.3. The traps are centered on a lattice and we consider only one active colloid per trap. We find that a one-dimensional lattice of traps supports time-independent configurations but a two-dimensional lattice of traps only supports time-dependent configurations. In particular, we show that the colloids exhibit a synchronized dynamics about the axis of symmetry in square and triangular lattices of traps. We conclude the section by relating synchrony to the entropy production in a triangular lattice. These dynamical systems of active colloids in external potentials display rich phenomenology which we rationalize by leading order estimates of hydrodynamic forces and torques acting on them. In section 4.4 we turn to mechanical quantities in the fluid, focusing on the fluid pressure in a suspension of active colloids confined to the interior of a spherical volume. We find that the dynamics of the colloids and the distribution of the fluid pressure are different for suspensions of extensile and contractile colloids. The difference in the collective dynamics of the colloids is understood qualitatively from the fluid flow created by the active colloids.

4.2 Active colloids in a harmonic potential

We first study the motion of active colloids in a harmonic potential. The principal question we focus on is the collective dynamics of the colloids. From estimates of the dimensionless groups presented in the previous Chapter, it is clear that Brownian motion can be ignored in the first approximation. Accordingly, we neglect noise and study the mechanics of the system, postponing the study of its statistical mechanics to a future work.

We consider self-propelling, polar, achiral active colloids, with non-zero values of $\mathbf{V}_i^{\mathcal{A}}$, $\mathbf{V}_i^{(2s)}$ and $\mathbf{V}_i^{(3t)}$. The fluid flow due to these modes is given in Figure (4.6). With this choice, an isolated colloid translates with velocity $\mathbf{V}_i^{\mathcal{A}} = v_s \boldsymbol{p}_i$ while producing dipolar

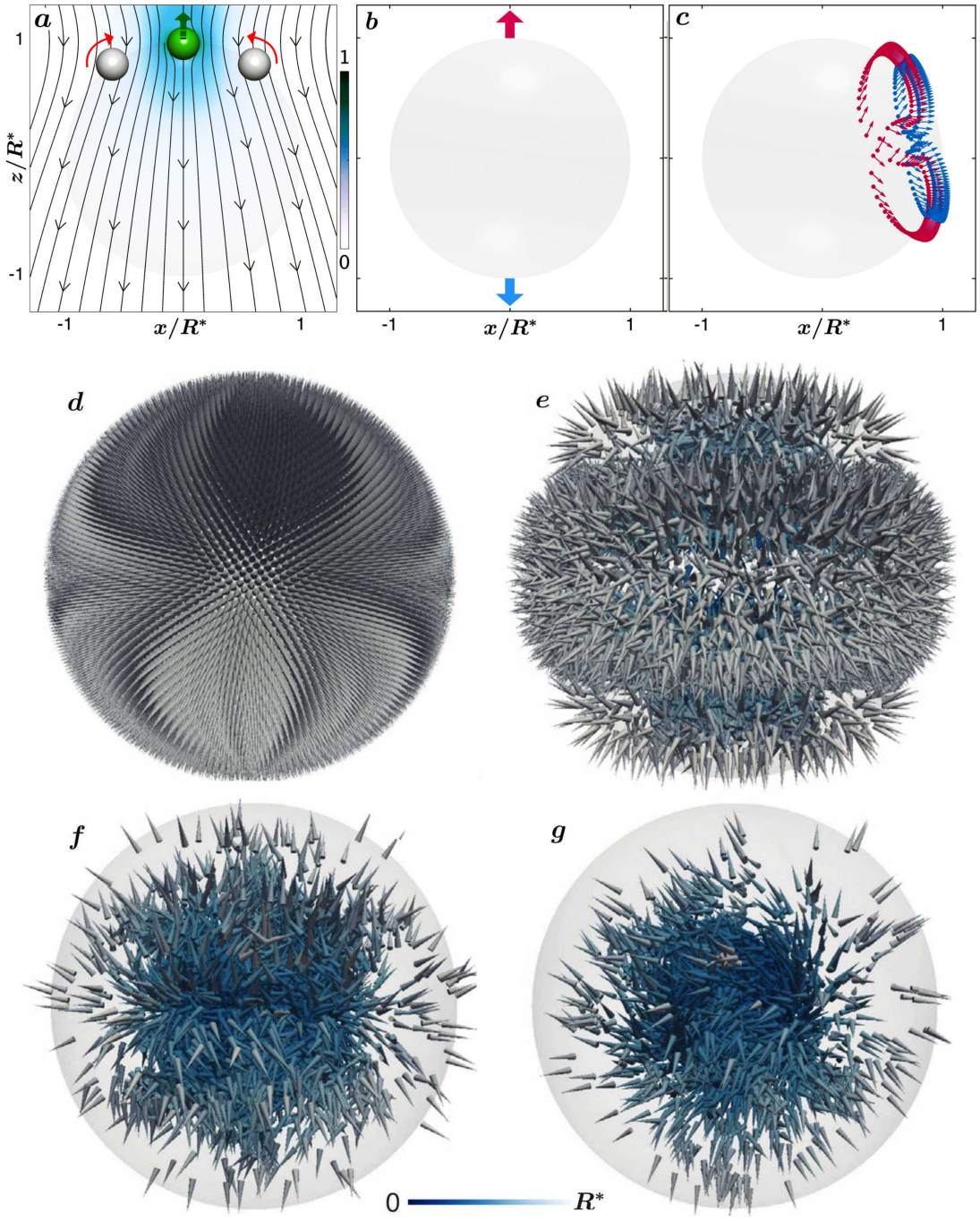

Figure 4.1: Collective dynamics of polar active colloids in a harmonic trap. (**a**). Streamlines of the flow due to a colloid at the north pole of the trap, while the red curved arrows on the tracers (white spheres) indicate the hydrodynamic torques acting on them. (**b**-**c**). Dynamic of two colloids: the first colloid (red) is initialized at the north pole, while the second (blue) is kept at an angle θ_0 with it. (**b**). $\theta_0 = 180$, and thus there is no hydrodynamic torque on the colloids (see Eq. 4.3) and the streamlines, while for any other angle ($\theta_0 = 115$ in (c)), the colloids form a closed orbit. (**d**-**g**). Snapshots from a simulation of 10^4 trapped colloids (cones colored by distance from the origin) are shown in steps of rotational time scale $\frac{8\pi\eta b}{k}$. With time steady-state convective currents are established, see Movie (4.1) and, the so-called self-assembled pump is formed in the trap [10, 13].

and quadrupolar flows of strengths proportional to $\mathbf{V}_i^{(2s)}$ and $\mathbf{V}_i^{(3t)}$ respectively [10, 45]. The centers of the trap is at the origin. There is a net external force acting on the colloids, which depends on the trap stiffness k and its displacement from the center $\boldsymbol{R}_i$. The moment of forces acting on the colloids about the trap center is zero. The body forces and torques on the i-th colloid is then

$$\mathbf{F}_i^P = -k\boldsymbol{R}_i, \qquad \mathbf{T}_i^P = 0. \tag{4.1}$$

First, we consider the dynamics ignoring hydrodynamic interactions. Then, force and torque balance give

$$-6\pi\eta b(\mathbf{V}_i - v_s\boldsymbol{p}_i) - k\boldsymbol{R}_i \;\; = 0, \qquad -8\pi\eta b^3\,\boldsymbol{\Omega}_i = 0. \tag{4.2}$$

In the absence of hydrodynamic and Brownian torques, there is no angular velocity and the colloid translates in a direction $\boldsymbol{p}_i$ chosen by the initial condition. It is brought to rest at a radius $R^* = 6\pi\eta b v_s/k = \mathcal{A}_T b$, when the propulsive and trap forces are balanced [10, 13]. Here $\mathcal{A}_T$ is the activity number defined in Eq. (3.27a), which quantifies the ratio of active propulsive force to the passive confining force. The stationary state, without hydrodynamic interactions, is one in which all colloids are confined at a distance R^* from the center of its trap and oriented radially outward in a direction that is, in general, different for each colloid. We use this state as the initial condition in our simulations of active colloids in a harmonic trap and in a lattice of traps.

This state is destabilized *with* hydrodynamic interactions [10, 13, 157] due to the torque induced by the flow of the $l\sigma = 1s$ and $2s$ modes [10]. The leading contributions to the hydrodynamic torque is

$$\mathbf{T}_i^H = -\boldsymbol{\gamma}_{ij}^{RT} \cdot (\mathbf{V}_i - v_s\boldsymbol{p}_i) - \boldsymbol{\gamma}_{ij}^{(R,2s)} \cdot \mathbf{V}_j^{(2s)}$$

which, upon using the explicit forms of the generalized friction tensors from Appendix

A.4, turns out to be

$$\mathbf{T}_i^H = 8\pi\eta b^3\Big[-\frac{\hat{\boldsymbol{r}}_{ij}}{r_{ij}^2}\times\frac{k\boldsymbol{R}_j}{6\pi\eta}+\frac{14(\boldsymbol{p}_j\cdot\hat{\boldsymbol{r}}_{ij})}{r_{ij}^3}(\boldsymbol{p}_j\times\hat{\boldsymbol{r}}_{ij})V_0^{(2s)}b^2\Big]+O(r_{ij}^{-3}) \tag{4.3}$$

Here $\boldsymbol{r}_{ij}=\boldsymbol{R}_i-\boldsymbol{R}_j$ and the force balance equation has been used to eliminate $\mathbf{V}_i-v_s\boldsymbol{p}_i$ in favor of the trapping force. The hydrodynamic torque vanishes when the colloids are collinear and their orientations are along the line joining their centers. Thus stable states of rest are possible even in the presence of hydrodynamic interactions for specially chosen initial conditions [10]. In general, though, the interplay of self-propulsion, confinement, and hydrodynamic interactions produce steady states with continuous motion.

We first study the effects of hydrodynamic interactions in a system of two active colloids in a harmonic trap. The hydrodynamic interaction can be understood pictorially by studying the flow diagram in the first panel of Figure (4.1). In the second panel, we show the dynamics of two active colloids initialized on the surface of the trap at an angle θ_0 between them. In our simulations, we find that the system of two active colloids is stable when they are collinear ($\theta_0 = 180$) while they form closed orbits for any other angle between them as shown in the remaining two panels of the first row of Figure (4.1). This is consistent with the expression of the hydrodynamic torque in Eq. (4.3), which vanishes if the colloids are collinear.

In the lower two panels of Figure (4.1), we show the dynamics of 10^4 active colloids in a harmonic trap. The colloids are initialized uniformly on the surface of the trap sphere whose radius is set by the balance of the trap and propulsion force, and is thus the stable state in absence of hydrodynamic interactions (see Eq. (4.2)). We have already demonstrated that two active colloids form orbits in a trap due to hydrodynamic torques induced by the confinement and the self-propulsion of the colloids. These colloidal orbits coalesce to form "self-assembled" pump where colloids undergo continuous convective-rolls in a trap [10, 13]. Thus steady-state convective currents are established in the system by a combined effect of self-propulsion, confinement, and hydrodynamic interactions.

4.3 Dynamics in an optical lattice

In this section, we study the dynamics of active colloids in a two-dimensional lattice of traps. Here, the main focus is to study the dynamics of the colloids and, in particular, their synchronization. The system we study can be realized experimentally in holographic tweezers. The centers of the N traps are at $\boldsymbol{R}_i^0$, arranged linearly or in a $\sqrt{N}\times\sqrt{N}$ square lattice. Each trap contains a single active colloid which feels a body force from that trap alone. The moment of force about the trap center is zero. Therefore, in a trap of stiffness k centered at $\boldsymbol{R}_i^0$

$$\mathbf{F}_i^P = -k(\boldsymbol{R}_i - \boldsymbol{R}_i^0), \qquad \mathbf{T}_i^P = 0. \tag{4.4}$$

Again, we start by ignoring hydrodynamic interactions to obtain the balance of forces and torques

$$-6\pi\eta b(\mathbf{V}_i - v_s\boldsymbol{p}_i) - k(\boldsymbol{R}_i - \boldsymbol{R}^0) \;\; = 0, \qquad -8\pi\eta b^3\,\boldsymbol{\Omega}_i = 0.$$

This, again, gives the confinement radius $R^* = 6\pi\eta b v_s/k = \mathcal{A}_T b$, when the propulsive and trap forces are balanced. The expression for hydrodynamic torques in this case is

$$\mathbf{T}_i^H = 8\pi\eta b^3\Big[-\frac{\hat{\boldsymbol{r}}_{ij}}{r_{ij}^2}\times\frac{k(\boldsymbol{R}_j-\boldsymbol{R}_j^0)}{6\pi\eta} + \frac{14(\boldsymbol{p}_j\cdot\hat{\boldsymbol{r}}_{ij})}{r_{ij}^3}(\boldsymbol{p}_j\times\hat{\boldsymbol{r}}_{ij})V_0^{(2s)}b^2\Big] + O(r_{ij}^{-3}).$$

The interesting difference from the previous section is that we do not add more than one colloid to a trap but add them in a lattice of traps. The collective dynamics in that case in then strikingly different, which we now explain in detail.

With the understanding from the previous section, we now present numerical results for dynamics in a lattice of traps. In a linear lattice of traps, we find stable stationary states, reached irrespective of initial conditions, in which all colloids are oriented *along* the line joining the trap centers and at a confinement radius that is slightly altered from R^* due to hydrodynamic interactions. We then study dynamics in a 3×3 square lattice of traps. The

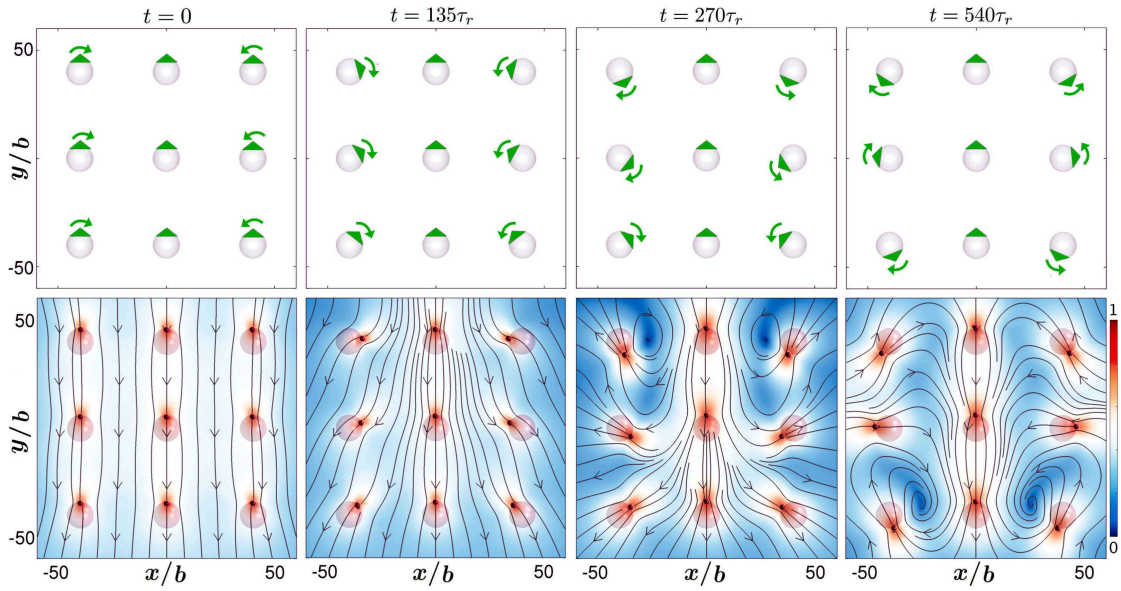

Figure 4.2: Synchronization of active colloids (green cones) in a square lattice of harmonic traps (schematic spheres). Instantaneous configurations from simulations of active colloids in 3×3 square lattice of harmonic traps (top panel) and corresponding streamlines of fluid flow (bottom-panel) overlaid on the pseudo-color plot of the normalized logarithmic flow speed at different times ($\tau_r = 8\pi\eta b/k$). The traps are shown by the schematics spheres while the positions and orientations of the colloids are shown by green cones, and curved green arrows show rotation. The colloids on the symmetry axis do not rotate, while those on the left and right rotate clockwise and counter-clockwise, respectively, in a synchronized manner.

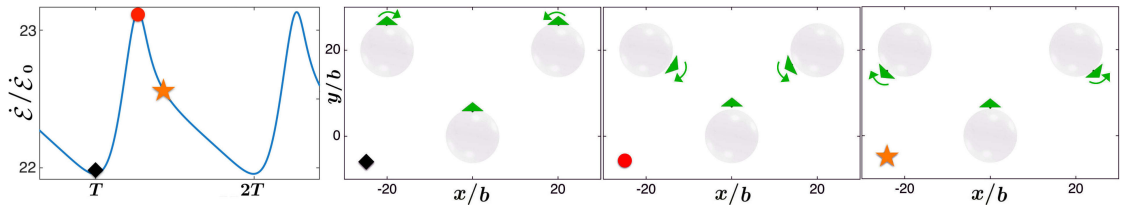

Figure 4.3: Power dissipation for the synchronized and periodic motion of three active colloids in a triangular lattice of harmonic traps (left panel), scaled by power dissipation of an isolated colloid $\dot{\mathcal{E}}_0$. The remaining plots show the configurations of the system at three instants (shown by corresponding markers) along the power dissipation curve. The traps are shown by the schematics spheres and the position and orientation of the colloids are shown by green cones, and curved green arrows show rotation.

dynamics is shown in Fig. (4.2) and in Movie (4.2). The initial condition is chosen to be a stable state in the absence of hydrodynamic interactions. We find that the particles at the center do not rotate by symmetry while particles on the left of this symmetry axis, rotate clockwise and particle on their right rotate counter-clockwise. This can be understood by the estimating the hydrodynamic torques on each colloid. The dynamics can also understood intuitively from the flow field of Fig. (4.2). The colloids at an equal distance from the symmetric plane have *synchronized* dynamics. This leads to a long ranged correlation between the particles. In summary, (a) there is a rotational instability in the system if the traps centers are not collinear, and (b) dynamics is synchronized about an axis of symmetry in non-collinear traps.

In Fig. (4.3), we estimate the power dissipation for the synchronized and periodic motion of three active colloids in a triangular lattice of harmonic traps. The dynamics of colloids in triangular lattice of traps is similar to the case of colloids in a square lattice of traps. The colloid in the central trap has no rotational dynamics due to symmetry while the on the left rotates clockwise and the colloid on the right rotates counter-clockwise. We find that the power dissipated in the system is minimum when the colloids are widely separated, while the dissipated power is maximum when they are closer to each other. Thus, the first configuration of Fig. (4.3), corresponds to the minimum of power dissipation, while the second is the maximum, as indicated by the markers on the power dissipation curve, and the third configuration is an intermediate value.

4.4 Active pressure in spherical confinement

In this section, we study the mechanical pressure in the fluid. The active contribution to the pressure in the fluid is given by the second term in Eq. (2.28b). We consider a suspension of active colloids confined by an external spherical potential such that they are always inside a sphere of radius R. The confining surface is not a physical boundary and

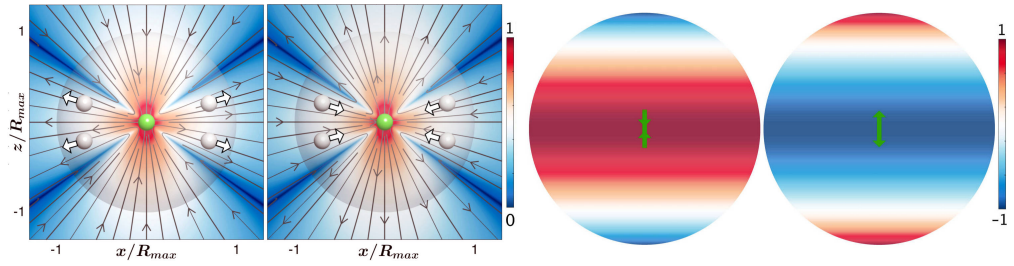

Figure 4.4: Streamlines of axisymmetric fluid flow around a contractile (left) and an extensile (right) apolar active colloid are shown in first two panels. The remaining two panel are the pseudo-color plots of the active fluid pressure on a sphere enclosing the contractile and extensile colloids respectively. The active colloid is colored in green while white color are for tracers, with a white arrow to show forces on them.

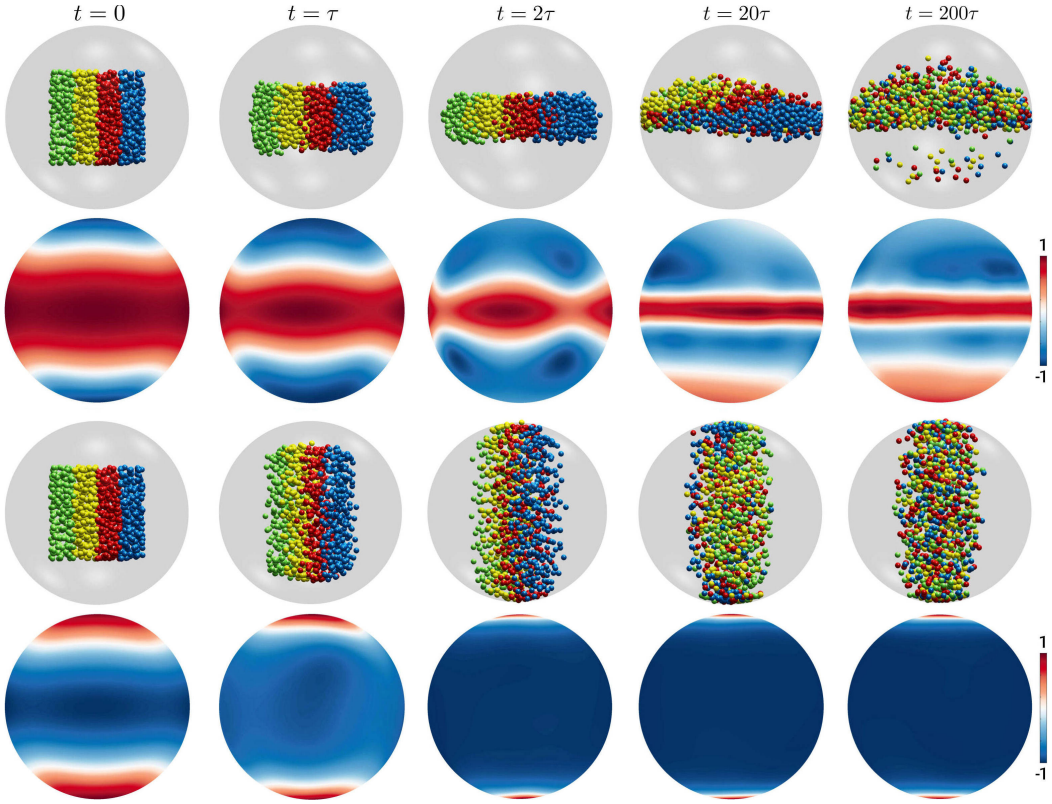

Figure 4.5: Dynamics of 1024 contractile and extensile active colloids in a spherical confinement and the active fluid pressure at the confining surface. The first row shows the lateral view of configurations from a simulation of contractile active colloids, confined in a spherical potential, at different times ($\tau = b/V_0^{(4a)}$). The colloids are colored by their initial positions. The second row shows the corresponding pseudo-color plots of the normalized active pressure at the confining surface. The remaining two rows are the same set of plots but for extensile active colloids. The dynamics and fluid pressure is completely different for suspension of contractile and extensile colloids.

there is free motion of the fluid across it. We use the results of the section 2.3 and 3.4 to calculate the fluid pressure at the confining surface due to the motion of the active colloids in the interior volume. This geometry is motivated by the confinement of bacteria inside a fluid drop with a porous interface.

We retain slip modes $l\sigma = 2s$ and $4a$ which correspond to the dipole and chiral octupole. Figure (4.6) contains the flow due to these modes. The first generates a long-ranged flow while the second produces self-rotation [45]. For simplicity, we choose these modes to be uniaxial, parametrized in terms of the orientation $\boldsymbol{p}_i$ of the colloid, as given in Eq. (A). The microscopic dynamics and the pressure distributions are sensitive to the sign of $V_0^{(2s)}$ as we shall see below. The fluid flow due to the chiral term, which decays as r_{ij}^{-4}, induces a net rotation of the system. The most dominant contribution to the fluid flow comes from the long-ranged dipolar flow, which decays as r_{ij}^{-2}. The fluid pressure decays as one power higher than the fluid flow. The dipole, thus, crucially determines the dynamic of active colloids in the spherical confinement and fluid pressure at the confining surface.

The confining potential $U^{\mathrm{c}}(R_i) = k^{\mathrm{c}} \exp \frac{1}{R-R_i}/(R_{max} - R_i)$ for $R_i > R$ and $U^{\mathrm{c}}(R_i) = 0$ otherwise. Here R_{max} is chosen to be few particle radius more than R in simulations and k^{c} is the strength of the potential. The colloids also have a short-ranged repulsive potential, which depend on the separation between the colloids, $\boldsymbol{r}_{ij} = \boldsymbol{R}_i - \boldsymbol{R}_j$. This potential is modeled using the WCA potential for separation $r_{ij} < r_{min}$, $U(r_{ij}) = \epsilon(\frac{r_{min}}{r_{ij}})^{12} - 2\epsilon(\frac{r_{min}}{r_{ij}})^6 + \epsilon$, and zero otherwise [158]. Here ϵ is the strength of the potential. The specification of the slip and body forces complete the description of our model. We start the simulations with a completely random distribution of hard spheres positioned symmetrically about the origin [159]. The orientations of all the colloids are pointing along the $\hat{\boldsymbol{z}}-$axis. The tendency of the hydrodynamic torques acting on the colloids to rotate their orientation is nullified by external torques $\mathbf{T}_i^P = T_0(\boldsymbol{p}_i \times \hat{\boldsymbol{z}})$ arising from bottom-heaviness. Thus the orientation of all the colloids remain along $\hat{\boldsymbol{z}}-$axis for all times. We then study the collective dynamics and measure the pressure on the "confining" surface.

The sign of the strength of the symmetric irreducible dipole, $V_0^{(2s)}$, is positive (negative) for an extensile (contractile) active colloid. We plot the fluid flow produced by a contractile and extensile active colloid in the first two panels in Fig. (4.4). The orientation of the colloids is assumed to be along the $\hat{z}$ direction. The source colloid is colored in green, while white arrows on the tracer colloids show the direction of the force acting on them. The directions of the forces on these colloids give a heuristic understanding of the dynamics in the spherical confinement as we explain below. The last two panels of Fig. (4.4) contain the fluid pressure due to contractile and extensile active colloid. It can be seen that the pressure along the equator is higher for contractile colloids while pressure at the poles is higher for extensile colloids. Collective dynamics of contractile and extensile colloids under spherical confinement follow from the flow field of the individual colloids.

A contractile colloid pushes the particles away in the plane perpendicular to the dipole axis, which leads to an instability in an initially isotropic suspension of colloids. The colloids final reach to a steady state which they organize into a continuously rearranging "oblate" structure. The dipoles tend to push each other as far as possible but the spherical confinement coupled with short-ranged repulsion make them undergo rolls, which accounts for the continuous rearrangement of the structure. In the first two rows of Fig. (4.5), we show instantaneous configurations of contractile colloids and the state of the active pressure at the confining sphere. The fluid pressure is then maximum on the equator of the confining sphere.

The last two rows of Fig. (4.5) show the corresponding configurations and fluid pressure on a confining sphere for extensile dipoles. The initial isotropic distribution of the colloids finally finds a steady state in a "prolate" distribution of extensile dipoles. The colloids continuously rearrange this structure as the dipolar flow tries to push them apart while the confining sphere holds them back. Moreover, the pressure is higher at the poles in this case. Movie (4.3) and (4.4) show the dynamics of contractile and extensile colloids, respectively, in a spherical confinement.

4.5 Conclusion

To summarize, we have shown that systems of active colloids in tandem with hydrodynamic interactions and external potentials show rich phenomenology. The motion of many hydrodynamically interacting active colloids in a harmonic potential was first studied by Nash *et al* [13] using lattice Boltzmann simulations and then by singularity [157] and boundary integral [10, 11] methods here. We show that the interplay between self-propulsion, confinement and hydrodynamically-induced reorientation yields orbits for a pair of confined particles [10]. These individual orbits coalesce to produce sustained convection in a confined suspension [10] producing the so-called 'self-assembled pump' [13]. We then study the motion of many active colloids in many traps to uncover strikingly different dynamics, where the colloids exhibit a synchronized dynamics about a plane of symmetry [11]. We have also reported the study of apolar active colloids (both contractile and extensile) in a spherical confinement. W show that the dynamics and the fluid pressure measured in a suspension of extensile and contractile active colloids are completely *different* [11]. Thus, we conclude that the dynamics of active colloids depend critically on nature of the activity and external potentials acting on colloids .

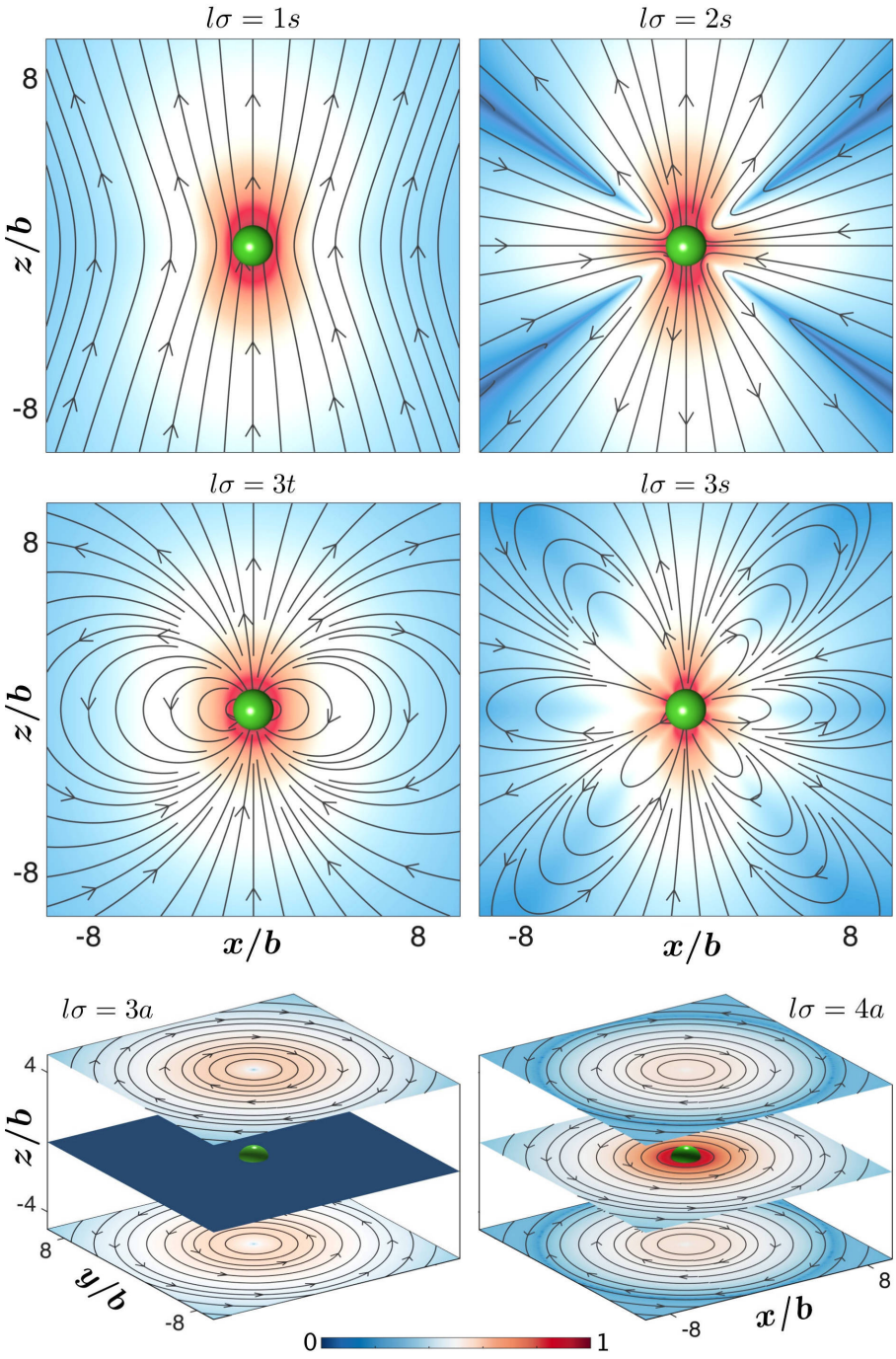

Figure 4.6: Irreducible axisymmetric and swirling components of fluid flow, Eq. (2.28a), of an active colloid in unbounded domain of fluid flow. The streamlines of the fluid flow have been overlaid on the pseudo-color plot of the normalized logarithmic flow speed. The first row contains the axisymmetric flow due to monopole ($l\sigma = 1s$) and symmetric irreducible dipole ($l\sigma = 2s$), while second row corresponds to vector quadrupole ($l\sigma = 3t$) and symmetric irreducible quadrupole ($l\sigma = 3s$). The last row has the flow from antisymmetric quadrupole ($l\sigma = 3a$) and octupole ($l\sigma = 4a$) respectively. A combination of these modes have been used in this chapter.

Chapter 5

Wall-bounded flows: Crystallization of active colloids at a plane wall

5.1 Introduction

The lack of detailed balance in active colloidal suspensions allows dissipation to determine stationary states. In this chapter, we show that slow viscous flow produced by polar or apolar active colloids near plane walls mediates attractive hydrodynamic forces that drive crystallization. Hydrodynamically mediated torques tend to destabilize the crystal but stability can be regained through critical amounts of bottom-heaviness or chiral activity. Numerical simulations show that crystallization is not nucleational, as in equilibrium, but is preceded by a spinodal-like instability. Harmonic excitations of the active crystal relax diffusively but the normal modes are distinct from an equilibrium colloidal crystal. The hydrodynamic mechanisms presented here are universal and rationalize recent experiments on the crystallization of active colloids

In active colloidal suspensions [5, 8], energy is continuously dissipated into the ambient viscous fluid. The balance between dissipation and fluctuation that prevails in equilib-

rium colloidal suspensions [25, 54] is, therefore, absent. Nonequilibrium stationary states in active suspensions, then, are determined by both dissipative and conservative forces, quite unlike passive suspensions where detailed balance prevents dissipative forces from determining phases of thermodynamic equilibrium. In this context, it is of great interest to enquire how thermodynamic phase transitions driven by changes in free energy are modified in the presence of sustained dissipation.

In two recent experiments disordered suspensions of active colloids have been observed to spontaneously order into two-dimensional hexagonal crystals when confined at a plane wall. Bottom-heavy synthetic active colloids which catalyze hydrogen peroxide when optically illuminated are used in the first experiment [5] while chiral fast-swimming bacteria of the species *Thiovulum majus* are used in the second experiment [8]. Given this remarkably similar crystallization in two disparate active suspensions it is natural to ask if the phenomenon is universal and to search for mechanisms, necessarily involving dissipation, that drive it.

Our current understanding of phase separation in particulate active systems is derived from the coarse-grained theory of motility-induced phase separation (MIPS) where active particles are advected by a density-dependent velocity [140–143]. Microscopic models with kinematics consistent with MIPS also show phase separation and crystallization of hard active disks have been reported in two dimensions [144, 145, 160, 161]. However, these models ignore exchange of the locally conserved momentum of the ambient fluid with that of the active particles and are, thus, best applied to systems where such exchanges can be ignored. Fluid flow is an integral part of the physics in [5, 8] and a momentum-conserving theory, currently lacking, is essential to identify the dissipative forces and torques that drive crystallization.

In this chapter we present a microscopic theory of active crystallization that connects directly to the experiments described above. Specifically, we account for the *three-dimensional* active flow in the fluid and the effect of a plane wall on this flow. Using

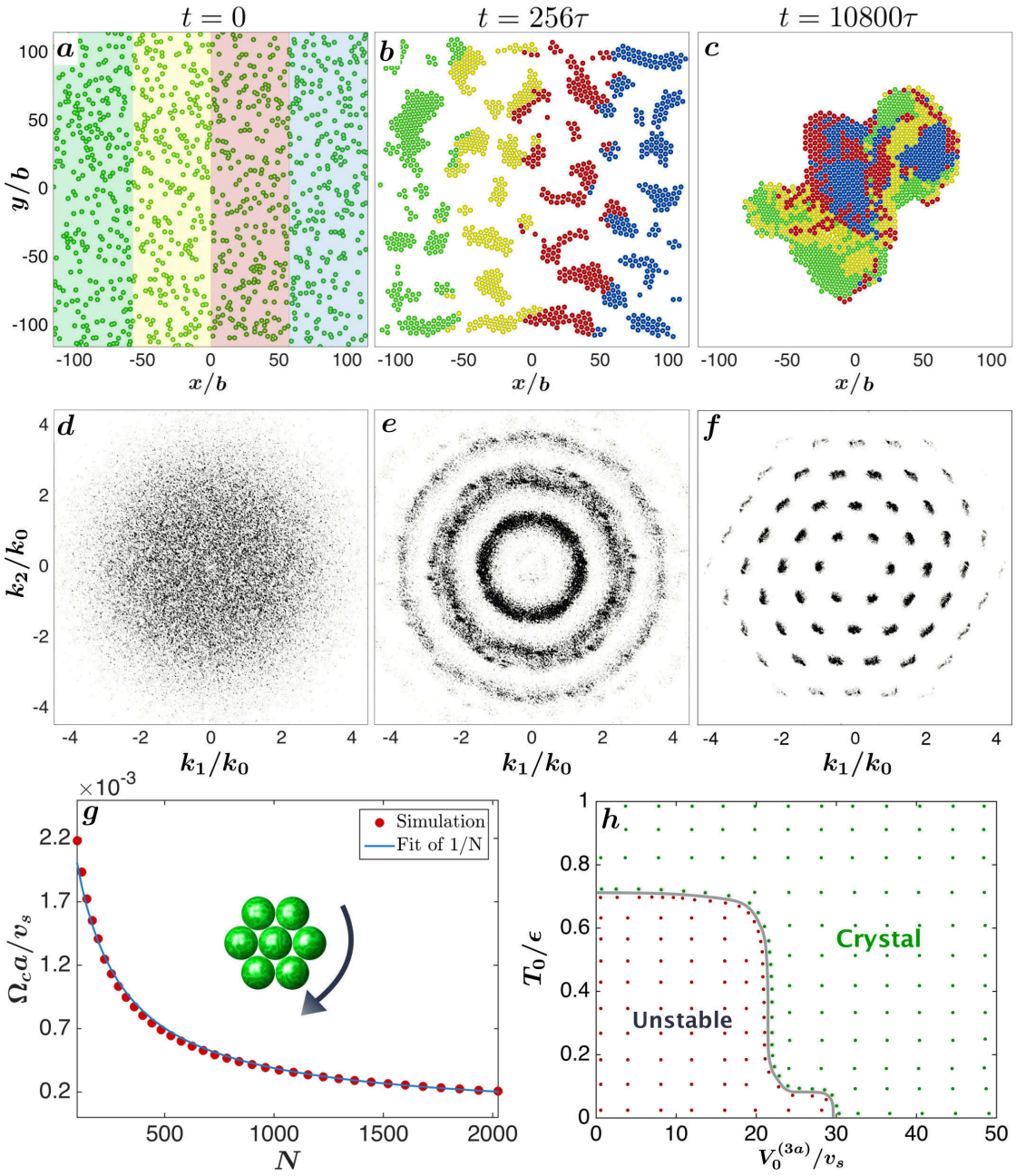

Figure 5.1: Panels (a)-(c) are instantaneous configurations during the crystallization of 1024 active colloids of radius b at a plane wall. The colloids are colored by their initial positions. Panels (d)-(f) show the structure factor $S(\boldsymbol{k})$ at corresponding instants. Wavenumbers are scaled by the modulus of the reciprocal lattice vector k_0 and the contribution from $\boldsymbol{k} = 0$ is discarded. Panel (g) shows the variation of the angular velocity $\boldsymbol{\Omega}_c$ of a crystallite with the number N of colloids in it. A typical configuration is shown in the inset. Panel (h) is the state diagram for orientational stability in terms of the measure of chirality $V_0^{(3a)}$ and bottom-heaviness T_0 (see text). Each dot represents one simulation. Here v_s is the self-propulsion speed of an isolated colloid, $\tau = b/v_s$, and ϵ is the scale of the repulsive steric potential.

the results of preceding chapters, we estimate Brownian forces and torques to be smaller than their active counterparts by factors of order 10^2 (for synthetic colloids in [5]) to 10^4 (for bacteria in [8]) making them largely irrelevant for active crystallization. We integrate the resulting deterministic balance equations numerically to obtain dynamical trajectories.

We now detail the organization of the chapter. In section 5.2 we enumerate the main numerical results of the chapter. Our model is described in section 5.3, while the universal mechanisms of crystallization is detailed in section 5.3. In section 5.5, we obtain the harmonic excitations of the crystal.

5.2 Numerical results

Our main numerical results are summarized in Fig. (5.1). Panels (a-c) show the spontaneous destabilization of the uniform state by attractive active hydrodynamic forces, the formation of multiple crystallites, and their coalescence into a single hexagonal crystal at late times. Panels (d-f) show the structure factor at corresponding times. The route to crystallization is not through activated processes that produce critical nuclei, but through a spinodal-like instability produced by the unbalanced long-ranged active attraction. The uniform state is, therefore, always unstable and crystallization occurs for all values of density, in contrast to the finite density necessary for crystallization in MIPS models [143]. Active hydrodynamic torques tend to destabilize the ordered state but stability is regained when these are balanced by external torques (from bottom-heaviness in [5]) or by chiral activity (from bacterial spin in [8]). Crystallites of chiral colloids rotate at an angular velocity that is inversely proportional to the number of colloids contained in them, as shown in panel (g). This is in excellent agreement with the experiment [8]. The critical values of bottom-heaviness and chirality above which orientational stability, and, hence, positional order, is ensured is shown in panel (h). We now present our model and detail the derivation of our results.

5.3 Model

The leading contributions from the slip

$$\begin{aligned} \boldsymbol{v}_i^{\mathcal{A}}(\boldsymbol{\rho}_i) = &- \underbrace{\mathbf{V}_i^{\mathcal{A}} + \tfrac{1}{15}\mathbf{V}_i^{(3t)}\cdot\mathbf{Y}^{(2)}(\hat{\boldsymbol{\rho}}_i)}_{\text{achiral, polar}} + \underbrace{\mathbf{V}_i^{(2s)}\cdot\mathbf{Y}^{(1)}(\hat{\boldsymbol{\rho}}_i)}_{\text{achiral, apolar}} \\ &- \underbrace{\boldsymbol{\Omega}_i^{\mathcal{A}}\times\boldsymbol{\rho}_i - \tfrac{1}{60}\boldsymbol{\varepsilon}\cdot\mathbf{V}_i^{(4a)}\cdot\mathbf{Y}^{(3)}(\hat{\boldsymbol{\rho}}_i)}_{\text{chiral, polar}} - \underbrace{\tfrac{1}{9}\boldsymbol{\varepsilon}\cdot\mathbf{V}_i^{(3a)}\cdot\mathbf{Y}^{(2)}(\hat{\boldsymbol{\rho}}_i)}_{\text{chiral, apolar}}, \end{aligned} \tag{5.1}$$

have coefficients of polar, apolar and chiral symmetry. Here $\boldsymbol{\varepsilon}$ is the Levi-Civita tensor. The retained modes have physical interpretations: for a single colloid in an unbounded fluid, $\mathbf{V}^{\mathcal{A}}$ ($l\sigma = 1s$) and $\boldsymbol{\Omega}^{\mathcal{A}}$ ($l\sigma = 2a$) are the linear and angular velocities in the absence of external forces and torques, $\mathbf{V}^{(2s)}$ is the active contribution to the stresslet, while $\mathbf{V}^{(3a)}$,$\mathbf{V}^{(3t)}$, and $\mathbf{V}^{(4a)}$ are strengths of the chiral torque dipole, polar vector quadrupole, and chiral octupole respectively. The tensors are parametrized uniaxially as per Eq. (2.5): $\mathbf{V}_i^{\mathcal{A}} = v_s\boldsymbol{p}_i$, $\boldsymbol{\Omega}_i^{\mathcal{A}} = \omega_s\boldsymbol{p}_i$, $\mathbf{V}_i^{(2s)} = V_0^{(2s)}(\boldsymbol{p}_i\boldsymbol{p}_i - \frac{\mathbf{I}}{3})$, etc. The fluid flow due to leading modes of slip near a plane wall is shown in Fig. (5.4).

The synthetic active colloids in [5] are polar and achiral (they self-propel but do not spin) while the bacteria in [8] are polar and chiral (they self-propel and spin). Both these cases are included in the leading contributions. The modes $l\sigma = 1s$ and $l\sigma = 2a$ contribute most dominantly to forces and torques and they attain their lower bounds far away from the wall, where their magnitudes are $F = 6\pi\eta b v_s$ and $T = 8\pi\eta b^3\omega_s$. The bacteria in [8] have radius $b \sim 4\mu$m, swimming speed $v_s \sim 500\,\mu$m/s and angular speed $\omega_s \sim 50\,s^{-1}$ in a fluid of viscosity $\eta = 10^{-3}$ kg/ms. This gives an estimate of $F \sim 40\times10^{-12}$ N and$T \sim 10^{-16}$ Nm. For the synthetic colloids in [5], $b \sim 2\mu$m, $v_s \sim 10\mu$m/s, which corresponds to $F \sim 10^{-13}$ N. Typical Brownian forces and torques are of order $O(k_B\mathrm{T/b}) \sim 10^{-15}$ N, and $O(k_B\mathrm{T}) \sim 10^{-21}$ Nm respectively. Thus active forces and torques overwhelm Brownian contributions by factors of 100 or more in these experiments and, henceforth, we neglect their effects.

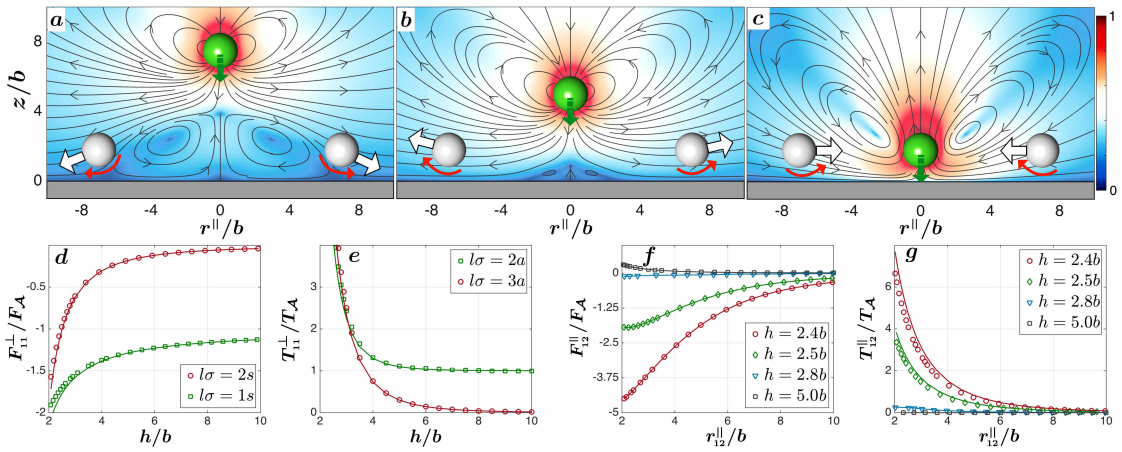

Figure 5.2: Distortion of the flow produced by leading polar ($l\sigma = 1s$) and apolar ($l\sigma = 2s$) slip terms in Eq. (2.6) as an active colloid of radius b, shown in green, approaches a plane wall. Tracer colloids are show in white. The streamlines of the fluid flow have been overlaid on the pseudocolor plot of logarithm of the magnitude of local flow normalised by its maximum. The flow in (c) results when the colloid is brought to rest near the wall. Hydrodynamic forces attract nearby colloids, as shown by the thick white arrows, leading to crystallization. Hydrodynamic torques tend to reorient the colloids as shown by the curved red arrows. The remaining graphs show quantitative variation of the active forces and torques from modes in Eq. (2.6) scaled by $F_{\mathcal{A}} = 6\pi\eta b v_s$ and $T_{\mathcal{A}} = 8\pi\eta b^2 v_s$ respectively as a function of height h of the colloid from the wall and distance, $\boldsymbol{r}_{ij} = \boldsymbol{R}_i - \boldsymbol{R}_j$, from other colloids . Solid and dotted lines represent analytical and numerical results respectively (see text). Here $\parallel$ and $\perp$ imply directions parallel and perpendicular to the wall at $\mathbf{z} = 0$.

5.4 Universal mechanisms

The kinetics of crystallization obtained from numerical solutions is shown in Movie (5.1), together with the evolution of the structure factor $S(\boldsymbol{k})$. The uniform state is destabilized, most notably for any initial density, by attractive active hydrodynamic forces. Steric repulsion between particles balances these to produce crystallites with hexagonal positional order. Rings in the structure factor first appear at wavenumbers that correspond to Bragg vectors of the lattice, reminiscent of a spinodal instability, representing the averaged scattering from randomly oriented crystallites. These sharpen into Bragg peaks as the crystallites coalesce and orientational order grows. Finally particles assemble into a single crystallite which continues to rotate, while the structure factor shows a clear sixfold symmetry. In Movie (5.2) we show the formation of a hexagonal unit cell from the simulation of seven polar and chiral active colloids. The crystallite rotates with an angular velocity parallel to the chiral axis of the colloids.

To better understand the mechanisms behind active crystallization we show, in Fig. (5.2), the active flow near a wall and the dominant contributions to the flow-mediated forces and torques. The top three panels show the increasing distortion of the flow produced by the leading polar ($l\sigma = 1s$) and apolar ($l\sigma = 2s$) modes for $\boldsymbol{p}_i$ normal to the wall and $V_0^{(2s)} < 0$. The flow develops a monopolar character as the colloid is brought to rest at a height h by the balance of hydrodynamic attraction, Fig. (5.2d), and steric repulsion from the wall. The induced monopole on the colloids leads to attractive forces between them below a critical height h from the wall as shown in Fig. (5.2f). Nearby colloids entrained in this flow are attracted towards the central colloid as shown in the rightmost panel and in Movie (5.3). The balance of the hydrodynamic attraction and steric repulsion determines lattice spacing d. We note that even an apolar colloid is attracted to the wall, Fig. (5.2d), and induces hydrodynamic attractive forces. Thus, unlike MIPS [143], polarity is not necessary for crystallization. The induced monopole also tends to reorient the colloids, by generating a torque in the plane of wall, as shown by the curved red arrows in Fig. (5.2c) and

quantified in Fig. (5.2g). Their destabilizing effect can be nullified by external torques $\mathbf{T}_i^P = T_0(\hat{\mathbf{z}}\times\boldsymbol{p}_i)$ in the plane of the wall due, for example, to bottom-heaviness. The orientation can also be stabilized by the chiral terms in Eq. (5.1), which produce torques $\perp$ to the wall, as shown in Fig. (5.2e). This chiral torque acting $\perp$ to the wall, when combined with destabilizing torque $\parallel$ to the wall, induces *active* precession of the orientation about the wall normal, thereby stabilizing the orientations. The role of the terms in Eq. (5.1) in generating positional order, orientational order and crystal rotation is given in Table (5.1). Activity *and* body forces pointing away from the wall are necessary for positional order while bottom-heaviness *or* chirality is necessary for orientational stability.

5.5 Harmonic excitations

We now study harmonic excitations $\mathbf{u}_i$ of a perfect hexagonal crystal by expanding the positions as $\boldsymbol{R}_i = \boldsymbol{R}_i^0 + \mathbf{u}_i$ around the stationary state $\boldsymbol{R}_i^0 = (X_i^0, Y_i^0, h)$ and ignoring orientational fluctuations. The orientations of the colloids are assumed to be normal to the wall. Force balance to leading order gives

$$-\boldsymbol{\gamma}_{ij}^{TT}\cdot\dot{\mathbf{u}}_j + \left(\boldsymbol{\nabla}_j\boldsymbol{\gamma}_{ij}^{TT}\cdot\mathbf{V}^{\mathcal{A}} - \boldsymbol{D}_{ij}\right)\cdot\mathbf{u}_j = 0, \tag{5.2}$$

where $\boldsymbol{D}_{ij} = -\boldsymbol{\nabla}_j\boldsymbol{\nabla}_i U\big|_0$, U is the sum of all steric potentials, and $\boldsymbol{\gamma}_{ij}^{TT}$ is the friction tensor corresponding to $l\sigma = l'\sigma' = 1s$ in Eq. (2.22). This shows that relaxation is determined by both activity and elasticity, unlike in an equilibrium colloidal crystal where elasticity alone relaxes strains. The normal modes of relaxation can be obtained by Fourier transforming in the plane and in time. The dispersion is found from the solutions of

$$\det\left|-i\omega\boldsymbol{\gamma}_{\boldsymbol{k}}^{TT} + i\boldsymbol{k}\boldsymbol{\gamma}_{\boldsymbol{k}}^{TT}\cdot\mathbf{V}^{\mathcal{A}} - \boldsymbol{D}_{\boldsymbol{k}}\right| = 0. \tag{5.3}$$

Here $\boldsymbol{k} = (k_1, k_2)$ is the wave-vector restricted to the first Brillouin zone, ω is the frequency and $\boldsymbol{D_k}$ is the dynamical matrix. The pair of dispersion relations for motion parallel to the wall are shown in Fig. (5.3). The dispersion for $k \ll k_0$, where k_0 is the magnitude of the reciprocal lattice vector, is quadratic in wavenumber

$$\omega_{\pm} = -i\frac{\gamma_{\perp}^{T} h v_s}{2\gamma_{\parallel}^{T}} f_{\pm}(\theta) k^2, \tag{5.4}$$

where $f_{\pm}(\theta)$ are angular factors, $\gamma_{\parallel}^{T}$ and $\gamma_{\perp}^{T}$ are one-body frictions parallel and perpendicular to the wall, and $\tan\theta = \frac{k_2}{k_1}$. The small-$k$ approximation is compared with the numerical solution in Fig. (5.3) and it is found to hold for $k \lesssim 0.1k_0$. These can be interpreted as overdamped phonon modes of the active crystal. Including fluid unsteadiness can produce underdamped phonons, as was pointed in [162] for passive colloids. The presence of the active term $i\boldsymbol{k}\boldsymbol{\gamma}_{\boldsymbol{k}}^{TT} \cdot \mathbf{V}^{\mathcal{A}}$ in Eq. (5.3) makes them differ from phonon modes of a colloidal crystal.

We now present a detailed derivation of the results described in this section. We seek a solution of the form $\mathbf{u}_i(t) = \mathbf{u}_{\boldsymbol{k}}(t)\, e^{i\boldsymbol{k}\cdot\boldsymbol{R}_i}$ for Eq. (5.2). Using this, the force balance condition becomes

$$-\boldsymbol{\gamma}_{\boldsymbol{k}}^{TT} \cdot \dot{\mathbf{u}}_k + \left(i\boldsymbol{k}\boldsymbol{\gamma}_{\boldsymbol{k}}^{TT} \cdot \mathbf{V}^{\mathcal{A}} - \boldsymbol{D_k}\right) \cdot \mathbf{u}_{\boldsymbol{k}} = 0. \tag{5.5}$$

Here, $\boldsymbol{D_k}$ is called the dynamical matrix [163]. $\boldsymbol{D_k}$ is the Fourier transform of $\boldsymbol{D}_{ij}$ and $\boldsymbol{\gamma}_{\boldsymbol{k}}^{TT}$ is the Fourier transform of the friction tensor

$$\boldsymbol{D_k} = \sum_{i=1}^{N} \boldsymbol{D}_{i1}\, e^{i\boldsymbol{k}\cdot(\boldsymbol{R}_i - \boldsymbol{R}_1)}, \qquad \boldsymbol{\gamma}_{\boldsymbol{k}}^{TT} = \sum_{i=1}^{N} \boldsymbol{\gamma}_{i1}^{TT}\, e^{i\boldsymbol{k}\cdot(\boldsymbol{R}_i - \boldsymbol{R}_1)}.$$

The normal modes of relaxation can be obtained by Fourier transforming Eq. (5.5), in time. The resulting Eq. (5.3) is to be solved to obtain the dispersion relations. To proceed, we write $\boldsymbol{\gamma}_{i1}^{TT}$ in terms of its planar Fourier transform

$$\boldsymbol{\gamma}_{i1}^{TT} = \int \hat{\boldsymbol{\gamma}}_{\boldsymbol{k}}^{TT}(\boldsymbol{k}; h) e^{-i\boldsymbol{k}'\cdot(\boldsymbol{R}_i - \boldsymbol{R}_1)} \frac{d^2k'}{(2\pi)^2},$$

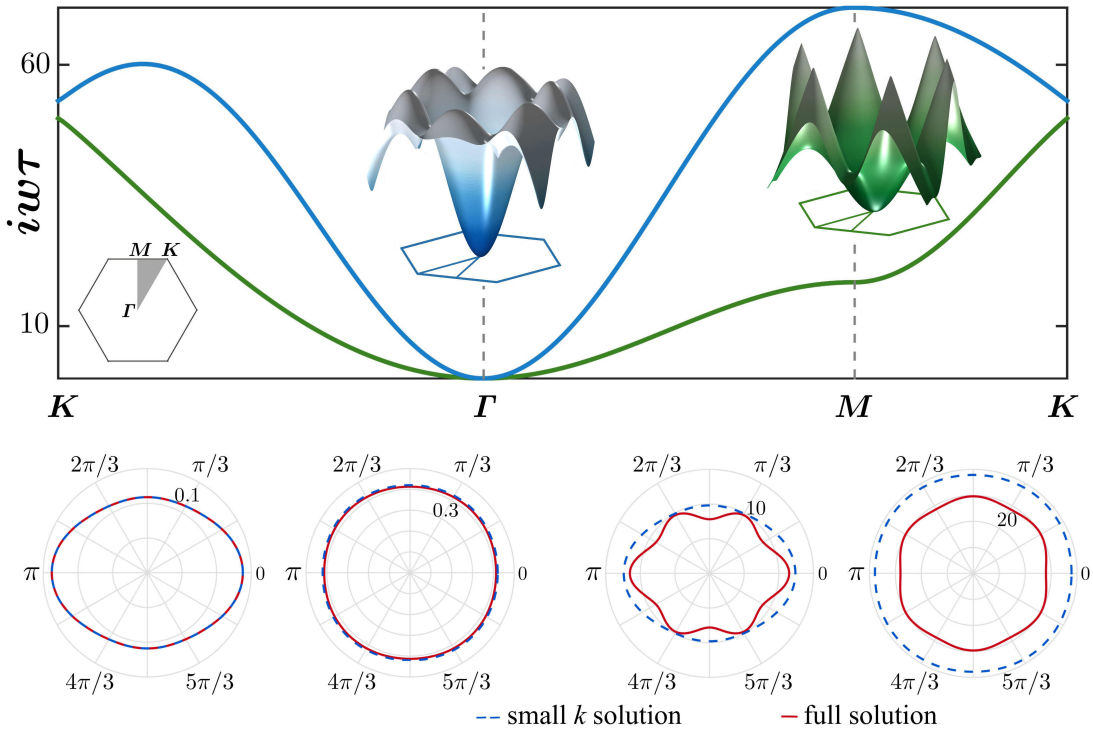

Figure 5.3: Branches of the dispersion relation for the two planar normal modes of relaxation of a hexagonal active crystal. The curves in upper panel show the dispersion along high symmetry directions of the Brillouin zone (first inset). The surfaces in the second and third insets show the dispersion over the entire Brillouin zone. Polar plots in the lower panel, have comparisons of full numerical solution (Eq. (5.3)) with the approximate solution at small k (Eq. (5.4)) for $k = 0.01k_0$ (left panel) and $k = 0.3k_0$ (right panel).

to obtain an expression for $\boldsymbol{\gamma}_{\boldsymbol{k}}^{TT}$

$$\boldsymbol{\gamma}_{\boldsymbol{k}}^{TT}(\boldsymbol{k};h) \;=\; \sum_i \int \hat{\boldsymbol{\gamma}}_{\boldsymbol{k}}^{TT}(\boldsymbol{k};h) e^{-i(\boldsymbol{k}'-\boldsymbol{k})\cdot(\boldsymbol{R}_i-\boldsymbol{R}_1)} \frac{d^2k'}{(2\pi)^2} = \frac{1}{A_c}\sum_\lambda \hat{\boldsymbol{\gamma}}_{\boldsymbol{k}}^{TT}(\boldsymbol{k}+\boldsymbol{q}_\lambda;h).$$

Here we have used the identity

$$\sum_i e^{-i\boldsymbol{k}\cdot\boldsymbol{R}_i} = \frac{(2\pi)^2}{A_c}\sum \boldsymbol{\delta}(\boldsymbol{k}-\boldsymbol{q}_\lambda), \tag{5.6}$$

where A_c is area of the unit cell and $\boldsymbol{q}_\lambda$ are reciprocal lattice vectors. We now identify two parts of $\boldsymbol{\gamma}_{\boldsymbol{k}}^{TT}$ as

$$\boldsymbol{\gamma}_{\boldsymbol{k}}^{TT}(\boldsymbol{k};h) = \hat{\boldsymbol{\gamma}}_{k_0}^{TT}(\boldsymbol{k};h) + \sum_{\lambda'} \hat{\boldsymbol{\gamma}}_{k_q}^{TT}(\boldsymbol{k}+\boldsymbol{q}_\lambda;h).$$

Here $\hat{\boldsymbol{\gamma}}^{TT}_{k_0}(\boldsymbol{k};h)$ corresponds to the $\boldsymbol{q}_\lambda = 0$ and terms at arbitrary non-zero q are denoted by $\hat{\boldsymbol{\gamma}}^{TT}_{k_q}(\boldsymbol{k};h)$. Their leading order forms can be written as

$$\hat{\boldsymbol{\gamma}}^{TT}_{k_0}(\boldsymbol{k};h) = \gamma^T \boldsymbol{I} + \frac{\gamma^T\gamma^T}{A_c}\mathcal{F}^k\,\hat{\mathbf{G}}^{\mathrm{w}}(\boldsymbol{k};h), \qquad \hat{\boldsymbol{\gamma}}^{TT}_{k_q}(\boldsymbol{k};h) = \frac{\gamma^T\gamma^T}{A_c}\mathcal{F}^k \sum_{\lambda'}\hat{\mathbf{G}}^{\mathrm{w}}(\boldsymbol{k}+\boldsymbol{q}_\lambda;h).$$

Here $\mathcal{F}^k = 1 - b^2k^2/3$ and $\hat{\mathbf{G}}^{\mathrm{w}}(\boldsymbol{k};h)$ is the two-dimensional Fourier transform of $\mathbf{G}^{\mathrm{w}}$ (see Appendix A.2). The prime on the summation on the right indicates that $\lambda = 0$ is excluded from the sum. We now turn to the calculation of the dynamical matrix,

$$\boldsymbol{D}_{\boldsymbol{k}} = \sum_{i=1}^{N}\left(\frac{\boldsymbol{I}}{r^2}U' + \frac{\boldsymbol{r}\boldsymbol{r}}{r^4}U''\right)_0\left(1 - e^{i\boldsymbol{k}\cdot\boldsymbol{R}_i}\right).$$

Here $U' = -12\epsilon[(r_{min}/d)^{12} - (r_{min}/d)^6]$ and $U'' = 12\epsilon[14(r_{min}/d)^{12} - 8(r_{min}/d)^6]$. We evaluate the above in the nearest neighbor approximation in the direction parallel to the wall. The expression for $\boldsymbol{D}_{\boldsymbol{k}}$ and $\boldsymbol{\gamma}^{TT}_{\boldsymbol{k}}$ can be evaluated numerically by summing over the reciprocal lattice vectors. The sum is unconditionally and rapidly convergent as the Green's function decays as r_{ij}^{-3} in the direction parallel to the wall. The dispersion is obtained numerically from Eq. (5.5) and the pair of dispersion relations for motion parallel to the wall are shown in Fig. (5.3).

Long-wavelength approximation: Analytical expression for the normal modes can be obtained in the $k \to 0$ limit. Keeping terms of the $O(k^2)$, Eq. (5.5) becomes

$$\begin{pmatrix} \dot{u}_{k_1} \\ \dot{u}_{k_2} \end{pmatrix} = -\frac{h\gamma_\perp^T v_s k^2}{\gamma_\parallel^T}\begin{pmatrix} c_1\cos^2\theta + C_2\sin^2\theta & c_3\sin\theta\cos\theta \\ c_3\sin\theta\cos\theta & c_4\sin^2\theta + c_5\cos^2\theta \end{pmatrix}\begin{pmatrix} u_{k_1} \\ u_{k_2} \end{pmatrix},$$

Here $k_1 = k\cos\theta$, $k_2 = k\sin\theta$ and c_i are positive constants, that can be determined in terms of the parameters of the steric potential and the friction tensors: $c_1 = \gamma_\perp^T h/2\eta A_c + \left(\frac{3}{2}U' + \frac{9}{8}U''+\right)/h\gamma_\parallel^T v_s$, $c_2 = \left(\frac{3}{2}U' + \frac{3}{8}U''+\right)/h\gamma_\parallel^T v_s$, $c_3 = \gamma_\perp^T h/2\eta A_c + \frac{3}{4}U''/h\gamma_\parallel^T v_s$, $c_4 = \gamma_\perp^T h/2\eta A_c + 3c_5$ and $c_5 = \left(\frac{1}{2}U' + \frac{3}{8}U''+\right)/h\gamma_\parallel^T v_s$. We can now diagonalize this matrix equation to obtain the relaxation of the overdamped modes after Fourier transforming in

time. The eigenvalues of the resulting equations give the dispersion relation of Eq. (5.4) in terms of an angular factor, $f_{\pm}(\theta) = c_{15}\cos^2\theta + c_{24}\sin^2\theta \pm [(c_{15}\cos^2\theta + c_{24}\sin^2\theta)^2 - 4(c_1c_5\cos^4\theta + c_2c_4\sin^4\theta - c_3^2\cos^2\theta\sin^2\theta + (c_1c_4 + c_2c_5)\cos^2\theta\sin^2\theta)]^{1/2}$, with $c_{15} = c_1 + c_5$ and $c_{24} = c_2 + c_4$. The long-wavelength approximation is found to be in concord with the complete numerical solution for $k \lesssim 0.1k_0$, as shown in Fig. (5.3).

5.6 Crystalline steady states

In this section we work out the steady states of the active crystals using the leading terms of the force and torque equations. Using the leading order force balance for i-th particle, the steady state condition for position is given as

$$\gamma_{ij}^{TT} \cdot \mathbf{V}_j^{\mathcal{A}} + \mathbf{F}_i^P = 0. \tag{5.7}$$

Here $\mathbf{V}_i^{\mathcal{A}} = -v_s\hat{\mathbf{z}}$ is self-propulsion of the colloid at a speed v_s, assumed to be moving $\perp$ to the wall. The body force $\mathbf{F}_i^P = -\boldsymbol{\nabla}_{\boldsymbol{R}_i}U$ is due to a short-ranged repulsive potential $U(r_{ij}) = \epsilon\left(\frac{r_{min}}{r_{ij}}\right)^{12} - 2\epsilon\left(\frac{r_{min}}{r_{ij}}\right)^{6} + \epsilon$, for $r_{ij} < r_{min}$ and zero otherwise [158], where ϵ is the potential strength and $\boldsymbol{r}_{ij} = \boldsymbol{R}_i - \boldsymbol{R}_j$. The same potential has been used to model colloid-colloid repulsion $\mathbf{F}_i^{PP}$ and the colloid-wall repulsive force $\mathbf{F}_i^{PW}$.

One- and two-body dynamics: To estimate the height at which the particle is brought to rest close to the wall, we use the $\hat{\boldsymbol{z}}-$component of the force balance

$$-\gamma_{\perp}^{T}v_s = F_3^{PW}.$$

Here F_3^{PW} is the repulsive force from the wall in $\hat{\boldsymbol{z}}$ direction, while $\gamma_{\perp}^{T}v_s$ is the attractive force of the colloid to the wall in same direction. The balance between the attraction and repulsion sets the height h at which the colloid is brought to rest. We now consider force

balance for a pair of particles in planar direction,

$$-v_s\gamma_{\parallel}^{T}\gamma_{\perp}^{T}\mathcal{F}_i^0\mathcal{F}_j^0 G_{\alpha 3}^{\mathrm{w}}(\boldsymbol{R}_i,\boldsymbol{R}_j)+F_{\alpha}^{PP}=0, \tag{5.8}$$

where α may takes either of the values 1 or 2 corresponding to two equivalent directions parallel to wall and $\mathcal{F}_i^l=\left(1+\frac{b^2}{4l+6}\nabla_{\boldsymbol{R}_i}^2\right)$ is an operator encoding the finite size of the sphere. We have used results provided in Appendix A.4, to write the expression for friction. The solution of this equation gives the lattice spacing d. For fixed particle-wall potential, increasing v_s decreases the resting height h and separation between *pairs, d*.

In Fig. (5.1), we show the state diagram, obtained from simulation, which shows that the crystal is stable over a critical strengths of either bottom-heaviness or chirality. For a symmetric distribution of the centers and orientation of the colloids, a crystal stabilized by external torque alone *does not rotate*, while the crystal *stabilized by chirality does rotate*. To obtain the non-rotating state of a crystal stabilized by external torque, the colloids are started in an initially symmetric state, while the orientations are normal to the wall. When the crystal is rotating at an angular velocity $\boldsymbol{\Omega}_c$ about its center of mass $\boldsymbol{R}_c$, the velocity the i-th colloid at position $\boldsymbol{R}_i$ can be then written as $\dot{\mathbf{R}}_i=\boldsymbol{\Omega}_c\times\boldsymbol{R}_i$. Force balance parallel to the wall is then

$$\boldsymbol{\gamma}_{ij}^{TT}\cdot\left[\boldsymbol{\Omega}_c\times(\boldsymbol{R}_j-\boldsymbol{R}_0^c)\right]+\boldsymbol{\gamma}_{ij}^{TR}\cdot\boldsymbol{\Omega}_j=0. \tag{5.9}$$

The angular speed perpendicular to wall is $\Omega=\Omega_i^{\mathcal{A}}$. This implies that in absence of chiral self-rotation there is *no* rotation of the crystal. Here The angular velocity of the crystal can be obtained by power counting - $\boldsymbol{\gamma}_{ij}^{TT}$ scales as r_{ij}^{-3} in direction parallel to wall while $\boldsymbol{\gamma}_{ij}^{TR}$ scales as r_{ij}^{-4}. The angular velocity of the crystal, then, scales as $\Omega_c\propto 1/R_c^2$. In Fig. (5.1) we show that rotation period of a crystal scales inversely as number of particles N in the crystal for an assembly of chiral particles, which is an excellent agreement with a recent experiment [8].

Slip mode	Positional clustering	Orientational stability	Cluster rotation
$\mathbf{V}^{\mathcal{A}}$	Yes	No	No
$\mathbf{V}^{(2s)}$	Yes	No	No
$\mathbf{V}^{(3t)}$	Yes	No	No
$\mathbf{V}^{(3a)}$	No	Yes	Yes
$\mathbf{V}^{(4a)}$	No	Yes	Yes

Table 5.1: Role of different terms in truncation of the slip expansion as given in Eq. (5.1) in active crystallization. It should be noted the rotation column is for a crystal of active colloids whose positions and orientations are completely symmetric about the center of the crystal. A crystal with any degree of asymmetry will rotate, irrespective of stability by bottom-heaviness or chirality.

5.7 Conclusion

In this work, we have considered only hydrodynamic forces and torques, unlike the case of MIPS [140–143] where Brownian torques drives reorientations [144, 145, 160, 161]. We have shown that the latter are at least two orders of magnitude weaker than the former for experiments in the class of [5, 8]. However, it is conceivable that thermal fluctuations will play a more significant role when the activity is comparatively weak, modifying both the nature of crystallization transition and the stability of the crystalline phase. The spinodal-like instability appears due to the uncompensated long-ranged attractive active forces. These can be compensated by entropic forces to stabilize the disordered phase at finite temperatures. A nucleational route to crystallization, with activity-enhanced rates, is then possible in the regime where the active forces reduce the nucleation barrier without driving it to zero. In the crystalline phase, thermal fluctuations will excite both phonon and topological modes. Phonon fluctuations will destroy long-range translational order [164, 165], but due to the activity-enhanced stiffness of these modes, large system sizes (compared to equilibrium) will be needed to observe the power-law decay of correla-

tions. Topological defects will be excited at higher temperatures and a defect unbinding transition [27, 166–169], modified by activity, may destroy translational order entirely, producing instead an "active" hexatic phase. These present exciting avenues for future research. We remark that wall-bounded clustering phenomena in algae [6] and charged colloids [170] are mediated by specific forms of the universal hydrodynamic mechanisms presented here.

Finally, we suggest that the flow-induced phase separation (FIPS) found here may provide a paradigm, complementary to MIPS, in which theoretical and experimental studies of momentum-conserving driven [171] and active matter [172–177] may be situated.

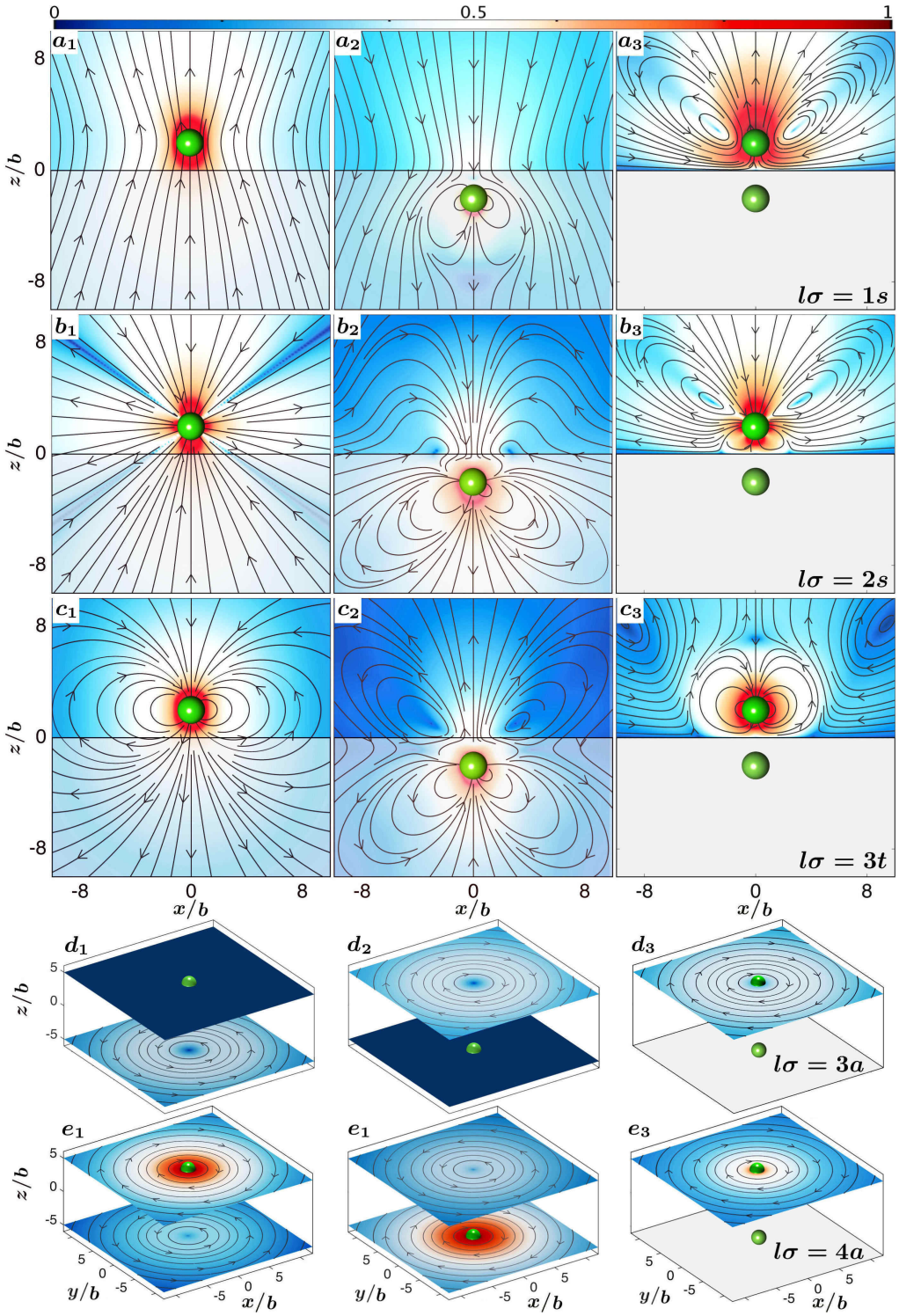

Figure 5.4: Irreducible axisymmetric and swirling components of fluid flow, Eq. (2.28a), induced by an active colloid at a height h from the wall. The streamlines of the fluid flow have been overlaid on the pseudo-color plot of the normalized logarithmic flow speed. The first column is the flow due to source alone while second column has the flow from the image, and their sum is plotted in the third column. The first three rows show axisymmetric flow produced by a monopole ($l\sigma = 1s$), symmetric dipole ($l\sigma = 2s$) and vector quadrupole ($l\sigma = 3t$) respectively, while the last two rows are the swirling flows due to antisymmetric quadrupole ($l\sigma = 3a$) and antisymmetric octupole ($l\sigma = 4a$) respectively.

Chapter 6

Periodic flows: Dynamics of polar active colloids

6.1 Introduction

In this chapter, we present a method to compute the many-body microhydrodynamic of active colloids in periodic geometries. Calculations of transport properties in an infinite suspension leads to divergent quantities while there are no such divergences in experiments. This problem of non-absolutely convergent expression for fluid flow has been addressed here. We explicitly remove the divergent contributions to the flow and then use the Ewald summation procedure to sum the absolutely convergent expression. The resulting convergent answer is then used to study active colloids in periodic Stokes flow.

The remainder of the chapter is organized as follows. In section 6.2, we derive a regularized expression for fluid flow and perform a Ewald summation of the regularized expression for accelerated convergence in numerical simulations. The expressions, thus derived, have been used to study the effects of hydrodynamic interaction on the motion of polar active colloid in section 6.3.

6.2 Regularization scheme and Ewald sum for active flows

Active colloids are force-free and torque-free. Still, in absence of external forces and torques, the fluid flow produced by an apolar active colloid decays as $1/r^2$, while that of a polar colloid decays as $1/r^3$ in an unbounded domain [10, 45]. Summing such flows for a large system gives non-convergent answers due to the long-ranged nature of the flow. To compute the expression for a regularized flow, which does not have any divergence, we follow the procedure due to O'Brien [52]. In O'Brien's method, an imaginary surface Γ' of length scale much larger than the colloidal radius, but smaller than the length scale associated with the system, is considered [128, 178]. The surface Γ' always remains in the fluid, and thus has variations at length scales of the order of the size of the colloids. To tackle the variations on the surface, we compute the integral on a new surface Γ which is allowed to cut the colloids and thus has no variations at the colloidal scale. The change of the surface in the integral has an effect of producing additional terms which can be computed analytically for spheres. Since, the length scale of the surface is much larger than colloidal dimension, the terms in the surface integral can be replaced by their suspension averages [99, 179]. The surface Γ can be finally assumed to be at infinity. The resulting expression of the flow is absolutely convergent as we now show.

To proceed, we first write the expression for fluid flow, which has contribution from colloidal surfaces, as in Eq. (2.9a), and from surface Γ' which contains many colloid

$$\begin{aligned} v_\alpha(\boldsymbol{r}) = &- \int \Big(G_{\alpha\beta}(\boldsymbol{r}, \boldsymbol{r}_j)\, f_\beta(\boldsymbol{r}) + K_{\beta\alpha\gamma}(\boldsymbol{r}, \boldsymbol{r}_j)\hat{\rho}_\gamma v_\beta(\boldsymbol{r}_j) \Big) d\mathrm{S}_j \\ &- \int_{\Gamma'} \Big(G_{\alpha\beta}(\boldsymbol{r}, \mathbf{r}')\, f_\beta(\boldsymbol{r}') + K_{\beta\alpha\gamma}(\boldsymbol{r}, \boldsymbol{r}') n_\gamma v_\beta(\boldsymbol{r}') \Big) d\mathrm{S}'. \end{aligned} \tag{6.1}$$

Here n_γ is the normal of the surface Γ'. This gives the flow due to rigid colloids without any approximation. The divergence is circumvented due to surface Γ' which ensure that there are finite number of colloids inside. Now we make the transformation from Γ' to another surface Γ which is allowed to cut the colloids which we were not doing to start

with. This has the effect of giving additional terms [128]. The expression for the surface integral after this transformation

$$\int_{\Gamma'}\Big(\mathbf{G}\cdot\boldsymbol{\sigma}-\mathbf{K}\cdot\boldsymbol{v}\Big)\cdot\mathbf{n}\,dS = \int_{\Gamma}\Big(\mathbf{G}\cdot\langle\boldsymbol{\sigma}\rangle-\mathbf{K}\cdot\langle\boldsymbol{v}\rangle+\boldsymbol{\nabla}\mathbf{G}\cdot\langle\mathbf{Q}\rangle\Big)\cdot\mathbf{n}\,dS$$
$$= \int_{\Gamma}\boldsymbol{\nabla}\cdot\Big(\mathbf{G}\cdot\langle\boldsymbol{\sigma}\rangle-\mathbf{K}\cdot\langle\boldsymbol{v}\rangle+\boldsymbol{\nabla}\mathbf{G}\cdot\langle\mathbf{Q}\rangle\Big)dV+\int_{S_f}\Big(\mathbf{G}\cdot\langle\boldsymbol{\sigma}\rangle-\mathbf{K}\cdot\langle\boldsymbol{v}\rangle+\phi\boldsymbol{\nabla}\mathbf{G}\cdot\langle\mathbf{Q}\rangle\Big)\cdot\mathbf{n}\,dS.$$

Here, ϕ is volume fraction, we have used the divergence theorem to convert the surface integral to volume integral and S_f is the field point where the flow is evaluated. Also, the single layer and the double layer propagators $\mathbf{G}$ and $\mathbf{K}$ do not vary much over Γ, and thus the quantities in the integral can be replace by the respective suspension averages [99, 179]. $\mathbf{Q}$ is the additional contribution due to the surface Γ[128, 178]. We write it in irreducible form as

$$\mathbf{Q}=\frac{3}{8\pi b}\int\mathbf{Y}^{(2)}(\hat{\boldsymbol{\rho}})\boldsymbol{f}\,dS_j+\frac{\boldsymbol{I}}{8\pi b}\int\boldsymbol{f}\,dS_j=\frac{9}{4\pi b}\mathbf{F}_i^{(3)}+\frac{\boldsymbol{I}}{8\pi b}\mathbf{F}_i^{H}.$$

These additional terms generate back-flow which cancels the divergent contributions to the flow. The resulting expression is then absolutely convergent and can be obtained explicitly [128, 178].

Using the absolutely convergent expression for the fluid flow, the rigid body motion of colloids is obtained in terms of the lattice sum of the Oseen tensor from the periodic images. These lattice sums converge slowly and they are not suitable for numerical simulations. For an accelerated convergence of these expression, Ewald summation of the Oseen tensor is essential. We compute the Ewald summation of the Oseen tensor using Beenakker's method [81, 180]. For convenience, the Oseen tensor is written in the following manner

$$\mathbf{G}^{\mathrm{o}}_{\alpha\beta}(\boldsymbol{R},\boldsymbol{R}') \;=\; \Big(\nabla^2\boldsymbol{I}-\boldsymbol{\nabla}\boldsymbol{\nabla}\Big)\frac{r}{8\pi\eta}=\Big(\nabla^2\boldsymbol{I}-\boldsymbol{\nabla}\boldsymbol{\nabla}\Big)\frac{\mathrm{erf}\,(\xi r)+\mathrm{erfc}\,(\xi r)}{8\pi\eta}=\mathbf{M}^{(1)}+\mathbf{M}^{(2)}.$$

Here $\mathrm{erf}(x)$ is the error function, $\mathrm{erf}(x)=\frac{2}{\sqrt{\pi}}\int_0^x e^{-t^2}dt$, and the sum of error function and

its complement is unity, $\mathrm{erf}(x) + \mathrm{erfc}(x) = 1$. Thus the rapidly decaying function in the real space will then converge very quickly while the term which is slowly varying in real space can be rendered convergent in the Fourier space with very less number of modes using the Poisson summation formula

$$\sum_m f(\mathbf{x}_m) = \frac{1}{V} \sum_n f(\boldsymbol{k}_n). \tag{6.2}$$

The second part of the sum can be calculated by taking the Fourier transform of the Green's function

$$\mathbf{G}(\boldsymbol{k}) = \frac{1}{\eta} \left(\frac{\boldsymbol{I} - \hat{\boldsymbol{k}}\hat{\boldsymbol{k}}}{k^2} \right). \tag{6.3}$$

Using this in the Fourier transform, the expression for $M^{(1)}$ and $M^{(2)}$ come out to be

$$\mathbf{M}^{(1)} = A(\xi r)\frac{\boldsymbol{I}}{r} + B(\xi r)\frac{\hat{\boldsymbol{r}}\hat{\boldsymbol{r}}}{r}, \qquad \mathbf{M}^{(2)}(\boldsymbol{k}) = \frac{C(k)}{\eta V} \cos(\boldsymbol{k}\cdot\boldsymbol{r}) \left(\frac{\boldsymbol{I} - \hat{\boldsymbol{k}}\hat{\boldsymbol{k}}}{k^2} \right), \tag{6.4a}$$

$$A(x) = \mathrm{erf}\,(\xi\rho) + \frac{2}{\sqrt{\pi}}(2x^3 - 3x^2)e^{-x^2}, \qquad B(x) = \mathrm{erf}\,(\xi\rho) + \frac{2}{\sqrt{\pi}}(x - 2x^3)e^{-x^2}, \tag{6.4b}$$

$$C(k) = \left(1 + \frac{1}{4}\xi^{-2}k^2 + \frac{1}{8}\xi^{-4}k^4 \right) e^{-\frac{1}{4}\xi^{-4}k^4}. \tag{6.4c}$$

This means the periodic Green's function in three dimensions can be written as

$$\mathbf{G}^{\mathrm{P}} = \sum \mathbf{M}^{(1)} + \frac{1}{V} \sum_k \mathbf{M}^{(2)}(\boldsymbol{k}),$$

where the sum is over all the colloids in the simulation box and its periodic images. It should be noted that in the Fourier transform $M^{(2)}(r = 0)$ has been assumed to contribute, and therefore, it needs to be subtracted explicitly from the expression of the fluid flow for consistency [180]. The expression is

$$M^{(2)}(r = 0) = \frac{1}{(2\pi)^3} \int M^{(2)}(\boldsymbol{k})\mathrm{d}\boldsymbol{k} = \frac{1}{\eta\sqrt{\pi}}\xi. \tag{6.5}$$

The derivatives of the periodic Green's function provide the expression for flow and rigid body motion due to higher modes, as shown in appendix A.3. Thus, the flow and rigidi body motion can be computed by repeated application of gradient operator with suitable contractions on the periodic Green's function. We illustrate this by providing the gradient and Laplacian of the Ewald summed Oseen tensor.

The gradient of the periodic Green's function is $\boldsymbol{\nabla}\mathbf{G}^{\mathrm{P}} = \boldsymbol{\nabla}\left(\mathbf{M}^{(1)} + \mathbf{M}^{(2)}\right)$. The contribution from the Fourier parts follows trivially

$$\boldsymbol{\nabla}\mathbf{M}^{(2)} = -\frac{C(k)\boldsymbol{k}}{\eta V}\sin(\boldsymbol{k}\cdot\boldsymbol{r})\left(\frac{\boldsymbol{I}-\hat{\boldsymbol{k}}\hat{\boldsymbol{k}}}{k^2}\right),$$

while the real space contribution is

$$\begin{aligned}
\nabla_\gamma \mathrm{M}^{(1)}_{\alpha\beta} &= \mathrm{D}\frac{\delta_{\alpha\beta}\, r_\gamma}{8\pi\eta r^3} + \mathrm{E}\frac{r_\alpha r_\beta r_\gamma}{8\pi\eta r^5} + \mathrm{B}\frac{\delta_{\alpha\gamma} r_\beta + \delta_{\beta\gamma} r_\alpha}{8\pi\eta r^3}, \\
D(\xi r) &= -\mathrm{erfc}(\xi r) + \frac{2}{\sqrt{\pi}} e^{-\xi^2 r^2}\Big[-\xi e + 10\xi^3 r^3 - 4\xi^5 r^5\Big], \\
E(\xi r) &= -3\mathrm{erfc}(\xi r) + \frac{2}{\sqrt{\pi}} e^{-\xi^2 r^2}\Big[-3\xi e - 2\xi^3 r^3 + 4\xi^5 r^5\Big].
\end{aligned}$$

We now calculate the Laplacian of the periodic Green's function. This can also be used to construct flow from $l\sigma = 3t$ mode. The expression is $\nabla^2\mathbf{G}^{\mathrm{P}} = \nabla^2\left(\mathbf{M}^{(1)} + \mathbf{M}^{(2)}\right)$. The contributions from terms in Fourier space is easily calculated: $\nabla^2 M^{(2)}_{\alpha\beta} = -k^2\, M^{(2)}_{\alpha\beta}$, while the real space contribution is

$$\begin{aligned}
\nabla^2 M^{(1)}_{\alpha\beta} = {} & \frac{\delta_{\alpha\beta}}{8\pi\eta r}\left[\frac{2\,\mathrm{erfc}(\xi r)}{r^2} + \frac{2}{\sqrt{\pi}} e^{-\xi^2 r^2}\Big(\frac{2\xi}{r} + 28\xi^3 r - 40\xi^5 r^3 + 8\xi^7 r^5\Big)\right] \\
& + \frac{r_\alpha r_\beta}{8\pi\eta r^3}\left[\Big(\frac{-6\,\mathrm{erfc}(\xi r)}{r^2} + \frac{2}{\sqrt{\pi}} e^{-\xi^2 r^2}\Big(-8\xi^7 r^5 + 32\xi^5 r^3 - 4\xi^3 r - \frac{6\xi}{r}\Big)\right].
\end{aligned}$$

Similarly, the fluid flow due to higher mode of the slip is obtained from the derivatives of the Ewald summed expression of the Oseen tensor. The streamlines of exterior flow due to leading modes of the slip in a periodic geometry is plotted in Figure (6.2).

6.3 Dynamics of polar active colloids

We now study the dynamics of polar active colloids in periodic boundary conditions of Stokes flow. We consider a minimal model of the slip, retaining only the lowest modes responsible for self-propulsion of an isolated active colloid in unbounded domain

$$\boldsymbol{v}^{\mathcal{A}} = -\mathbf{V}_i^{\mathcal{A}} + \tfrac{1}{15}\mathbf{V}_i^{(3t)} \cdot \mathbf{Y}^{(2)}(\hat{\boldsymbol{\rho}}), \qquad \mathbf{V}_i^{\mathcal{A}} = v_s \boldsymbol{p}_i.$$

Here v_s is the self-propulsion speed and $\boldsymbol{p}_i$ is the orientation of the i-th colloid, such that self-propulsion velocity is $\mathbf{V}_i^{\mathcal{A}} = v_s \boldsymbol{p}_i$. This slip truncation, which retains only the vector quadrupole ($l\sigma = 3t$) and the active translational velocity, corresponds to polar and achiral symmetry. The exterior flow field decays as $1/r^3$ and has a polar nature. Fluid flow field due to a linear array of polar colloids in periodic geometry of Stokes flow is plotted in panel (a) of Fig. (6.1). We now consider two illustrations involving polar active colloids in the periodic geometry of Stokes flow.

We, first, calculate the renormalized speed of a simple cubic array of spherical active colloids as a function of the box size and thus estimate the dependence of the self-propulsion speed with the volume fraction. In panel (b) of (6.1), we plot the renormalized speed of the simple cubic lattice of polar active colloids as a function of volume fraction, $\phi = N4\pi b^3/(3L^3)$. The corresponding result for the self-propulsion speed of the lattice is a linear function of volume fraction for small ϕ.

Stokes flow past periodic arrays of spheres has been studied previously in the context of sedimentation of passive colloids [73, 126, 128, 181, 182]. In all of those studies, it has been found that at low volume fraction the sedimentation speed of the array is proportional to $\phi^{1/3}$. On the other hand, we have shown that the self-propulsion velocity of an array of active colloids scales as ϕ. The difference in the behavior is rationalized by the different scalings of exterior fluid flow decay due to a sedimenting passive colloid ($u \propto 1/r$) and a self-propelling active colloid ($u \propto 1/r^3$).

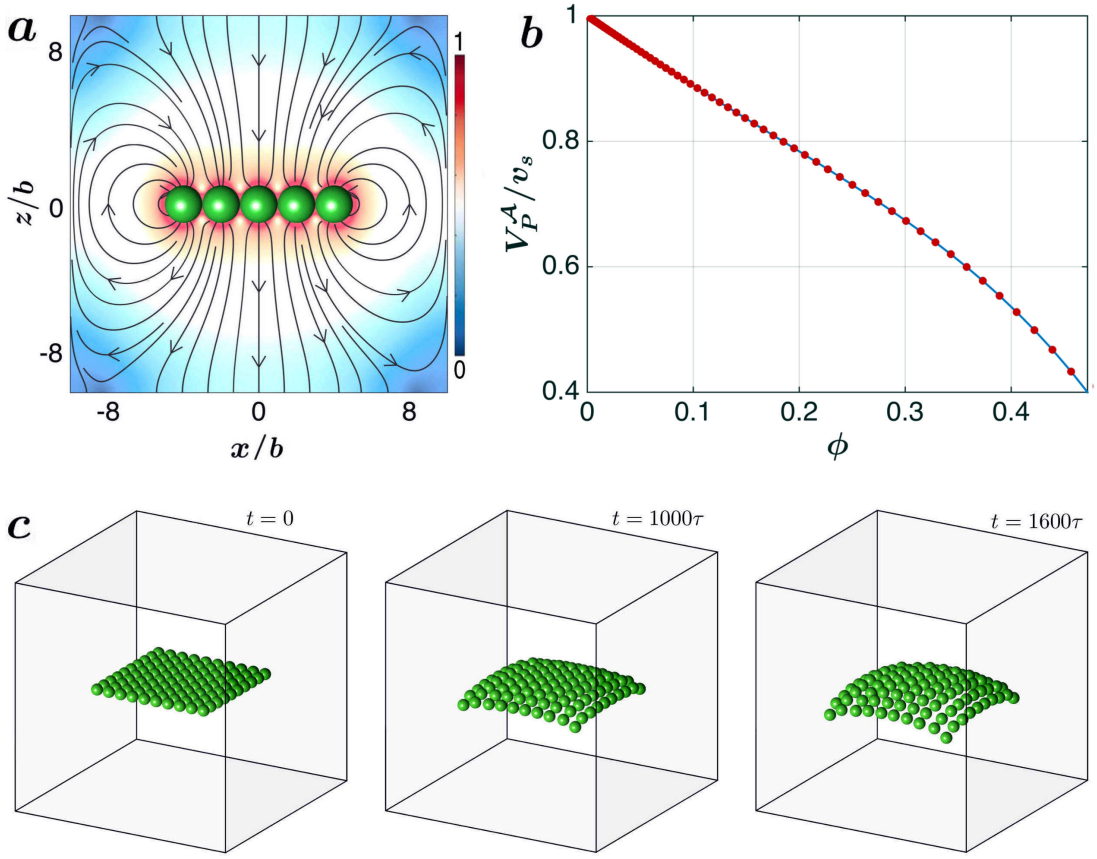

Figure 6.1: Dynamics of polar active colloids in periodic domain of Stokes flow. (**a**) Streamlines of fluid flow due to a linear array of polar active colloids with their orientation along the z-direction. The color map represents the logarithm of the flow speed normalized to its maximum. (**b**) Self-propulsion speed of a simple cubic array of active colloids ($V_P^{\mathcal{A}}$) with volume fraction, $\phi = N4\pi b^3/(3L^3)$, v_s is the speed of an isolated colloid in unbounded flow. The net self-propulsion in periodic Stokes flow speed varies linearly with volume fraction as shown (see text). (**c**) Crowley-like instability of a square lattice of active colloids, which are moving perpendicular to the plane, at three distinct instants, $\tau = b/v_s$. The colloids are plotted in a co-moving frame of reference. See text for details of the mechanism.

In panel (c) of Figure (6.1), we plot snapshots from a simulation of a polar active colloids in the periodic geometry of Stokes flow. The centers of the colloids are initialized on a square lattice and their orientations are along a direction perpendicular to the lattice. With time, the dynamics of colloids in the center is different from those on the edges, which is a Crowley-like instability in the positional order of the lattice. The Crowley instability results from the polar nature of the flow produced by sedimenting colloids [183–185], while the present instability is due to the polar nature of flow produced by the vector quadrupole mode of the active slip.

6.4 Conclusion

In this chapter, we have presented a method to compute the many-body hydrodynamic interaction of N spherical colloids with active boundary layers in periodic geometry of Stokes flow. We explicitly remove the divergent contributions to the flow and then use the Ewald summation procedure to sum the absolutely convergent expression. The formalism is then used to study the dependence of the self-propulsion speed with volume fraction in a suspension of polar active colloids. We also show an instability in the dynamics of a lattice of polar active colloids.

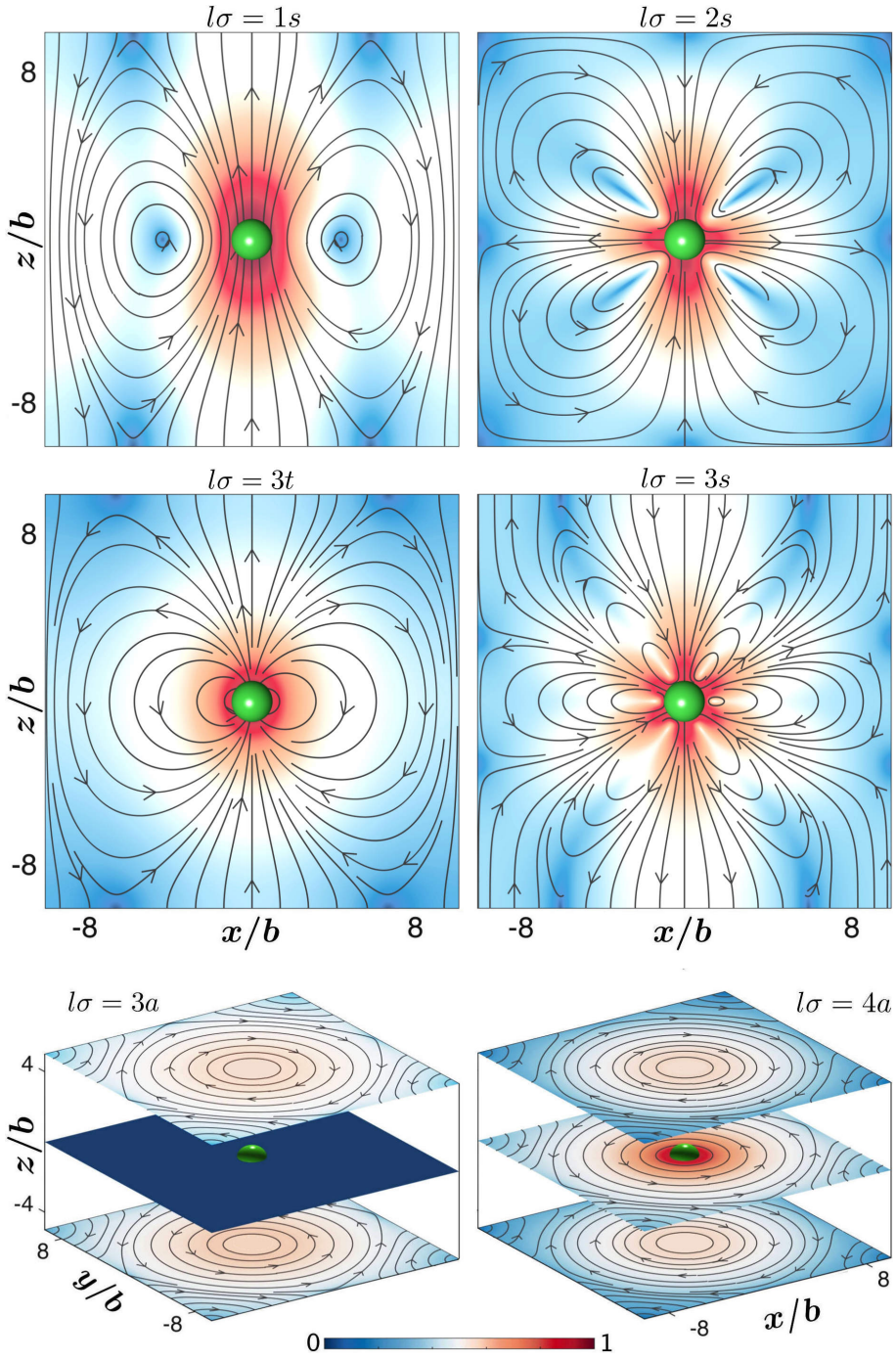

Figure 6.2: Irreducible axisymmetric and swirling components of fluid flow, Eq. (2.28a), due to an active colloids in periodic domain. The streamlines of the fluid flow have been overlaid on the pseudo-color plot of the normalized logarithmic flow speed. The first row contains the axisymmetric flow due to monopole ($l\sigma = 1s$) and symmetric irreducible dipole ($l\sigma = 2s$), while second row corresponds to vector quadrupole ($l\sigma = 3t$) and symmetric irreducible quadrupole ($l\sigma = 3s$). The last row has the flow from antisymmetric quadrupole ($l\sigma = 3a$) and octupole ($l\sigma = 4a$) respectively. A combination of these modes have been used in this chapter.

Chapter 7

Boundaries determine collective behaviour of active colloids

7.1 Introduction

In this chapter, we address the problem of how boundaries and confinement affect the collective dynamics of active colloids. This is a collaborative work and we provide theoretical understandings of the experimental observations [186].

The chapter is organized as follows. In section 7.2, we describe the experimental system and the main observations of the experiments. In this section, we also detail the theoretical model used to the provide a theoretical understanding of experimental observations. We use the formalism developed in preceding chapter by choosing a minimal set of modes which reproduces the experimental flow. We then simulate active colloidal in geometries corresponding to the experiments [186]. The experimental observations are described in section 7.2, while the theoretical model is give in section 7.3. Fluid-induced phase separation mechanism, obtained from the study of hydrodynamic forces and torques, is given in section 7.4. The chapter is concluded by a discussion of our results.

7.2 Experimental observations

The experiments are done using emulsion droplets as the active colloids, whose motion is fully three-dimensional [50, 187]. The self-propelling droplet is set into motion by internal spontaneously broken symmetry [187], which can be visualized due to the the liquid crystallinity of the droplet medium. We investigate the following cases (Fig. 7.1): (i) a Hele-Shaw geometry where the confinement of the droplets is restricted to one swimmer diameter (Fig. 7.1A) (ii) a Hele-Shaw geometry where the confinement is a few (3–5) swimmer diameters (Fig. 7.1B) (iii) at a plane wall bounding a bulk fluid (Fig. 7.1C) and finally (iv) at a air-water interface (Fig. 7.1D). Keeping all parameters fixed, we study the effects of changing the confining boundaries.

Swimmers form travelling lines in the Hele-Shaw geometries with the separation H between the plane walls playing a crucial role in determining the collective behaviour of the particles. Snapshots of the typical interactions and resultant structures in the motions of the swimmers are shown in the last row of Fig. (7.1A, B). These lines of swimmers are short-lived for $H \sim 2b$, while these lines are highly stable (long-lived) for a larger separation ($H \sim 8b$), as shown in Fig. (7.1B).

When the boundaries are very far apart, the three-dimensional propulsion mechanism of swimmer induces attractive hydrodynamic forces between the swimmers bringing them closer into aggregates. Steric repulsion between particles balances the attractive hydrodynamic forces to produce crystallites of the swimmers with hexagonal positional order at a single wall [9]. However, due to the high strength of activity, there is an out-of-plane motion from the two-dimensional crystalline structure (Fig. 7.1C). The crystalline aggregate is stabilized by a three-dimensional vortex comprising of swimmers which are pumped out of the crystalline plane and then added back by the recirculating flow. At an air-water interface, on the other hand, the attractive hydrodynamic forces lead to crystallization and there is no out-of-plane motion.

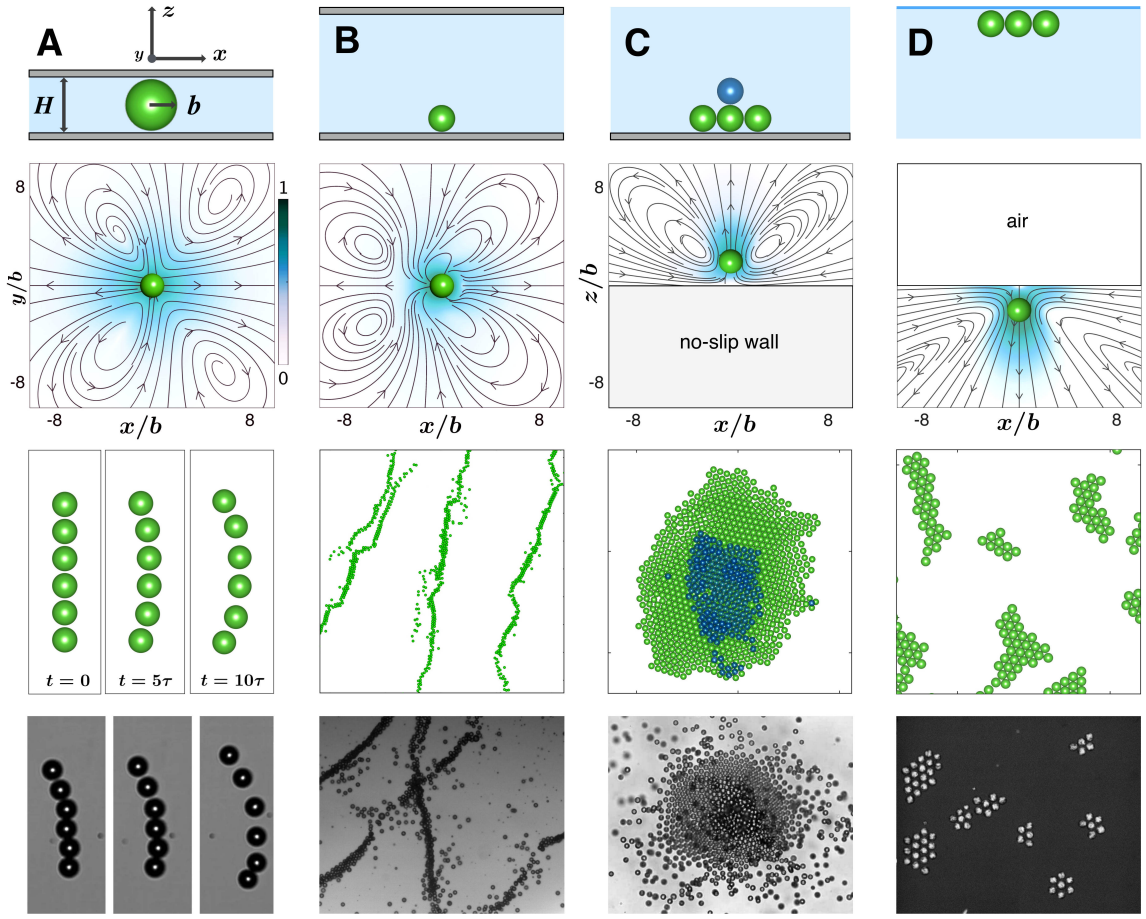

Figure 7.1: The role of boundaries in determining the collective behaviour of swimmers. Top row: Schematic of confinement. The exterior flow field produced by the swimmers in each geometry is shown in the second row, while corresponding snapshots from simulation and experiment are shown in third and fourth rows respectively. Travelling lines of swimmers can be formed in a Hele-Shaw cell. These lines are unstable if the separation of the cell equals the swimmer diameter (**A**, $H/b \sim 2$), while these lines are highly stable when the separation H is a few swimmer diameters (**B**, $H/b \sim 8$). Aggregation of the swimmers, leading to crystallization, is observed at a plane wall (**C**, chamber depth $H/b \sim 400$) and at the air-water interface (**D**, chamber depth $H/b \sim 400$). At a plane wall, swimmers are expunged from the crystalline core, while the crystal is stabilized by the recirculation of the fluid flow. At the air-water interface, on the other hand, there is no out-of-plane motion. Here $\tau = b/v_s$.

7.3 Model

Our theoretical model for the swimmers consists of spheres of radius b with an active flow field prescribed on its surface. This implies that the boundary condition at the interface between the i-th sphere and the fluid is given by Eq. (2.2). We retain leading terms of slip expansion of Eq. (2.3a) to reproduce the experimental observations. The choice of the truncation is done by comparing the experimental and theoretical flow [45]. Our minimal truncation of the slip is

$$\boldsymbol{v}_i^{\mathcal{A}}(\boldsymbol{\rho}_i)+ \quad = \mathbf{V}_i^{(2s)} \cdot \mathbf{Y}^{(1)}(\boldsymbol{\rho}_i) - \tfrac{1}{75}\mathbf{V}_i^{(4t)} \cdot \mathbf{Y}^{(3)}(\boldsymbol{\rho}_i). - \mathbf{V}_i^{\mathcal{A}} + \tfrac{1}{15}\mathbf{V}_i^{(3t)} \cdot \mathbf{Y}^{(2)}(\boldsymbol{\rho}_i). \tag{7.1}$$

The droplet swimmer used to model the experiments is represented by three leading modes of a tensorial spherical harmonic expansion of the active slip in Eq. (2.2). The fluid flow due to these modes is in good agreement with the experimentally measured exterior flow around the swimmer. With this slip model we study the role of boundaries in determining the collective dynamics. A geometry-dependent comparison of the flow streamlines colloid due to the leading modes of the slip is given in Fig. (7.4). It should be noted that the fluid flow around the particle is same in all the geometries considered. The behavior away from the particle, on the other hand, is modified importantly by the presence of boundaries. With this understanding, we proceed further to understand the role of boundaries in determining the collective behavior of active colloids.

Brownian forces on swimmers are typically $O(k_BT/b) \approx 10^{-16}$ N, while the typical active forces on our swimmers are of the order $F_{\mathcal{A}} = 6\pi\eta b v_s \approx 10^{-11}$ N. Thus, the active hydrodynamic forces are orders of magnitude larger than the Brownian forces, and therefore, we ignore the effects of thermal fluctuations in the fluid. The colloid-colloid and the colloid-wall repulsive interaction is modeled using the short-ranged repulsive WCA potential [158], which is given as, $U(r) = \epsilon\left(\frac{r_{min}}{r}\right)^{12} - 2\epsilon\left(\frac{r_{min}}{r}\right)^{6} + \epsilon$, for $r < r_{min}$ and zero otherwise, where ϵ is the potential strength.

The simulations are performed by numerical integration of the Langevin equations of Chapter 3, which are obtained in a terms of series of sum of mobility matrices and propulsion tensors. The series sum is truncated based on the minimal model of the active slip in Eq. (7.1), while the mobility matrices and propulsion tensors are obtained in terms of the Green's functions of Stokes flow appropriate to each geometry. A list of Green's functions of Stokes flow in the geometries considered here is given in Appendix A.2. The coefficients of the slip expansion are chosen to ensure that the theoretical flow field is qualitatively similar to the experimentally measured flow field. These parameters are then kept fixed for all the simulations reported. The evaluation of the rigid body motion of the colloids and the flow disturbance created by them has been performed using PyStokes [17]. The numerical integration of the resulting equations are performed using an adaptive time step integrator, which uses the backward differentiation formula [188]. Random packing of hard-spheres [159] is used as the initial distribution of particles in all the simulation.

7.4 Collective behavior and boundaries of the flow

In this section, we provide mechanisms for the collective behaviour observed in the experiments by studying the active hydrodynamic forces on the particles. It is observed in the experiments that lines of swimmers transverse to the swimming direction can be formed in a Hele-Shaw geometry. These lines emerge due attractive parallel forces between colloids as shown in the second row of Fig. (7.2A and B). These lines are transient for $H \sim 2b$, while they are long-lived (stable) if $H \sim 8b$. This difference in the behaviour is understood by studying the perpendicular component of forces between two swimmers as shown in the third row Fig. (7.2A and B). The force is an order of magnitude higher for $H \sim 2b$, in comparison to $H \sim 8b$. Thus, swimmers experiences a much larger perpendicular force due to their neighbors, which destabilizes the line, when the Hele-Shaw thickness equals the particle diameter. These forces change quantitatively for an interme-

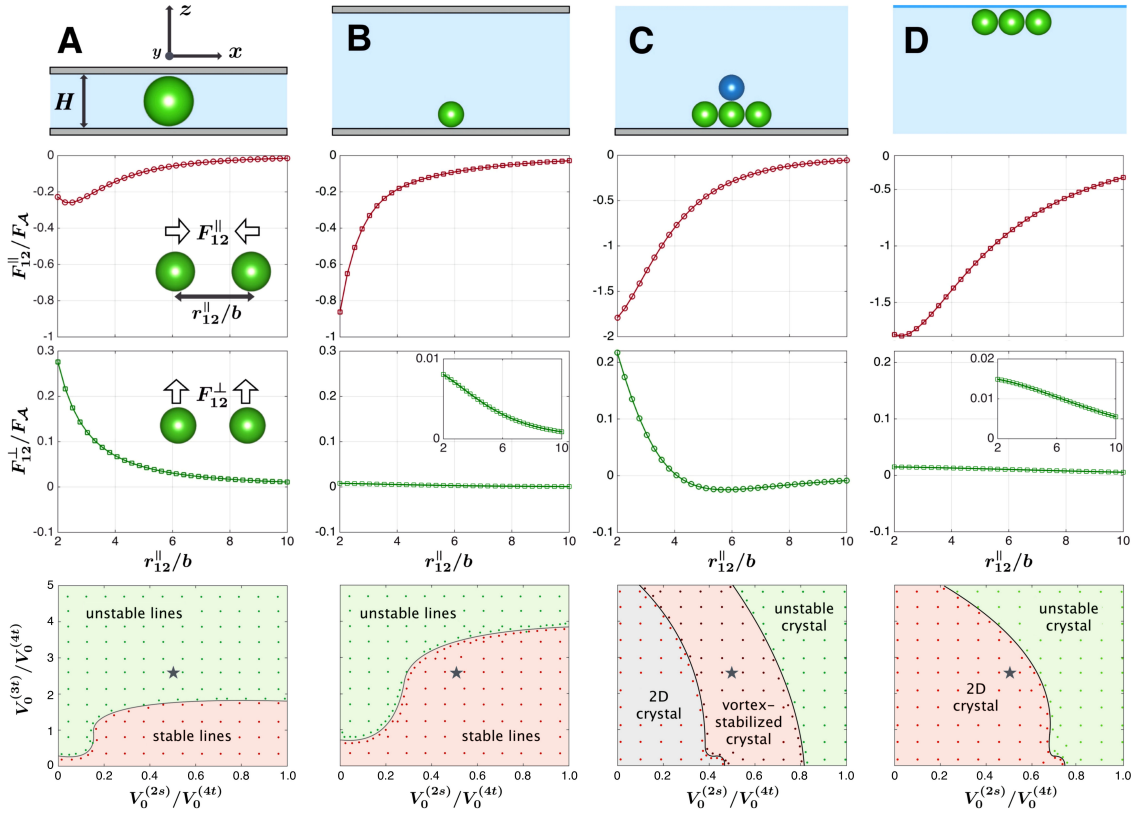

Figure 7.2: Active forces on the swimmers are modified by the presence of boundaries. The attractive nature of the parallel force (second row) between two swimmers in a Hele-Shaw (**A**. $H/b \sim 2$ and **B**. $H/b \sim 8$) leads to the formation of traveling lines. The perpendicular force (third row) is an order of magnitude larger for $H/b \sim 2$, and thus account for the short-lived lines in this case. Attractive parallel forces in the plane of the wall (**C**) and the interface (**D**) result in clustering of the swimmers. The perpendicular active force (third row) is an order of magnitude larger near a wall as compared to the interface, and explains the out-of-plane motion from the crystalline structure at a plane wall. The insets in third row show the decay profile of the forces clearly. The phase diagram, corresponding to each geometry, is given in the last row. Here the star denotes the parameters corresponding to the simulation.

diate separation ($H \sim 8b$) of Hele-Shaw geometry – the attractive parallel forces between swimmers become stronger than in the previous case (second row of Fig. (7.2)), while the net force in the perpendicular direction is reduced significantly. Thus, the gradient of forces acting on the swimmer determines if the lines are stable (long-lived) or unstable (transient) in a Hele-Shaw cell.

The attractive long-ranged hydrodynamic forces acting on the swimmers in a plane parallel to the wall and the interface (Fig. 7.2C, D) lead to the crystallization of the swimmers as shown in Fig. 7.1C and D. The perpendicular-component (out-of-plane from the wall) of active force on a swimmer is an order of magnitude higher near a wall (Fig. 7.2C), in comparison to the interface (Fig. 7.2D) causing out-of-plane motion from the crystalline structure near the wall, while the closed streamlines (see Fig. 7.1C) account for the recirculation of the swimmer to the crystalline plane. In effect, the out-of-plane forces and the recirculation lead to a vortex-stabilized crystal at the wall. This understanding from the studying the flow and active forces have also been verified in numerical simulations, as shown in the bottom row of Fig. (7.1). It should be noted that these active hydrodynamic forces are dissipative and non-conservative [9, 11] and they cannot be obtained in general from a potential, as seems to be the case in [51].

The phase diagram for each geometry, in the plane of the strengths of symmetric irreducible dipole ($V_0^{(2s)}$) and the vector quadrupole ($V_0^{(3t)}$), is shown in the last row of Fig. (7.2). Here the star denotes the parameters used to explain the experimental observations. The phase-boundaries are drawn by running several simulations (shown by the dots) and keeping the number of particles fixed. It should be noted that the location of these phase-boundaries change by a small amount if the number of particles change. In Fig. (7.2A) and Fig. (7.2A), we show the phase diagram when $H \sim 2b$ and $H \sim 8b$ respectively. It should be noted that stable and unstable lines of swimmers are possible in both the cases. In panel (C), we show the phases of colloids near a plane wall. At small strengths of $V_0^{(2s)}$, a two-dimensional crystal is formed at a plane [9], while a vortex-stabilized crystal

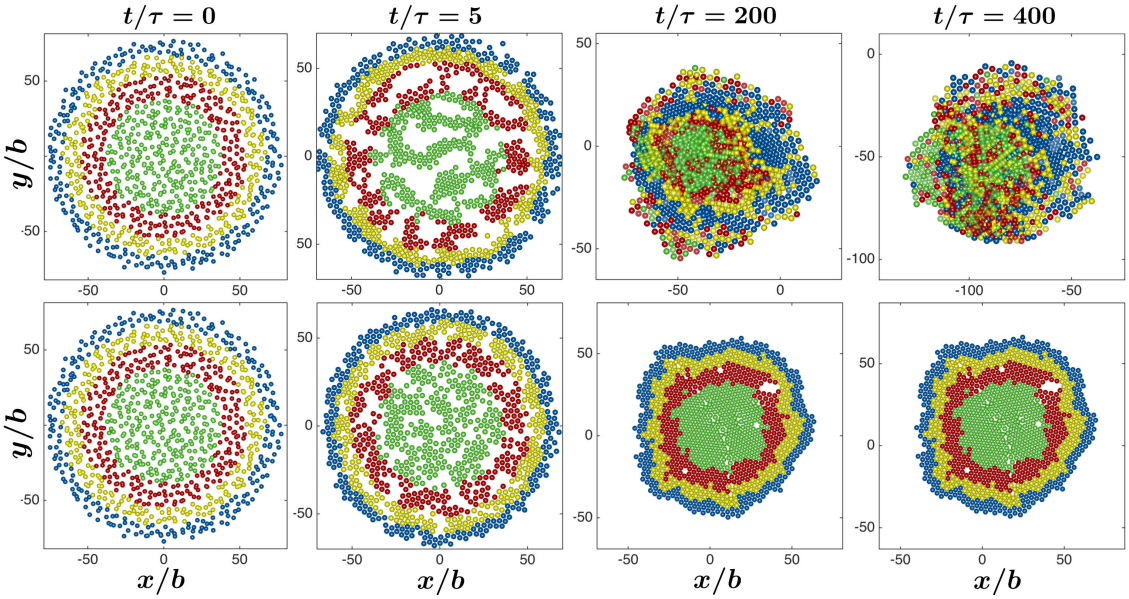

Figure 7.3: Kinetics of aggregation of swimmers at a plane wall (top row) and at a plane interface (bottom row). The colors are used to indicate and track the initial positions of the swimmers. Snapshots are shown at equal time intervals ($\tau = b/v_s$)

is formed at intermediate values. At higher values, a crystalline state appears from a uniform state but is unstable to forces perpendicular to the plane. Similarly, in panel (D), a two-dimensional crystal is formed at a plane interface for small values of $V_0^{(2s)}$, while an unstable crystal is formed at higher strenghts.

In Fig. (7.3) we show the kinetics of aggregation of identically prepared systems of disordered particles at a plane wall (first row) and at a plane surface (second row). It can be seen that these particles pack them into a crystalline structure at the plane surface and there is no relative motion of the particles in the crystals. At a plane wall, on the other hand, due to a higher magnitude of out-of-plane forces the particles keep moving out from the plane of the crystal and enter the crystal from the side due to recirculation of the flow at the wall as shown in Fig. (7.1C). Thus a highly dynamic aggregate is formed, where the advective motions of the swimmers lead to a mixing within the crystalline plane and exchange of neighbors (Fig. 7.3) on a much faster timescale than in the case of active crystals at an interface whose motion is confined to a plane. These observations are of relevance for encounter rates in bound states of biological systems[6, 8].

7.5 Conclusion

To summarize, in this chapter, we have shown that the active hydrodynamic forces are modified by presence of boundaries in the flow and lead to distinct emergent phenomena. The geometries of flow used here are usually realized in various experimentally and natural settings. Thus our results are applicable to a more wider class of problems than previously thought. In particular, the emergent structures such as travelling lines or vortex-stabilized crystals should be viewed as dynamical phases that are obtained due to flow-mediated active forces and torques on the colloids in the presence of boundaries. It should also be noted that traveling bands in our case are formed purely by attractive hydrodynamic forces, and do not require any aligning interactions between them.

It is instructive to compare the flow-induced phase separation (FIPS) mechanisms established in this chapter and in Chapter 5 with the complementary paradigm of motility-induced phase separation (MIPS) [143]. MIPS is a coarse-grained theory, where the colloidal fluid is advected by a density-dependent velocity which encodes the fact that the density is larger in the regions where the particles move slowly and the input that an enhanced density may reduce collective motility. The resulting positive feedback can produce density-segregated stationary states, which has also been obtained in microscopic models whose kinematics conform MIPS. In particular, crystallization of hard discs in two-dimension have been reported in simulations [144, 145, 160, 161].

In contrast, FIPS has a dynamical origin, and is equally applicable to both polar and apolar active colloids. FIPS mechanisms are obtained from the balance of forces and torques to obtain steady states. The forces and torques, being mediated by the fluid flow, are sensitive to the presence of boundaries and are, generically, anisotropic and long-ranged, containing both attractive and repulsive components. Thus, the boundaries of the flow appear essential for the operation of the FIPS mechanism, and a dissolution of the aggregated structure as boundaries become remote would point to it as the operative mechanism. There may also exist distinctive signatures of the flow in the emergent structures

of the aggregates. For example, the vortex-stabilized crystal (Fig. 7.3) constitutes further evidence for a FIPS-like underlying mechanism driving the aggregation of particles.

Thus, in this chapter and in Chapter 5, we have shown that the collective steady states of momentum-conserving active matter systems are determined using the FIPS mechanisms. FIPS is of dynamical origin and obtained from the balance of forces and torques. Since active forces and torques on colloids are modified qualitatively and quantitatively by the presence of boundaries in the flow, new collective phenomena of active colloids appear in different geometries of Stokes flow.

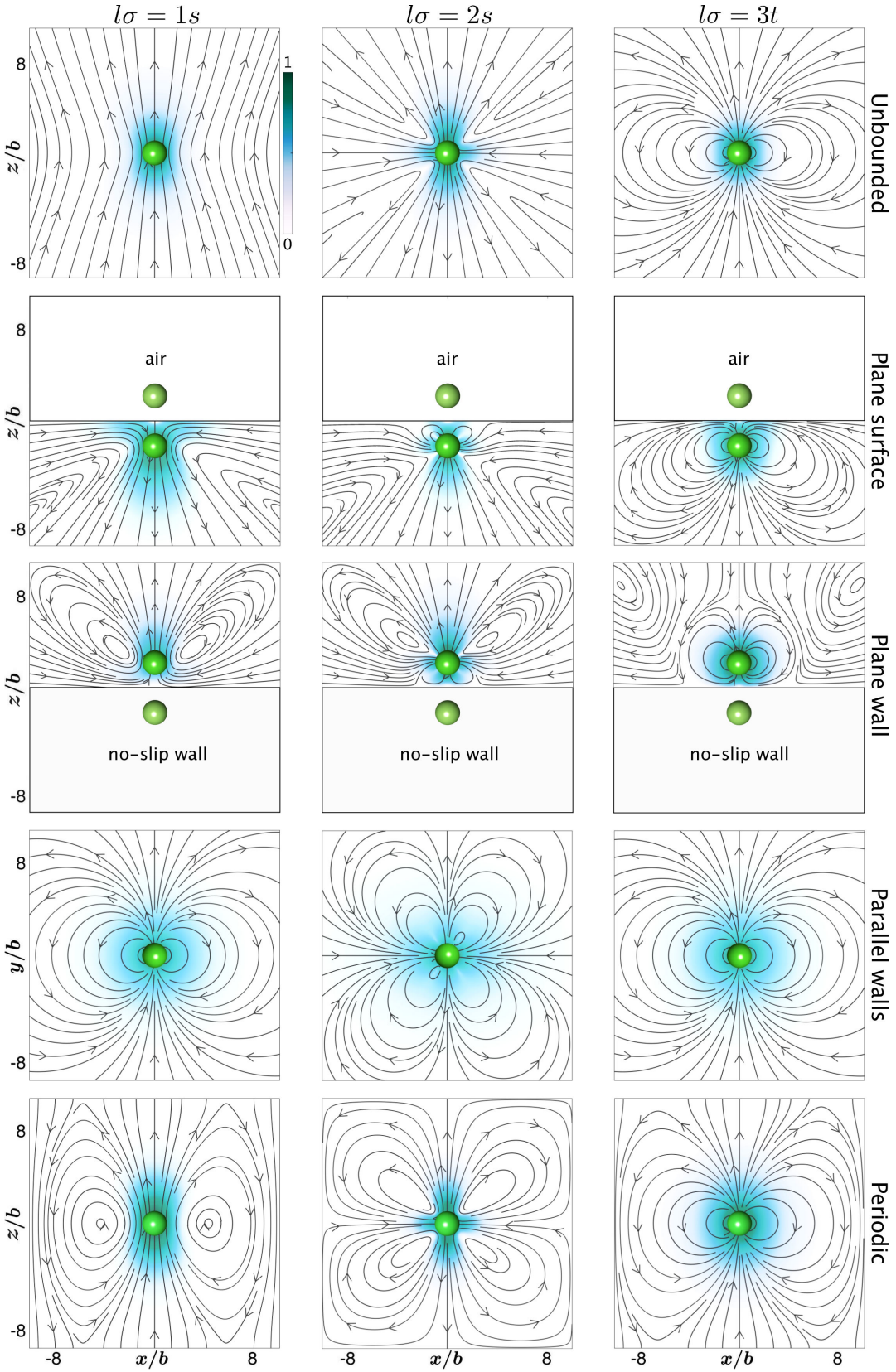

Figure 7.4: Comparison of streamlines of the fluid flow in different geometries around an active colloid due to the long-ranged modes ($l\sigma = 1s$, $2s$ and $3t$) of Eq. (2.28a). The labels on the top indicate the mode, while those on right are for the geometry of the flow.

Chapter 8

Contracted Smoluchowski description of active colloids

8.1 Introduction

The Langevin description of active colloidal suspensions has been derived in Chapter 3. An equivalent description of the system is also possible in terms of the Smoluchowski equation for the distribution function of positions and orientations of all the colloids. In this chapter, we arrive at the Smoluchowski equation using the results of Chapter 2 and Chapter 3.

The Smoluchowski equation for the distribution function of active colloids is given in section (8.2). Using this, we show the activity-induced breakdown of the fluctuation-dissipation relation in active colloidal suspensions. A contacted description of one-body and two-body density is also given in this section. In section (8.3), we provide a method to obtain the distribution function by reducing the Smoluchowski equation to a Hamilton-Jacobi equation. The chapter is concluded by a summary and directions for further work.

8.2 Smoluchowski descriptions of active colloids

The Smoluchowski equation for the distribution function $\Psi(\boldsymbol{R}_1,\ldots,\boldsymbol{R}_N;\boldsymbol{p}_1,\ldots,\boldsymbol{p}_N) \equiv \Psi(\boldsymbol{R}^N;\boldsymbol{p}^N)$ of positions and orientations follows immediately from the Langevin equations of section (3.4). We write it in the form of a conservation law in configuration space

$$\frac{\partial\Psi}{\partial t} = -\sum_{ij}\mathcal{L}_{ij}\Psi = -\sum_{ij}\left(\boldsymbol{\nabla}_{\boldsymbol{R}_i}\cdot\boldsymbol{\mathcal{V}}_{\boldsymbol{R}ij} + \boldsymbol{p}_i\times\boldsymbol{\nabla}_{\boldsymbol{p}_i}\cdot\boldsymbol{\mathcal{V}}_{\boldsymbol{p}ij}\right)\Psi, \tag{8.1}$$

where the "velocities" $\boldsymbol{\mathcal{V}}_{\boldsymbol{R}ij}$ and $\boldsymbol{\mathcal{V}}_{\boldsymbol{p}ij}$ are

$$\boldsymbol{\mathcal{V}}_{\boldsymbol{R}ij} = \boldsymbol{\mu}_{ij}^{TT}\cdot\left(\mathbf{F}_j^P - k_BT\,\boldsymbol{\nabla}_{\boldsymbol{R}_j}\right) + \boldsymbol{\mu}_{ij}^{TR}\cdot\left(\mathbf{T}_j^P - k_BT\,\boldsymbol{p}_j\times\boldsymbol{\nabla}_{\boldsymbol{p}_j}\right) + \sum_{l\sigma=2s}^{\infty}\boldsymbol{\pi}_{ij}^{(T,l\sigma)}\cdot\mathbf{V}_j^{(l\sigma)} + \mathbf{V}_i^{\mathcal{A}},$$
$$\boldsymbol{\mathcal{V}}_{\boldsymbol{p}ij} = \boldsymbol{\mu}_{ij}^{RT}\cdot\left(\mathbf{F}_j^P - k_BT\,\boldsymbol{\nabla}_{\boldsymbol{R}_j}\right) + \boldsymbol{\mu}_{ij}^{RR}\cdot\left(\mathbf{T}_j^P - k_BT\,\boldsymbol{p}_j\times\boldsymbol{\nabla}_{\boldsymbol{p}_j}\right) + \sum_{l\sigma=2s}^{\infty}\boldsymbol{\pi}_{ij}^{(R,l\sigma)}\cdot\mathbf{V}_j^{(l\sigma)} + \boldsymbol{\Omega}_i^{\mathcal{A}}.$$

Here $\mathbf{F}_j^P = -\boldsymbol{\nabla}_{\boldsymbol{R}_j}U$, $\mathbf{T}_j^P = -\boldsymbol{p}_j\times\boldsymbol{\nabla}_{\boldsymbol{p}_j}U$, and U is a potential that contains both positional and orientational interactions. Note the position of the mobility in the second derivative terms: the $\boldsymbol{\nabla\mu\nabla}$ order (in contrast with two other inequivalent permutations) is provided unambiguously by the adiabatic elimination of momenta.

In the absence of activity, the equation obeys the fluctuation-dissipation relation and the Gibbs distribution $\Psi \sim \exp(-U/k_BT)$ is the stationary solution. The Gibbs distribution implies that there are no circulating currents between the configurations of the system, which is the principle of detailed balance for systems at equilibrium. In contrast, in the presence of activity, the Gibbs distribution is no longer the stationary distribution. This is due to contributions from the active slip here and is easily verifiable by substitution.

In active systems, the condition of detailed balance is no longer satisfied and, in general, only the divergence of the current is zero. Circulation currents are a generic possibility in such circumstances and have, indeed, been observed in models of active colloidal systems [10, 13, 140, 189]. There is no prescription like Gibbs distribution for systems driven

far-from-equilibrium. The distribution function has to be derived for each system from the balance of the forces and torques acting on the colloids. The forces and torques are specific to a system and thus account for the wide variety of phenomenon seen in nonequilibrium systems.

The Smoluchowski equation above is a partial differential equation in $6N$ variables and is generally intractable as it stands. However, by standard reduction methods, equations for the one and two particle distribution functions may be obtained from it, providing a principled way of recovering coarse-grained macroscopic equations from the microscopic dynamics [190–194]. To this end, we define the n-body density $c^{(n)}$ as,

$$c^{(n)}(\boldsymbol{R}^n, \boldsymbol{p}^n, t) = \frac{N!}{(N-n)!} \int \Psi(\boldsymbol{R}^N; \boldsymbol{p}^N) \prod_{i=n+1}^{N} d\boldsymbol{R}_i d\boldsymbol{p}_i. \tag{8.2}$$

Using the Smoluchowski equation, we obtain the dynamics of one-body density

$$\begin{aligned}
\frac{\partial c^{(1)}}{\partial t} &= -N \sum_{ij} \int \boldsymbol{\mathcal{L}}_{ij} \Psi(\boldsymbol{R}^N; \boldsymbol{p}^N) \prod_{i=2}^{N} d\boldsymbol{R}_i d\boldsymbol{p}_i \\
&= -N \sum_{ij} \left(\boldsymbol{\nabla}_{\boldsymbol{R}_1} \cdot \int \boldsymbol{\mathcal{V}}_{\boldsymbol{R}_{ij}} \Psi + \boldsymbol{p}_i \times \boldsymbol{\nabla}_{\boldsymbol{R}_1} \cdot \int \boldsymbol{\mathcal{V}}_{\boldsymbol{p}_{ij}} \Psi \right) \prod_{i=2}^{N} d\boldsymbol{R}_i d\boldsymbol{p}_i.
\end{aligned}$$

We now use the fact that one-body mobilities are diagonal and scalar $\boldsymbol{\mu}_{11}^{RR} = \mu^R \mathbf{I}$, $\boldsymbol{\mu}_{11}^{TT} = \mu^T \mathbf{I}$ in an unbounded fluid flow. The one-body density, then satisfies,

$$\begin{aligned}
\frac{\partial c^{(1)}}{\partial t} &= \boldsymbol{\nabla}_{\boldsymbol{R}_1} \cdot \left(\mu^T \boldsymbol{\nabla}_{\boldsymbol{R}_1} U - \mathbf{V}_1^{\mathcal{A}} \right) c^{(1)} + k_B T \mu^T \boldsymbol{\nabla}_{\boldsymbol{R}_1}^2 c^{(1)} \\
&\quad + \mu^R \boldsymbol{p}_1 \times \boldsymbol{\nabla}_{\boldsymbol{p}_1} \cdot (c^{(1)} \boldsymbol{p}_1 \times \boldsymbol{\nabla}_{\boldsymbol{p}_1} U - \boldsymbol{\Omega}_1^{\mathcal{A}} + k_B T \, \boldsymbol{p}_1 \times \boldsymbol{\nabla}_{\boldsymbol{p}_1} c^{(1)}) \\
&\quad - N(N-1) \left(\boldsymbol{\nabla}_{\boldsymbol{R}_1} \cdot \int \boldsymbol{\mathcal{V}}_{\boldsymbol{R}_{12}} \Psi \, d\boldsymbol{R}_2 d\boldsymbol{p}_2 + \boldsymbol{p}_1 \times \boldsymbol{\nabla}_{\boldsymbol{R}_1} \cdot \int \boldsymbol{\mathcal{V}}_{\boldsymbol{p}_{12}} \Psi \, d\boldsymbol{R}_2 d\boldsymbol{p}_2 \right) \prod_{i=3}^{N} d\boldsymbol{R}_i d\boldsymbol{p}_i.
\end{aligned}$$

We now use the definition of $c^{(2)}$ and the operator $\boldsymbol{\mathcal{L}}_{ij}$ to obtain

$$\frac{\partial c^{(1)}}{\partial t} = -\boldsymbol{\mathcal{L}}_{11} \, c^{(1)} - \int \boldsymbol{\mathcal{L}}_{12} \, c^{(2)} \, d\boldsymbol{R}_2 d\boldsymbol{p}_2. \tag{8.3}$$

In obtaining the above expression we have assumed that the potentials generating the forces and torques have no inter-particle contributions.

We now write the dynamics of one-body colloidal density in terms of currents

$$\frac{\partial c^{(1)}}{\partial t} = -\nabla_{\boldsymbol{R}_1} \cdot \left(\boldsymbol{J}^{\mathcal{P}}_{\boldsymbol{R}_{11}} + \boldsymbol{J}^{\mathcal{P}}_{\boldsymbol{R}_{12}} + \boldsymbol{J}^{\mathcal{A}}_{\boldsymbol{R}_{11}} + \boldsymbol{J}^{\mathcal{A}}_{\boldsymbol{R}_{12}} \right) - \boldsymbol{p}_1 \times \nabla_{p_1} \cdot \left(\boldsymbol{J}^{\mathcal{P}}_{p_{11}} + \boldsymbol{J}^{\mathcal{P}}_{p_{12}} + + \boldsymbol{J}^{\mathcal{A}}_{p_{11}} + \boldsymbol{J}^{\mathcal{A}}_{p_{12}} \right), \quad (8.4)$$

where we have separated the one-body and two-body contributions from activity and passive interaction. The passive contribution to the current are

$$\begin{aligned}
\boldsymbol{J}^{\mathcal{P}}_{\boldsymbol{R}_{11}} &= -\left(\mu^T \nabla_{\boldsymbol{R}_1} U \right) c^{(1)} - k_B T \mu^T \nabla_{\boldsymbol{R}_1} c^{(1)}, \\
\boldsymbol{J}^{\mathcal{P}}_{p_{11}} &= -\mu^R \, \boldsymbol{p}_1 \times \nabla_{p_1} \cdot (c^{(1)} \boldsymbol{p}_1 \times \nabla_{p_1} U + k_B T \, \boldsymbol{p}_1 \times \nabla_{p_1} c^{(1)}), \\
\boldsymbol{J}^{\mathcal{P}}_{\boldsymbol{R}_{12}} &= \int \left[\boldsymbol{\mu}^{TT}_{12} \cdot \left(-\nabla_{\boldsymbol{R}_2} U - k_B T \, \nabla_{\boldsymbol{R}_2} \right) + \boldsymbol{\mu}^{TR}_{12} \cdot \left(-\boldsymbol{p}_2 \times \nabla_{p_2} U - k_B T \, \boldsymbol{p}_2 \times \nabla_{p_2} \right) \right] c^{(2)} \, d\boldsymbol{R}_2 d\boldsymbol{p}_2, \\
\boldsymbol{J}^{\mathcal{P}}_{p_{12}} &= \int \left[\boldsymbol{\mu}^{RT}_{12} \cdot \left(-\nabla_{\boldsymbol{R}_2} U - k_B T \, \nabla_{\boldsymbol{R}_2} \right) + \boldsymbol{\mu}^{RR}_{12} \cdot \left(-\boldsymbol{p}_2 \times \nabla_{p_2} U - k_B T \, \boldsymbol{p}_2 \times \nabla_{p_2} \right) \right] c^{(2)} \, d\boldsymbol{R}_2 d\boldsymbol{p}_2,
\end{aligned}$$

while the active contributions are

$$\begin{aligned}
\boldsymbol{J}^{\mathcal{A}}_{\boldsymbol{R}_{11}} &= \mathbf{V}^{\mathcal{A}}_1 c^{(1)}, \qquad \boldsymbol{J}^{\mathcal{A}}_{p_{11}} = \boldsymbol{\Omega}^{\mathcal{A}}_1 c^{(1)}, \\
\boldsymbol{J}^{\mathcal{A}}_{\boldsymbol{R}_{12}} &= \int \sum_{l\sigma=2s}^{\infty} \boldsymbol{\pi}^{(T,l\sigma)}_{ij} \cdot \mathbf{V}^{(l\sigma)}_j c^{(2)} \, d\boldsymbol{R}_2 d\boldsymbol{p}_2, \\
\boldsymbol{J}^{\mathcal{A}}_{p_{12}} &= \int \sum_{l\sigma=2s}^{\infty} \boldsymbol{\pi}^{(R,l\sigma)}_{ij} \cdot \mathbf{V}^{(l\sigma)}_j c^{(2)} \, d\boldsymbol{R}_2 d\boldsymbol{p}_2.
\end{aligned}$$

We now consider the contributions from the inter-particle forces to the currents. In this case, three-particle densities have to considered, as we now show. The inter-particle forces acting on the $i-$th colloid is given as

$$\mathbf{F}_i = -\sum_{i \neq j} \nabla_{\boldsymbol{R}_i} U_{ij}.$$

The above gives additional contributions to the currents in Eq. (8.4). The modified ex-

pression of the currents $\boldsymbol{J}^{\mathcal{P}}_{\boldsymbol{R}_{11}}$, $\boldsymbol{J}^{\mathcal{P}}_{\boldsymbol{R}_{12}}$ and $\boldsymbol{J}^{\mathcal{P}}_{\boldsymbol{p}_{12}}$, presence of inter-particle forces, are

$$
\begin{aligned}
\boldsymbol{J}^{\mathcal{P}}_{\boldsymbol{R}_{11}} &= -\mu^T \nabla_{\boldsymbol{R}_1} U c^{(1)} - k_B T \mu^T \nabla_{\boldsymbol{R}_1} c^{(1)} - \mu^T \nabla_{\boldsymbol{R}_1} \cdot \int d\boldsymbol{R}_2 d\boldsymbol{p}_2\, c^{(2)} \nabla_{\boldsymbol{R}_1} U_{12}, \\
\boldsymbol{J}^{\mathcal{P}}_{\boldsymbol{R}_{12}} &= \int \left[\boldsymbol{\mu}^{TT}_{12} \cdot \left(-\nabla_{\boldsymbol{R}_2} U - k_B T \nabla_{\boldsymbol{R}_2}\right) + \boldsymbol{\mu}^{TR}_{12} \cdot \left(-\boldsymbol{p}_2 \times \nabla_{\boldsymbol{p}_2} U - k_B T\, \boldsymbol{p}_2 \times \nabla_{\boldsymbol{p}_2}\right)\right] c^{(2)}\, d\boldsymbol{R}_2 d\boldsymbol{p}_2 \\
&\quad - \int \nabla_{\boldsymbol{R}_1} \cdot \boldsymbol{\mu}^{TT}_{12} \cdot \left(c^{(2)} \nabla_{\boldsymbol{R}_2} U_{12} + \int c^{(3)} \nabla_{\boldsymbol{R}_2} U_{32}\, d\boldsymbol{R}_3 d\boldsymbol{p}_3\right) d\boldsymbol{R}_2 d\boldsymbol{p}_2, \\
\boldsymbol{J}^{\mathcal{P}}_{\boldsymbol{p}_{12}} &= \int \left[\boldsymbol{\mu}^{RT}_{12} \cdot \left(-\nabla_{\boldsymbol{R}_2} U - k_B T \nabla_{\boldsymbol{R}_2}\right) + \boldsymbol{\mu}^{RR}_{12} \cdot \left(-\boldsymbol{p}_2 \times \nabla_{\boldsymbol{p}_2} U - k_B T\, \boldsymbol{p}_2 \times \nabla_{\boldsymbol{p}_2}\right)\right] c^{(2)}\, d\boldsymbol{R}_2 d\boldsymbol{p}_2 \\
&\quad - \int \boldsymbol{p}_1 \times \nabla_{\boldsymbol{R}_1} \cdot \boldsymbol{\mu}^{RT}_{12} \cdot \left(c^{(2)} \nabla_{\boldsymbol{R}_2} U_{12} + \int c^{(3)} \nabla_{\boldsymbol{R}_2} U_{32}\, d\boldsymbol{R}_3 d\boldsymbol{p}_3\right) d\boldsymbol{R}_2 d\boldsymbol{p}_2.
\end{aligned}
$$

And similar contribution for inter-particle torques.

From the above equations, it is obvious that we need $c^{(2)}$ and $c^{(3)}$ to obtain dynamics of $c^{(1)}$. It can be shown that the higher order terms also follow the same trend till we come to $N-$colloid density function. This system of equations is called the Bogoliubov-Born-Green-Kirkwood-Yvon (BBGKY) hierarchy and closure schemes to these equations in available [195].

Standard reduction methods give equations for the one and two particle distribution functions, providing a principled way of recovering coarse-grained macroscopic equations from the microscopic dynamics [190–194]. The coarse-grained description, thus obtained from the microscopic equations, can be used to derive the hydrodynamic description of active matter [33, 36]. The leading hydrodynamic modes of the system are given as

$$
\frac{\partial \rho(\boldsymbol{R}, t)}{\partial t} + \int \sum_{ij} \boldsymbol{\mathcal{L}}_{ij} \Psi = 0, \tag{8.5a}
$$

$$
\frac{\partial \mathbf{m}(\boldsymbol{R}, t)}{\partial t} + \int \mathbf{Y}^{(1)}(\boldsymbol{p}) \sum_{ij} \boldsymbol{\mathcal{L}}_{ij} \Psi = 0, \tag{8.5b}
$$

$$
\frac{\partial \mathbf{Q}(\boldsymbol{R}, t)}{\partial t} + \int \mathbf{Y}^{(2)}(\boldsymbol{p}) \sum_{ij} \boldsymbol{\mathcal{L}}_{ij} \Psi = 0. \tag{8.5c}
$$

We will pursue these directions of investigations in more detail in a future work.

8.3 Hamilton-Jacobi method for the distribution function

Explicit expression of the distribution function can be obtained from the Smoluchowski equation by reducing it to a Hamilton-Jacobi equation in the limit of large system size [14, 15]. We now define intensive variables $\boldsymbol{r}_i = \boldsymbol{R}_i/L$, where L is the length scale of the system. In the intensive variables, Eq. (8.1) becomes

$$\frac{1}{L}\frac{\partial \Psi(\boldsymbol{r}_i^N, t)}{\partial t} = -\sum_{ij} \mathcal{L}_{ij}\left(\boldsymbol{r}^N, \frac{1}{L}\boldsymbol{\nabla}_{r^N}, \frac{1}{L^2}\boldsymbol{\nabla}^2_{r^N}\right)\Psi(\boldsymbol{r}^N, t). \tag{8.6}$$

Here we have suppressed the orientational fluctuations, for example, by bottom-heaviness. We consider a solution of distribution function of the form [196]

$$\Psi(\tilde{\boldsymbol{R}}^N) \sim \exp(LJ(\boldsymbol{r}_i^N, t)).$$

In the limit of $L \to \infty$, the Smoluchowski equation then reduces to a Hamilton-Jacobi equation for $J(\boldsymbol{r}_i^N, t)$

$$\frac{\partial J(\boldsymbol{r}_i^N, t)}{\partial t} + H(\boldsymbol{r}^N, \boldsymbol{\nabla}_{r^N} J) = 0. \tag{8.7}$$

Here, we have only considered terms of order $1/L$. Thus we assume that the Brownian forces and torques are sub-dominant, as was shown to be the case in typical experiments of active colloids in Chapter 3. The solution of the above is the obtained using the well-established Hamilton-Jacobi theory of classical mechanics [197]. We consider the phase space of positions $\boldsymbol{r}_i$ and momenta $\boldsymbol{q}_i = \boldsymbol{\nabla}_{r_i} J$. The expression for $J(\boldsymbol{r}_i^N)$ is then

$$J(\boldsymbol{r}_i^N, t) = \int_0^t \left(\boldsymbol{q}_i(t') \cdot \dot{\boldsymbol{r}}_i - H(\boldsymbol{r}_i^N, \boldsymbol{q}^N)\right) + J(\boldsymbol{r}_0^N, 0). \tag{8.8}$$

Thus given the initial $J(\boldsymbol{r}_0^N, 0)|_{\boldsymbol{r}_0^N}$, find $\boldsymbol{q}_i = \boldsymbol{\nabla}_{r_i} J|_{\boldsymbol{r}_0}$ and then evolve the phase space till time t to obtain the $J(\boldsymbol{r}_i^N, t)$. It should be noted that the Hamilton-Jacobi theory, which is ob-

tained from the Smoluchowski equation in the $L \to \infty$ limit, ignores the fluctuations about the most likely trajectory. Thus, it is only applicable to a certain class of phenomena, like nucleation, when such a condition is satisfied.

8.4 Conclusion

In this chapter, we have derived the Smoluchowski equation for distribution of positions and orientations in active colloidal suspensions. Using the Smoluchowski equation, we explicitly demonstrate the breakdown of the fluctuation-dissipation in active colloidal suspensions. We have also given a contracted Smoluchowski description of active colloids. A method to obtain the distribution function of the Smoluchowski equation by reducing it to a Hamilton-Jacobi equation is also presented. A more detailed work using the equations derived in this chapter will be presented in future.

Chapter 9

Electrohydrodynamic flows: Self-assembly of nanoparticles

9.1 Introduction

This thesis focuses on the study of hydrodynamic interaction in systems of active colloids. A complete theoretical formalism has been developed in the preceding chapters to address the microhydrodynamics of active colloids. The generality of the method allows us to study *passive* particles in the same approach. Unlike, active colloids, passive colloids move under the effect of external potentials. Motion of charged particle in externally applied field is such an example. In addition to the external field, the fluid-mediated interaction of particles also needs to be considered to obtain a complete description of charge particles in a fluid flow.

In this Chapter, we address a system of hydrodynamically interacting charged and neutral passive particles in the presence of external electric field. This is a collaborative work and we provide theoretical explanations to the phenomena observed in the system by studying the interplay of electric and hydrodynamic stresses [198].

The remainder of the chapter is organized as follows. In section (9.2), we describe the experimental observations and the theoretical model used to explain the reported phenomenon reported. The electrohydrodynamic mechanism of self-assembly of nanoparticles has been described in section (9.3). We conclude the chapter by summarizing the results and indicating avenues of further research.

9.2 Experimental observations and the model

Electrohydrodynamics is the study of the effects of electrostatic forces on fluid flow and vice versa [16]. Electrohydrodynamic flows result from the motion of free charges on the surface of a fluid by application of a tangential electric field. In our experiment, free charged ions are sprayed using electrospray on the air-water inter- face of a container with an electrode on its surface. Formation of nanoparticle-nanosheet (NP-NS) is observed at the air water interface.

On the basis of these experimental results it is possible to infer a mechanism for the NP-NS formation. The self-assembly process is robust against alterations of metal in the electrospray and the liquid surface on which the spray falls. Thus, generic physical mechanisms, rather than specific chemical mechanisms must be at play, which leads us to conjecture as follows. The deposition of the spray on the liquid surface creates additional ionic species in the liquid, a fraction of which are adsorbed at the liquid-air interface, producing a strongly charged electrical double layer [199]. It is known, for instance, that such a double layer forms at room temperature at the air-water interface with a *negative* ζ-potential of few tens of millivolts. The presence of an electric field tangential to the liquid-air interface provides an electromotive force on the double layer, setting it in motion. The direction of motion is along the electric field if the ζ-potential is positive but opposite to it if the ζ-potential is negative. Viscous stresses in the liquid sets adjacent fluid layers into motion which develops into a steady-state fluid flow. This steady-state fluid flow must

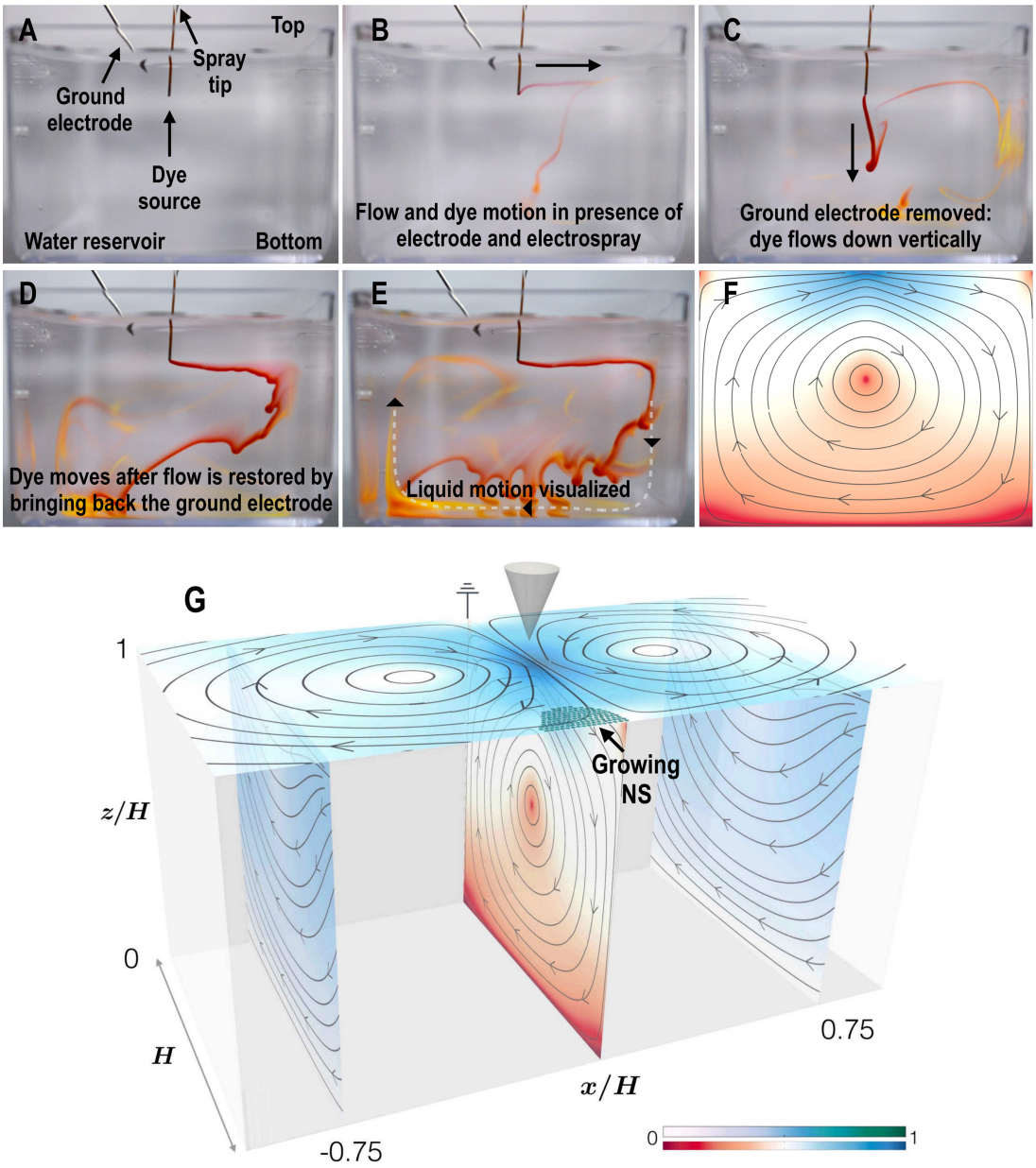

Figure 9.1: Dye visualization of the electrohydrodynamic flow in the symmetry plane of the liquid container (A) shows the experimental setup. (B) shows the advection of the dye by the flow when the spray is present (C) shows the cessation of flow, with the dye falling vertically, when the spray is absent (D) shows the resumption of the advection as the spray is again turned on and (E) shows circulation of the dye as it is carried along by the fluid streamlines. (F) shows the streamlines of a theoretically computed flow which compares well with circulation seen in (E). (G) Theoretically computed streamlines of electrohydrodynamic flow in long channel whose cross-section is a square of sides H. The spray from the cone deposits charges at the air-liquid interface which are then set into motion by the tangential electric field. For a negative interfacial ζ-potential the resulting in a flow *away* from the ground electrode. The bulk fluid, though electrically neutral, is set into motion due to viscous stresses. The combined action of the surface and bulk flow guides the nanoparticles into ordered aggregates at the edge of the channel opposite to the electrode.

have a circulatory character due to the finite compressibility of the liquid and the finite volume of the container and can, thus, continuously advect NPs dispersed in the bulk of the liquid to the liquid-air interface. The NPs thus advected to the surface are then guided by fluid flow to assemble into packed structures, which are crystalline if the flow is weak and glassy if the flow is strong.

To test the validity of this conjecture, we visualize the surface and bulk flow in the liquid both in the presence and in the absence of electrospray, the results of which are shown in the left panel of Fig. (9.1). The experimental set up is shown in panel (A). In the presence of electrospray, the dye does *not* fall vertically, as would be expected, but is advected tangential to the liquid-air interface, see panel (B). In contrast, when the spray is absent, the dye falls vertically under gravity, with no detectable tangential convection, see panel (C). The tangential convection resumes when the spray is restored and the process can be repeated at will with completely predictable results, see panels (E) and (F). The general circulatory pattern of the bulk fluid flow reveals itself once the dye is transported along the fluid streamlines, given a sufficient duration of spraying. Panel (G) shows the results of a theoretical computation of these streamlines, which is in excellent qualitative agreement with the experiment. We now outline the quantitative aspects of the electrohydrodynamic computation that yields the streamlines.

9.3 Electrohydrodynamic assembly of nanoparticles

The basis of the theoretical computation is the electrohydrodynamic system of equations first proposed by Taylor and Melcher [16], where conservation of fluid momentum and electric charge are combined with constitutive equations for the mechanical and electrical stress, assuming that the fluid is mechanically Newtonian and electrically a linear dielectric and an Ohmic conductor. In the regime of slow viscous flow relevant to the present

experiment, this implies

$$\boldsymbol{\nabla} \cdot (\boldsymbol{\sigma}^H + \boldsymbol{\sigma}^E) = 0, \tag{9.1}$$

where $\sigma^H_{ij} = -p\delta_{ij} + \eta_{ijkl}\nabla_k v_l$, and $\sigma^E_{ij} = \epsilon(E_i E_j - \frac{1}{2}\delta_{ij}E^2)$, are, respectively, Cartesian components of the mechanical and electrical stress tensors, v_i and E_i are the Cartesian components of the fluid flow and the electric field in the liquid, η_{ijkl} is the Newtonian tensor of viscosities and ϵ the permittivity of the fluid. The fluid flow is assumed to be incompressible, $\boldsymbol{\nabla} \cdot \boldsymbol{v} = 0$, and the electric field is assumed to be irrotational, $\boldsymbol{\nabla} \times \boldsymbol{E} = 0$. The medium is assumed to be a linear dielectric, $\boldsymbol{D} = \epsilon \boldsymbol{E}$, and an Ohmic conductor, $\boldsymbol{J} = \sigma \boldsymbol{E}$, where $\boldsymbol{D}$ is the electric displacement, $\boldsymbol{J}$ is the current density and ϵ and σ are permittivity and the conductivity of the liquid. The electric charge distribution ρ obeys the Maxwell and continuity equations

$$\boldsymbol{\nabla} \cdot \boldsymbol{D} = \rho, \tag{9.2}$$

$$\frac{\partial \rho}{\partial t} + \boldsymbol{\nabla} \cdot (\boldsymbol{J} + \rho \boldsymbol{v}) = 0, \tag{9.3}$$

and the above three coupled systems of equations, when supplemented by interfacial boundary conditions, determines the fluid flow, electric field, and charge distribution.

Using the continuity equation, we have

$$\left(\frac{\partial}{\partial t} + \boldsymbol{v} \cdot \boldsymbol{\nabla}\right)\rho + \frac{\sigma}{\epsilon}\rho = 0. \tag{9.4}$$

This sets a relaxation time scale $\tau = \epsilon/\sigma$. The relaxation time in a fluid is the ratio of the dielectric constant and the conductivity. The interfacial force density $\boldsymbol{f}^S$ can be obtained from the electrical stress tensor as

$$\boldsymbol{f}^S = \boldsymbol{\nabla} \cdot \boldsymbol{\sigma}^E = \rho \boldsymbol{E} - \frac{1}{2} E^2 \boldsymbol{\nabla} \epsilon. \tag{9.5}$$

Here we have used the Maxwell equation $\boldsymbol{\nabla} \cdot \boldsymbol{D} = \rho$, to obtain the above expression of in-

terfacial force density. We assume the fluid to be homogeneous, such that the permittivity ϵ is constant, and the second term in the above equation goes to zero. The expression of the interfacial force density $\boldsymbol{f}^S$ is then $\boldsymbol{f}^S = \rho \boldsymbol{E}$. We now use the above expression for the interfacial force density to obtain the fluid flow.

We solve the above equations in a rectangular geometry whose length is much greater than its square cross-sectional width H. We assume the limit in which the charge relaxation time $\tau = \epsilon/\sigma$ ($\sim 10^{-5}$ s for water) and the flow time scale $\tau' = \eta H/\gamma$ ($\sim 10^{-4}$ s for water, where γ is the surface tension) are both rapid compared to the remaining time scales. This ensures that the bulk remains electro-neutral and all free charges accumulate at the interface. The boundary integral representation of the Stokes equation has been used to determine the fluid in terms of the Green's function of the Stokes equation. The explicit expression of the boundary integral representation of Stoke flow has been given in Chapter 2. We write a solution to this equation using a Green's function $\mathbf{G}$, which vanishes on all the boundaries of the flow, and a interfacial force density which is obtained from Eq. (9.5). Then, the integral has contributions only from the interface. We assume a constant tangential electric field $\boldsymbol{E}$ and a Gaussian free charge density profile ρ at the interface. Finally, we neglect the double layer integral, as it is sub-dominant compared to the single layer. With these assumptions, the integral can be completed and the streamlines of the flow can be numerically computed. The approximate solution of the flow at any point $\boldsymbol{r}$ in the bulk is then given as

$$\boldsymbol{v}(\boldsymbol{r}) = \int \boldsymbol{G}(\boldsymbol{r}, \boldsymbol{r}') \cdot \boldsymbol{f}^S(\boldsymbol{r}') dS \approx \sum_j \boldsymbol{G}(\boldsymbol{r}, \boldsymbol{R}_j) \cdot (Q(2\pi\sigma_e^2)^{-1/2} \exp(-r^2/2\sigma_e^2)\boldsymbol{E}).$$

Here, we have used the expression $\boldsymbol{f}^S(\boldsymbol{r}) = \rho \boldsymbol{E}$ for the interfacial force density The integration is completed by considering the fact that the density of the charges on the surface of the container can be written as $\rho(\boldsymbol{r}) = \sum_j Q\delta(\boldsymbol{r} - \mathbf{R}_j)(2\pi\sigma_e^2)^{-1/2} \exp(-r^2/2\sigma_e^2)$, where σ_e is the characteristic width and Q is the strength of the charge. It should be noted that the charge density is a two-dimensional sheet sheet Gaussian density in the plane. We ensure

that the ratio σ_e/H is consistent with the experiment. The Green's function $\boldsymbol{G}$ is obtained from the series sum of the Lorentz-Blake tensorabout the side walls. The Lorentz-Blake tensor ensures no-slip condition at the bottom wall by construction, while the boundary condition at side walls is implemented by the series sum of the Lorentz-Blake tensor. The result of the above computation is shown in panel (G) of Fig. (9.1). The circulatory streamlines are clearly visible in both the bulk and surface flows. It is this flow pattern that advects particles from the bulk to the surface where the surface flow drives them to self-assemble at the end of the container farthest from the ground electrode. Flow streamlines due to electrohydrodynamic flows for a rectangular channel of depth $\gg H$ is shown in Fig. (9.2). The flow streamlines in this case is also similar to panel (G) of Fig. (9.1), and thus, the same phenomenon to nanosheet formation is expected to be present in both shallow and deep containers.

9.4 Conclusion

In this chapter, we theoretically explain the formation of nanosheets by studying the electrohydrodynamic flow at the air-water interface. We show that, both, tangential electric field and free surface charges are necessary for any electrohydrodynamic flow and thus for the formation of the nanosheet. The flow at the surface can be controlled by adding more electrodes at specific points on the container and also by having electrodes of different polarity. These provide exciting new directions to extend this work.

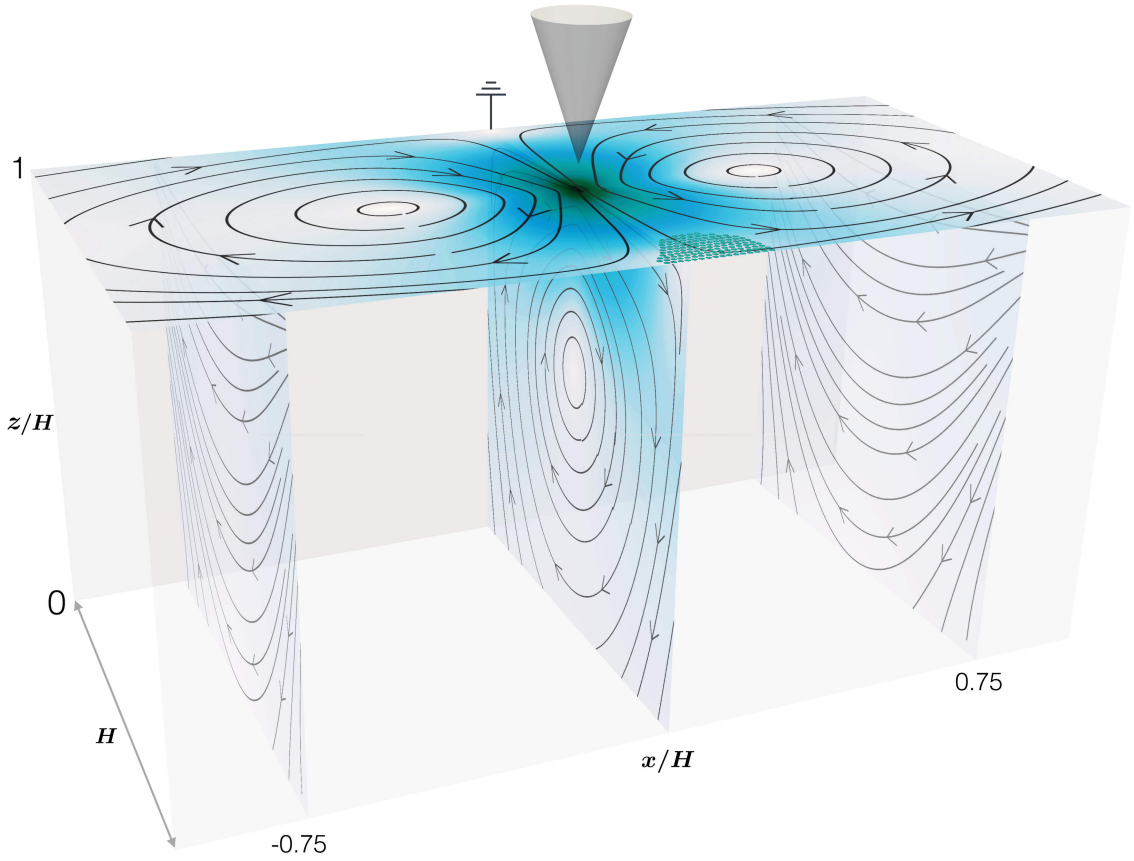

Figure 9.2: Electrohydrodynamic flow in a rectangular geometry. The bottom wall is assumed to be at depth $\gg H$. The qualitative features of the flow are similar to that in Fig. (9.1G) except the fact that the flow vanishes at the bottom of the container in Fig. (9.1G), while here the bottom is assumed to be at a higher depth.

Chapter 10

PyStokes

10.1 Introduction

In Chapter 2 and Chapter 3 of this thesis, a microscopic description of active colloidal suspensions has been derived. We have obtained the Langevin equations for active colloids in terms of mobility matrices and propulsion tensors. These mobility matrices and propulsion tensors are many-body functions of the colloidal configuration and their numerical computation is essential to simulate active colloidal suspensions To this end, we have developed a library - PyStokes - to compute these objects and to obtain Stokes flow produced by active colloidal spheres. All the computer simulations presented in this thesis are performed using PyStokes.

We now detail the organization of the chapter. A brief introduction to the library and a description of supported geometries of Stokes flow is provided in section 10.2, while examples for usage is given in section 10.3. Apart from the theory developed in the previous chapters of the thesis where the resolution of explicit fluid degrees of freedom is not needed, the library also supports an additional explicit fluid solver. This method is also based on the irreducible approach to Stokes flow and is described in detail in section 10.4. We conclude the chapter by indicating future plans for additional features.

10.2 PyStokes: Introduction

PyStokes is a Cython [200] library to simulate the motion of spherical active colloids and to compute external flow field produced by them. The development of PyStokes codebase happens on GitLab, while a stable, well-documented, free, and open-source version is available on GitHub.

The PyStokes library currently supports following geometries:

- For **unbounded domains**, the Oseen tensor has been used to compute the exterior fluid flow around colloids and their rigid body motion.

- For **fluid-fluid interfaces**, expressions of Green's functions from [201, 202] have been employed to obtain the mobility matrices and propulsion tensors, and thus compute the rigid body motion of active colloids.

- For **wall-bounded domains**, the Lorentz-Blake Green's function [203] has been used to construct flows that vanish at a plane wall and to compute the rigid body motion of colloids. For flow bounded between parallel wall, we either use a series sum of Green's function [204, 205], or the approximate solution of Liron and Mochon [204], to obtain the flow and rigid body motion.

- For **periodic domains**, O'Brien's [52] method is used to derive an unconditionally convergent expression for the flow. Ewald summation of the resulting terms is implemented to accelerate convergence using Beenakker's method [180].

The library includes all long-ranged terms for Stokes flow. Additionally, all the leading terms of polar, apolar and chiral symmetry of active slip have also been included. This ensures that we include a minimal set of coefficients to produce active translations and rotations. In the next section we provide examples of usage of the library.

10.3 PyStokes: Usage

In this section, we provide example usage of PyStokes. In the Python pseudocode below, we have simulated the motion of an active colloid using the PyStokes and PyForces library. PyForces is a library, to be used along with PyStokes, for computing body forces and torques on the colloids.

```
## Simulation of an active colloid near a no-slip wall using PyStokes
import pystokes, pyforces
import numpy as np

b, Np  = 1, 1                # radius (b) and number of colloids (Np)
T, Tp  = 128, 1024           # simulation duration and number of points
rm,re,wrm,we = 2*b,1,1*b,1   # parameters for repulsive WCA potential

# allocate memory for position (r), orientation (p),
# force (F), velocity (v) and angular velocity (o)
r,p   = np.zeros(3*Np),np.zeros(3*Np),np.zeros(3*Np)
F,v,o = np.zeros(3*Np),np.zeros(3*Np),np.zeros(3*Np),np.zeros(3*Np)

# provide an initial condition
r[2]=10; p[2]=-1;  V3t=p

# instantiate wallBounded and forceFields classes from PyStokes and PyForces
wRbm = pystokes.periodic.Flow(b, Np, eta=1.0)
ff   = pyforces.forceFields.Forces(Np)

#compute the velocity and angular velocity using PyStokes
ff.wallWCA(F,r,rm,re,wrm,we)   # force given position and parameters
wRbm.stokesletV(v, r, F)       # update velocity due to body forces
wRbm.potDipoleV(v, r, V3t)     # update velocity due to self-propulsion
wRbm.stokesletO(o, r, F)       # update angular velocity - body forces

#Complete the simulation using a suitable integrator.
```

The flow field around the colloids gives additional insights into the collective dynamics. A python pseudocode to compute the flow using PyStokes is provided below.

```
## Computation of flow at given points in 3D using PyStokes
import pystokes, pyforces
import numpy as np

b, Np  = 1, 1                 # radius (b) and number of colloids (Np)
L, Ng  = 10, 32               # length of domain and number of grid pts
rm,re,wrm,we = 2*b,1,1*b,1    # parameters for repulsive WCA potential

# allocate memory for position, orientation, force and velocity
r,p,F,v = np.zeros(3*Np),np.zeros(3*Np),np.zeros(3*Np),np.zeros(3*Np)
Nt=Ng*Ng; rt,vv = np.zeros(3*Nt), np.zeros(3*Nt)

##assign position and orientation
r[2]=10; p[2]=-1;  V3t=p

#instantiate wallBounded and forceFields classes from PyStokes and PyForces
wFlow = pystokes.periodic.Flow(b, Np, eta=1.0)
ff    = pyforces.forceFields.Forces(Np)

ff.wallWCA(F,r,rm,re,wrm,we)          # force given position and parameters
uFlow.stokesletV(vv, rt, r, F)        # update flow - body forces
uFlow.potDipoleV(vv, rt, r, V3t)      # update flow - self-propulsion

# Visualize the flow using any desired software.
```

It should be noted that we can simulate active colloids and compute flow field in distinct geometries just by changing the class instantiation. The rest of the code remains same for a given model. This allows us to systematically explore the role of boundaries in the flow for a given model. In Fig. (10.1), we plot the snapshots of the configuration and flow field around an active colloid self-propelling towards a plane wall at four different instants from a simulation using PyStokes.

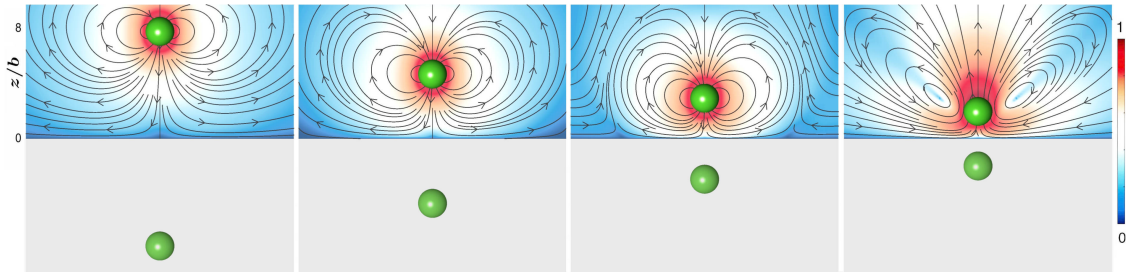

Figure 10.1: Computation of rigid body motion and flow of an active colloid self-propelling towards a plane wall. Four snapshots at increasing times are shown. The streamlines are shown in the domain of the flow while the image of the colloid is shown with respect to the wall at $z = 0$. The colorbar represents the normalized logarithm of the flow speed.

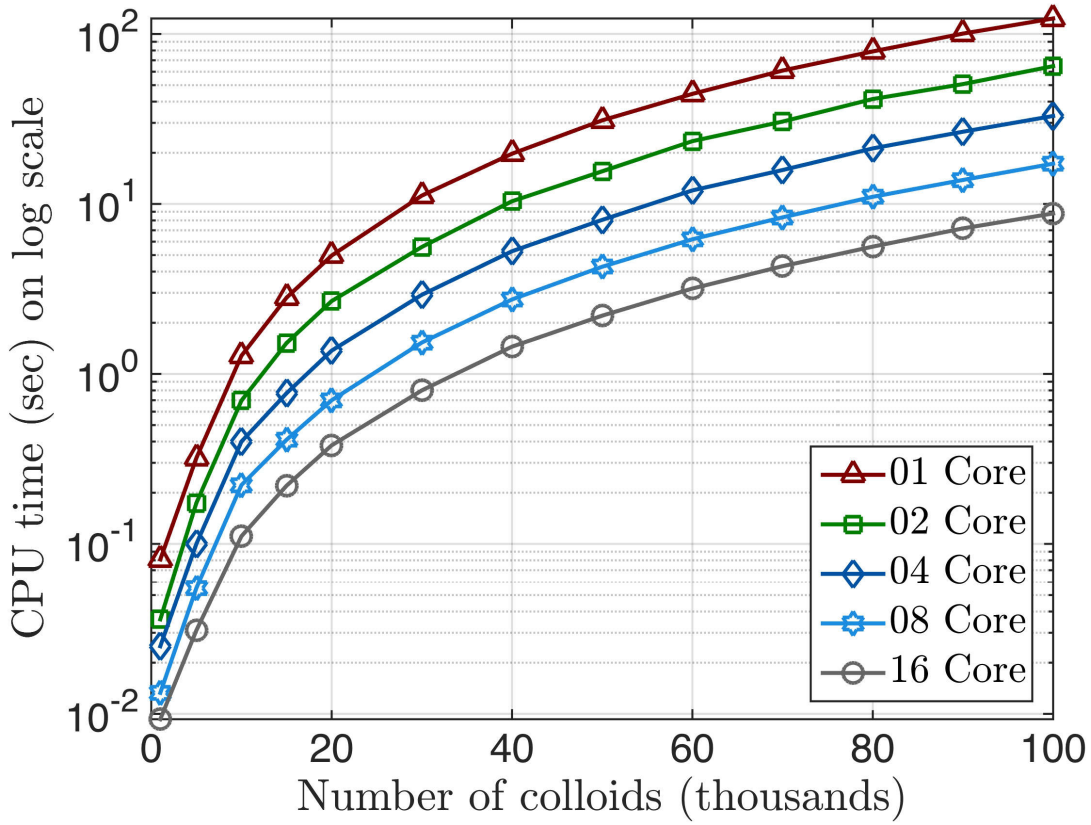

Figure 10.2: Benchmarks to numerically compute rigid body motion due to the propulsion tensor $\pi^{(T,3t)}$ in the unbounded geometry of Stokes flow, on a 16-core machine, using PyStokes. The present implementation shows a linear scaling with the number of cores, while it scales quadratically with number of particles when the matrix-vector products are computed directly.

10.4 Mollified irreducible multipole approach

In addition to the implementations of theory presented in this thesis, there is an additional application in PyStokes on the mollified irreducible multipole approach (MIMA). MIMA is a Stokes solver which resolves the fluid degrees of freedom [13, 132, 150, 151, 206]. We use the single-layer form of the boundary integral representation of Stokes flow [45, 81] to obtain the exterior fluid flow using the MIMA as

$$\boldsymbol{v}(\boldsymbol{r}) = -\int \mathbf{G}(\boldsymbol{r}) \cdot \boldsymbol{q}(\boldsymbol{r})\, d\boldsymbol{r}. \tag{10.1}$$

Here $\boldsymbol{q}$ is the single layer density. The integral is then evaluated following Eq. (A.3) to obtain

$$\boldsymbol{v}(\boldsymbol{r}) = -\sum_{l=1}^{\infty} b^{l-1} \left(1 + \frac{b^2}{4(l-1)+6}\nabla^2\right) \boldsymbol{\nabla}^{(l-1)} \mathbf{G}(\boldsymbol{r}) \cdot \mathbf{Q}^{(l)}, \tag{10.2}$$

where $\mathbf{Q}^{(l)}$ are the irreducible tensorial harmonic coefficients of the effective single layer density [45, 81]. Using the definition of Fourier transform in Appendix A.2, the expression for the flow for $r \geq b$ becomes

$$\boldsymbol{v}(\boldsymbol{r}) = -\frac{1}{(2\pi)^3} \int e^{i\boldsymbol{k}\cdot\boldsymbol{r}}\, \mathbf{G}(\boldsymbol{k}) \cdot \mathbf{f}(\boldsymbol{k})\, d^3\boldsymbol{k}, \tag{10.3a}$$

$$\boldsymbol{f}(\boldsymbol{k}) = -\sum_{l=1}^{\infty} b^{l-1} \left(1 - \frac{b^2}{4(l-1)}k^2\right) (-i\boldsymbol{k})^{(l-1)} \cdot \mathbf{Q}^{(l)}. \tag{10.3b}$$

Here $\boldsymbol{f}(\boldsymbol{k})$ is the effective force per unit area in the Fourier space. This effective force density is, then, given by the Dirac delta distribution in the coordinate space as

$$\boldsymbol{f}(\boldsymbol{r}) = -\sum_{l=1}^{\infty} b^{l-1} \left(1 + \frac{b^2}{4(l-1)}\nabla^2\right) \boldsymbol{\nabla}^{(l-1)} \delta(\boldsymbol{r}) \cdot \mathbf{Q}^{(l)}. \tag{10.4}$$

The above expression of the force density satisfies the Stokes equation $-\nabla p + \eta\nabla^2\boldsymbol{v} = \boldsymbol{f}(\boldsymbol{r})$ and produces the correct exterior fluid flow. We now make a smoothed approximation to the Dirac delta distribution by replacing it with a mollifier $M_l(\boldsymbol{r})$ to obtain the mollified

force density

$$\boldsymbol{f}^M(\boldsymbol{r}) = -\sum_{l=1}^{\infty} b^{l-1}\left(1 + \frac{b^2}{4(l-1)+6}\nabla^2\right)\boldsymbol{\nabla}^{(l-1)} M_l(\boldsymbol{r}) \cdot \mathbf{Q}^{(l)}.$$

The final expression of the mollified exterior flow is then obtained as

$$\boldsymbol{v}^M(\boldsymbol{r}) = \frac{1}{(2\pi)^3}\sum_{l=1}^{\infty}\int e^{i\boldsymbol{k}\cdot\boldsymbol{r}}\boldsymbol{v}^M(\boldsymbol{k})\,d\boldsymbol{k}, \tag{10.5a}$$

$$\boldsymbol{v}^M(\boldsymbol{k}) = b^{l-1}\left(\left(1 - \frac{b^2}{4(l-1)+6}k^2\right)(-i\boldsymbol{k})^{(l-1)}\, M_l(\boldsymbol{k})\,\mathbf{G}(\boldsymbol{k})\cdot\mathbf{Q}^{(l)}\right). \tag{10.5b}$$

The above expression for the fluid flow is very convenient for discretization and allows the solution using Fourier transforms. We ensure that $M_l(\mathbf{k}) \to 1$ as $kb \to 0$ such that the original and mollified flow fields agree optimally. Additionally, we assume the mollifier is isotropic $M_l(\mathbf{k}) = M_l(k^2)$. The flow due to irreducible $l\sigma$ modes is obtained by projecting-out the irreducible modes of $\mathbf{Q}^{(l)}$ using Eq. (2.4). The rigid body motion of the colloids is computed by interpolating the flow at their locations.

10.5 Conclusion

In this chapter, we have provided a brief description of our homegrown library PyStokes. The library performs fast and efficient evaluation of Stokes flow with a user-friendly front-end. The library scales linearly with the number of cores, while it takes an $O(N^2)$ computational effort to compute rigid body motion due to a propulsion tensor for an N colloids system when matrix-vector products are computed directly, as shown in Fig. (10.2). Thus, with current many-core architectures, a dynamic simulation of about $N \sim 10^5$ is possible. For larger number of particles, accelerated summation methods are desirable, which can reduce the cost to $O(N \log N)$ [93, 94] or even $O(N)$ [76, 95, 96]. This can be implemented in the present numerical architecture as an improvement over the direct kernel sum, while rest of the structure of the library remains same.

Chapter 11

Conclusions

In this thesis, we have developed a formalism for studying the hydrodynamic interaction between active colloids. This formalism does not need to resolve the explicit fluid degrees of freedom and conserves momentum in both the bulk fluid and at the boundaries. To this end, we have used the boundary-domain integral representation of the Stokes flow to derive a complete expression for the force per unit area on the surface of active colloids. The expression is obtained by expanding the boundary fields, force per unit area and active slip, in the tensorial spherical harmonics and solving a linear system of equations. The solution is best expressed as an infinite set of linear relations - generalized Stokes laws - between the coefficients of the force per unit and the slip (Chapter 2). The linear relations between the coefficients of the force per unit area and the slip is given in terms of generalized friction tensors, which are many-body functions of the colloidal configuration. We have obtained explicit forms of the generalized friction tensors in terms of a Green's function of Stokes equation using the Jacobi iterative method.

The generalized Stokes laws are then used to derive explicit expressions for hydrodynamic forces, torques on active colloids. The expression for the forces and torques have been used to derive Langevin equations for active colloids in Chapter 3. The Langevin equations are obtained in terms of mobility matrices and propulsion tensors. The mobility

matrices are familiar from the theory of passive suspensions [56, 57], while the propulsion tensor are newly introduced [10]. In contrast to only four mobility matrices for passive colloids, there is an infinite number of propulsion tensors, which account for rich and diverse phenomena in active colloidal suspensions with no analogue in passive suspensions. The Langevin equations have been implemented in a numerical library for numerical simulations of experimentally realizable situation to derive testable predictions. A summary of main theoretical and numerical results of the thesis is given Table (11.1) and (11.2) respectively.

In Chapter 4 we have shown that the collective dynamics of active colloids in the unbounded geometry of Stokes flow is determined by the interplay of the activity and the external potential confining them. We have demonstrated the formation of orbits in a system of two harmonically trapped polar active colloids by studying the balance of one-body forces and two-body torques [10]. These individual orbits coalesce to produce sustained convection-rolls, the so-called self-assembled pump [13]. Next, we studied the synchronization of active colloids in a 2D lattice of harmonic traps and shown that the entropy production is related to the synchronization [11]. In a system of apolar active colloids in a spherical confinement, we have found that the collective dynamics is determined by the contractile or the extensile nature of colloids.

In our simulations, we have also found that the emergent phenomena in active colloidal suspensions are determined by the boundaries in the flow. For example, we have shown in Chapter 5 that distortion of fluid flow by a plane wall leads to long-ranged attractive forces between active colloids, which drives their crystallization. Similarly, in Chapter 7, we have shown that strikingly new phenomena appear in identical systems of active colloids by changing the boundaries of the flow alone. This difference in the emergent behaviour is understood by studying the dissipative active forces and torque on the colloids, which depend on the boundaries of the flow. Thus we have elucidated the role of boundaries in determining the emergent behaviour of active colloids.

Section	Topic
2.2	Generalized Stokes laws
2.3.1	Rigid body traction
2.3.2	Active traction
2.4	Flow, pressure, and stress in the fluid
2.5	Entropy production in the fluid
2.6	Active suspension stress
3.3	Brownian traction
3.4	Langevin descriptions of active colloids
5.5	Harmonic excitations of an active crystal
8.2	Smoluchowski descriptions of active colloids
8.3	Hamilton-Jacobi method for the distribution function
10.4	Mollified irreducible multipole approach

Table 11.1: Summary of main theoretical results of the thesis.

Study of active colloids in periodic geometries of Stokes flow has been considered in Chapter 6. In this chapter, we have first determined the effective speed of a simple cubic lattice of self-propelling colloids, which varies linearly with the volume fraction. We have, then, studied a Crowley-like instability in a layer of polar active colloids. In Chapter 8, we describe the mechanism for the formation of nanosheets at the air-water interface by studying the electrohydrodynamic flow in a rectangular geometry. Smoluchowski description of active colloids has been pursued in Chapter 9 and a Hamilton-Jacobi approach has been employed to obtain a solution for the distribution function. A brief introduction to our numerical library PyStokes is given in Chapter 10, along with some representative examples and benchmarks.

Section	Model	Emergent behaviour
4.2	Polar active colloids ($l\sigma = 2s, 3t$) in a harmonic trap Geometry: unbounded flow	Formation of self-assembled pump
4.3	Polar active colloids ($l\sigma = 2s, 3t$) in 2D lattice of harmonic traps Geometry: unbounded flow	Synchronization of the colloids is related to entropy production
4.4	Apolar active colloids ($l\sigma = 2s$) in a spherical confinement Geometry: unbounded flow	Collective dynamics differs for contractile and extensile apolar colloids
5.3	Active colloids ($l\sigma = 2s, 3t, 3a, 4a$) near a wall Geometry: flow bounded by a plane wall	Crystallization of active colloids
6.3	Polar active colloids ($l\sigma = 3t$) Geometry: periodic flow	Crowley-like instability of a lattice of colloids
7.2	Active colloids ($l\sigma = 2s, 3t, 4t$) Geometry: parallel wall ($H \sim b$)	Transient lines of active colloids
7.2	Active colloids ($l\sigma = 2s, 3t, 4t$) Geometry: parallel wall ($H \sim 10b$)	Long-lived lines of active colloids
7.2	Active colloids ($l\sigma = 2s, 3t, 4t$) Geometry: plane wall	Vortex-stabilized crystal of active colloids
7.2	Active colloids ($l\sigma = 2s, 3t, 4t$) Geometry: plane surface	Two-dimensional crystal of active colloids
9.3	Nanoparticles in a tangential electric field Geometry: rectangular channel	Formation of a nanosheet on the channel surface

Table 11.2: Summary of main numerical results of the thesis.

The theory developed in this thesis assumes that all the non-hydrodynamic parts of the problem, determining the active slip, has been solved separately. The slip mechanism for synthetic active colloids [4] is phoretic, and at high Péclet number, we need to solve for advection and diffusion simultaneously. The study in this thesis can be extended to study both the hydrodynamic and non-hydrodynamic part using boundary integral representation of respective problems. The study can also be extended to study the effect of shape anisotropy in determining the fluid flow and collective motion in an active suspension. The formalism can also be applied to study fluctuations in suspensions of active polymers [130, 132, 133, 177, 207, 208], membranes, etc.

The thesis focuses more on the deterministic parts of the problem, though the stochastic equations have been presented. In a future work, we will explore the stochastic aspects more fully [189, 209], using the Langevin and Smoluchowski descriptions derived in this thesis. In particular, renormalization group ideas applied to different scales, for example, at microscopically scale there is no detailed balance in active matter, but the coarse-grained equations of motions [33, 36, 148, 210] may still show emergent detailed balance. Though we have developed the formalism for active systems, the results are equally applicable to driven systems in the limit of zero activity, and in the presence of external drive. Thus, the theoretical techniques and numerical tools of this thesis provide a broader scope for further studies in the field of nonequilibrium statistical physics.

Appendix A

Appendices

In the initial chapters of this thesis, we have obtained a complete microscopy theory of active colloidal suspensions by using the boundary-domain integral representation of Stokes equation. The results are obtained in terms of boundary integrals and linear system of equations. In this chapter, we provide the details of the evaluation of the integrals and the solution of the linear system of equations.

We now detail the organization of the appendices. In section (A.1), we derive the boundary-domain integral representation of the Stokes equation. A comparison of the boundary-domain representation of the Stokes equation and the Laplace equation is also shown. In section (A.2), we write a general expression of the Green's functions of Stokes flow. We have also given a list of Green's functions used in this thesis and provide a derivation of their Fourier transforms. Detailed derivations of the boundary integrals is given in section (A.3.) We also derive explicit expressions of the matrix elements of the linear system of active colloidal suspensions in this section. Using the explicit forms of the expression derived in section (A.3), we provide the iterative Jacobi solution of generalized friction tensors in section (A.4). The appendix also includes some details on the implementation of these results to perform numerical simulations.

A.1 Derivation of boundary-domain integral equation

For completeness, we now outline the main steps in the derivation of the boundary-domain integral representation of Stokes flow. Consider two solenoidal vector fields $\boldsymbol{v}_1$ and $\boldsymbol{v}_2$, such that $\nabla \cdot \boldsymbol{v}_1 = 0$ and $\nabla \cdot \boldsymbol{v}_2 = 0$. Introduce two scalar fields p_1 and p_2 and define

$$\boldsymbol{\sigma}_1(\boldsymbol{v}_1, p_1) = -p_1 \boldsymbol{I} + \eta\left(\nabla \boldsymbol{v}_1 + \nabla \boldsymbol{v}_1^T\right),$$
$$\boldsymbol{\sigma}_2(\boldsymbol{v}_2, p_2) = -p_2 \boldsymbol{I} + \eta\left(\nabla \boldsymbol{v}_2 + \nabla \boldsymbol{v}_2^T\right).$$

The solenoidal property of the vector fields gives the following identity

$$\boldsymbol{\nabla} \cdot (\boldsymbol{\sigma}_1 \cdot \boldsymbol{v}_2) = \left(-\boldsymbol{\nabla} p_1 + \eta \nabla^2 \boldsymbol{v}_1\right) \cdot \boldsymbol{v}_2,$$
$$\boldsymbol{\nabla} \cdot (\boldsymbol{\sigma}_2 \cdot \boldsymbol{v}_1) = \left(-\boldsymbol{\nabla} p_2 + \eta \nabla^2 \boldsymbol{v}_2\right) \cdot \boldsymbol{v}_1.$$

Subtracting the above two equations we get

$$\boldsymbol{\nabla} \cdot (\boldsymbol{\sigma}_1 \cdot \boldsymbol{v}_2 - \boldsymbol{\sigma}_2 \cdot \boldsymbol{v}_1) = \left(-\boldsymbol{\nabla} p_1 + \eta \nabla^2 \boldsymbol{v}_1\right) \cdot \boldsymbol{v}_2 - \left(-\boldsymbol{\nabla} p_2 + \eta \nabla^2 \boldsymbol{v}_2\right) \cdot \boldsymbol{v}_1.$$

Integrating this result over the entire volume V and using the divergence theorem gives

$$\int \left[\left(-\boldsymbol{\nabla} p_1 + \eta \nabla^2 \boldsymbol{v}_1\right) \cdot \boldsymbol{v}_2 - \left(-\boldsymbol{\nabla} p_2 + \eta \nabla^2 \boldsymbol{v}_2\right) \cdot \boldsymbol{v}_1\right] \mathrm{d}V = -\int (\boldsymbol{\sigma}_1 \cdot \boldsymbol{v}_2 - \boldsymbol{\sigma}_2 \cdot \boldsymbol{v}_1) \cdot \hat{\boldsymbol{\rho}}\, d\mathrm{S}_i.$$

Here S_i are the surfaces of the spheres in the volume V and we vector fields $\boldsymbol{v}_1$ and $\boldsymbol{v}_2$ vanish at any other boundary in the volume of the fluid.

We now obtain integral representation for the pair $(\boldsymbol{v}_1, p_1)$ that satisfies the fluctuating Stokes equation $\boldsymbol{\nabla} \cdot \boldsymbol{\sigma}_1 = -\nabla p_1 + \eta \nabla^2 \boldsymbol{v}_1 = -\boldsymbol{\xi}$, where $\boldsymbol{\xi}$ is the thermal force acting on the fluid. To do so, we chose $(\boldsymbol{v}_2, p_2)$ to be a fundamental solution of the Stokes equation satisfying $\boldsymbol{\nabla} \cdot \boldsymbol{\sigma}_2 = -\nabla p_2 + \eta \nabla^2 \boldsymbol{v}_2 = -\boldsymbol{g}\delta(\boldsymbol{r} - \boldsymbol{r}')$, where $\boldsymbol{g}$ is an arbitrary constant [81]. Using this, the second term of the volume integral is completed to give $\boldsymbol{v}_1(\boldsymbol{r})$. The first term

of the volume integral gives contributions from Brownian forces. The surface integrals now contain the Green's function of Stokes flow and its derivatives (see Eq. (2.10)). The boundary-domain integral representation of the Stokes equation is then

$$v_\alpha(\boldsymbol{r}) = \int G_{\alpha\beta}(\boldsymbol{r},\boldsymbol{r}')\xi_\beta(\boldsymbol{r}')\,dV' - \int \Big(G_{\alpha\beta}(\boldsymbol{r},\boldsymbol{r}_i)f_\beta(\boldsymbol{r}_i) - K_{\beta\alpha\gamma}(\boldsymbol{r},\boldsymbol{r}_i)\hat{\rho}_\gamma v_\beta(\boldsymbol{r}_i)\Big)\,d\mathrm{S}_i. \tag{A.1}$$

Equating the above expression for the bulk fluid velocity to the boundary condition and evaluating the third integral as a principal value leads to an integral equation on the colloidal boundaries as given in Eq. (3.4). It should also be noted that the above expression reduces to Eq. (2.9a) in the limit of vanishing thermal traction.

Boundary-domain integral equation for electrostatics

The electrostatic problem of computing the potential due to N spheres has a similar form as that of Stokes equation. Here, the potential is determined by Poisson's equation,$\nabla^2\psi = \tilde{\rho}/\tilde{\epsilon}$, where $\tilde{\rho}$ is charge density and $\tilde{\epsilon}$ is the permittivity, whose integral representation is

$$\psi(\boldsymbol{r}) = \int \tilde{G}(\boldsymbol{r},\boldsymbol{r}')\,\tilde{\rho}(\boldsymbol{r}')\,\mathrm{d}V' - \int \Big(\tilde{G}(\boldsymbol{r},\boldsymbol{r}_i)\,\tilde{\sigma}(\boldsymbol{r}_i) - \tilde{K}_\alpha(\boldsymbol{r},\boldsymbol{r}_i)\hat{\rho}_\alpha\psi(\boldsymbol{r}_j)\Big)\,d\mathrm{S}_i, \tag{A.2}$$

where $\tilde{G}(\boldsymbol{r}) = \frac{1}{4\pi\tilde{\epsilon}r}$, $\tilde{K}_\alpha(\boldsymbol{r}) = \tilde{\epsilon}\nabla_\alpha\tilde{G}$, and $\tilde{\sigma}$ is surface charge density [211]. Thus, there is a close analogy between microhydrodynamics and electrostatics, with the correspondence

$$\boldsymbol{v} \leftrightarrow \psi, \qquad \boldsymbol{f} \leftrightarrow \tilde{\sigma}, \qquad \eta \leftrightarrow \tilde{\epsilon}. \tag{A.3}$$

The analogy is not wholly complete since $\tilde{K}_\alpha$ is the normal derivative of the Green's function of the Laplace equation, while $K_{\beta\alpha\gamma}$ is the sum of derivatives of the Green's function of the Stokes equation and the pressure Green's function. However, it does provide a heuristic for understanding microhydrodynamic phenomena guided by electrostatic analogies. This analogy is used in the notation "single layer" and "double layer" for the second and third terms of the integral representation of Stokes equation in Eq. (A.1).

A.2 The Green's functions of Stokes equation

A Green's function of Stokes equation satisfies Eq. (2.10) of Chapter 2, and thus, represents the solution of the singularly forced Stokes equation and the continuity equation. We write the Green's function for arbitrary geometry of the Stokes flow as a sum

$$G_{\alpha\beta}(\boldsymbol{R}', \boldsymbol{R}) = G^{\mathrm{o}}_{\alpha\beta}(\boldsymbol{R}' - \boldsymbol{R}) + G^{*}_{\alpha\beta}(\boldsymbol{R}', \boldsymbol{R}^{*}), \tag{A.4}$$

where $\mathbf{G}^{\mathrm{o}}(\boldsymbol{r}) = (\nabla^2 \boldsymbol{I} - \boldsymbol{\nabla}\boldsymbol{\nabla})(r/8\pi\eta)$ is the Oseen tensor and $G^{*}_{\alpha\beta}(\boldsymbol{R}', \boldsymbol{R}^{*})$ is the correction necessary to satisfy the boundary condition. A variety of Green's functions can be expressed in this form, including those for flow between parallel walls and in periodic domains. The above choice can also be written in terms of a scalar function ϕ as

$$\mathbf{G}(\boldsymbol{R}', \boldsymbol{R}) = (\nabla^2 \boldsymbol{I} - \boldsymbol{\nabla}\boldsymbol{\nabla})\,\Phi(\boldsymbol{R}', \boldsymbol{R}). \tag{A.5}$$

Here Φ is a biharmonic field such that the corresponding Green's function satisfies the Stokes equation [212]. In general $\Phi = \frac{r}{8\pi\eta} + \Phi^{*}$, where the additional term Φ^{*} ensures that the boundary conditions are satisfied. For an unbounded flow $\Phi^{*} = 0$. This choice would be convenient to obtain Green's function in a complicated geometry as one need to solve for a scalar Φ and not a tensor. A list of Green's functions, corresponding to generic geometries of Stokes flow, is given in Table (A.1). In addition, we can obtain an approximate expression for a Green's function of a complex geometry, with more than one boundary in the flow, by the use of a linear combination of these generic Green's functions.

Explicit expression for the Green's function of fluid pressure and fluid stress follow the Green's function of fluid velocity using Eq. (2.10). These expressions of the Green's function are then used to obtain the generalized friction tensors, mobility matrices and propulsion tensors in the corresponding geometries of Stokes flow. Derivations of the explicit expressions of these quantities are given in the following appendices.

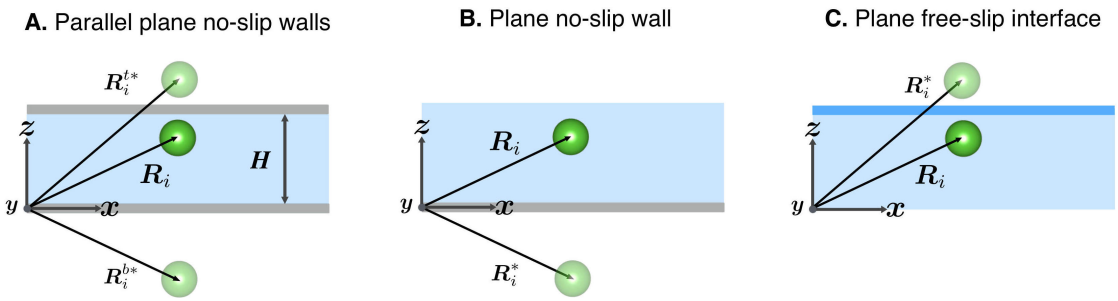

Figure A.1: The coordinate system used to describe the i-th spherical active and its image system in the following geometries of Stokes flow: **A**. parallel no-slip plane walls, **B**. a plane no-slip wall, and **C**. a plane free-slip surface.

	Green's function
Unbounded fluid	$G^{\mathrm{o}}_{\alpha\beta}(\boldsymbol{R}_i-\boldsymbol{R}_j)=\frac{1}{8\pi\eta}\left(\nabla^2\delta_{\alpha\beta}-\nabla_\alpha\nabla_\beta\right)r_{ij}.$
Plane interface (fluid-gas)	$G^{\mathrm{i}}_{\alpha\beta}(\boldsymbol{R}_i,\boldsymbol{R}_j)=G^{\mathrm{o}}_{\alpha\beta}(\boldsymbol{r}_{ij})+(\delta_{\beta\rho}\delta_{\rho\gamma}-\delta_{\beta3}\delta_{3\gamma})G^{\mathrm{o}}_{\alpha\gamma}(\boldsymbol{r}^*_{ij}).$
Plane interface (fluid-fluid)	$G^{\mathrm{f}}_{\alpha\beta}(\boldsymbol{R}_i,\boldsymbol{R}_j)=G^{\mathrm{o}}_{\alpha\beta}(\boldsymbol{r}_{ij})+\mathcal{M}^F_{\beta\gamma}G^{\mathrm{o}}_{\alpha\gamma}(\boldsymbol{r}^*_{ij})-$ $2h\frac{\lambda}{1+\lambda}\nabla_{r^*_{ij}}G^{\mathrm{o}}_{\alpha3}(\boldsymbol{r}^*_{ij})\mathcal{M}^F_{\beta\gamma}+h^2\frac{\lambda}{1+\lambda}\nabla^2_{r^*_{ij}}G^{\mathrm{o}}_{\alpha\beta}(\boldsymbol{r}^*_{ij})\mathcal{M}^F_{\beta\gamma}.$
Plane no-slip wall	$G^{\mathrm{w}}_{\alpha\beta}(\boldsymbol{R}_i,\boldsymbol{R}_j)=$ $G^{\mathrm{o}}_{\alpha\beta}(\boldsymbol{r}_{ij})-G^{\mathrm{o}}_{\alpha\beta}(\boldsymbol{r}^*_{ij})-2h\nabla_{r^*_{ij}}G^{\mathrm{o}}_{\alpha3}(\boldsymbol{r}^*_{ij})\mathcal{M}_{\beta\gamma}+h^2\nabla^2_{r^*_{ij}}G^{\mathrm{o}}_{\alpha\gamma}(\boldsymbol{r}^*_{ij})\mathcal{M}_{\beta\gamma}.$
Parallel plane no-slip walls	$G^{2\mathrm{w}}_{\alpha\beta}(\boldsymbol{R}_i,\boldsymbol{R}_j)=G^{\mathrm{o}}_{\alpha\beta}(\boldsymbol{r}_{ij})+G^{*}_{\alpha\beta}(\boldsymbol{R}_i,\boldsymbol{R}^{b*}_j)+G^{*}_{\alpha\beta}(\boldsymbol{R}_i,\boldsymbol{R}^{t*}_j)+G^{\delta}_{\alpha\beta},$ $G^{2\mathrm{w}}_{\alpha\beta}(\boldsymbol{R}_i,\boldsymbol{R}_j)=\frac{3hz(H-z)(H-h)}{\pi\eta H^3}\left(\frac{\delta_{\alpha\beta}}{2r^2_{\parallel}}-\frac{r_\alpha r_\beta}{r^4_{\parallel}}\right),\qquad H\sim 2b.$

Table A.1: The Green's functions of Stokes equation for a system of two colloids at $\boldsymbol{R}_i$ and $\boldsymbol{R}_j$ respectively [201–205, 213]. Here $\boldsymbol{r}_{ij}=\boldsymbol{R}_i-\boldsymbol{R}_j$, and $\boldsymbol{r}^*_{ij}=\boldsymbol{R}_i-\boldsymbol{R}^*_j$, where $\boldsymbol{R}^*_j=\boldsymbol{\mathcal{M}}\cdot\boldsymbol{R}$ is the image of the jth colloid at a distance h from the interface/wall at $z=0$. $\boldsymbol{\mathcal{M}}=\boldsymbol{I}-2\hat{\boldsymbol{z}}\hat{\boldsymbol{z}}$, $\lambda=\eta_2/\eta_1$, $\mathcal{M}^F_{\beta\gamma}=\left(\frac{1-\lambda}{1+\lambda}\delta_{\beta\rho}\delta_{\rho\gamma}-\delta_{\beta3}\delta_{3\gamma}\right)$, where ρ takes values $1,2$. We use two distinct Green's functions for the parallel plane no-slip walls - one using a sum of Lorentz-Blake tensors, along with a correction $G^{\delta}_{\alpha\beta}$ to satisfy the boundary conditions at the two walls [205], while the other is an approximate solution, when the separation $H\sim 2b$ [204]. Here $r_{\parallel}$ is a measure of the distances in the plane parallel to the walls. The coordinate system used to describe the i-th spherical active colloid and its image system, in these geometries, is given in Fig. (A.1).

Fourier transform of the Oseen tensor

We now derive the Fourier transforms of the Green's functions of fluid velocity, pressure and stress in an unbounded domain of fluid flow

$$\mathbf{G}^{\mathrm{o}}(\boldsymbol{R}_i, \boldsymbol{R}_j) = (\boldsymbol{I}\nabla^2 - \boldsymbol{\nabla}\boldsymbol{\nabla})\frac{r_{ij}}{8\pi\eta} = \frac{1}{8\pi\eta}\left(\frac{\boldsymbol{I}}{r_{ij}} + \frac{\boldsymbol{r}_{ij}\boldsymbol{r}_{ij}}{r_{ij}^3}\right), \tag{A.6a}$$

$$\mathbf{P}^{\mathrm{o}}(\boldsymbol{R}_i, \boldsymbol{R}_j) = -\frac{1}{4\pi}\boldsymbol{\nabla}\frac{1}{r_{ij}} = \frac{1}{4\pi}\frac{\boldsymbol{r}_{ij}}{r_{ij}^3}, \tag{A.6b}$$

$$\mathbf{K}^{\mathrm{o}}(\boldsymbol{R}_i, \boldsymbol{R}_j) = -\mathbf{1}\mathbf{P}^{\mathrm{o}} + \eta\left(\boldsymbol{\nabla}\mathbf{G}^{\mathrm{o}} + (\boldsymbol{\nabla}\mathbf{G}^{\mathrm{o}})^T\right) = -\frac{3}{4\pi}\frac{\boldsymbol{r}_{ij}\boldsymbol{r}_{ij}\boldsymbol{r}_{ij}}{r_{ij}^5}. \tag{A.6c}$$

Here $\boldsymbol{r}_{ij} = \boldsymbol{R}_i - \boldsymbol{R}_j$. To proceed, we define the Fourier transform of a function $\varphi(\boldsymbol{r})$ as

$$\hat{\varphi}(\boldsymbol{k}) = \mathbb{F}[\varphi(\boldsymbol{r})] = \int \varphi(\boldsymbol{r})\, e^{-i\boldsymbol{k}\cdot\boldsymbol{r}}\, d\boldsymbol{r}, \qquad \varphi(\boldsymbol{r}) = \mathbb{F}^{-1}[\hat{\varphi}(\boldsymbol{k})] = \frac{1}{(2\pi)^3}\int \hat{\varphi}(\boldsymbol{k})\, e^{i\boldsymbol{k}\cdot\boldsymbol{r}}\, d\boldsymbol{k}. \tag{A.7}$$

From the definition of Dirac delta

$$\delta(\boldsymbol{r}) = \frac{1}{(2\pi)^3}\int e^{i\boldsymbol{k}\cdot\boldsymbol{r}}\, d\boldsymbol{k},$$

along with the fact that $\nabla^2(1/r) = -4\pi\delta(\boldsymbol{r})$ and $\nabla^2 r = 2/r$, we have

$$\mathbb{F}\left[\frac{1}{4\pi r}\right] = \frac{1}{k^2}, \qquad \mathbb{F}\left[\frac{1}{8\pi}\left(\frac{\delta_{\alpha\beta}}{r} - \frac{r_\alpha r_\beta}{r^3}\right)\right] = \frac{k_\alpha k_\beta}{k^4}.$$

The Fourier transform of the unbounded Green's function, Eq. (A.6), is then

$$\hat{G}^{\mathrm{o}}_{\alpha\beta}(\boldsymbol{k}) = \frac{\delta_{\alpha\beta} - \hat{k}_\alpha\hat{k}_\beta}{\eta k^2}, \qquad \hat{p}^{\mathrm{o}}_{\alpha}(\boldsymbol{k}) = -\frac{i}{\eta}\frac{\hat{k}_\alpha}{k}, \tag{A.8}$$

$$\hat{K}^{\mathrm{o}}_{\alpha\beta\gamma}(\boldsymbol{k}) = \frac{i}{\eta}\left[\frac{\delta_{\alpha\gamma}k_\beta}{k^2} + k_\gamma\left(\frac{\delta_{\alpha\beta} - \hat{k}_\alpha\hat{k}_\beta}{k^2}\right) + k_\alpha\left(\frac{\delta_{\beta\gamma} - \hat{k}_\beta\hat{k}_\gamma}{k^2}\right)\right] = \frac{i}{\eta}\left[\frac{\overbrace{\hat{k}_\alpha\delta_{\beta\gamma}} - 2\hat{k}_\alpha\hat{k}_\beta\hat{k}_\gamma}{k}\right]. \tag{A.9}$$

Here $i = \sqrt{-1}$ is the unit imaginary number and $\overbrace{\hat{k}_\alpha\delta_{\beta\gamma}} = \hat{k}_\alpha\delta_{\beta\gamma} + \hat{k}_\beta\delta_{\alpha\gamma} + \hat{k}_\gamma\delta_{\alpha\beta}$. Inter alia, these expressions are useful in obtaining the diagonal elements of the linear system.

Fourier transform of the Lorentz-Blake tensor

The Lorentz-Blake tensor $\mathbf{G}^{\mathrm{w}}$ is our choice of the Green's to study flow bounded by a plane wall [203, 214]. Lorentz-Blake tensor can be written in form of Eq. (A.4), as

$$G^{\mathrm{w}}_{\alpha\beta} = G^{\mathrm{o}}_{\alpha\beta}(\boldsymbol{r}_{ij}) + G^{*}_{\alpha\beta}(\boldsymbol{R}_i, \boldsymbol{R}^{*}_j) = G^{\mathrm{o}}_{\alpha\beta}(\boldsymbol{r}_{ij}) - G^{\mathrm{o}}_{\alpha\beta}(\boldsymbol{r}^{*}_{ij}) + G^{v}_{\alpha\beta}(\boldsymbol{R}_i, \boldsymbol{R}^{*}_j), \tag{A.10}$$

$$G^{v}_{\alpha\beta}(\boldsymbol{R}_i, \boldsymbol{R}^{*}_j) = \frac{1}{8\pi\eta}\left[2h^2\left(\frac{\delta_{\alpha\nu}}{r^{*3}} - \frac{3r^{*}_{\alpha}r^{*}_{\nu}}{r^{*5}}\right)\mathcal{M}_{\nu\beta} - 2h\left(\frac{r^{*}_{3}\delta_{\alpha\nu} + \delta_{\nu 3}r^{*}_{\alpha} - \delta_{\alpha 3}r^{*}_{\nu}}{r^{*3}} - \frac{3r^{*}_{\alpha}r^{*}_{\nu}r^{*}_{3}}{r^{*5}}\right)\mathcal{M}_{\nu\beta}\right].$$

The correction $G^{*}_{\alpha\beta}$ is interpreted as a sum of three images, a Stokeslet, a dipole, and a degenerate quadrupole, located at $\boldsymbol{R}^{*} = \boldsymbol{\mathcal{M}}\cdot\boldsymbol{R}$, where $\boldsymbol{\mathcal{M}} = \boldsymbol{I} - 2\hat{\boldsymbol{z}}\hat{\boldsymbol{z}}$ is the mirror operator with respect to the wall [9, 49, 215–218]. Here h is the height of the colloid from the wall.

We define the two-dimensional (2D) Fourier transform of a function $\varphi(\boldsymbol{r}) = \varphi(r_1, r_2, h)$ as

$$\hat{\varphi}(\boldsymbol{k}; h) = \mathbb{F}_{\rho}\left[\varphi(\boldsymbol{r})\right] = \int \varphi(\boldsymbol{r}) e^{-i(k_1 r_1 + k_2 r_2)}\, dr_1 dr_2, \quad \varphi(\boldsymbol{r}) = \frac{1}{(2\pi)^2}\int \hat{\varphi}(\boldsymbol{k}; h) e^{i(k_1 r_1 + k_2 r_2)}\, dk_1 dk_2.$$

Here $\boldsymbol{r}$ is a 3D vector, while $\boldsymbol{k}$ is a 2D vector defined in the plane of the transform (or the wall). The 2D Fourier transform of $G^{v}_{\alpha\beta}$, last term of Eq. (A.10), is then [203]

$$\hat{G}^{v}_{\alpha\beta}(\boldsymbol{k}; h) = \frac{he^{-2kh}}{2\eta k}\left[ik_{\mu}(\delta_{\alpha 3}\delta_{\beta\mu} + \delta_{\beta 3}\delta_{\alpha\mu}) + h\Big(ikk_{\mu}\{\delta_{\alpha 3}\delta_{\beta\mu} - \delta_{\beta 3}\delta_{\alpha\mu}\} - k_{\mu}k_{\nu}\delta_{\alpha\mu}\delta_{\beta\nu} - \delta_{\alpha 3}\delta_{\beta 3}k^2\Big)\right]$$

where μ and ν take values $1, 2$. We now use the following relation

$$\mathbb{F}_{\rho}\left[\frac{1}{2\pi r}\right] = \frac{e^{-kh}}{k},$$

and its appropriate derivatives to obtain the transform of the remaining terms in Eq. (A.10). The 2D Fourier transform of the Lorentz-Blake tensor is then, with $\mathcal{K} = 1 - e^{-2kh}$,

$$\hat{\mathbf{G}}^{\mathrm{w}} = \hat{\mathbf{G}}^{v} + \frac{1}{4\eta k^3}\begin{pmatrix} \mathcal{K}k_2^2 + 2hkk_1^2e^{-2kh} & -\mathcal{K}k_1k_2 - 2hkk_1k_2e^{-2kh} & -i2hk^2k_1e^{-2kh} \\ -\mathcal{K}k_1k_2 - 2hkk_1k_2e^{-2kh} & \mathcal{K}k_1^2 + 2hkk_2^2e^{-2kh} & -i2hk^2k_2e^{-2kh} \\ -i2hk^2k_1e^{-2kh} & -i2hk^2k_1e^{-2kh} & \mathcal{K}k^2 - 2hk^3e^{-2kh} \end{pmatrix}.$$

A.3 Evaluation of boundary integrals and matrix elements

In this section, we evaluate the boundary integrals of Chapter 2. The boundary integrals can be computed exactly for spherical active colloids by expanding the boundary fields in terms of tensorial spherical harmonics $\mathbf{Y}^{(l)}(\hat{\boldsymbol{\rho}}_i)$. They are defined as [71, 72]

$$Y^{(l)}_{\alpha_1\alpha_2\ldots\alpha_l}(\hat{\boldsymbol{\rho}}) = (-1)^l \rho^{l+1} \nabla_{\alpha_1} \ldots \nabla_{\alpha_l} \rho^{-1}, \tag{A.11}$$

$$Y^{(0)} = 1,\ Y^{(1)}_{\alpha} = \hat{\rho}_\alpha,\ Y^{(2)}_{\alpha\beta} = \left(\hat{\rho}_\alpha\hat{\rho}_\beta - \tfrac{\delta_{\alpha\beta}}{3}\right),\ Y^{(3)}_{\alpha\beta\gamma} = \left(\hat{\rho}_\alpha\hat{\rho}_\beta\hat{\rho}_\gamma - \tfrac{1}{5}[\hat{\rho}_\alpha\delta_{\beta\gamma} + \hat{\rho}_\beta\delta_{\alpha\gamma} + \hat{\rho}_\gamma\delta_{\alpha\beta}]\right).$$

These are orthogonal basis function on the surface of a sphere

$$\frac{1}{4\pi b^2}\int \mathbf{Y}^{(l)}(\hat{\boldsymbol{\rho}})\,\mathbf{Y}^{(l')}(\hat{\boldsymbol{\rho}})\,d\mathrm{S} = \delta_{ll'}\,\frac{l!\,(2l-1)!!}{(2l+1)}\Delta^{(l)}. \tag{A.12}$$

We expand the traction and slip in this basis, see Eq. (2.3). The orthogonality of the basis functions can be used to obtain the expansion coefficients in terms of surface integrals of traction and slip as [57]

$$\mathbf{F}^{(l)}_i = \frac{1}{(l-1)!(2l-3)!!}\int \boldsymbol{f}(\boldsymbol{R}_i+\boldsymbol{\rho}_i)\mathbf{Y}^{(l-1)}(\hat{\boldsymbol{\rho}}_i)d\mathrm{S}_i, \tag{A.13a}$$

$$\mathbf{V}^{(l)}_i = \frac{2l-1}{4\pi b^2}\int \boldsymbol{v}^{\mathcal{A}}(\boldsymbol{R}_i+\boldsymbol{\rho}_i)\mathbf{Y}^{(l-1)}(\hat{\boldsymbol{\rho}}_i)d\mathrm{S}_i. \tag{A.13b}$$

The coefficients of the traction and velocity are tensors of rank l and can be written as irreducible tensor of rank l, $l-1$ and $l-2$ [10]. The decomposition of traction and slip coefficients is given as [10, 77, 219]

$$\mathbf{F}^{(l)}_i = \mathbf{F}^{(ls)}_i - \frac{l-1}{l}\boldsymbol{\Delta}^{(l-1)}\cdot(\boldsymbol{\varepsilon}\cdot\mathbf{F}^{(la)}_i) + \frac{l(l-1)}{2(2l-1)}\boldsymbol{\Delta}^{(l-1)}\cdot(\boldsymbol{\delta}\mathbf{F}^{(lt)}_i), \tag{A.14a}$$

$$\mathbf{V}^{(l)}_i = \mathbf{V}^{(ls)}_i - \frac{l-1}{l}\boldsymbol{\Delta}^{(l-1)}\cdot(\boldsymbol{\varepsilon}\cdot\mathbf{V}^{(la)}_i) + \frac{l(l-1)}{2(2l-1)}\boldsymbol{\Delta}^{(l-1)}\cdot(\boldsymbol{\delta}\mathbf{V}^{(lt)}_i). \tag{A.14b}$$

The corresponding relations to obtain $l\sigma$ modes from the lth coefficient of the traction and the slip respectively is given in Eq. (2.4).

Evaluation of boundary integrals for fluid flow, pressure and stress

With these informations, we proceed to solve the boundary integrals of Eq. (2.27). The key idea in evaluating the boundary integrals is to Taylor expand the Green's function about the center of the sphere, and express the l-th degree polynomial of the radius vector in terms of tensorial spherical harmonics. Orthogonality of the tensorial spherical harmonics and biharmonicity of the Green's function reduces this infinite number of terms in the Taylor series to exactly two. To show these steps explicitly, the Taylor expansion is

$$\mathbf{G}(\boldsymbol{r}, \boldsymbol{R}+\boldsymbol{\rho}) = \sum_{l=1}^{\infty} \frac{1}{(l-1)!} (\boldsymbol{\rho}\cdot\boldsymbol{\nabla})^{(l-1)} \mathbf{G}(\boldsymbol{r}, \boldsymbol{R}+\boldsymbol{\rho})\Big|_{\boldsymbol{\rho}=0}. \tag{A.15}$$

We now consider the expression $(\boldsymbol{\rho}\cdot\boldsymbol{\nabla})^{(l-1)} = (\rho_{\alpha_1}\rho_{\alpha_2}\rho_{\alpha_3}\cdots\rho_{\alpha_{l-1}})(\nabla_{\alpha_1}\nabla_{\alpha_2}\nabla_{\alpha_3}\cdots\nabla_{\alpha_{l-1}})$, where we note that $(\rho_{\alpha_1}\rho_{\alpha_2}\rho_{\alpha_3}\cdots\rho_{\alpha_{l-1}})$ is not in its irreducible form. Now to make use of the orthogonality of tensorial spherical harmonics, we write $\boldsymbol{\rho}^{(l)}$ as [56]

$$\rho_{\alpha_1}\rho_{\alpha_2}\cdots\rho_{\alpha_{l+1}} = b^{l-1}\frac{Y^{(l-1)}_{\alpha_1\alpha_2\cdots\alpha_{l+1}}}{(2l-3)!!} + \frac{b^{l-1}}{2l-3}\sum_{\alpha_j\alpha_k\text{pairs}} \delta_{\alpha_j\alpha_k}\frac{Y^{(l-3)}_{\alpha_1\alpha_2\cdots\alpha_{j-1}\alpha_{j+1}\cdots\alpha_{k-1}\alpha_{k+1}\cdots\alpha_{l-1}}}{(2l-7)!!} + O(l-5),$$

from which it follows that

$$(\boldsymbol{\rho}\cdot\boldsymbol{\nabla})^{(l-1)} = b^{l-1}\left[\frac{\mathbf{Y}^{(l-1)}\boldsymbol{\nabla}^{(l-1)}}{(2l-3)!!} + \frac{1}{2l-3}\sum_{jk\text{ pairs}}\frac{\mathbf{Y}^{(l-3)}\boldsymbol{\nabla}^{(l-3)}\nabla^2}{(2l-7)!!} + O(l-5)\right].$$

On using the series sum of Eq. (A.15) in Eq. (2.27a), only two terms remain on integration, while all other terms go to zero either by biharmonicity or due to the orthogonality of $\mathbf{Y}^{(l)}$s. Thus, the solution of the boundary integral, Eq. (2.27a), for the fluid flow is

$$\boldsymbol{G}^{(l)}_j(\boldsymbol{r}, \boldsymbol{R}_j) = b^{l-1}\mathcal{F}^{l-1}_j \boldsymbol{\nabla}^{(l-1)}_{\boldsymbol{R}_j}\mathbf{G}(\boldsymbol{r}, \boldsymbol{R}_j), \tag{A.16a}$$

$$\mathcal{F}^l_j = \left(1 + \tfrac{b^2}{4l+6}\nabla^2_{\boldsymbol{R}_j}\right). \tag{A.16b}$$

Here the operator $\mathcal{F}^l_j$ encodes the finite size of the colloids.

Following the same method, it is straightforward to show that remaining boundary integrals of Eq. (2.27) are obtained in terms of the derivatives of respective Green's functions. Explicitly, they are

$$\boldsymbol{K}_j^{(l)}(\boldsymbol{r},\boldsymbol{R}_j) = \frac{4\pi b^{l+1}}{(l-2)!(2l-1)!!}\mathcal{F}_j^{l-1}\boldsymbol{\nabla}_{\boldsymbol{R}_j}^{(l-2)}\mathbf{K}(\boldsymbol{r},\boldsymbol{R}_j), \tag{A.17}$$

$$\boldsymbol{P}_j^{(l)}(\boldsymbol{r},\boldsymbol{R}_j) = b^{l-1}\mathcal{F}_j^{l-1}\boldsymbol{\nabla}_{\boldsymbol{R}_j}^{(l-1)}\mathbf{G}(\boldsymbol{r},\boldsymbol{R}_j). \tag{A.18}$$

$$\boldsymbol{Q}_j^{(l)}(\boldsymbol{r},\boldsymbol{R}_j) = \frac{4\pi b^{l+1}}{(l-2)!(2l-1)!!}\mathcal{F}_j^{l-1}\boldsymbol{\nabla}_{\boldsymbol{R}_j}^{(l-2)}\mathbf{Q}(\boldsymbol{r},\boldsymbol{R}_j), \tag{A.19}$$

$$\boldsymbol{S}_j^{(l)}(\boldsymbol{r},\boldsymbol{R}_j) = b^{l-1}\mathcal{F}_j^{l-1}\boldsymbol{\nabla}_{\boldsymbol{R}_j}^{(l-1)}\mathbf{S}(\boldsymbol{r},\boldsymbol{R}_j). \tag{A.20}$$

$$\boldsymbol{M}_j^{(l)}(\boldsymbol{r},\boldsymbol{R}_j) = \frac{4\pi b^{l+1}}{(l-2)!(2l-1)!!}\mathcal{F}_j^{l-1}\boldsymbol{\nabla}_{\boldsymbol{R}_j}^{(l-2)}\mathbf{M}(\boldsymbol{r},\boldsymbol{R}_j), \tag{A.21}$$

These are then used to arrive at Eq. (2.28), where tensors relating the irreducible slip modes to fluid velocity, pressure, and stress are

$$\begin{aligned}
\boldsymbol{\Pi}_j^{(l\sigma)} &= -\Big(\boldsymbol{G}_i^{(l'\sigma')}(\boldsymbol{r},\boldsymbol{R}_i)\cdot\boldsymbol{\gamma}_{ij}^{(l'\sigma',l\sigma)} - \boldsymbol{K}_j^{(l\sigma)}(\boldsymbol{r},\boldsymbol{R}_j)\Big),\\
\boldsymbol{\Lambda}_j^{(ls)} &= -\Big(\boldsymbol{P}_i^{(l's)}(\boldsymbol{r},\boldsymbol{R}_i)\cdot\boldsymbol{\gamma}_{ij}^{(l's,ls)} - \boldsymbol{Q}_j^{(ls)}(\boldsymbol{r},\boldsymbol{R}_j)\Big),\\
\boldsymbol{\Gamma}_j^{(l\sigma)} &= -\Big(\boldsymbol{S}_i^{(l'\sigma')}(\boldsymbol{r},\boldsymbol{R}_i)\cdot\boldsymbol{\gamma}_{ij}^{(l'\sigma',l\sigma)} - \boldsymbol{M}_j^{(l\sigma)}(\boldsymbol{r},\boldsymbol{R}_j)\Big)\cdot
\end{aligned}$$

Here, we use the definition of projection operators to define, $\boldsymbol{G}_i^{(l\sigma)} = \mathbf{P}^{(l\sigma)}\cdot\boldsymbol{G}_i^{(l)}$, and similar operation of projection on the boundary integrals of fluid pressure and fluid stress. It is instructive to note that only symmetric irreducible contribution to pressure survive, owing to its harmonic property. First three terms for the flow expression are $\boldsymbol{G}_i^{(l\sigma)}$ are:

$$\boldsymbol{G}_i^{(ls)} = \mathbf{G}, \qquad \boldsymbol{G}_i^{(2s)} = \tfrac{1}{2}\Big[\boldsymbol{\nabla}_i\mathbf{G} + (\boldsymbol{\nabla}_i\mathbf{G})^T\Big], \qquad \boldsymbol{G}_i^{(2a)} = \tfrac{1}{2}\boldsymbol{\nabla}_i\times\mathbf{G}.$$

The irreducible decomposition of the slip ensures that, at any order, there are at most three kinds of derivatives, which are the irreducible gradient of the Green's function (ls), its curl (la) and its Laplacian (lt).

Evaluation of matrix elements

The integrals appearing in the linear system, Eq. (2.16 and 2.20), are solved exactly to give matrix elements in terms of a Green's function of Stokes flow. A general expression of the Green's function $\mathbf{G}$ is given, in Eq. (A.4), as a sum of Oseen tensor and a correction $\mathbf{G}^*$ to satisfy the boundary condition. Explicit expression of the matrix elements are then given as [10]

$$\boldsymbol{G}_{ij}^{(l,l')}(\boldsymbol{R}_i,\boldsymbol{R}_j) = \begin{cases} \mathcal{G}_{ii}^{(l,l')} + b^{l+l'-2}\mathcal{F}_i^{l-1}\mathcal{F}_j^{l'-1}\boldsymbol{\nabla}_{\boldsymbol{R}_i}^{(l-1)}\boldsymbol{\nabla}_{\boldsymbol{R}_j}^{(l'-1)}\mathbf{G}^*(\boldsymbol{R}_i,\boldsymbol{R}_j) & j=i, \\ b^{l+l'-2}\mathcal{F}_i^{l-1}\mathcal{F}_j^{l'-1}\boldsymbol{\nabla}_{\boldsymbol{R}_i}^{(l-1)}\boldsymbol{\nabla}_{\boldsymbol{R}_j}^{(l'-1)}\mathbf{G}(\boldsymbol{R}_i,\boldsymbol{R}_j) & j\neq i, \end{cases}$$

$$\mathcal{G}_{ii}^{(l,l')} = \delta_{ll'}\frac{2l-1}{16\pi^2\eta b}\int \mathbf{Y}^{(l-1)}(\hat{\boldsymbol{\rho}})(\boldsymbol{I}-\hat{\boldsymbol{\rho}}\hat{\boldsymbol{\rho}})\mathbf{Y}^{(l-1)}(\hat{\boldsymbol{\rho}})\,d\Omega.$$

The expressions for the elements of the double layer integral also follow similarly [10]

$$\boldsymbol{K}_{ij}^{(l,l')}(\boldsymbol{R}_i,\boldsymbol{R}_j) = \begin{cases} -\frac{1}{2}\delta_{ll'}\boldsymbol{\Delta}^{(l-1)} + \dfrac{4\pi b^{(l+l'-1)}\mathcal{F}_i^{l-1}\mathcal{F}_j^{l'-1}}{(l'-2)!(2l'-1)!!}\boldsymbol{\nabla}_{\boldsymbol{R}_i}^{(l-1)}\boldsymbol{\nabla}_{\boldsymbol{R}_j}^{(l'-2)}\mathbf{K}^*(\boldsymbol{R}_i,\boldsymbol{R}_j) & j=i, \\ \dfrac{4\pi b^{(l+l'-1)}\mathcal{F}_i^{l-1}\mathcal{F}_j^{l'-1}}{(l'-2)!(2l'-1)!!}\boldsymbol{\nabla}_{\boldsymbol{R}_i}^{(l-1)}\boldsymbol{\nabla}_{\boldsymbol{R}_j}^{(l'-2)}\mathbf{K}(\boldsymbol{R}_i,\boldsymbol{R}_j) & j\neq i. \end{cases}$$

The off-diagonal terms of the linear system have been obtained using Taylor expansion and the orthogonality of the tensorial spherical harmonics, following the steps in the derivation of Eq. (A.16a).

For the diagonal terms, $i = j$, the correction term does not contain singularities in the domain of flow and, therefore, the boundary integrals in the definition of the matrix elements can be expressed in terms of derivatives of the correction. Singular terms from the Oseen tensor can be calculated explicitly by performing Fourier transform of Oseen tensor and using well-known results for integrals of Bessel functions. The contribution to

the diagonal matrix element from the single layer of the boundary integral is

$$\boldsymbol{G}_{ii}^{\mathrm{o}(l,l')} = \frac{(2l-1)(2l'-1)}{(4\pi b^2)^2(2\pi)^3} \int e^{i(\boldsymbol{\rho}-\boldsymbol{\rho}')\cdot\boldsymbol{k}} \mathbf{Y}^{(l-1)}(\hat{\boldsymbol{\rho}}) \left(\frac{\boldsymbol{I}-\hat{\boldsymbol{k}}\hat{\boldsymbol{k}}}{\eta k^2}\right) \mathbf{Y}^{(l')}(\hat{\boldsymbol{\rho}'})\, \mathrm{d}\boldsymbol{k}\, d\mathrm{S}_i\, d\mathrm{S}_i. \tag{A.22}$$

This above integration is completed using plane wave expansion in terms of tensorial spherical harmonics as

$$e^{i\boldsymbol{k}\cdot\boldsymbol{\rho}} = \sum_{q=0}^{\infty} \frac{(i)^q(2q+1)}{q!\,(2q-1)!!} j_q(k\rho)\Big(\mathbf{Y}^{(q)}(\hat{\boldsymbol{k}})\cdot\mathbf{Y}^{(q)}(\hat{\boldsymbol{k}})\Big), \tag{A.23}$$

and using using the orthogonality of $\mathbf{Y}^{(l)}s$, and the spherical Bessel function $\int_0^\infty j_l(kb)\, j_{l'}(kb)\,\mathrm{d}k = \delta_{ll'}\frac{\pi}{2b(2l+1)}$. The expression of the single-layer diagonal-matrix elements is then [45, 57]

$$\boldsymbol{G}_{ii}^{\mathrm{o}(l,l')} \equiv \boldsymbol{\mathcal{G}}_{ii}^{(l,l')} = \delta_{ll'}\frac{(2l-1)}{16\pi^2\eta b} \int \mathbf{Y}^{(l)}(\hat{\boldsymbol{\rho}})\,(\boldsymbol{I}-\hat{\boldsymbol{\rho}}\hat{\boldsymbol{\rho}})\,\mathbf{Y}^{(l)}(\hat{\boldsymbol{\rho}})\, d\Omega. \tag{A.24}$$

The double layer contribution is obtained in a similar way by Fourier transforming the stress tensor to obtain the expression

$$\boldsymbol{K}_{ii}^{\mathrm{o}(l,l')} = \frac{i(2l-1)}{(32\pi^4 b^2)(l'-1)!(2l'-3)!!} \int e^{i(\boldsymbol{\rho}-\boldsymbol{\rho}')\cdot\boldsymbol{k}} \mathbf{Y}^{(l-1)} \left[\frac{\overbrace{\boldsymbol{I}\hat{\boldsymbol{k}}} - 2\hat{\boldsymbol{k}}\hat{\boldsymbol{k}}\hat{\boldsymbol{k}}}{\eta k}\right]\cdot\hat{\boldsymbol{\rho}}'\, \mathbf{Y}^{(l-1)}\, \mathrm{d}\boldsymbol{k}\, d\mathrm{S}_i\, d\mathrm{S}_i.$$

Expanding the plane wave in spherical Bessel function and using $\hat{\boldsymbol{k}}\cdot\big[\overbrace{\boldsymbol{I}\hat{\boldsymbol{k}}} - 2\hat{\boldsymbol{k}}\hat{\boldsymbol{k}}\hat{\boldsymbol{k}}\big] = \boldsymbol{I}$, the diagonal contribution from double layer integral is [10]

$$\boldsymbol{K}_{ii}^{\mathrm{o}(l,l')} = -\tfrac{1}{2}\delta_{ll'}\boldsymbol{\Delta}^{(l-1)}. \tag{A.25}$$

The exact expressions for these boundary integrals, in terms of Green's functions of Stokes flow, have been used to obtain explicit expression for generalized friction tensors and rigid body motion of spherical active colloids.

A.4 Jacobi method for the generalized friction tensors

In this appendix, we obtain the expression for the generalized friction tensors using the classical Jacobi iteration applied to the linear system of equations for active colloidal suspension. Explicit expressions for the matrix elements have been provided in section A.3. The solution obtained using Jacobi iteration is the mathematical basis of the physically motivated "method of reflections" first used by Smoluchowski [90].

The linear system of equation for active colloidal suspension, derived in Chapter 2, is

$$\tfrac{1}{2}\mathbf{V}_i^{(l\sigma)} = -\boldsymbol{G}_{ij}^{(l\sigma,l'\sigma')}(\boldsymbol{R}_i,\boldsymbol{R}_j)\cdot\mathbf{F}_j^{(l'\sigma')} + \boldsymbol{K}_{ij}^{(l\sigma,l'\sigma')}(\boldsymbol{R}_i,\boldsymbol{R}_j)\cdot\mathbf{V}_j^{(l'\sigma')}, \tag{A.26}$$

Here the first two modes of $\mathbf{V}^{(l\sigma)}$ include rigid body motion such that $\mathbf{V}^{(1s)} = \mathbf{V} - \mathbf{V}^{\mathcal{A}}$ and $\mathbf{V}^{(2a)} = b(\boldsymbol{\Omega} - \boldsymbol{\Omega}^{\mathcal{A}})$. We then rewrite the linear system of equations in standard form for the Jacobi iterative scheme as

$$-\boldsymbol{G}_{ij}^{(l\sigma,l'\sigma')}(\boldsymbol{R}_i,\boldsymbol{R}_j)\cdot\mathbf{F}_j^{(l'\sigma')} = \left(\tfrac{1}{2}\boldsymbol{I}_{ij}^{(l\sigma,l'\sigma')} - \boldsymbol{K}_{ij}^{(l\sigma,l'\sigma')}\right)\cdot\mathbf{V}_j^{(l'\sigma')}. \tag{A.27}$$

Here $\mathbf{I}$ is the identity operator. From here we want to calculate the generalized friction tensors

$$\boldsymbol{\gamma}_{ij}^{(l\sigma,l'\sigma')} = \left[\boldsymbol{G}^{-1}\right]_{ik}^{(l\sigma,l''\sigma'')}\cdot\left(\tfrac{1}{2}\boldsymbol{I}_{kj}^{(l''\sigma'',l'\sigma')} - \boldsymbol{K}_{kj}^{(l''\sigma'',l'\sigma')}\right) = \left[\boldsymbol{G}^{-1}\right]_{ik}^{(l\sigma,l'\sigma')}\cdot\left(\boldsymbol{B}_{kj}^{(l''\sigma'',l'\sigma')}\right). \tag{A.28}$$

The right hand side of the linear system consists of the known velocity coefficients. Jacobi's solution at the nth iteration is then

$$\left(\boldsymbol{\gamma}_{ij}^{(l\sigma,l'\sigma')}\right)^{[n]} = \frac{1}{G_{ii}^{(l\sigma,l\sigma)}}\left[\boldsymbol{B}_{ij}^{(l\sigma,l'\sigma')} - \sum{}'\boldsymbol{G}_{ik}^{(l\sigma,l''\sigma'')}\cdot\left(\boldsymbol{\gamma}_{kj}^{(l''\sigma'',l'\sigma')}\right)^{[n-1]}\right]. \tag{A.29}$$

Here the prime over summation indicates that the diagonal term ($i = j = k$ and $l\sigma = l'\sigma'$) is not included in the summation as per definition of Jacobi iteration [220].

The one-body solution of the linear system can be calculated *exactly* in an unbounded domain of fluid flow. The generalized friction matrix is here fully diagonal and the Jacobi iteration trivially converges. The solution of the linear system is then

$$\mathbf{F}_i^{(l\sigma)} = -\gamma_{ii}^{(l\sigma,l\sigma)}\mathbf{V}_i^{(l\sigma)} = -\frac{1}{G_{ii}^{(l\sigma,l\sigma)}}\mathbf{V}_i^{(l\sigma)}. \tag{A.30}$$

First three of them correspond to force, torque and stresslet. They are

$$G_{ii}^{(1s,1s)} = \frac{1}{6\pi\eta b}, \qquad G_{ii}^{(2a,2a)} = \frac{1}{8\pi\eta b}, \qquad G_{ii}^{(2s,2s)} = \frac{3}{20\pi\eta b}.$$

where $G_{ii}^{(l\sigma,l\sigma)}$ are the diagonals of the $l\sigma$ block of the single-layer matrix. It should be noted that at this order there is no hydrodynamic interaction; an active colloid translated at self-propulsion velocity $\mathbf{V}^{\mathcal{A}}$ and self-rotates with angular velocity $\mathbf{\Omega}^{\mathcal{A}}$. This exact result for one-body system was obtained previously by several authors from a direct solution of the Stokes equation [38, 43, 44], through the use of the reciprocal identity [70] and from the boundary integral approach [10, 45].

For a system of many active colloids the Jacobi iteration must begin with an initial guess for the solution. As the linear system is diagonally dominant, the one-particle solution is always a good starting guess. Thus the zeroth order solution is gives as

$$\left(\boldsymbol{\gamma}_{ij}^{(l\sigma,l'\sigma')}\right)^{[0]} = \frac{\delta_{ij}\delta_{ll'}\delta_{\sigma\sigma'}}{G_{ii}^{(l\sigma,l\sigma)}}. \tag{A.31}$$

Hydrodynamic interaction between two colloids appear at first order of the Jacobi iteration in Eq. (A.29). The solution for the $l\sigma = l'\sigma' = 1s$ at $n = 1$ are

$$\left(\boldsymbol{\gamma}_{11}^{TT}\right)^{[1]} = \gamma^T, \qquad \left(\boldsymbol{\gamma}_{12}^{TT}\right)^{[1]} = -\gamma^T\gamma^T\mathcal{F}^1\mathcal{F}^1\mathbf{G}(\boldsymbol{R}_1,\boldsymbol{R}_2) - \frac{28\pi\eta b\gamma^T}{3}\mathcal{F}^1\mathcal{F}^2\boldsymbol{\nabla}\mathbf{G}(\boldsymbol{R}_1,\boldsymbol{R}_2) + \ldots$$

Here $\gamma^T = 6\pi\eta b$ is the friction for an isolated colloid in an unbounded flow and is the *zeroth* guess of the Jacobi iteration and $\mathbf{G}$ is a Green's function of Stokes. Correction to

the self-friction due to presence of other colloids appears at second order of Eq. (A.29)

$$\left(\boldsymbol{\gamma}_{11}^{TT}\right)^{[2]} = \gamma^T \left(\gamma^T \mathcal{F}^1 \mathcal{F}^1 \mathbf{G}(\boldsymbol{R}_1, \boldsymbol{R}_2)\right)^2 + \gamma^T \left(\frac{28\pi\eta b^2}{3} \mathcal{F}^1 \mathcal{F}^2 \boldsymbol{\nabla} \mathbf{G}(\boldsymbol{R}_1, \boldsymbol{R}_2)\right)^2 + \ldots \tag{A.32}$$

The same approach is then applied to derive the arbitrary orders of the generalized friction tensor for all combinations of $l\sigma$ and $l'\sigma'$. The first order approximation to friction tensors in term of Green's function $\mathbf{G}$ of Stokes flow

$$\begin{aligned}
\left(\boldsymbol{\gamma}_{ij}^{TT}\right)^{[1]} &= -\gamma^T \gamma^T \mathcal{F}_i^0 \mathcal{F}_j^0 \mathbf{G}, & \left(\boldsymbol{\gamma}_{ij}^{RT}\right)^{[1]} &= -\tfrac{1}{2}\gamma^T \gamma^R \boldsymbol{\nabla}_{\boldsymbol{R}_i} \times \mathbf{G}, \\
\left(\boldsymbol{\gamma}_{ij}^{TR}\right)^{[1]} &= -\tfrac{1}{2}\gamma^T \gamma^R \boldsymbol{\nabla}_{\boldsymbol{R}_j} \times \mathbf{G}, & \left(\boldsymbol{\gamma}_{ij}^{RR}\right)^{[1]} &= -\tfrac{1}{4}\gamma^R \gamma^R \boldsymbol{\nabla}_{\boldsymbol{R}_i} \times \left(\boldsymbol{\nabla}_{\boldsymbol{R}_j} \times \mathbf{G}\right), \\
\left(\boldsymbol{\gamma}_{ij}^{(T,2s)}\right)^{[1]} &= -c^{2s} \gamma^T \mathcal{F}_i^0 \mathcal{F}_j^1 \boldsymbol{\nabla}_{\boldsymbol{R}_j} \mathbf{G}, & \left(\boldsymbol{\gamma}_{ij}^{(R,2s)}\right)^{[1]} &= -\tfrac{c^{2s}}{2} \gamma^R \boldsymbol{\nabla}_{\boldsymbol{R}_i} \times \left(\boldsymbol{\nabla}_{\boldsymbol{R}_j} \mathbf{G}\right), \\
\left(\boldsymbol{\gamma}_{ij}^{(T,3a)}\right)^{[1]} &= -c^{3a} \gamma^T \boldsymbol{\nabla}_{\boldsymbol{R}_j} (\boldsymbol{\nabla}_{\boldsymbol{R}_j} \times \mathbf{G}), & \left(\boldsymbol{\gamma}_{ij}^{(R,3a)}\right)^{[1]} &= -\tfrac{c^{3a}}{2} \gamma^R \boldsymbol{\nabla}_{\boldsymbol{R}_i} \times \left(\boldsymbol{\nabla}_{\boldsymbol{R}_j} (\boldsymbol{\nabla}_{\boldsymbol{R}_j} \times \mathbf{G})\right), \\
\left(\boldsymbol{\gamma}_{ij}^{(T,3t)}\right)^{[1]} &= c^{3t} \gamma^T \boldsymbol{\nabla}_{\boldsymbol{R}_j}^2 \mathbf{G}, & \left(\boldsymbol{\gamma}_{ij}^{(R,3t)}\right)^{[1]} &= 0, \\
\left(\boldsymbol{\gamma}_{ij}^{(T,4a)}\right)^{[1]} &= c^{4a} \gamma^T \boldsymbol{\nabla}_{\boldsymbol{R}_j} \boldsymbol{\nabla}_{\boldsymbol{R}_j} (\boldsymbol{\nabla}_{\boldsymbol{R}_j} \times \mathbf{G}), & \left(\boldsymbol{\gamma}_{ij}^{(R,4a)}\right)^{[1]} &= \tfrac{c^{4a}}{2} \gamma^R \boldsymbol{\nabla}_{\boldsymbol{R}_i} \times \left(\boldsymbol{\nabla}_{\boldsymbol{R}_j} \boldsymbol{\nabla}_{\boldsymbol{R}_j} (\boldsymbol{\nabla}_{\boldsymbol{R}_j} \times \mathbf{G})\right).
\end{aligned}$$

Here $\gamma^T = 6\pi\eta b$, $\gamma^R = 8\pi\eta b^3$, $c^{2s} = \frac{28\pi\eta b^2}{3}$, $c^{3a} = \frac{13\pi\eta b^3}{9}$, $c^{3t} = \frac{4\pi\eta b^3}{5}$, $c^{4a} = \frac{121\pi\eta b^4}{10}$. The friction tensor corresponding to $l\sigma = 2t$ are obtained in terms of the pressure Green's function as

$$\boldsymbol{\gamma}_{ij}^{(2t,T)} = \mathbf{P}(\boldsymbol{R}_i, \boldsymbol{R}_j), \quad \boldsymbol{\gamma}_{ij}^{(2t,ls)} = \tfrac{l(l-1)}{2(2l-1)} \boldsymbol{\nabla}_{\boldsymbol{R}_j}^{(l)} \mathbf{P}(\boldsymbol{R}_i, \boldsymbol{R}_j), \quad \boldsymbol{\gamma}_{ij}^{(2t,la)} = 0, \quad \boldsymbol{\gamma}_{ij}^{(2t,lt)} = 0.$$

These expression of the friction tensors are then used to obtain explicit forms of the mobility and propulsion tensors. Table (A.2) contains the leading order expressions of the mobility and propulsion tensors.

In the preceding appendices, we have seen that all the relevant quantities, in our approach, are obtained in terms of a Green's function of the Stokes equation. This fact is utilized in our numerical implementation of the theory to simulate distinct geometries of the flow by using the corresponding Green's function and their higher derivatives, as described in

	$i \neq j$	$i = j$
$\boldsymbol{\mu}_{ij}^{TT}$	$\mathcal{F}_i^0 \mathcal{F}_j^0 \mathbf{G}$	$(6\pi\eta b)^{-1}\boldsymbol{I} + \mathcal{F}_i^0 \mathcal{F}_j^0 \mathbf{G}^*$
$\boldsymbol{\mu}_{ij}^{TR}$	$\frac{1}{2}\boldsymbol{\nabla}_{\boldsymbol{R}_j} \times \mathbf{G}$	$\frac{1}{2}\boldsymbol{\nabla}_{\boldsymbol{R}_j} \times \mathbf{G}^*$
$\boldsymbol{\mu}_{ij}^{RT}$	$\frac{1}{2}\boldsymbol{\nabla}_{\boldsymbol{R}_i} \times \mathbf{G}$	$\frac{1}{2}\boldsymbol{\nabla}_{\boldsymbol{R}_i} \times \mathbf{G}^*$
$\boldsymbol{\mu}_{ij}^{RR}$	$\frac{1}{4}\boldsymbol{\nabla}_{\boldsymbol{R}_i} \times \boldsymbol{\nabla}_{\boldsymbol{R}_j} \times \mathbf{G}$	$(8\pi\eta b^3)^{-1}\boldsymbol{I} + \frac{1}{4}\boldsymbol{\nabla}_{\boldsymbol{R}_i} \times \boldsymbol{\nabla}_{\boldsymbol{R}_j} \times \mathbf{G}^*$
$\boldsymbol{\pi}_{ij}^{(T,ls)}$	$c_{ls}\mathcal{F}_i^0 \mathcal{F}_j^{(l-1)} \boldsymbol{\nabla}_{\boldsymbol{R}_j}^{(l-1)} \mathbf{G},\ l \geq 2$	$c_{ls}\mathcal{F}_i^0 \mathcal{F}_j^{(l-1)} \boldsymbol{\nabla}_{\boldsymbol{R}_j}^{(l-1)} \mathbf{G}^*,\ l \geq 2$
$\boldsymbol{\pi}_{ij}^{(R,ls)}$	$\frac{c_{ls}}{2}\boldsymbol{\nabla}_{\boldsymbol{R}_i} \times \boldsymbol{\nabla}_{\boldsymbol{R}_j}^{(l-1)} \mathbf{G},\ l \geq 2$	$\frac{c_{ls}}{2}\boldsymbol{\nabla}_{\boldsymbol{R}_i} \times \boldsymbol{\nabla}_{\boldsymbol{R}_j}^{(l-1)} \mathbf{G}^*,\ l \geq 2$
$\boldsymbol{\pi}_{ij}^{(T,la)}$	$c_{la}\boldsymbol{\nabla}_{\boldsymbol{R}_j}^{(l-2)}(\boldsymbol{\nabla}_{\boldsymbol{R}_j} \times \mathbf{G}),\ l \geq 3$	$c_{la}\boldsymbol{\nabla}_{\boldsymbol{R}_j}^{(l-2)}(\boldsymbol{\nabla}_{\boldsymbol{R}_j} \times \mathbf{G}^*),\ l \geq 3$
$\boldsymbol{\pi}_{ij}^{(R,la)}$	$\frac{c_{la}}{2}\boldsymbol{\nabla}_{\boldsymbol{R}_i} \times \boldsymbol{\nabla}_{\boldsymbol{R}_j}^{(l-2)}(\boldsymbol{\nabla}_{\boldsymbol{R}_j} \times \mathbf{G}),\ l \geq 3$	$\frac{c_{la}}{2}\boldsymbol{\nabla}_{\boldsymbol{R}_i} \times \boldsymbol{\nabla}_{\boldsymbol{R}_j}^{(l-2)}(\boldsymbol{\nabla}_{\boldsymbol{R}_j} \times \mathbf{G}^*),\ l \geq 3$
$\boldsymbol{\pi}_{ij}^{(T,lt)}$	$c_{lt}\boldsymbol{\nabla}_{\boldsymbol{R}_j}^{(l-3)}(\nabla_{\boldsymbol{R}_j}^2 \mathbf{G}),\ l \geq 3$	$c_{lt}\boldsymbol{\nabla}_{\boldsymbol{R}_j}^{(l-3)}(\nabla_{\boldsymbol{R}_j}^2 \mathbf{G}^*),\ l \geq 3$

Table A.2: The leading order expressions of the mobility and propulsion tensors [10]. Here, $\mathbf{G} = \mathbf{G}^{\mathrm{o}} + \mathbf{G}^*$ is a Green's function of Stokes equation. It is written as the sum of Oseen tensor $\mathbf{G}^{\mathrm{o}}$ and a correction $\mathbf{G}^*$ to satisfy the boundary condition in the domain of the flow. See Eq. (A.4) and the corresponding description for further details. The operator $\mathcal{F}_j^l$, see Eq. (A.16b), encodes finite size of the colloids, and $c_{l\sigma}$ are constants obtained from the solution of the linear system.

Chapter 10. It should be noted that the higher derivatives of a given Green's function, for example, the Lorentz-Blake tensor, may lead to unwieldy expressions. In the case of the Lorentz-Blake tensor, we can save considerable computation time by choosing to apply the mirror operator to the coefficients of the slip, when computing the rigid body motion, for a dynamic simulation of active colloids near a plane wall. Similar savings in the computation time is also achievable for the simulations of active colloids near a fluid-fluid or a fluid-air interface.

Bibliography

[1] W. F. Paxton, K. C. Kevin C., C. C. Olmeda, A. Sen, S. K. St. Angelo, Y. Cao, T. E. Mallouk, P. E. Lammert, and V. H. Crespi, "Catalytic nanomotors: Autonomous movement of striped nanorods," J. Am. Chem. Soc. **126**, 13424–13431 (2004).

[2] J. R. Howse, R. A. L. Jones, A. J. Ryan, T. Gough, R. Vafabakhsh, and R. Golestanian, "Self-motile colloidal particles: From directed propulsion to random walk," Phys. Rev. Lett. **99**, 048102 (2007).

[3] H.-R. Jiang, N. Yoshinaga, and M. Sano, "Active motion of a janus particle by self-thermophoresis in a defocused laser beam," Phys. Rev. Lett. **105**, 268302 (2010).

[4] S. J. Ebbens and J. R. Howse, "In pursuit of propulsion at the nanoscale," Soft Matter **6**, 726–738 (2010).

[5] J. Palacci, S. Sacanna, A. P. Steinberg, D. J. Pine, and P. M. Chaikin, "Living crystals of light-activated colloidal surfers," Science **339**, 936–940 (2013).

[6] K. Drescher, K. C. Leptos, I. Tuval, T. Ishikawa, T. J. Pedley, and R. E. Goldstein, "Dancing volvox: Hydrodynamic bound states of swimming algae," Phys. Rev. Lett. **102**, 168101 (2009).

[7] K. Drescher, R. E. Goldstein, N. Michel, M. Polin, and I. Tuval, "Direct measurement of the flow field around swimming microorganisms," Phys. Rev. Lett. **105**, 168101 (2010).

[8] A. P. Petroff, X.-L. Wu, and A. Libchaber, "Fast-moving bacteria self-organize into active two-dimensional crystals of rotating cells," Phys. Rev. Lett. **114**, 158102 (2015).

[9] R. Singh and R. Adhikari, "Universal hydrodynamic mechanisms for crystallization in active colloidal suspensions," Phys. Rev. Lett. **117**, 228002 (2016).

[10] R. Singh, S. Ghose, and R. Adhikari, "Many-body microhydrodynamics of colloidal particles with active boundary layers," J. Stat. Mech **2015**, P06017 (2015).

[11] R. Singh and R. Adhikari, "Generalized Stokes laws for active colloids and their applications," arXiv:1603.05735 (2016).

[12] R. Singh and R. Adhikari, "Fluctuating hydrodynamics and the Brownian motion of an active colloid near a wall," Eur. J. Comp. Mech , 1–20 (2017).

[13] R. W. Nash, R. Adhikari, J. Tailleur, and M. E. Cates, "Run-and-Tumble Particles with Hydrodynamics: Sedimentation, Trapping, and Upstream Swimming," Phys. Rev. Lett. **104**, 258101 (2010).

[14] R. Kubo, K. Matsuo, and K. Kitahara, "Fluctuation and relaxation of macrovariables," J. Stat. Phys. **9**, 51–96 (1973).

[15] K. Kitahara, "The Hamilton-Jacobi-Equation approach to fluctuation phenomena," Adv. Chem. Phys. **26**, 85–111 (1975).

[16] J. R. Melcher and G. I. Taylor, "Electrohydrodynamics: A review of the role of interfacial shear stresses," Ann. Rev. Fluid Mech. **1**, 111–146 (1969).

[17] R. Singh, A. Laskar, and R. Adhikari, "PyStokes: Hampi," (2014).

[18] W. B. Russel, D. A. Saville, and W. R. Schowalter, *Colloidal dispersions* (Cambridge university press, 1989).

[19] J. K. G. Dhont, *An introduction to dynamics of colloids* (Elsevier, 1996).

[20] M. E. Cates and M. R. Evans, *Soft and fragile matter: Nonequilibrium dynamics, metastability and flow* (Institute of Physics Publishing, Bristol, 2000).

[21] M. Kleman and O. D. Laverntovich, *Soft matter physics: an introduction* (Springer Science & Business Media, 2007).

[22] M. S. Elliot and W. C. K. Poon, "Conventional optical microscopy of colloidal suspensions," Adv. Colloid Int. Sci. **92**, 133–194 (2001).

[23] V. Prasad, D. Semwogerere, and E. R. Weeks, "Confocal microscopy of colloids," J. Phys.: Cond. Mat. **19**, 113102 (2007).

[24] J. N. Israelachvili, *Intermolecular and surface forces* (Academic press, Amsterdam, 2011).

[25] A. Einstein, "The theory of the Brownian movement," Ann. Phys. (Berlin) **322**, 549 (1905).

[26] J. Perrin, *Brownian movement and molecular reality* (Taylor & Francis, 1910).

[27] P. M. Chaikin and T. C. Lubensky, *Principles of condensed matter physics* (Cambridge University Press, 2000).

[28] W. C. K. Poon, "Colloids as big atoms," Science **304**, 830–831 (2004).

[29] J. Zhang, E. Luijten, B. A Grzybowski, and S. Granick, "Active colloids with collective mobility status and research opportunities," Chem. Soc. Rev. **46**, 5551–5569 (2017).

[30] L. Berthier and G. Biroli, "Theoretical perspective on the glass transition and amorphous materials," Rev. Mod. Phys. **83**, 587 (2011).

[31] S. Auer and D. Frenkel, "Prediction of absolute crystal-nucleation rate in hard-sphere colloids," Nature **409**, 1020–1023 (2001).

[32] V. N. Manoharan, "Colloidal matter: Packing, geometry, and entropy," Science **349**, 1253751 (2015).

[33] S. Ramaswamy, "The Mechanics and Statistics of Active Matter," Annu. Rev. Condens. Mat. Phys. **1**, 323–345 (2010).

[34] M. E. Cates, "Diffusive transport without detailed balance in motile bacteria: does microbiology need statistical physics?" Rep. Prog. Phys. **75**, 042601 (2012).

[35] M. E. Cates and F. C. MacKintosh, "Active soft matter," Soft Matter **7**, 3050–3051 (2011).

[36] M. C. Marchetti, J. F. Joanny, S. Ramaswamy, T. B. Liverpool, J. Prost, Madan Rao, and R. Aditi Simha, "Hydrodynamics of soft active matter," Rev. Mod. Phys. **85**, 1143–1189 (2013).

[37] S. Ramaswamy, "Active matter," J. Stat. Mech. **2017**, 054002 (2017).

[38] J. L. Anderson, "Colloid transport by interfacial forces," Annu. Rev. Fluid Mech. **21**, 61–99 (1989).

[39] R. Golestanian, T. B. Liverpool, and A. Ajdari, "Propulsion of a molecular machine by asymmetric distribution of reaction products," Phys. Rev. Lett. **94**, 220801 (2005).

[40] M. Smoluchowski, Bull. Acad. Sci. Cracovie , 182–199 (1903).

[41] B. V. Derjaguin, G. P. Sidorenkov, E. A. Zubashchenkov, and E. V. Kiseleva, "Kinetic phenomena in boundary films of liquids," Kolloidn. Zh **9**, 335–47 (1947).

[42] B. V. Derjaguin, N. V. Churaev, and V. M. Muller, "Surface forces in transport phenomena," (Springer, 1987).

[43] M. J. Lighthill, "On the squirming motion of nearly spherical deformable bodies through liquids at very small Reynolds numbers," Commun. Pure. Appl. Math. **5**, 109–118 (1952).

[44] J. R. Blake, "A spherical envelope approach to ciliary propulsion," J. Fluid Mech. **46**, 199–208 (1971).

[45] S. Ghose and R. Adhikari, "Irreducible representations of oscillatory and swirling flows in active soft matter," Phys. Rev. Lett. **112**, 118102 (2014).

[46] O. S. Pak and E. Lauga, "Generalized squirming motion of a sphere," J. Eng. Math. **88**, 1–28 (2014).

[47] B. U. Felderhof and R. B. Jones, "Stokesian swimming of a sphere at low Reynolds number by helical surface distortion," Phys. Fluids **28**, 073601 (2016).

[48] T. J. Pedley, "Spherical squirmers: models for swimming micro-organisms," IMA J. Appl. Math. **81**, 488–521 (2016).

[49] C. Brennen and H. Winet, "Fluid mechanics of propulsion by cilia and flagella," Annu. Rev. Fluid Mech. **9**, 339–398 (1977).

[50] S. Thutupalli, R. Seemann, and S. Herminghaus, "Swarming behavior of simple model squirmers," N. J. Phys. **13**, 073021 (2011).

[51] R. Niu, T. Palberg, and T. Speck, "Self-assembly of colloidal molecules due to self-generated flow," Phys. Rev. Lett. **119**, 028001 (2017).

[52] R. W. O'brien, "A method for the calculation of the effective transport properties of suspensions of interacting particles," J. Fluid Mech. **91**, 17–39 (1979).

[53] W. Sutherland, "A dynamical theory of diffusion for non-electrolytes and the molecular mass of albumin," Phil. Mag. Series **9**, 781–785 (1905).

[54] R. Kubo, "The fluctuation-dissipation theorem," Rep. Prog. Phys. **29**, 255 (1966).

[55] M. Smoluchowski, "On the mutual action of spheres which move in a viscous liquid," Bull. Acad. Sci. Cracovie A **1**, 28–39 (1911).

[56] P. Mazur and W. van Saarloos, "Many-sphere hydrodynamic interactions and mobilities in a suspension," Physica A: Stat. Mech. Appl. **115**, 21–57 (1982).

[57] A. J. C. Ladd, "Hydrodynamic interactions in a suspension of spherical particles," J. Chem. Phys. **88**, 5051–5063 (1988).

[58] J. G. Kirkwood, "The statistical mechanical theory of transport processes I. general theory," J. Chem. Phys. **14**, 180–201 (1946).

[59] J. G. Kirkwood and J. Riseman, "The intrinsic viscosities and diffusion constants of flexible macromolecules in solution," J. Chem. Phys. **16**, 565–573 (1948).

[60] R. Zwanzig, "Hydrodynamic fluctuations and Stokes law friction," J. Res. Natl. Bur. Std.(US) B **68**, 143–145 (1964).

[61] R. Zwanzig, "Langevin theory of polymer dynamics in dilute solution," Advances in Chemical Physics: Stochastic Processes in Chemical Physics, Volume 15 , 325–331 (1969).

[62] G. K. Batchelor, "Brownian diffusion of particles with hydrodynamic interaction," J. Fluid Mech. **74**, 1–29 (1976).

[63] G. K. Batchelor, "The effect of Brownian motion on the bulk stress in a suspension of spherical particles," J. Fluid Mech. **83**, 97–117 (1977).

[64] R. J. A. Tough, P. N. Pusey, H. N. W. Lekkerkerker, and C. Van Den Broeck, "Stochastic descriptions of the dynamics of interacting Brownian particles," Mol. Phys. **59**, 595–619 (1986).

[65] W. B. Russel, "Brownian motion of small particles suspended in liquids," Ann. Rev. Fluid Mech. **13**, 425–455 (1981).

[66] H. Faxén, "Der widerstand gegen die bewegung einer starren kugel in einer zähen flüssigkeit, die zwischen zwei parallelen ebenen wänden eingeschlossen ist," Ann. der Physik **373**, 89–119 (1922).

[67] W. K. Tung, *Group theory in physics* (World Scientific Publishing, 1985).

[68] S. Hess, *Tensors for physics* (Springer, 2015).

[69] J. L. Anderson and D. C. Prieve, "Diffusiophoresis caused by gradients of strongly adsorbing solutes," Langmuir **7**, 403–406 (1991).

[70] H. A. Stone and A. D. T. Samuel, "Propulsion of microorganisms by surface distortions," Phys. Rev. Lett. **77**, 4102–4104 (1996).

[71] U. Weinert, "Spherical tensor representation," Arch. Rational Mech. Anal. **74**, 165–196 (1980).

[72] J. Applequist, "Traceless Cartesian tensor forms for spherical harmonic functions: new theorems and applications to electrostatics of dielectric media," J. Phys. A: Math. Gen. **22**, 4303 (1989).

[73] A. A. Zick and G. M. Homsy, "Stokes flow through periodic arrays of spheres," J. Fluid Mech. **115**, 13–26 (1982).

[74] K. Ichiki, "Improvement of the Stokesian dynamics method for systems with a finite number of particles," J. Fluid Mech. **452**, 231–262 (2002).

[75] B. Shanker and H. Huang, "Accelerated Cartesian expansions–a fast method for computing of potentials of the form $R^{-\nu}$ for all real ν," J. Comput. Phys. **226**, 732–753 (2007).

[76] L. Greengard and Vladimir Rokhlin, "A fast algorithm for particle simulations," J. Comp. Phys. **73**, 325–348 (1987).

[77] P. Brunn, "The effect of Brownian motion for a suspension of spheres," Rheol. Acta **15**, 104–119 (1976).

[78] F. K. G. Odqvist, "Über die bandwertaufgaben der hydrodynamik zäher flüssigkeiten," Mathematische Zeitschrift **32**, 329–375 (1930).

[79] O. A. Ladyzhenskaia, *The mathematical theory of viscous incompressible flow*, Mathematics and its applications (Gordon and Breach, 1969).

[80] G. Youngren and A. Acrivos, "Stokes flow past a particle of arbitrary shape: a numerical method of solution," J. Fluid Mech. **69**, 377–403 (1975).

[81] C. Pozrikidis, *Boundary Integral and Singularity Methods for Linearized Viscous Flow* (Cambridge University Press, 1992).

[82] G. P. Muldowney and J. J. L. Higdon, "A spectral boundary element approach to three-dimensional Stokes flow," J. Fluid Mech. **298**, 167–192 (1995).

[83] A. H.-D. Cheng and D. T. Cheng, "Heritage and early history of the boundary element method," Eng. Anal. Bound. Elem. **29**, 268–302 (2005).

[84] L. G. Leal, *Advanced transport phenomena: Fluid mechanics and convective transport processes* (Cambridge University Press, 2007).

[85] S. Kim and S. J. Karrila, *Microhydrodynamics: Principles and Selected Applications* (Butterworth-Heinemann, 1992).

[86] H. Brenner, "The Stokes resistance of an arbitrary particle," Chem. Engg. Sci. **18**, 1–25 (1963).

[87] H. Brenner, "The Stokes resistance of an arbitrary particle - IV arbitrary fields of flow," Chem. Engg. Sci. **19**, 703–727 (1964).

[88] B. U. Felderhof, "Force density induced on a sphere in linear hydrodynamics: I. Fixed sphere, stick boundary conditions," Physica A **84**, 557–568 (1976).

[89] D. J. Jeffrey and Y. Onishi, "Calculation of the resistance and mobility functions for two unequal rigid spheres in low-Reynolds-number flow," J. Fluid Mech. **139**, 261–290 (1984).

[90] K. Ichiki and J. F. Brady, "Many-body effects and matrix inversion in low-Reynolds-number hydrodynamics," Phys. Fluids **13**, 350–353 (2001).

[91] P. Mazur, "Hydrodynamic interactions: a many-body problem in the theory of suspensions," Canadian J. Phys. **63**, 24–29 (1985).

[92] M. R. Hestenes and E. Stiefel, "Methods of conjugate gradients for solving linear systems," J. Res. Natl. Bur. Stand. **49**, 409 (1952).

[93] J. Barnes and P. Hut, "A hierarchical $O(N \log N)$ force-calculation algorithm," Nature **324**, 446–449 (1986).

[94] A. Sierou and J. F. Brady, "Accelerated Stokesian dynamics simulations," J. Fluid Mech. **448**, 115–146 (2001).

[95] A. S. Sangani and G. Mo, "An $O(N)$ algorithm for Stokes and Laplace interactions of particles," Phys. Fluids **8**, 1990–2010 (1996).

[96] A. J. C. Ladd, "Numerical simulations of particulate suspensions via a discretized boltzmann equation. Part 1. Theoretical foundation," J. Fluid Mech. **271**, 285–309 (1994).

[97] N. Liron and E. Barta, "Motion of a rigid particle in Stokes flow: a new second-kind boundary-integral equation formulation," J. Fluid Mech. **238**, 579–598 (1992).

[98] L. D. Landau and E. M. Lifshitz, *Fluid mechanics*, Vol. 6 (Pergamon Press, New York, 1959).

[99] G. K. Batchelor, "The stress system in a suspension of force-free particles," J. Fluid Mech. **41**, 545–570 (1970).

[100] T. Ishikawa and T. J. Pedley, "The rheology of a semi-dilute suspension of swimming model micro-organisms," J. Fluid Mech **588**, 399–435 (2007).

[101] W. E. Uspal, M. N. Popescu, and M. Dietrich, S .and Tasinkevych, "Self-propulsion of a catalytically active particle near a planar wall: from reflection to sliding and hovering," Soft Matter **11**, 434–438 (2015).

[102] R. F. Fox and G. E. Uhlenbeck, "Contributions to non-equilibrium thermodynamics. I. Theory of hydrodynamical fluctuations," Phys. Fluids **13**, 1893–1902 (1970).

[103] E. H. Hauge and A. Martin-Löf, "Fluctuating hydrodynamics and Brownian motion," J. Stat. Phys. **7**, 259–281 (1973).

[104] D. Bedeaux and P. Mazur, "Brownian motion and fluctuating hydrodynamics," Physica **76**, 247–258 (1974).

[105] C. W. J. Beenakker and P. Mazur, "Self-diffusion of spheres in a concentrated suspension," Physica A: Stat. Mech. Appl. **120**, 388–410 (1983).

[106] B. Noetinger, "Fluctuating hydrodynamics and Brownian motion," Physica A: Stat. Mech. Appl. **163**, 545–558 (1990).

[107] J.-N. Roux, "Brownian particles at different times scales: a new derivation of the Smoluchowski equation," Physica A: Stat. Mech. Appl. **188**, 526–552 (1992).

[108] N. G. van Kampen, "Itô versus Stratonovich," J. Stat. Phys. **24**, 175–187 (1981).

[109] C. W. Gardiner, *Handbook of stochastic methods* (Springer Berlin, 1985).

[110] N. G. van Kampen, *Stochastic processes in physics and chemistry* (Elsevier, 1992).

[111] Y. L. Klimontovich, "Itô, Stratonovich and kinetic forms of stochastic equations," Physica A: Stat. Mech. Appl. **163**, 515–532 (1990).

[112] Y. L. Klimontovich, "Nonlinear Brownian motion," Physics-Uspekhi **37**, 737–766 (1994).

[113] G. Volpe, L. Helden, T. Brettschneider, J. Wehr, and C. Bechinger, "Influence of noise on force measurements," Phys. Rev. Lett. **104**, 170602 (2010).

[114] G. Volpe and J. Wehr, "Effective drifts in dynamical systems with multiplicative noise: a review of recent progress," Rep. Prog. Phys. **79**, 053901 (2016).

[115] R. Mannella and P. V. E. McClintock, "Comment on "Influence of noise on force measurements"," Phys. Rev. Lett. **107**, 078901 (2011).

[116] A. W. C. Lau and T. C. Lubensky, "State-dependent diffusion: Thermodynamic consistency and its path integral formulation," Phys. Rev. E **76**, 011123 (2007).

[117] C. W. Gardiner, "Adiabatic elimination in stochastic systems. I. formulation of methods and application to few-variable systems," Phys. Rev. A **29**, 2814–2822 (1984).

[118] S. Chandrasekhar, "Stochastic problems in physics and astronomy," Rev. Mod. Phys. **15**, 1–89 (1943).

[119] S. Chandrasekhar, "Brownian motion, dynamical friction, and stellar dynamics," Rev. Mod. Phys. **21**, 383–388 (1949).

[120] T. J. Murphy and J. L. Aguirre, "Brownian motion of N interacting particles," J. Chem. Phys. **57**, 2098–2104 (1972).

[121] G. Wilemski, "On the derivation of Smoluchowski equations with corrections in the classical theory of Brownian motion," J. Stat. Phys. **14**, 153–169 (1976).

[122] H. Risken, *The Fokker-Planck equation* (Springer Berlin, 1996).

[123] J. Happel and H. Brenner, *Low Reynolds number hydrodynamics: with special applications to particulate media*, Vol. 1 (Prentice-Hall, 1965).

[124] B. U. Felderhof, "Hydrodynamic interaction between two spheres," Physica A: Stat. Mech. Appl. **89**, 373–384 (1977).

[125] R. Schmitz and B. U. Felderhof, "Mobility matrix for two spherical particles with hydrodynamic interaction," Physica A: Stat. Mech. Appl. **116**, 163–177 (1982).

[126] K. C. Nunan and J. B. Keller, "Effective viscosity of a periodic suspension," J. Fluid Mech. **142**, 269–287 (1984).

[127] L. Durlofsky, J. F. Brady, and G. Bossis, "Dynamic simulation of hydrodynamically interacting particles," J. Fluid Mech. **180**, 21–49 (1987).

[128] J. F. Brady, R. J. Phillips, J. C. Lester, and G. Bossis, "Dynamic simulation of hydrodynamically interacting suspensions," J. Fluid Mech. **195**, 257–280 (1988).

[129] B. Cichocki, B. U. Felderhof, K. Hinsen, E. Wajnryb, and J. Blawzdziewicz, "Friction and mobility of many spheres in Stokes flow," J. Chem. Phys. **100**, 3780–3790 (1994).

[130] A. Laskar and R. Adhikari, "Brownian microhydrodynamics of active filaments," Soft matter **11**, 9073–9085 (2015).

[131] D. L. Ermak and J. A. McCammon, "Brownian dynamics with hydrodynamic interactions," J. Chem. Phys. **69**, 1352–1360 (1978).

[132] G. Jayaraman, S. Ramachandran, S. Ghose, A. Laskar, M. Saad Bhamla, P. B. Sunil Kumar, and R. Adhikari, "Autonomous Motility of Active Filaments due to Spontaneous Flow-Symmetry Breaking," Phys. Rev. Lett. **109**, 158302 (2012).

[133] A. Laskar, R. Singh, S. Ghose, G. Jayaraman, P. B. Sunil Kumar, and R. Adhikari, "Hydrodynamic instabilities provide a generic route to spontaneous biomimetic oscillations in chemomechanically active filaments," Sci. Rep. **3** (2013), 10.1038/srep01964.

[134] J. S. Guasto, K. A. Johnson, and J. P. Gollub, "Oscillatory flows induced by microorganisms swimming in two dimensions," Phys. Rev. Lett. **105**, 168102 (2010).

[135] X. Chen, X. Yang, M. Yang, and H. P. Zhang, "Dynamic clustering in suspension of motile bacteria," EPL **111**, 54002 (2015).

[136] A. Sokolov, I. S. Aranson, J. O. Kessler, and R. E. Goldstein, "Concentration dependence of the collective dynamics of swimming bacteria," Phy. Rev. Lett. **98**, 158102 (2007).

[137] T. Vicsek, A. Czirók, E. Ben-Jacob, I. Cohen, and O. Shochet, "Novel type of phase transition in a system of self-driven particles," Phys. Rev. Lett. **75**, 1226 (1995).

[138] J. Toner and Y. Tu, "Long-range order in a two-dimensional dynamical XY model: How birds fly together," Phys. Rev. Lett. **75**, 4326 (1995).

[139] G. Grégoire and H. Chaté, "Onset of collective and cohesive motion," Phys. Rev. Lett. **92**, 025702 (2004).

[140] J. Tailleur and M. E. Cates, "Statistical mechanics of interacting run-and-tumble bacteria," Phys. Rev. Lett. **100**, 218103 (2008).

[141] M. E. Cates, D. Marenduzzo, I. Pagonabarraga, and J. Tailleur, "Arrested phase separation in reproducing bacteria creates a generic route to pattern formation," Proc. Natl. Acad. Sci. **107**, 11715–11720 (2010).

[142] M. E. Cates and J. Tailleur, "When are active brownian particles and run-and-tumble particles equivalent? consequences for motility-induced phase separation," EPL **101**, 20010 (2013).

[143] M. E. Cates and J. Tailleur, "Motility-induced phase separation," Annu. Rev. Condens. Mat. Phys. **6**, 219–244 (2015).

[144] S. Henkes, Y. Fily, and M. C. Marchetti, "Active jamming: Self-propelled soft particles at high density," Phys. Rev. E **84**, 040301 (2011).

[145] G. S. Redner, M. F. Hagan, and A. Baskaran, "Structure and dynamics of a phase-separating active colloidal fluid," Phys. Rev. Lett. **110**, 055701 (2013).

[146] B. A. Finlayson and L. E. Scriven, "Convective instability by active stress," Proc. Roy. Soc. A **310**, 183–219 (1969).

[147] R. A. Simha and S. Ramaswamy, "Hydrodynamic Fluctuations and Instabilities in Ordered Suspensions of Self-Propelled Particles," Phys. Rev. Lett. **89**, 058101 (2002).

[148] D. Saintillan and M. J.. Shelley, "Instabilities and Pattern Formation in Active Particle Suspensions: Kinetic Theory and Continuum Simulations," Phys. Rev. Lett. **100**, 178103 (2008).

[149] S. Ramachandran, P. B. Sunil Kumar, and I. Pagonabarraga, "A lattice-boltzmann model for suspensions of self-propelling colloidal particles," Eur. Phys. J. E **20**, 151–158 (2006).

[150] R. W. Nash, R. Adhikari, and M. E. Cates, "Singular forces and pointlike colloids in lattice Boltzmann hydrodynamics," Phys. Rev. E **77**, 026709 (2008).

[151] B. Delmotte, E. E. Keaveny, F. Plouraboué, and E. Climent, "Large-scale simulation of steady and time-dependent active suspensions with the force-coupling method," J. Comput. Phys. **302**, 524–547 (2015).

[152] I. Llopis and I. Pagonabarraga, "Dynamic regimes of hydrodynamically coupled self-propelling particles," Euro. Phys. Lett. **75**, 999 (2006).

[153] T. Ishikawa, M. P. Simmonds, and T. J. Pedley, "Hydrodynamic interaction of two swimming model micro-organisms," J. Fluid Mech. **568**, 119–160 (2006).

[154] T. Ishikawa, J. T. Locsei, and T. J. Pedley, "Development of coherent structures in concentrated suspensions of swimming model micro-organisms," J. Fluid Mech. **615**, 401–431 (2008).

[155] K. Kyoya, D. Matsunaga, Y. Imai, T. Omori, and T. Ishikawa, "Shape matters: Near-field fluid mechanics dominate the collective motions of ellipsoidal squirmers," Phys. Rev. E **92**, 063027 (2015).

[156] H. Moyses, J. Palacci, S. Sacanna, and D. G. Grier, "Trochoidal trajectories of self-propelled janus particles in a diverging laser beam," Soft Matter **12**, 6357–6364 (2016).

[157] M. Hennes, K. Wolff, and H. Stark, "Self-induced polar order of active Brownian particles in a harmonic trap," Phys. Rev. Lett. **112**, 238104 (2014).

[158] J. D. Weeks, D. Chandler, and H. C. Andersen, "Role of repulsive forces in determining the equilibrium structure of simple liquids," J. Chem. Phys. **54**, 5237–5247 (1971).

[159] M. Skoge, A. Donev, F. H. Stillinger, and S. Torquato, "Packing hyperspheres in high-dimensional Euclidean spaces," Phys. Rev. E **74**, 041127 (2006).

[160] Y. Fily and M. C. Marchetti, "Athermal phase separation of self-propelled particles with no alignment," Phys. Rev. Lett. **108**, 235702 (2012).

[161] J. Bialké, T. Speck, and H. Löwen, Phys. Rev. Lett. **108**, 168301 (2012).

[162] J. F. Joanny, J. Colloid Interface Sci. **71**, 622–624 (1979).

[163] M. Born and K. Huang, *Dynamical theory of crystal lattices* (Clarendon Press, 1954).

[164] R. Peierls, "Quelques propriétés typiques des corps solides," Ann. I. H. Poincaré **5**, 177–222 (1935).

[165] L. D. Landau, "Zur theorie der phasenumwandlungen ii," Phys. Z. Sowjetunion **11**, 26–35 (1937).

[166] J. M. Kosterlitz and D. J. Thouless, "Ordering, metastability and phase transitions in two-dimensional systems," J. Phys. C **6**, 1181 (1973).

[167] B. I. Halperin and D. R. Nelson, "Theory of two-dimensional melting," Phys. Rev. Lett. **41**, 121 (1978).

[168] D. R. Nelson and B. I. Halperin, "Dislocation-mediated melting in two dimensions," Phys. Rev. B **19**, 2457 (1979).

[169] A. P. Young, "Melting and the vector coulomb gas in two dimensions," Phys. Rev. B **19**, 1855 (1979).

[170] T. M. Squires, "Effective pseudo-potentials of hydrodynamic origin," J. Fluid Mech. **443**, 403–412 (2001).

[171] K. Yeo, E. Lushi, and P. M. Vlahovska, "Collective dynamics in a binary mixture of hydrodynamically coupled microrotors," Phys. Rev. Lett. **114**, 188301 (2015).

[172] M. Trau, D. A. Saville, and I. A. Aksay, "Field-induced layering of colloidal crystals," Science **272**, 706–709 (1996).

[173] Y. Solomentsev, M. Böhmer, and J. L. Anderson, Langmuir **13**, 6058–6068 (1997).

[174] R. Matas-Navarro, R. Golestanian, T. B. Liverpool, and S. M. Fielding, Phys. Rev. E **90**, 032304 (2014).

[175] W. Wang, W. Duan, Su. Ahmed, A. Sen, and T. E. Mallouk, "From one to many: Dynamic assembly and collective behavior of self-propelled colloidal motors," Acc. of Chem. Res. **48**, 1938–1946 (2015).

[176] M. S. D. Wykes, J. Palacci, T. Adachi, L. Ristroph, X. Zhong, M. D. Ward, J. Zhang, and M. J. Shelley, "Dynamic self-assembly of microscale rotors and swimmers," Soft Matter **12**, 4584–4589 (2016).

[177] A. Pandey, P. B. Sunil Kumar, and R. Adhikari, "Flow-induced nonequilibrium self-assembly in suspensions of stiff, apolar, active filaments," Soft Matter **12**, 9068–9076 (2016).

[178] A. B. Glendinning and W. B. Russel, "A pairwise additive description of sedimentation and diffusion in concentrated suspensions of hard spheres," J. Coll. Int. Sci. **89**, 124–143 (1982).

[179] G. K Batchelor, "Sedimentation in a dilute dispersion of spheres," J. Fluid Mech. **52**, 245–268 (1972).

[180] C. W. J. Beenakker, "Ewald sum of the Rotne–Prager tensor," J. Chem. Phys. **85**, 1581–1582 (1986).

[181] H. Hasimoto, "On the periodic fundamental solutions of the Stokes equations and their application to viscous flow past a cubic array of spheres," J. Fluid Mech. **5**, 317–328 (1959).

[182] P. G. Saffman, "On the settling speed of free and fixed suspensions," Stud. Appl. Math. **52**, 115–127 (1973).

[183] J. M. Crowley, "Clumping instability of a falling horizontal lattice," Phys. Fluids **19**, 1296–1300 (1976).

[184] J. M. Crowley, "Viscosity-induced instability of a one-dimensional lattice of falling spheres," J. Fluid Mech. **45**, 151–159 (1971).

[185] S. Ramaswamy, "Issues in the statistical mechanics of steady sedimentation," Adv. Phys. **50**, 297–341 (2001).

[186] S. Thutupalli, D. Geyer, R. Singh, R. Adhikari, and H. A. Stone, "Boundaries determine the collective dynamics of self-propelled particles," arXiv:1710.10300 .

[187] S. Herminghaus, Corinna C. Maass, C. Krüger, S. Thutupalli, L. Goehring, and C. Bahr, "Interfacial mechanisms in active emulsions," Soft Matter **10**, 7008–7022 (2014).

[188] H. P. Langtangen and L. Wang, "Odespy," (2012).

[189] É. Fodor, C. Nardini, M. E. Cates, J. Tailleur, P. Visco, and F. van Wijland, "How far from equilibrium is active matter?" Phys. Rev. Lett. **117**, 038103 (2016).

[190] A. R. Altenberger and J. M. Deutch, "Light scattering from dilute macromolecular solutions," J. Chem. Phys. **59**, 894–898 (1973).

[191] G. D. J. Phillies, "Effects of intermacromolecular interactions on diffusion. I. Two-component solutions," J. Chem. Phys. **60**, 976–982 (1974).

[192] B. J. Ackerson, "Correlations for interacting Brownian particles," J. Chem. Phys. **64**, 242–246 (1976).

[193] B. U. Felderhof, "Diffusion of interacting Brownian particles," J. Phys. A **11**, 929 (1978).

[194] T. Ohtsuki and K. Okano, "Diffusion coefficients of interacting Brownian particles," J. Chem. Phys. **77**, 1443–1450 (1982).

[195] P. Résibois and M. De Leener, *Classical kinetic theory of fluids* (John Wiley & Sons, 1977).

[196] H. Touchette, "The large deviation approach to statistical mechanics," Phys. Rep. **478**, 1–69 (2009).

[197] H. Goldstein, *Classical mechanics* (Addison-Wesley, 1980).

[198] D. Sarkar, R. Singh, A. Som, Manju C. K., R. Adhikari, and T. Pradeep, "Electrohydrodynamic assembly of ambient ion-derived nanoparticles," Submitted .

[199] O. Björneholm et al, "Water at interfaces," Chem. Rev. **116**, 7698–7726 (2016).

[200] S. Behnel, R. Bradshaw, C. Citro, L. Dalcin, D. S. Seljebotn, and K. Smith, "Cython: The best of both worlds," Comp. Sci. & Eng. **13**, 31–39 (2011).

[201] J. R. Blake, "On the movement of mucus in the lung," J. Biomech. **8**, 179–190 (1975).

[202] K Aderogba, "On Stokeslets in a two-fluid space," J. Eng. Math. **10**, 143–151 (1976).

[203] J. R. Blake, "A note on the image system for a Stokeslet in a no-slip boundary," Proc. Camb. Phil. Soc. **70**, 303–310 (1971).

[204] N. Liron and S. Mochon, "Stokes flow for a Stokeslet between two parallel flat plates," J. Eng. Math. **10**, 287–303 (1976).

[205] M. E Staben, A. Z. Zinchenko, and R. H. Davis, "Motion of a particle between two parallel plane walls in low-Reynolds-number poiseuille flow," Phys. Fluids **15**, 1711–1733 (2003).

[206] M. R. Maxey and B. K. Patel, "Localized force representations for particles sedimenting in Stokes flow," Int. J Multiphase flow **27**, 1603–1626 (2001).

[207] A. Laskar and R. Adhikari, "Filament actuation by an active colloid at low Reynolds number," New J. Phys. **19**, 033021 (2017).

[208] R. K. Manna, P. B. S. Kumar, and R. Adhikari, "Colloidal transport by active filaments," J. Chem. Phys. **146**, 024901 (2017).

[209] U. Seifert, "Stochastic thermodynamics, fluctuation theorems and molecular machines," Rep. Prog. Phys. **75**, 126001 (2012).

[210] D. L. Koch and G. Subramanian, "Collective hydrodynamics of swimming microorganisms: Living fluids," Annu. Rev. Fluid Mech. **43**, 637–659 (2011).

[211] J. D. Jackson, *Classical electrodynamics* (Wiley, 1962).

[212] R. Farwig, "A note on the reflection principle for the biharmonic equation and the Stokes system," Acta Appl. Math. **37**, 41–51 (1994).

[213] K. Aderogba and J. R. Blake, "Action of a force near the planar surface between semi-infinite immiscible liquids at very low Reynolds numbers," Bull. Australian Math. Soc. **19**, 309–318 (1978).

[214] H. A. Lorentz, "A general theorem concerning the motion of a viscous fluid and a few consequences derived from it," Versl. Konigl. Akad. Wetensch. Amst **5**, 168–175 (1896).

[215] A. P. Berke, L. Turner, H. C. Berg, and E. Lauga, "Hydrodynamic attraction of swimming microorganisms by surfaces," Phys. Rev. Lett. **101**, 038102 (2008).

[216] E. Lauga and T. R. Powers, "The hydrodynamics of swimming microorganisms," Rep. Prog. Phys. **72**, 096601 (2009).

[217] R. E. Goldstein, "Green algae as model organisms for biological fluid dynamics," Ann. Rev. Fluid Mech. **47**, 343–375 (2015).

[218] A. J. T. M. Mathijssen, D. O. Pushkin, and Julia M Yeomans, "Tracer trajectories and displacement due to a micro-swimmer near a surface," J. Fluid Mech. **773**, 498–519 (2015).

[219] R. Schmitz, "Force multipole moments for a spherically symmetric particle in solution," Physica A: Stat. Mech. Appl. **102**, 161–178 (1980).

[220] Y. Saad, *Iterative methods for sparse linear systems* (SIAM, 2003).